

**STUDY OF THE EFFECTS OF NEUTRAL GAS HEATING  
IN A RADIO FREQUENCY INDUCTIVELY COUPLED  
PLASMA**

**KANESH KUMAR A/L JAYAPALAN**

**DEPARTMENT OF PHYSICS  
FACULTY OF SCIENCE  
UNIVERSITY OF MALAYA  
KUALA LUMPUR**

**2015**

**STUDY OF THE EFFECTS OF NEUTRAL GAS  
HEATING IN A RADIO FREQUENCY INDUCTIVELY  
COUPLED PLASMA**

**KANESH KUMAR A/L JAYAPALAN**

**THESIS SUBMITTED IN FULFILMENT OF  
THE REQUIREMENTS FOR THE DEGREE OF  
DOCTOR OF PHILOSOPHY**

**DEPARTMENT OF PHYSICS  
FACULTY OF SCIENCE  
UNIVERSITY OF MALAYA  
KUALA LUMPUR**

**2015**

**UNIVERSITY OF MALAYA**  
**ORIGINAL LITERARY WORK DECLARATION**

Name of Candidate: KANESH KUMAR A/L JAYAPALAN

I.C/Passport No: XXXXXXXXXX

Registration/Matric No: SHC080017

Name of Degree: DOCTOR OF PHILOSOPHY

Title of Thesis: STUDY OF THE EFFECTS OF NEUTRAL GAS HEATING IN A  
RADIO FREQUENCY INDUCTIVELY COUPLED PLASMA

Field of Study: INDUCTIVELY COUPLED PLASMAS

I do solemnly and sincerely declare that:

- (1) I am the sole author/writer of this Work;
- (2) This Work is original;
- (3) Any use of any work in which copyright exists was done by way of fair dealing and for permitted purposes and any excerpt or extract from, or reference to or reproduction of any copyright work has been disclosed expressly and sufficiently and the title of the Work and its authorship have been acknowledged in this Work;
- (4) I do not have any actual knowledge nor do I ought reasonably to know that the making of this work constitutes an infringement of any copyright work;
- (5) I hereby assign all and every rights in the copyright to this Work to the University of Malaya ("UM"), who henceforth shall be owner of the copyright in this Work and that any reproduction or use in any form or by any means whatsoever is prohibited without the written consent of UM having been first had and obtained;
- (6) I am fully aware that if in the course of making this Work I have infringed any copyright whether intentionally or otherwise, I may be subject to legal action or any other action as may be determined by UM.

Candidate's Signature

Date:

Subscribed and solemnly declared before,

Witness's Signature

Date:

Name:

Designation:

## ABSTRACT

A 13.56 MHz, planar coil, inductively coupled plasma reactor was experimentally and theoretically characterized; with emphasis on the effects of neutral gas heating on the distribution of the H mode magnetic fields of the source coil and the E-H mode transition characteristics of the discharge.

The radially resolved electron density,  $n_e$ , electron temperature,  $T_e$  and electron energy distribution function (EEDF) were measured using a Langmuir probe at different axial distances above the dielectric plate for 0.03, 0.07 and 0.2 mbar argon pressures. The range of  $n_e$  and  $T_e$  obtained were  $(0.065 \pm 0.004)$ - $(4.0 \pm 0.6) \times 10^{17} \text{ m}^{-3}$  and  $(1.38 \pm 0.08)$ - $(3.8 \pm 0.2) \text{ eV}$  assuming Maxwellian distribution. The measured  $n_e$  distribution at 0.2 mbar suggested significant influence of neutral gas heating. EEDF plots showed that the distributions were Maxwellian-like.

The radially resolved absolute axial magnetic field,  $|B_z|$ , and absolute radial magnetic fields,  $|B_r|$ , were measured using electrostatically compensated magnetic probes in the appropriate orientations. The fields were measured at different axial distances above the dielectric plate for the chamber in evacuated condition and for 0.03, 0.07 and 0.2 mbar argon pressures. R.f. power was set at 180 W. Maximum  $|B_z|$  and  $|B_r|$  fields were obtained when the chamber was in evacuated condition with values of  $(1.507 \pm 0.005) \times 10^{-4} \text{ T}$  and  $(7.67 \pm 0.01) \times 10^{-5} \text{ T}$ , respectively.

The peak E-H mode transition current,  $I_{tr}$  and peak H-E mode transition current,  $I_{mt}$  were measured using a current probe for 0.02-0.2 mbar argon pressures. The minimum value for  $I_{tr}$  was  $(13.5 \pm 0.5) \text{ A}$  at 0.08 mbar, whereas, the minimum value for  $I_{mt}$  was  $(8.3 \pm 0.1) \text{ A}$  at 0.3 mbar. As pressure is increased, hysteresis between E-H mode and H-E mode transitions was observed to become more distinct.

The line averaged neutral gas temperature,  $T_n$ , was measured using a fiber probe with the actinometry optical emission spectroscopy (AOES) technique at 0.03, 0.05, 0.07, 0.1 and 0.2 mbar argon pressure for different axial distances above the dielectric plate. R.f. power was varied from 100 W to 200 W. The range of  $T_n$  obtained was  $(350 \pm 30)$ - $(840 \pm 30)$  K.

For theoretical characterization, two predictive models were used. The first was an electromagnetic field model that simulates  $|B_z|$  and  $|B_r|$ , using empirically fitted, spatially resolved electron density,  $n_e(r, z)$  and electron temperature,  $T_e(r, z)$ . Simulations were run for spatially averaged  $T_n$  and heuristically fitted, spatially distributed temperature,  $T_n(r, z)$ .  $T_n(r, z)$  gave the closest agreement to the measured magnetic fields.

The second model was a power deposition model that simulates  $I_{tr}$  and  $I_{mt}$ . Simulations were run for  $T_n = 300$  K and at elevated  $T_n$ . Calculations better matched the measured values only when neutral gas heating was considered. The effect of hysteresis in mode transition of the discharge was also demonstrated using a fitted 3D power evolution plot.

These results indicate that neutral gas heating plays an important role in influencing plasma parameters. Thus, knowledge of the effects of neutral gas heating is essential in providing better understanding of the formation and maintenance of the plasma discharge.

## ABSTRAK

Reaktor plasma makmal yang berjanakan gegelung sesatah enam lilitan pada frekuensi 13.56 MHz telah dicirikan secara eksperimen dan teori; dengan penekanan diberikan kepada kesan-kesan pemanasan gas neutral terhadap taburan medan magnetik mod H yang dijanakan oleh gegelung sesatah serta ciri-ciri peralihan mod E-H plasma.

Ketumpatan elektron,  $n_e$ , suhu elektron,  $T_e$  dan fungsi taburan tenaga elektron, EEDF telah diukur mengikut jejari reaktor dengan menggunakan kuar Langmuir pada jarak paksi berbeza di atas plet dielektrik untuk tekanan argon 0.03, 0.07 dan 0.2 mbar. Julat  $n_e$  dan  $T_e$  yang diperolehi ialah  $(0.065 \pm 0.004)$ - $(4.0 \pm 0.6) \times 10^{17} \text{ m}^{-3}$  dan  $(1.38 \pm 0.08)$ - $(3.8 \pm 0.2) \text{ eV}$  dengan andaian taburan Maxwell. Ukuran taburan  $n_e$  pada tekanan 0.2 mbar telah menunjukkan pengaruh pemanasan gas neutral yang ketara. EEDF yang diplot memberikan taburan yang menyerupai taburan Maxwell.

Medan magnet mutlak paksian,  $|B_z|$  dan medan magnet mutlak jejarian,  $|B_r|$  juga telah diukur mengikut jejari reaktor dengan menggunakan kuar magnetik lawanan elektrostatik pada orientasi masing-masing.  $|B_z|$  dan  $|B_r|$  juga telah diukur pada jarak paksi berbeza di atas plat dielektrik untuk reaktor pada keadaan vakum dasar dan pada tekanan argon 0.03, 0.07 dan 0.2 mbar. Kuasa frekuensi radio telah ditetapkan pada 180 W. Medan  $|B_z|$  dan  $|B_r|$  maksima (masing-masing bernilai  $(1.507 \pm 0.005) \times 10^{-4} \text{ T}$  dan  $(7.67 \pm 0.01) \times 10^{-5} \text{ T}$ ) telah diperolehi untuk reaktor pada keadaan vakum dasar.

Arus puncak peralihan mod E ke mod H,  $I_{tr}$  dan arus puncak peralihan mod H ke mod E,  $I_{mt}$  telah diukur dengan menggunakan kuar arus untuk julat tekanan argon 0.02-0.2 mbar. Nilai minima untuk  $I_{tr}$  ialah  $(13.5 \pm 0.5) \text{ A}$  pada tekanan 0.08 mbar, manakala nilai minima untuk  $I_{mt}$  ialah  $(8.3 \pm 0.1) \text{ A}$  pada tekanan 0.3 mbar. Apabila tekanan argon meningkat, kesan histerisis di antara peralihan mod E-H dan peralihan mod H-E bertambah ketara.

Suhu purata satah gas neutral,  $T_n$ , telah diukur menggunakan kuar gentian optik dengan teknik aktinometri spektroskopi pancaran optik (AOES) pada tekanan argon 0.03, 0.05, 0.07, 0.1 dan 0.2 mbar untuk jarak paksi berbeza di atas plet dielektrik. Kuasa frekuensi radio telah dibezakan dari 100-200 W. Julat  $T_n$  yang diperoleh ialah  $(350 \pm 30)$ - $(840 \pm 30)$  K.

Untuk pencirian teori, dua model ramalan telah digunakan. Model ramalan pertama ialah model medan elektromagnetik yang mensimulasikan  $|B_z|$  dan  $|B_r|$  dengan menggunakan taburan ketumpatan elektron ruangan,  $n_e(r, z)$  serta taburan suhu elektron ruangan,  $T_e(r, z)$  yang suaikan secara empirikal. Simulasi telah dijalankan dengan menggunakan suhu purata  $T_n$  serta taburan suhu ruangan yang diperoleh daripada penyesuaian heuristik,  $T_n(r, z)$ . Simulasi dengan  $T_n(r, z)$  telah memberikan persetujuan yang terbaik dengan medan magnet ukuran.

Model ramalan kedua ialah model pemendapan kuasa yang mensimulasikan  $I_{tr}$  dan  $I_{mt}$ . Simulasi telah dijalankan pada suhu  $T_n = 300$  K dan pada suhu  $T_n$  tertinggi. Nilai-nilai simulasi lebih menyetujui nilai-nilai ukuran hanya apabila kesan pemanasan gas neutral diambil kira. Kesan histerisis terhadap peralihan mod plasma juga telah ditunjukkan dengan menggunakan plot evolusi kuasa 3 dimensi yang disuaikan.

Keputusan-keputusan ini menunjukkan bahawa pemanasan gas neutral memainkan peranan penting dalam mempengaruhi parameter plasma. Oleh itu, pengetahuan tentang kesan pemanasan gas neutral adalah penting untuk memberikan pemahaman yang lebih baik tentang pembentukan dan pengekalannya plasma.

## **ACKNOWLEDGEMENT**

I would firstly, like to convey my heartfelt gratitude to my supervisor, Associate Professor Dr. Chin Oi Hoong for her support and guidance towards the completion of my Ph.D. Her presence and confidence in my abilities have given me the motivational strength to persevere through the toughest times of my candidature.

I would also like to give my sincere appreciation to our centre's technician Mr. Jasbir Singh Atma Singh for his invaluable assistance, especially in purchasing and provision of the required equipment and materials for this study.

I would next, like to extend the warmest thanks to all my peers and colleagues (in past and in present) whom have supported me with advice and kindness. Their friendship and camaraderie has made my journey in University Malaya a more positive and memorable one. Special thanks to my lab mates, Choo Chee Yee, Tamilmany K. Thandavan, Chan Li San and Siti Sarah Safaai for their help in experiments and in situations which needed the extra pairs of hands.

I would also like to express my deepest appreciation to my parents for their unwavering support throughout the numerous years of commitment and investment made in pursuit of this higher degree. It is only their patience, love and encouragement that have brought me this far in life.

I would finally, like to acknowledge the University Malaya Research Grants (UMRG) PS329-2010A and RG135-10AFR and Short Term Research Fund (PJP) FS280/2007C for funding of experimental and simulation work found in this thesis.

## LIST OF PUBLICATIONS

1. Chin, O. H., **Jayapalan, K. K.**, & Wong, C. S. (2014, August). Effect of neutral gas heating in argon radio frequency inductively coupled plasma. In *International Journal of Modern Physics Conference Series* (Vol. 32, p. 60320).
2. **Jayapalan, K. K.**, & Chin, O. H. (2014). Effect of neutral gas heating on the wave magnetic fields of a low pressure 13.56 MHz planar coil inductively coupled argon discharge. *Physics of Plasmas*, 21(4), 043510.
3. **Jayapalan, K. K.**, & Chin, O. H. (2012). The effects of neutral gas heating on H mode transition and maintenance currents in a 13.56 MHz planar coil inductively coupled plasma reactor. *Physics of Plasmas*, 19(9), 093501.
4. **Jayapalan, K. K.**, & Chin, O. H. (2009, July). Simulation and Experimental Study of a 13.56 MHz Planar Coil, Inductively Coupled Plasma Reactor. In *Frontiers in Physics: 3rd International Meeting* (Vol. 1150, No. 1, pp. 440-443).

## LIST OF CONFERENCE PRESENTATIONS

1. National Physics Conference (PERFIK) 2014, Sunway Resort Hotel and Spa, Kuala Lumpur, Malaysia: 18-19, November 2014.  
Contributed paper (poster presentation) titled 'Determination of Neutral Gas Temperature Using Actinometry Optical Emission Spectroscopy (AOES)'.
2. 3<sup>rd</sup> International Meeting on Frontiers of Physics (IMFP) 2009, Awana Golf and Country Resort, Genting Highlands, Kuala Lumpur, Malaysia: 12-16th January 2009.  
Contributed paper (oral presentation) titled 'Simulation and experimental study of a 13.56 MHz planar coil, inductively coupled plasma reactor'.
3. 4<sup>th</sup> Mathematics and Physical Science Graduate Conference (MPSGC) 2008, University of Malaya, Kuala Lumpur, Malaysia: 15-18 December 2008.  
Contributed paper (oral presentation) titled 'Hysteresis modeling for a 13.56 MHz planar coil, inductively coupled plasma system'.
4. 2<sup>nd</sup> International Conference on Science and Technology (ICSTIE) 2008-Applications in Industry and Education, University Teknologi MARA, Pulau Pinang, Malaysia: 12-13 December 2008.  
Contributed paper (oral presentation) titled 'Simulation Of hysteresis between E- and H-mode transitions for a 13.56 MHz planar coil ICP reactor'.
5. National Physics Conference (PERFIK) 2007, Heritage Bay Club, Pulau Duyong, Kuala Terengganu, Terengganu, Malaysia: 26-28 December 2007.  
Contributed paper (oral presentation) titled 'Mapping of the electromagnetic field distribution in a planar coil, inductively coupled plasma reactor'.
6. 3<sup>rd</sup> Mathematics and Physical Science Graduate Conference (MPSGC) 2008, University of Malaya, Kuala Lumpur, Malaysia: 12-14 December 2007.  
Contributed paper (poster presentation) titled 'Theoretical investigation of the electromagnetic field in a 13.56 MHz RF planar coil, inductively coupled plasma reactor'.

# TABLE OF CONTENTS

<b>ABSTRACT</b>	iii
<b>ABSTRAK</b>	v
<b>ACKNOWLEDGEMENT</b>	vii
<b>LIST OF PUBLICATIONS</b>	viii
<b>LIST OF CONFERENCE PRESENTATIONS</b>	viii
<b>TABLE OF CONTENTS</b>	ix
<b>LIST OF FIGURES</b>	xiv
<b>LIST OF TABLES</b>	xx
<b>LIST OF SYMBOLS</b>	xxi
<b>CHAPTER 1: INTRODUCTION</b>	<b>1</b>
1.0. Introduction and Motivation of Study	1
1.1. Objectives of Study	4
1.1.1. Experiment	4
1.1.2. Simulation	5
1.2. Layout of Thesis	6
<b>CHAPTER 2: LITERATURE REVIEW</b>	<b>8</b>
2.0. History and Origins	8
2.1. E mode, H mode and Hysteresis	11
2.2. Theoretical Development and Simulation of Electrodeless Discharges and ICPs	15
2.3. Measurement of Neutral Gas Heating and the Effects of Neutral Gas Depletion	27

<b>CHAPTER 3: EXPERIMENT</b>	<b>35</b>
3.0. Experimental Setup	35
3.1. Langmuir Probe Setup	37
3.1.1. Langmuir Probe Diagnostics Setup	39
3.1.2. Langmuir Probe Theory and Analysis	40
3.2. Magnetic Probe Setup	47
3.2.1. Probe Theory and Analysis	49
3.3. Current and Voltage Probes	51
3.4. Actinometry Optical Emission Spectroscopy (AOES) Setup	52
3.4.1. AOES Theory and Analysis	53
<b>CHAPTER 4: RESULTS, ANALYSIS AND DISCUSSION - EXPERIMENT</b>	<b>68</b>
4.0. Measurement of Discharge Electrical Characteristics	68
4.0.1. Electron Density, $n_e$ and Electron Temperature, $T_e$	68
4.0.2. Electron Energy Probability Function (EPPF)	77
4.1. Measurement of Discharge Magnetic Fields	81
4.1.1. Absolute Axial, $ B_z $ and Radial, $ B_r $ Magnetic Fields	81
4.2. Measurement of Peak Coil Transition and Maintenance Currents	84
4.2.1. H Mode Peak Transition, $I_{tr}$ and Maintenance, $I_{mt}$ Currents	85
4.3. Measurement of Discharge Neutral Gas Temperature via AOES	87
4.3.1. Measured Neutral Gas Temperature, $T_n$	87
<b>CHAPTER 5: SIMULATION</b>	<b>92</b>
5.0. Electromagnetic Field Model	92
5.1. Analytical H mode fields	96
5.1.1. Separation of Variables Method for the H mode Fields	99

5.1.2. Solving for H mode Boundary Constants	105
5.2. Numerical H mode fields	109
5.2.1. Calculation of Effective Collision Frequency, $\nu_{\text{eff}}(r, z)$	111
5.2.2. Five Point Stencil Algorithm	114
5.3. Analytical E mode fields	117
5.3.1. Separation of Variables Method for the E mode Fields	120
5.3.2. Solving for E mode Boundary Constants	124
5.4. Power Balance Model	128
5.4.1. Absorbed Electron Power, $P_{\text{abs}}$	128
5.4.2. Electron Power Loss, $P_{\text{loss}}$	131
<b>CHAPTER 6: RESULTS, ANALYSIS AND DISCUSSION - SIMULATION</b>	<b>135</b>
6.0. Predictive Simulation of the Discharge Magnetic Fields	135
6.0.1. Empirical fitting of the Spatially Resolved Electron Density, $n_e(r, z)$ and Spatially Resolved Electron Temperature, $T_e(r, z)$	135
6.0.2. Heuristic fitting of the Spatially Resolved Neutral Gas Temperature, $T_n(r, z)$	143
6.0.3. Spatially averaged neutral gas temperatures, $T_{n,\text{ave}}$	149
6.0.4. Comparison of Measured and Simulated Magnetic Fields	149
6.1. Predictive Simulation of H mode Transition and Maintenance Currents	155
6.1.1. E-H mode Transition Dynamics and Hysteresis Effects in Discharge	155
6.1.2. Comparison of Measured H mode Transition Current, $I_{\text{tr}}$ and H mode Maintenance Current, $I_{\text{mt}}$ with Simulation	160
<b>CHAPTER 7: SUMMARY AND CONCLUSION</b>	<b>164</b>
7.0. Overview	164

7.1. Experimental Characterization	164
7.1.1. Measurement of Electron Density, $n_e$ and Electron Temperature, $T_e$ and Electron Energy Distribution Function (EEDF)	164
7.1.2. Measurement of Absolute Axial Magnetic Field, $ B_z $ and Radial Magnetic Field, $ B_r $	167
7.1.3. Measurement of Peak H mode Transition, $I_{tr}$ and H mode Maintenance Currents, $I_{mt}$	168
7.1.4. Measurement Neutral Gas Temperature, $T_n$	169
7.2. Theoretical Characterization	170
7.2.1. Predictive Simulation of the Discharge Magnetic Fields	171
7.2.2. Predictive Simulation of H mode Transition and Maintenance Currents	171
7.3. Suggestions for Future Work	172
<b>REFERENCES</b>	<b>175</b>
<b>APPENDIX A: LANGMUIR PROBE PARAMETRIC SOLVER</b>	<b>187</b>
<b>APPENDIX B: AOES <math>T_n</math> SOLVER</b>	<b>194</b>
B.1. AOES Line Width and Line Position Convolution Solver	194
B.2. AOES Minimum $\chi^2$ Neutral Gas Temperature Solver	201
<b>APPENDIX C: ANALYTICAL H MODE FIELD MODEL</b>	<b>205</b>
<b>APPENDIX D: POWER BALANCE MODEL</b>	<b>212</b>

<b>APPENDIX E: AUXILLARY DATA AND RELATED PROGRAMS</b>	<b>219</b>
E.1. Argon Collision Cross Section Spreadsheet ('ArgonCC.xls')	219
E.2. Bessel Zeros Function Code	221
E.3. Empty Excel Sheet Delete Code	223
<b>APPENDIX F: FITTING PARAMETERS FOR SIMULATION</b>	<b>224</b>

## LIST OF FIGURES

Figure	Caption	Page
1.1	Laboratory 13.56 MHz r.f. argon ICP operating at (a) E mode and (b) H mode at 0.1 mbar.	2
1.2	The measured effects of hysteresis in the planar coil ICP reactor at 0.1 mbar argon pressure. The power required to cause a transition from E to H mode is higher (~82 W) than the power required for maintaining H mode (~ 66 W) (Lim, 2010).	2
1.3	The two types of coil configurations used in ICP design: (a) helical and (b) planar (Lieberman & Lichtenberg, 2005).	3
2.1	Cross-wound solenoid as demonstrated by Townsend and Donaldson (1928) which effectively cancels most of the electrostatic fields within the solenoid. The winds at the upper ends ( $A_2C_2-5$ and $B_2D_2-1$ ) still carry an electrostatic field.	9
2.2	The combination circuit used in MacKinnon's experiment with both damped and c. w. oscillation capability. A Hartley oscillator (labeled Hartley Helix) is used for c. w. operation of the pancake coil, whereas, a Leyden jar, spark gap and X-ray transformer was used for damped operation (MacKinnon, 1929).	10
2.3	Current amplitude differences between (a) damped oscillation generated by a spark gap and (b) c. w. oscillation produced by an oscillator. The much higher amplitude of current in damped oscillation provides the energy required for excitation of a ring discharge (MacKinnon, 1929).	10
2.4	A 3 dimensional plot visualizing the possible operating points and branching paths taken by a modeled ICP system. Hysteresis of E to H mode ((2)-(3)) and H to E mode ((5)-(6)) transitions is also shown (El Fayoumi, Jones & Turner, 1998).	13
2.5	The (a) measured and (b) simulated magnetic field lines for an evacuated, planar coil, ICP source at 0.56 MHz (El Fayoumi & Jones, 1998).	20
2.6	Example of a basic Particle in Cell-Monte Carlo Collision (PIC-MCC) algorithm. Representative particles are updated for changes in their spatial properties under the influence of an electromagnetic field and by randomized collisions at discrete time steps (Birdsall, 1991).	21
2.7	Measured neutral gas density, $n_n$ ( $m^{-3}$ ) (black circles) versus radius, $r$ (m) of an ICP reactor operating at 10 mTorr argon pressure and 2000 W power. Neutral gas depletion is seen nearing the discharge center at $r = 0$ m. Grey line shows the initial neutral gas density before discharge ignition (Shimada, Tynan & Cattolica, 2007).	27

2.8	Graphs show (a) measured neutral gas temperature with increasing power at 0.05, 0.5 and 5 Pa and (b) measured contribution of electron pressure and gas temperature towards neutral gas depletion with increasing chamber pressure at 1000 W. Depletion of neutrals due to gas temperature becomes increasingly important as chamber pressure is increased (O'Connell et al., 2008).	31
2.9	Measured neutral gas temperature versus (a) discharge power and (b) logarithm of pressure for an argon discharge using AOES. The highest neutral gas temperature obtained was 1850 K at 600 W (Li et al., 2011).	34
3.1	Inductively Coupled Plasma (ICP) setup used for experiments.	36
3.2	Langmuir probe and mount schematics.	38
3.3	Langmuir probe diagnostics setup.	39
3.4	Measured Langmuir probe $I$ - $V$ signal and differential curve ( $d^2I_{\text{probe}}/dV^2_{\text{probe}}$ ) at 0.032 m axial height for 0.2 mbar pressure and 180 W r.f. power. <b>I</b> represents the ion saturation region, <b>II</b> represents the electron retardation region and <b>III</b> represents the electron saturation region. Measurement was taken at the plasma center ( $R = 0$ m).	40
3.5	The four different current collection regimes for a Langmuir probe (Maurice, 2003).	42
3.6	Magnetic probe schematics and circuit.	48
3.7	Oscilloscope screen capture for the axial magnetic probe at 0.032 m axial distance above the dielectric plate, 0.07 mbar argon pressure and 180 W r.f. power. Measurement was taken at the plasma center ( $R = 0$ m).	49
3.8	Axial and radial magnetic probe calibration curves.	50
3.9	Measured peak planar coil voltage, $V_{\text{p, vac}}$ (V) versus peak planar coil current, $I_{\text{p, vac}}$ (A) at evacuated condition.	51
3.10	AOES probe and mount schematics.	53
3.11	Measured H mode Ar/N <sub>2</sub> emission spectra showing the nitrogen second positive system ( $\text{N}_2\text{C}^3\Pi_u - \text{N}_2\text{B}^3\Pi_g$ ) at 0.05 mbar pressure (~95% Ar/~5% N <sub>2</sub> ) and 200 W r.f. power. The chosen peak for simulation (0-2) is indicated.	55
3.12	Discrete synthetic spectrum for the 0-2 vibrational emission peak of the nitrogen second positive system $\text{N}_2\text{C}^3\Pi_u \rightarrow \text{N}_2\text{B}^3\Pi_g$ at $T_n = 550$ K	61
3.13	Calibration curve for the HR4000 spectrometer.	61
3.14	Voigt profile fitted to the measured Hg peak at 435.8 nm.	63

3.15	The discrete synthetic spectra (a) is convolved with instrumental broadening (c) via Voigt function resulting in the convolved synthetic spectrum (b). The convolved synthetic spectrum takes the shape of the experimentally measured 0-2 vibro-rotational peak seen in Figure 3.11.	65
3.16	Demonstration of the measured spectrum intensity, $x$ and convolved spectrum intensity, $x_0$ ; interpolated to coincide with the central bin wavelength.	66
3.17	(a) $\chi^2$ plot showing minimum fitting value at 550 K (b) Experimental 0-2 vibro-rotational peak at 0.05 mbar Ar/N <sub>2</sub> pressure and 200 W r.f. power fitted with the convolved synthetic spectrum at 550 K.	67
4.1a	Maxwellian (i) electron density, $n_e$ and (ii) electron temperature, $T_e$ measured at 0.032 m distance above the dielectric plate for 0.03, 0.07 and 0.2 mbar argon pressures. R.f. power was set at 180 W.	69
4.1b	EEDF (i) electron density, $n_e$ and (ii) electron temperature, $T_e$ measured at 0.032 m distance above the dielectric plate for 0.03, 0.07 and 0.2 mbar argon pressures. R.f. power was set at 180 W.	70
4.2a	Maxwellian (i) electron density, $n_e$ and (ii) electron temperature, $T_e$ measured at 0.060 m distance above the dielectric plate for 0.03, 0.07 and 0.2 mbar argon pressures. R.f. power was set at 180 W.	71
4.2b	EEDF (i) electron density, $n_e$ and (ii) electron temperature, $T_e$ measured at 0.060 m distance above the dielectric plate for 0.03, 0.07 and 0.2 mbar argon pressures. R.f. power was set at 180 W.	72
4.3a	Maxwellian (i) electron density, $n_e$ and (ii) electron temperature, $T_e$ measured at 0.114 m distance above the dielectric plate for 0.03, 0.07 and 0.2 mbar argon pressures. R.f. power was set at 180 W.	73
4.3b	EEDF (i) electron density, $n_e$ and (ii) electron temperature, $T_e$ measured at 0.114 m distance above the dielectric plate for 0.03, 0.07 and 0.2 mbar argon pressures. R.f. power was set at 180 W.	74
4.4	Electron energy probability function (EEPF) at 0.032 m distance above the dielectric plate for 0.03, 0.07 and 0.2 mbar argon pressures with corresponding parametric fit. R.f. power was at 180 W.	79
4.5	Electron energy probability function (EEPF) at 0.060 m distance above the dielectric plate for 0.03, 0.07 and 0.2 mbar argon pressures with corresponding parametric fit. R.f. power was at 180 W.	79
4.6	Electron energy probability function (EEPF) at 0.114 m distance above the dielectric plate for 0.03, 0.07 and 0.2 mbar argon pressures with corresponding parametric fit. R.f. power was at 180 W.	80

4.7	Measured absolute magnitudes of the (i) axial and (ii) radial magnetic fields at 0.032 m distance above the dielectric plate for evacuated, 0.03 mbar, 0.07 mbar and 0.2 mbar argon pressures. R.f. power was set at 180 W.	82
4.8	Measured absolute magnitudes of the (i) axial and (ii) radial magnetic fields at 0.060 m distance above the dielectric plate for evacuated, 0.03 mbar, 0.07 mbar and 0.2 mbar argon pressures. R.f. power was set at 180 W.	83
4.9	Measured H mode peak coil transition current, $I_{tr}$ (E-H) and H mode peak coil maintenance current, $I_{mt}$ (H-E) for 0.02-0.2 mbar argon pressure.	85
4.10	Measured neutral gas temperature, $T_n$ at 0.03, 0.05, 0.07, 0.1 and 0.2 mbar Ar/N <sub>2</sub> pressures for (i) increasing and (ii) decreasing r.f. power. Measurement was made at 0.032 m distance above the dielectric plate.	88
4.11	Measured neutral gas temperature, $T_n$ at 0.03, 0.05, 0.07, 0.1 and 0.2 mbar Ar/N <sub>2</sub> pressures for (i) increasing and (ii) decreasing r.f. power. Measurement was made at 0.060 m distance above the dielectric plate.	89
5.1	Numerical model diagram of the laboratory ICP reactor.	93
5.2	Analytical model diagram of the laboratory ICP reactor.	97
5.3	The five point stencil algorithm illustrated. The field values at the four adjacent (blue) grid points are used to calculate the new field value for the center (red) grid point.	114
5.4	Program flowchart for the numerical H mode fields.	116
6.1a	Empirically fitted 2D Gaussian based distribution of electron density $n_e(r, z)$ used for the magnetic field simulation at 0.03 mbar argon pressure and 180 W r.f. power. (i) Fitment with measured values at 0.032 m, 0.060 m and 0.114 m distance above the dielectric plate. (ii) Modeled 2D contour plot (labels in m <sup>-3</sup> ).	137
6.1b	Empirically fitted 2D Gaussian based distribution of electron density $n_e(r, z)$ used for the magnetic field simulation at 0.07 mbar argon pressure and 180 W r.f. power. (i) Fitment with measured values at 0.032 m, 0.060 m and 0.114 m distance above the dielectric plate. (ii) Modeled 2D contour plot (labels in m <sup>-3</sup> ).	138
6.1c	Empirically fitted 2D Gaussian based distribution of electron density $n_e(r, z)$ used for the magnetic field simulation at 0.2 mbar argon pressure and 180 W r.f. power. (i) Fitment with measured values at 0.032 m, 0.060 m and 0.114 m distance above the dielectric plate. (ii) Modeled 2D contour plot (labels in m <sup>-3</sup> ).	139

6.2a	Empirically fitted 2D Gaussian based distribution of electron temperature $T_e(r, z)$ used for the magnetic field simulation at 0.03 mbar argon pressure and 180 W r.f. power. (i) Fitment with measured values at 0.032 m, 0.060 m and 0.114 m distance above dielectric plate. (ii) Modeled 2D contour plot (labels in eV).	140
6.2b	Empirically fitted 2D Gaussian based distribution of electron temperature $T_e(r, z)$ used for the magnetic field simulation at 0.07 mbar argon pressure and 180 W r.f. power. (i) Fitment with measured values at 0.032 m, 0.060 m and 0.114 m distance above dielectric plate. (ii) Modeled 2D contour plot (labels in eV).	141
6.2c	Empirically fitted 2D Gaussian based distribution of electron temperature $T_e(r, z)$ used for the magnetic field simulation at 0.2 mbar argon pressure and 180 W r.f. power. (i) Fitment with measured values at 0.032 m, 0.060 m and 0.114 m distance above dielectric plate. (ii) Modeled 2D contour plot (labels in eV).	142
6.3	Heuristically fitted 2D contour plot for spatially resolved neutral gas temperature, $T_n(r, z)$ at (a) 0.03 mbar (b) 0.07 mbar and (c) 0.2 mbar argon pressure. Labeled temperatures are in K.	144- 145
6.4	Calculated absorbed electron power, $P_{\text{abs}}$ with (a) average measured electron density within the coil radius, $n_{e,\text{coil}}$ ( $\text{m}^{-3}$ ) and (b) calculated effective collision frequency, $\nu_{\text{eff}}$ versus argon pressure.	148
6.5a	Measured and simulated (i) axial magnetic fields, $ \text{Re}(B_z) $ and (ii) radial magnetic fields, $ \text{Re}(B_r) $ versus radial distance, $R$ for 0.03 mbar argon pressure at 0.032 m distance above the dielectric plate. R.f. input power was at 180 W and $I_p = 14.4$ A.	150
6.5b	Measured and simulated (i) axial magnetic fields, $ \text{Re}(B_z) $ and (ii) radial magnetic fields, $ \text{Re}(B_r) $ versus radial distance, $R$ for 0.07 mbar argon pressure at 0.032 m distance above the dielectric plate. R.f. input power was at 180 W and $I_p = 14.2$ A.	151
6.5c	Measured and simulated (i) axial magnetic fields, $ \text{Re}(B_z) $ and (ii) radial magnetic fields, $ \text{Re}(B_r) $ versus radial distance, $R$ for 0.2 mbar argon pressure at 0.032 m distance above the dielectric plate. R.f. input power was at 180 W and $I_p = 13.4$ A.	152
6.6	Simulated electron absorbed power and electron power loss versus electron density for 15 A peak r.f. coil current at 0.02 mbar argon pressure. <b>I</b> , <b>II</b> , and <b>III</b> represent the E mode, unstable operation, and H mode, respectively. Electron temperature, $T_e$ , neutral gas temperature, $T_n$ , and the factor $C_{\text{D-M}}$ were set at 4.2 eV, 433 K and $6.6 \times 10^4$ , respectively.	156

- 6.7 A 3D plot of absorbed electron power,  $P_{\text{abs}}$  (magenta surface) and electron power loss,  $P_{\text{loss}}$  (dark blue surface) versus electron density,  $n_e$  and peak coil current,  $I_p$  at 0.02 mbar argon pressure. Electron temperature,  $T_e$  was set at 4.2 eV, neutral gas temperature,  $T_n$  set at 433K and  $C_{\text{D-M}} = 6.6 \times 10^4$ . The white arrows indicate the working path of the system, whereas the red arrows indicate mode transitions. 157
- 6.8 The simulated absorbed electron power (solid line) and power loss (dashed line) curves depicting (a) the current at which either E mode (13 A) or H mode operation (18 A) alone occurs. 158
- 6.9 The simulated absorbed electron power (solid line) and power loss (dashed line) curves depicting the threshold currents for E to H (16.41 A) and H to E (14.19 A) mode transitions. 159
- 6.10 Simulated (Sim.) and measured (Exp.) (a) H mode transition currents,  $I_{\text{tr}}$  (b) H mode maintenance currents,  $I_{\text{mt}}$  at 0.02-0.3 mbar argon pressure range. 161

## LIST OF TABLES

<b>Table</b>	<b>Caption</b>	<b>Page</b>
2.1	Chronological summary of the theoretical development and simulation of electrodeless discharges and ICPs.	25-26
3.1	List of parameters used to determine the probe collection regime.	44
3.2	List of rotational constants required for simulation of $N_2C^3\Pi_u-N_2B^3\Pi_g$ state transition (Huber & Herzberg, 1979, pp. 418-420).	58
3.3	Lists the line strength equations of the $^3\Pi$ degenerate state transitions for the rotational branches R, Q and P (Kovac, 1969).	60
6.1	Comparison of parameters of present setup with other reported works of similar ICPs.	146
6.2	Calculated values for effective collision frequency, $\nu_{\text{eff}}$ and total absorbed electron power, $P_{\text{abs}}$ with measured average coil electron density, $n_{\text{e,coil}}$ , average coil electron temperature, $T_{\text{e,coil}}$ and peak coil current, $I_p$ (for 180 W input r.f. power) and set peak neutral gas temperature, $T_{\text{n,peak}}$ at 0.03, 0.07 and 0.2 mbar argon pressure.	147
7.1	EPPF fitment trends at 0.03, 0.07 and 0.2 mbar argon pressure for 0.032 m, 0.060 m and 0.114 m axial distances above the dielectric plate.	167
7.2	Measured maximum and minimum $T_n$ for increasing and decreasing r.f. power steps and different axial distances above the dielectric plate.	170
E.1	Electron energies (eV) and the corresponding argon collision cross sections ( $\text{m}^{-2}$ )	219-220
F.1	Empirical fitting parameters for spatially resolved electron density, $n_e(r, z)$ for different argon pressure.	224
F.2	Empirical fitting parameters for spatially resolved electron density, $T_e(r, z)$ for different argon pressure.	225
F.3	Heuristic fitting parameters for spatially resolved neutral gas temperature, $T_n(r, z)$ for different argon pressures. Fitted $T_n$ values were pegged at the minimum of 300 K (room temperature).	226

# LIST OF SYMBOLS

## Common Constants

$k_B$  = Boltzmann constant

$m_e$  = Electron mass

$e$  = Electronic charge

$h$  = Planck's constant

$c$  = Speed of light

$\epsilon_0$  = Free space permittivity

$\mu_0$  = Free space permeability

$M_{Ar}$  = Argon ion mass

$n_{air}$  = Refractive index of air

## Common Dimensional Parameters

$r, \theta, z$  = Radial, azimuthal and axial cylindrical coordinates

$a, d, b$  = Coil radius, dielectric radius and inner chamber radius

$L, H, D$  = Effective height of chamber, full inner height of chamber and coil-chamber spacing

$M, W$  = Height of indented cylinder and edge width of indented cylinder

$R$  = Radial distance from chamber center ( $z$ -axis)

$t$  = Temporal term for electromagnetic fields

## Common Plasma Parameters

$n_e, n_{e,cm}, n_e(r, z)$  = Electron density, electron density in cm, average coil electron density and spatially resolved electron density

$T_e, T_{e,eff}, T_{e,ave}, T_e(r, z)$  = Electron temperature, effective electron temperature, spatially averaged electron temperature and spatially resolved electron temperature

$n_{e,coil}, T_{e,coil}$  = Average coil electron density and average coil electron temperature

$T_n, T_{n,ave}, T_n(r, z)$  = Neutral gas temperature, spatially averaged neutral gas temperature, spatially resolved neutral gas temperature

$\lambda_{\text{mfp}}, \lambda_{\text{en}}, \lambda_{\text{in}}, \lambda_{\text{ii}}$  = Particle free mean path, electron-neutral free mean path, ion-neutral free mean path and ion-ion free mean path

$V_s$  = Potential difference in plasma sheath

$n_g, n_g(r, z)$  = Neutral gas density and spatially resolved neutral gas density

$\sigma_e, \sigma_{\text{in}}$  = Electron-neutral total collision cross section and ion-neutral scattering cross section

$T_i$  = Ion temperature

$\ln \Lambda$  = Coulomb logarithm

$P$  = Filling pressure or argon gas pressure

$\varepsilon, \langle \varepsilon \rangle$  = Electron energy and average electron energy

$f(\varepsilon)$ , EEDF = Electron energy density function

$g(\varepsilon)$ , EEPF = Electron energy probability function

$\nu, \nu_{\text{eff}}, \nu_{\text{eff}}(r, z)$  = Collision frequency, effective collision frequency and spatially resolved effective collision frequency

$\omega_p, \omega_p(r, z)$  = Plasma frequency and spatially resolved plasma frequency

$\alpha^2, \alpha^2(r, z)$  = Spatial conductivity parameter and spatially resolved spatial conductivity parameter

$\nu_{\text{en}}, \nu_{\text{ei}}, \nu_{\text{st}}$  = Electron neutral collision frequency, electron ion collision frequency and stochastic collision frequency

$\omega, \omega_{\text{eff}}$  = Drive frequency and effective drive frequency

$\nu_c(\varepsilon), \sigma_c(\varepsilon)$  = Collision frequency term of argon gas and collision cross section of argon gas

$p_i, p_e$  = Ion pressure and electron pressure

$\bar{v}_e$  = Average electron velocity

$\delta$  = Anomalous skin depth

$u_B$  = Bohm velocity

$A_{\text{eff}}$  = Effective surface area for particle loss in the reactor

$h_l, h_r$  = Radial and axial plasma diffusion terms near the sheath edge

$\varepsilon_T$  = Total energy lost per electron-ion pair created by the discharge

$\varepsilon_c, \varepsilon_i, \varepsilon_e$  = Total collisional energy loss per ion-electron pair, mean kinetic energy lost per ion and mean kinetic energy lost per electron

$\varepsilon_{iz}, \varepsilon_{ex}$  = Argon ionization threshold energy and argon excitation threshold energy

$K_{iz}, K_{ex}, K_{el}$  = Argon ionization, excitation and elastic scattering rate constants

### Electrical Probe Parameters

$I_{ion}, I_{ion,sat}$  = Ion current and ion saturation current

$I_{probe}, V_{probe},$   
 $I, V$  = Probe current and voltage, measured current and voltage

$V_{float}, V_{plasma}$  = Floating potential and plasma potential

$I_{elec}, I_{elec,sat}$  = Electron current and electron saturation current

$R_{probe}$  = Probe radius

$l_{sheath}$  = Sheath width

$A_p$  = Probe collection area

$I_p, V_p$  = Peak coil current and coil voltage

$I_{p,evac}, V_{p,evac}$  = Peak coil current and coil voltage at evacuated condition

$I_{tr}, I_{mt}$  = Peak E to H mode transition coil current (H mode transition current)  
and peak H to E mode transition coil current (H mode maintenance current)

### Magnetic Probe Parameters

$V_{COIL1},$   
 $V_{COIL2},$   
 $V_{NOISE}$  = Voltage signals from first (1) and second (2) winding of magnetic probe  
and from electrostatic noise

$V_{MATH},$   
 $V_{MATH,PEAK}$  = Differential and peak differential voltage signals from oscilloscope

$V_{FIELD,AVE}$  = Average magnetic field voltage

$R_H, N_H$  = Helmholtz coil radius and number of coil windings

$I_{H,PEAK},$   
 $B_{H,PEAK}$  = Peak current and peak magnetic field through Helmholtz coil

$m_H, C_H$  = Magnetic probe calibration constants

## Optical Emission Spectroscopy Parameters and Notations

$T_{N_2}, T_{N_2,rot}$  = Translational temperature of nitrogen neutrals and vibro-rotational ground state temperature of the nitrogen neutrals

$\lambda_i$  = Line position of the spectral line for rotational transition branch,  $i = R, Q$  and  $P$

$\nu_i$  = Vibro-rotational wavenumber of the spectral line for rotational transition branch,  $i = R, Q$  and  $P$

$\nu, J$  = Vibrational and rotational quantum number

' , '' = Notations for upper and lower transition states, i.e.,  $J'$  is the upper state rotational quantum number

$T_{elec}, G(\nu), F_\nu(J)$  = Electronic, vibrational and rotational terms for spectroscopy

$\overline{\nu_{\nu',\nu''}}$  = Electronic-vibrational constant for a single vibrational emission peak

$\omega_e, \omega_e x_e, \omega_e y_e, B_e, \alpha_e, \beta_e$  = Vibrational and rotational constants

${}^3\Pi_x$  = Degenerate state for the rotational transition branches where,  $x = 0, 1, 2$

$C_{spec}$  = Parametric constant for rotational line intensity

$S_J$  = Rotational line strength

$\lambda_{exp}, \lambda_{calib}$  = Measured and standard (calibration) emission peak wavelengths

$m_{OES}, C_{OES}$  = Optical emission spectroscopy (OES) probe/spectrometer calibration constants

$I(\lambda), I(\lambda_{peak})$  = Intensity at emission wavelength,  $\lambda$  and peak emission wavelength,  $\lambda_{peak}$

$\lambda, \lambda', \lambda_{peak}$  = Emission wavelength, integration wavelength and peak emission wavelength

$w_l, w_g, w_v$  = Full width half maximum (FWHM) for Lorentzian, Gaussian and Voigt functions/profiles

$\nu_{ave}$  = Average molecular velocity

$f(\lambda)$  = Voigt function at wavelength  $\lambda$

$I_{conv}(\lambda), I(\lambda')$  = Convoluted intensity at wavelength  $\lambda$  and intensity at the integration wavelength,  $\lambda'$

$\chi^2$  = Chi-squared statistical value

$P_{\text{line}}$  = Probability (weight) of discrete lines for  $\chi^2$  analysis

$N_{\text{bin}}$  = Total number of bins for  $\chi^2$  analysis

$x, x_o$  = Measured spectrum intensity and synthetic spectrum intensity at the same wavelength

### Parameters and Notations for Analytical Field Simulation

$i, j$  = Imaginary units

$\mathcal{E}, \mathcal{B}, \mathcal{J}$  = Time varying electric field, magnetic field and current density

$E, B, J$  = Electric field, magnetic field and current density vectors

$E_r, E_\theta, E_z$  = Scalar radial electric field, azimuthal electric field and axial electric field components

$B_r, B_\theta, B_z$  = Scalar radial magnetic field, azimuthal magnetic field and axial magnetic field components

$\rho, K_\theta$  = Charge density and surface charge density terms

$N$  = Number of turns in the coil

$R(r), Z(z)$  = Single variable functions for separation of variables method

$\mu, \mu_n$  = Bessel function root (subscript  $n$  denotes eigen values)

$\lambda, k, q, s$  ( $\lambda_n, k_n, q_n, s_n$ ) = Separation constants (eigen values for separation constants)

$A, A_1, A_2, A_n;$   
 $B, B_1, B_2, B_n;$  = Boundary constants for analytical solutions of the electromagnetic fields (subscript  $n$  denotes the eigen values for the boundary constants)

$C, C_1, C_2,$   
 $C_n;$

$D, D_n;$

$E, E_n;$

$F, F_n;$

$v_n, u_n$

$E_o$  = Uniform radial electric field

$\epsilon_p, \epsilon_r$  = Plasma permittivity term and dielectric constant of medium

## Parameters and Notations for Numerical Field Simulation

$\Delta r, \Delta z$  = Discretized radial spacing and axial spacing for numerical simulation

$k$  = Superscript for number of iterations

$n, m$  = Subscripts for radial and axial grid positions

## Parameters for Power Balance Simulation

$P_{\text{abs}}, P_{\text{loss}}$  = Absorbed electron power and electron power loss

$P_{\text{h}}, P_{\text{e}}, P_{\text{stoc}}$  = H mode field power, E mode field power and power from stochastic heating of plasma capacitive sheath

$d\mathbf{S}$  = Integration term for induction coil area (Poynting vector)

$B_r^*, B_\theta^*$  = Complex conjugate of the radial magnetic field and complex conjugate of the azimuthal magnetic field

$S$  = Time averaged capacitive sheath thickness

$J_s$  = First harmonic component of current density through the sheath

$V_s(r)$  = First harmonic component of voltage across the plasma sheath at the coil-dielectric interface

$\varepsilon_{\text{cD}}, \varepsilon_{\text{cM}}$  = Druyvesteyn and Maxwellian electron-electron collision energy loss factors

$C_{\text{D-M}}$  = Exponential factor for the transition point between Druyvesteyn and Maxwellian EEDFs

## Empirical and Heuristic Fitting Parameters

$\alpha_P, \beta_P$  = EEPF fitting constants for argon pressure,  $P$

$n_{\text{e,peak}}$  = Fitted peak electron density

$T_{\text{e,peak}}$  = Fitted peak electron temperature

$T_{\text{n,peak}}$  = Fitted peak neutral gas temperature

$\sigma_{r,n_e}, \sigma_{z,n_e}$  = Radial and axial fitting parameter for electron density

$\sigma_{r,T_e}, \sigma_{z,T_e}$  = Radial and axial fitting parameter for electron temperature

$\sigma_{r,T_n}, \sigma_{z,T_n}$  = Radial and axial fitting parameter for neutral gas temperature

# CHAPTER 1: INTRODUCTION

## 1.0. Introduction and Motivation of Study

Radio frequency or r.f. inductively coupled plasmas (ICPs) have been extensively used for the past two decades for various semiconductor processes including plasma enhanced chemical vapor deposition (PECVD) and reactive ion etching (RIE). These processes demand for high purity and high density plasmas which are able to give the precise substrate modification required for fabricating present day electronic devices (Hopwood, 1992). ICPs are induced mainly by the magnetic fields of a non-contact, externally positioned source coil and are typically referred to as "electrodeless". The nature of this "electrodeless" configuration allows for reduced impurities in generation of plasma; especially in comparison to other plasmas with internal electrodes (Chen, 2008).

ICPs in practice have both capacitive and inductive means of power coupling which together contribute towards the overall plasma. The primary mode of the plasma, known as the H mode, is generated via predominant inductive coupling of the axial and radial magnetic fields of the r.f. coil. The secondary mode of the plasma, known as the E mode, is generated via capacitive axial and radial electric fields formed by the potential difference across the coil. The E mode is usually found at lower input powers where ionization from the potential difference of the coil is insufficient to ignite the inductive discharge and power coupling from the electromagnetic fields of the coil is low (Lieberman & Lichtenberg, 2005). An ICP at H mode and at E mode can be differentiated by distinct features in electron density and luminosity (Figure 1.1). At H mode, the plasma is highly luminous and has a high electron density ( $10^{16}$ - $10^{18}$  m<sup>-3</sup>)

whereas, at E mode, the plasma is at low luminosity and has an electron density of about one to two orders lower (Chabert & Braithwaite, 2011).

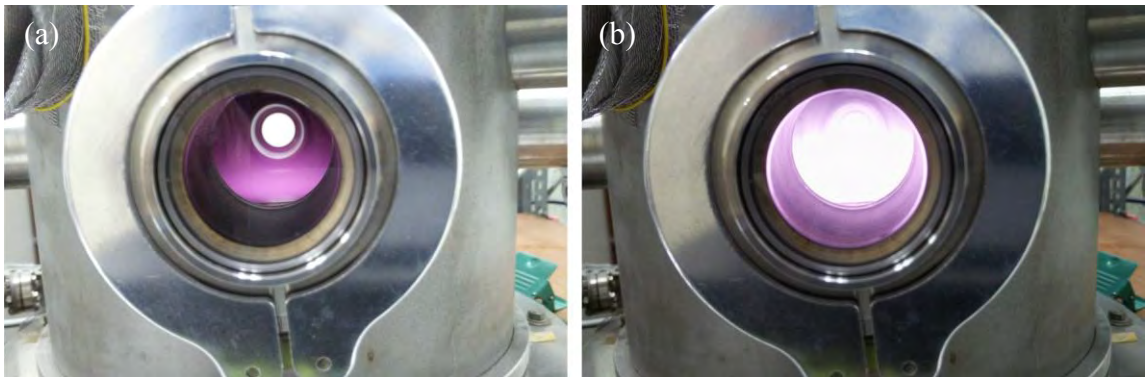


**Figure 1.1:** Laboratory 13.56 MHz r.f. argon ICP operating at (a) E mode and (b) H mode at 0.1 mbar.

Transitions between E mode and H mode occur in sudden „jumps“ of luminosity when a threshold input power is applied. The threshold current which triggers these jumps depends not only on external parameters (i.e., gas pressure, coil size, impedance matching and gas type) but also on whether the input current is incremented or decremented (Figure 1.2).

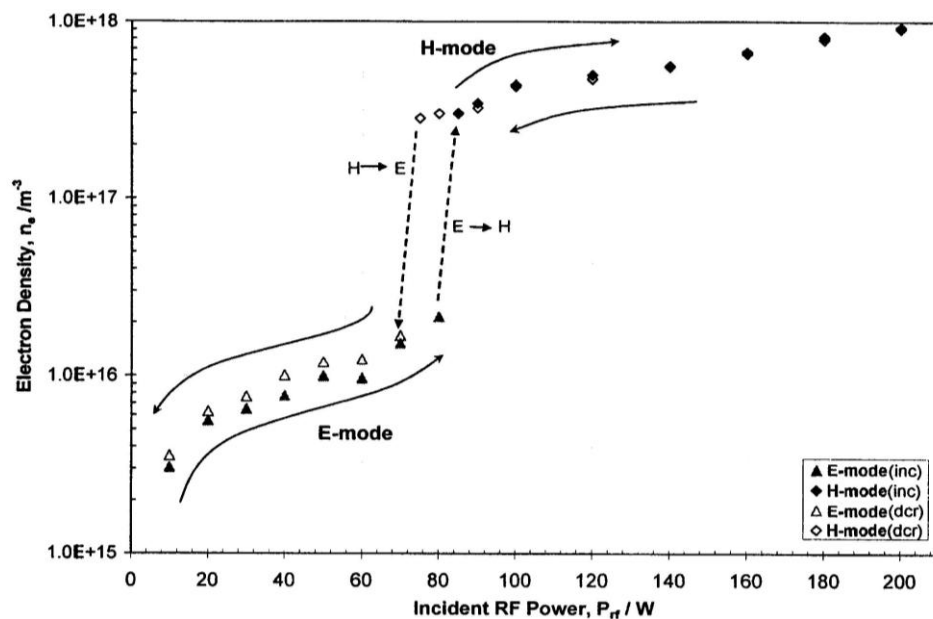


**Figure 1.2:** The measured effects of hysteresis in the planar coil ICP reactor at 0.1 mbar argon pressure. The power required to cause a transition from E to H mode is higher ( $\sim 82$  W) than the power required for maintaining H mode ( $\sim 66$  W) (Lim, 2010).

This hysteresis phenomenon has become a point of interest for many researchers in this field of study and is well documented (Cunge, et al., 1999, Daltrini et al., 2008, El-Fayoumi, Jones & Turner, 1998, and Xu, et al., 2000).

The magnetic fields required for formation of an ICP can be generated from either one of two types of source coil configurations, i.e., the helical coil configuration or the planar coil configuration (Figure 1.3).

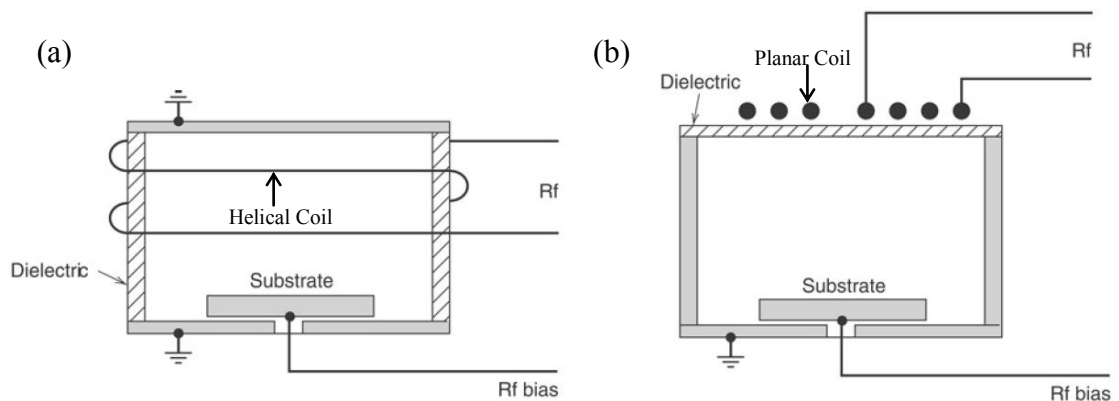


**Figure 1.3:** The two types of coil configurations used in ICP design: (a) helical and (b) planar (Lieberman & Lichtenberg, 2005).

For industrial ICPs, the planar coil configuration is preferred due to the distribution of the induced fields which results in higher uniformity in power deposition and plasma density (Steward, et al., 1995 and Xu, et al., 2001). In material processing applications such as PECVD and RIE, a silicon substrate is typically placed in the vicinity of the plasma to be treated by ion bombardment. With a higher uniformity in plasma density, better process control is achieved in terms of reproducibility and evenness of substrate treatment (Ogle, 1990). The optimization and simulation of the source magnetic fields for control of plasma uniformity has been a frequent subject of applied ICP research (Cuomo et al., 1994, Hopwood et al., 1993, Patrick et al., 1995, Paranjpe, 1994, and El-Fayoumi & Jones, 1998).

In recent years, spectroscopic measurement techniques have revealed that ICP neutral gas temperatures are much higher than the previously stipulated near-room temperatures commonly associated with low temperature discharges. Measurements made by Li et al. (2011) for argon ICPs have shown neutral gas temperatures of up to 1750 K for the r.f. input power 200 W. In simulation, intrinsic ICP parameters such as electron density and electron temperature have been reported to be influenced by elevated neutral gas temperatures; with comparison of measured results and simulation giving better agreement (Hash et al., 2001 and Ostrikov, et al., 2002). Temperature effects on extrinsic ICP parameters, such as magnetic field distribution and discharge mode transitions, however, have yet to be explicitly characterized. Thus, in this work, the effects of neutral gas temperature on these parameters will be experimentally and theoretically studied.

## **1.1. Objectives of Study**

This study aims to experimentally and theoretically characterize the effects of neutral gas heating on key ICP parameters; with focus on predictive simulation of the discharge magnetic fields and E-H mode transition currents at elevated temperature. The study is divided into two parts:

### **1.1.1. Experiment**

For experiment, the following plasma parameters will be measured with several diagnostic probes and techniques:

*(a) Electron density,  $n_e$  and electron temperature,  $T_e$*

A laboratory Langmuir probe will be used to measure the radially resolved electron density,  $n_e$  and electron temperature,  $T_e$  at 0.032, 0.060 and 0.114 m axial distances

above the dielectric plate for 0.03, 0.07 and 0.2 mbar argon pressures. R.f. power is set at 180 W. The electron energy density distribution (EEDF) is also measured at the chamber center for all cases.

*(b) Absolute axial magnetic field,  $|B_z|$  and radial magnetic field,  $|B_r|$*

Two electrostatically compensated magnetic probes will be used to measure the absolute axial magnetic field,  $|B_z|$  and radial magnetic field  $|B_r|$  magnitudes at 0.032 and 0.060 m axial distances above the dielectric plate for 0.03, 0.07 and 0.2 mbar argon pressures. R.f. power is set at 180 W.

*(c) H mode transition current,  $I_{tr}$  and H mode maintenance current,  $I_{mt}$*

A current probe will be used to measure the H mode transition current,  $I_{tr}$  and H mode maintenance current,  $I_{mt}$  at the argon pressure range of 0.02-0.3 mbar.

*(d) Neutral gas temperature,  $T_n$*

An optical fiber probe will be used to measure the neutral gas temperature,  $T_n$  via actinometry optical emission spectroscopy (AOES) technique. Measurements will be made at 0.03, 0.05, 0.07, 0.1 and 0.2 mbar Ar/N<sub>2</sub> pressures for 0.032 m and 0.060 m axial distances above the dielectric plate and for increasing and decreasing steps of r.f. power, i.e., 100-200 W and 200-100 W.

### **1.1.2. Simulation**

For simulation, two models will be developed based on existing derivations, i.e., the electromagnetic model (El-Fayoumi & Jones, 1998) and the power balance model (El-Fayoumi, Jones & Turner, 1998):

*(a) Electromagnetic model*

The absolute axial magnetic field  $|B_z|$  and radial magnetic field  $|B_r|$  magnitudes will be simulated for argon pressures of 0.03, 0.07, and 0.2 mbar. The required spatially resolved electron density distribution,  $n_e(r, z)$  and electron temperature distribution,  $T_e(r, z)$  are empirically fitted whereas, the required neutral gas temperature distribution,  $T_n(r, z)$  is heuristically fitted (i.e., with modeled distributions). The neutral gas temperature is also set at average measured and room temperature (300 K) distributions for comparison.

*(b) Power balance model*

The H mode transition current,  $I_{tr}$  and H mode maintenance current,  $I_{mt}$  will be simulated for the argon pressure range of 0.02-0.3 mbar. Calculations are made to take into account the power contributions of H mode, E mode and stochastic heating of plasma electrons via capacitive sheath, the non-linear effects of electron energy distribution towards power balance and the effects of neutral gas heating. The simulated results are compared with measured values. Hysteresis in the system (from differences in transition currents) is also demonstrated.

## **1.2. Layout of Thesis**

This thesis is divided into seven chapters. The present chapter, “Chapter 1: Introduction” covers the introduction, motivation, objectives and layout of the thesis study. “Chapter 2: Literature Review” comprises of a chronological review of research on ICPs, including ICP history and origins, ICP modes and hysteresis, theoretical development and simulation of ICPs and neutral gas heating and depletion in ICPs. “Chapter 3: Experiment” covers the experimental setup, methodology and plasma diagnostic probes (theory and analysis) used in measurement of ICP parameters.

“Chapter 4: Results and Discussion - Experiment” discusses the immediate results and findings obtained from measurement. Derivations of equations for electromagnetic and power balance models along with methodology for numerical simulation are covered in “Chapter 5: Simulation”. “Chapter 6: Results and Discussion - Simulation” discusses the key results and findings of predictive simulation using measured and empirically fitted parameters from Chapter 4 and the derived models from Chapter 5. The thesis is concluded with “Chapter 7: Summary and Conclusion” which gives the summaries and conclusions drawn from the results obtained in Chapters 4 and 6.

## CHAPTER 2: LITERATURE REVIEW

### 2.0. History and Origins

The advent of research in inductively coupled discharges began with the discovery of the ‘electrodeless ring discharge’ by Johann Wilhelm Hittorf (Hittorf, 1884). In Hittorf’s experiment, a Leyden jar and spark gap was used to send sparks (or damped oscillating pulses) at high frequency through a wire which was coiled helically around a vacuum tube; resulting in a bright ring shaped discharge. Hittorf attributed the formation of the discharge to the excitation of electrons by the electromagnetic fields of the coil. More detailed experimentation and explanation towards this phenomenon was later done by Sir J. J. Thomson (Thomson, 1927). Sir Thomson’s work included the effects of light and gas impurities towards discharge maintenance and the development of a theory which describes the discharge’s electromagnetic characteristics. His derivations also highlighted the dependence of the discharge ignition on input spark frequency and tube gas pressure. His theoretical work, however, was disputed the following year by Townsend and Donaldson (1928). They argued that the calculated electrostatic field intensity between the ends of a typical solenoid was more than 30 times larger than its electromagnetic field intensity and thus, the cause of the discharge was predominantly electrostatic. This notion was also demonstrated experimentally by using a continuous wave (c.w.) oscillator (i.e., replacing the previous Leyden jar and spark gap) which was connected to a cross-wound solenoid. The solenoid was wound in a manner that cancels out much of the electrostatic field (Figure 2.1); leaving only electromagnetic fields within the coil. The upper end of the coil which was unwound however, still had electrostatic fields.

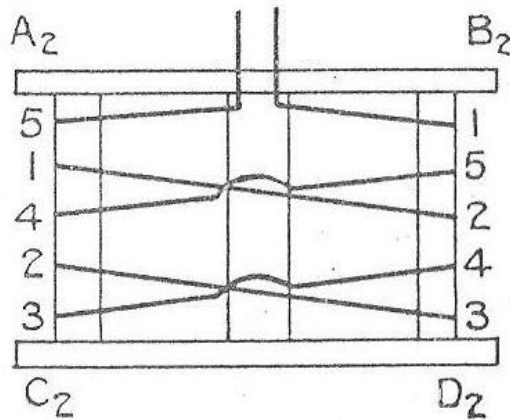


**Figure 2.1:** Cross-wound solenoid as demonstrated by Townsend and Donaldson (1928) which effectively cancels most of the electrostatic fields within the solenoid. The winding at the upper ends ( $A_2C_2$ -5 and  $B_2D_2$ -1) still carry an electrostatic field.

When a bulb of low pressure gas was inserted into the coil, only the upper end of the bulb produced a discharge. This led to the presumption that the coil's electromagnetic field alone was insufficient to sustain the discharge and that electrodeless discharges were mainly electrostatic in origin.

It was subsequently in November 1929, that MacKinnon (1929) accurately described the properties of the inductive discharge. He found that both the electrostatic and electromagnetic properties of the discharge were coincident and that the predominance of either state was dependent on the level of excitation of the electrons (i.e., at lower electron excitation the discharge would be predominantly electrostatic and at higher electron excitation the discharge would be predominantly electromagnetic). Using iodine as the discharge gas, a pancake (flat spiral) coil and a discharge circuit with both damped and c.w. oscillation capability (Figure 2.2), he observed that with damped oscillation, the discharge formed into a bright ring with the same electromagnetic characteristics reported by Thomson (1927).

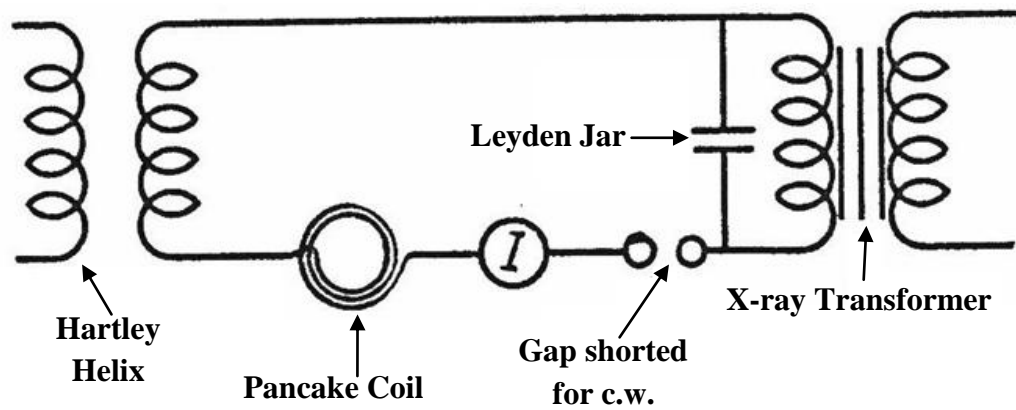


**Figure 2.2:** The combination circuit used in MacKinnon's experiment with both damped and c.w. oscillation capability. A Hartley oscillator (labeled Hartley Helix) was used for c.w. operation of the pancake coil, whereas, a Leyden jar, spark gap and X-ray transformer was used for damped operation (MacKinnon, 1929).

With c.w. oscillation however, the discharge was a diffused glow similar to that obtained by Townsend and Donaldson (1928) and had electrostatic characteristics. The ring discharge did not occur for c.w. oscillation despite being set at a much higher current than the damped oscillation. Yet, by replacing iodine with mercury vapor and by heating the discharge bulb, MacKinnon was able to reproduce the ring discharge with c.w. oscillation. He subsequently concluded that the discrepancies between Townsend et al. and Thomson's findings were mainly due to the limitations of the c.w. oscillator used by the former, which was unable to produce the high amplitude necessary to create sufficient excitation for a ring discharge (Figure 2.3).

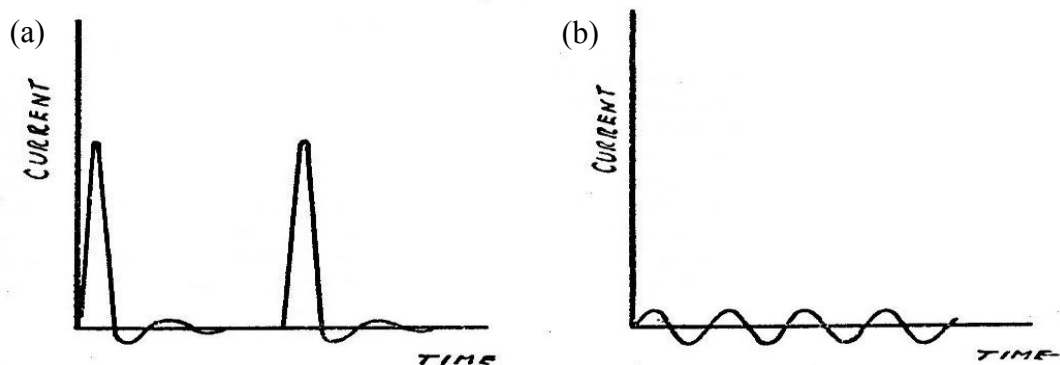


**Figure 2.3:** Current amplitude differences between (a) damped oscillation generated by a spark gap and (b) c.w. oscillation produced by an oscillator. The much higher amplitude of current in damped oscillation provides the energy required for excitation of a ring discharge (MacKinnon, 1929).

MacKinnon's observations were later confirmed by several other researchers (Stuhlman & Whitaker, 1930, Smith, Lynch & Hilberry, 1931 and Knipp & Knipp, 1931).

### **2.1. E Mode, H Mode and Hysteresis**

In 1947, George I. Babat classified the electromagnetic and electrostatic phenomena in electrodeless discharges based on the nature of their elementary conductance currents (Babat, 1947). Taking from the terminology commonly used to identify electric wave (E-) and magnetic wave (H-) propagation in hollow metal waveguides, Babat referred to the electrostatic phenomenon as E-discharge and the electromagnetic phenomenon as H-discharge. According to Babat, in an E-discharge, the plasma conductance currents were divergent and were continued by dielectric currents, whereas in an H-discharge the plasma conductance currents were in a closed loop. Subsequently, the terms E-discharge and H-discharge were formalized into E mode and H mode (Amorim, Maciel & Sudano, 1991).

Though transitions between modes were well documented throughout the years (MacKinnon, 1929, Knipp & Knipp, 1931, Babat, 1947, Jones, 1953 and Amorim, Maciel & Sudano, 1991), research interest towards its mechanism only peaked during the 1990s. In 1996, Kortshagen, Gibson & Lawler (1996) investigated light emission from the E to H and H to E mode transition cycle of a 0.1 Torr discharge using a 0.5 m monochromator and a photomultiplier tube (PMT). The trace obtained from the experiment (i.e., PMT signal vs. coil current) showed that the emitted light was discontinuous (to about 2 orders of magnitude) at the points of transition and followed different working paths when transiting between E to H and H to E mode; indicating hysteresis. In their work, Kortshagen et al. also developed an analytical model to

estimate the minimum currents required for maintaining an E mode and H mode discharge.

El Fayoumi, Jones and Turner (1998) published a detailed experimental and theoretical report on hysteresis and modes transitions in a 0.56 MHz, planar coil, argon ICP system. In their experiment, the electrical operating points of the plasma were altered by mismatching the system impedance. The corresponding changes in peak coil current, plasma resistance and dissipated power were then recorded. Hysteresis between mode transitions in the system was confirmed when the impedance mismatch required to transit from E to H mode was smaller than the mismatch required to transit back. The theoretical model developed by El-Fayoumi et al. for the simulation of hysteresis used a combination of electromagnetic theory and circuit analysis to solve the power balance equation. In this model, the intersections between the absorbed electron power curve (i.e., comprising of the sum of H-mode power, E-mode power and stochastic power) and the electron power loss curve denoted the possible operating points of the system at a given input coil current and electron density. This was further visualized by El Fayoumi et al. into a 3 dimensional plot (electron power vs. coil current vs. electron density) which showed the branching E mode and H mode paths taken by the discharge during its transition cycle (Figure 2.4).

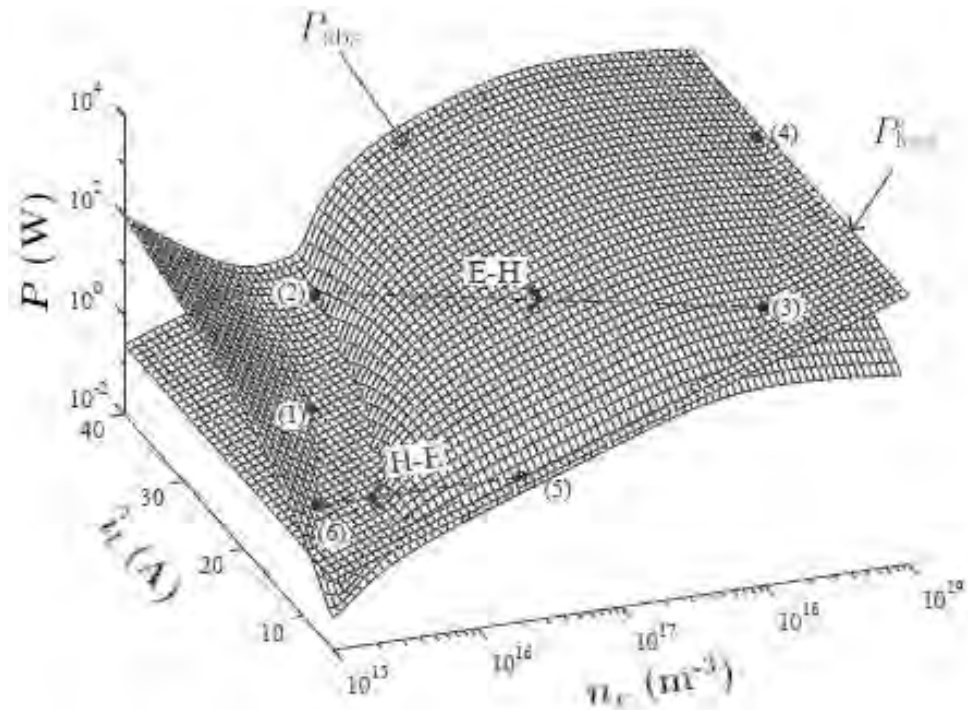


**Figure 2.4:** A 3 dimensional plot visualizing the possible operating points and branching paths taken by a modeled ICP system. Hysteresis of E to H mode ((2)-(3)) and H to E mode ((5)-(6)) transitions is also shown (El Fayoumi, Jones & Turner, 1998).

In the following year, workers Turner and Lieberman (1999) extended the model presented by El-Fayoumi, Jones and Turner (1998) by taking into account the additional effects of non-linearities into the power balance equation of the discharge. These include the effects of sheath capacitance and sheath thickness towards absorbed electron power and multistep ionization and electron-electron collisions towards electron power loss. Multistep ionization via metastable levels was attributed as one of the causes that contributed to hysteresis due to the non-linearity (reduction of electron power loss at higher plasma densities) of the total energy required to sustain an ion-electron pair.

Czerwiec and Graves (2004) studied hysteresis and mode transitions for the rare gases (argon, krypton and xenon) at low pressures using optical emission spectroscopy. Argon gas measurements at different modes showed differences in the peak intensities of argon I transitions with the  $2p_1 \rightarrow 1s_2$  transition at 750.4 nm being highest in E mode

and the  $2p_3 \rightarrow 1s_5$  transition at 763.51 nm and the  $2p_9 \rightarrow 1s_5$  transition at 811.53 nm being highest in H-mode. The shift in peak intensities of the argon emission lines were linked to the added role of metastable excitation states. The hysteresis loop (E to H mode and H to E mode) of argon and krypton were also demonstrated.

Also in 2004, the temporal dynamics of E to H mode transition for argon plasma at atmospheric pressure were examined by researchers Razzak et al. (2004) using a 4500 f/s high speed camera (FASTCAM-*ultima* SE) and CCD camera. From experimental investigation, they found that on E to H mode transition, the E mode plasma develops multiple streamer-like discharges of axial direction which were subsequently, transformed into a bright ring which forms the H mode plasma. Transition dynamics was also seen in the behavior of the plasma loading impedance, whereby an almost linear increase in loading impedance was observed during E to H mode transition. In this study, Razzak et al. also developed a theoretical model to estimate transition time (400-900 ms) which showed good agreement with the experimentally measured range (500-1000 ms).

Daltrini et al. (2008) discovered that hysteresis in inductively coupled plasmas was mostly due to power losses in the system's impedance matching network. It was found that when plasma parameters (i.e., electron density, electron temperature, argon metastable density and ion density) were plotted against plasma power (corrected for coil and hardware losses) instead of input r.f. power, no hysteresis was observed. It was also seen that when plotting against corrected plasma power, an inaccessible region was formed between modes at which no stable discharge was produced.

The influence of impedance matching on hysteresis and mode transitions was also shown by workers Gao et al. (2010) in their report which demonstrated the relationship between matching network capacitance and plasma parameters. In their experiment at 30 mTorr and 100 mTorr argon pressure, the capacitance of a  $\Gamma$ -type matching network capacitor was varied between 114-127 pF and the corresponding changes of input current, input voltage, forward power, phase angle and plasma density were recorded. It was found that the increase in matching capacitance expanded the hysteresis loop of circuit parameters and plasma density (versus applied power). Also, at higher matching capacitances (120.0 pF, 121.2 pF and 123.3 pF), the hysteresis loop for input current was found to be inverse, i.e., E to H mode transition caused a jump from lower to higher input current instead of the expected higher to lower jump.

Lee, Kim and Chung (2013) demonstrated the absence of hysteresis between mode transitions when using an automated matching network (which removes system impedance matching discrepancies) at 13.56 MHz r.f. frequency and 100 mTorr argon pressure. However, when the same experiment was run at 350 mTorr argon pressure, hysteresis was still observed. Lee et al. attributed this to the effects of non-linear power balance which occurs more distinctly at higher pressures. It was thus, concluded that both impedance matching and non-linear power balance play a part in contributing to the hysteresis phenomenon.

## **2.2. Theoretical Development and Simulation of Electrodeless Discharges and ICPs**

The first theoretical treatment for the electromagnetic fields of an electrodeless discharge was given by Thomson (1927). Sir Thomson correlated the peak cyclotron velocity of a single plasma electron with the ionization potential of the discharge, stating that the discharge will only be initiated if the electron reaches the minimum

kinetic velocity given by the ionization potential. He further concluded that in order to obtain this velocity, the initiating electron must not encounter collisions from other particles; thus, deriving the threshold pressure required to initiate the discharge from the free mean path of the electron. Thomson (1930), derived from the input oscillating electric fields, the conditions of electron ionization energy, discharge tube length, pressure and ion recombination rate required to maintain an electrodeless discharge. These maintenance conditions were shown to hold good approximation with available experimental data (Kirchner, 1925).

Townsend (1932) developed a parallel plate model describing the electrostatically driven electrodeless discharge. The discharge was assumed to occur in a quartz chamber midway between two parallel plate electrodes with a high frequency oscillating electric field. Townsend derived the analytical approximations for electron density and electron excitation energy in terms of the mean electrostatic force between particles and electron diffusion and ionization coefficients. The expansion to Thomson's (1927) electromagnetic theory for electrodeless discharges was later done by Kunz (1932). Kunz derived the electromagnetically induced ring current of the discharge and also circuit parameters such as self inductance, mutual inductance, oscillation frequency difference (with and without plasma) and discharge conductivity. He also included the derivations of discharge conductivity and self inductance for the electrostatic case. Kunz's circuit theory of the electrodeless discharge can be said to be the precursor of modern day circuit theory for ICPs.

Eckert (1962) published a paper detailing a plasma diffusion theory for electrodeless discharges based on Schottky's (1924) electron balance solution for the positive plasma column. The experimental parameters for hydrogen were used to illustrate the theory.

From the model, Eckert deduced that the maximum obtainable electron density for an electrodeless discharge was strongly dependent on the product of discharge frequency and magnetic field, moderately dependent on gas pressure and independent of chamber radius. Henriksen, Keefer and Clarkson (1971) derived a closed form solution of the electromagnetic fields for a low pressure electrodeless discharge using non-uniform complex plasma conductivity with a parabolic distribution. The magnitude of field variations within the discharge were found to be qualitatively similar to previous studies which generally assumed uniform and weakly reactive (real) plasma conductivity (Thomson, 1927 and Eckert, 1962). Two years later, Keefer, Sprouse and Loper (1973) solved the 1D cylindrical energy balance equation for a confined, inductive electrodeless arc with the consideration of convective energy transport due to radial inflow of gas. Using experimental values of electrical and thermal conductivity and specific radiation for argon at atmospheric pressure, the arc temperature profile calculated by Keefer's model (i.e., with convection) showed better agreement with experimental results compared to a reference model without convection.

Boulos (1976) presented a model which calculates the 2D flow and temperature fields of an atmospheric, argon inductive plasma torch at 3 MHz r.f. frequency and 3.77 kW power. The simulated coil was helical and of radius, 2.4 cm. The corresponding momentum, continuity and energy equations were solved simultaneously using 1D magnetic and electric field equations. Results demonstrated the existence of a magnetic pumping effect (via recirculation eddy currents) which was responsible for radial inflow at the center of the coil. Back flow at the upstream end of the coil was of the order of  $20 \text{ ms}^{-1}$  and was responsible for particle repulsion in the area. Significant reduction of heat flux to the plasma tube was also seen when gas flow rate was increased. The model was further expanded by Mostaghimi and Boulos (1989) to include 2D electromagnetic

fields which enabled the prediction of coil geometry effects on the flow and temperature fields of the discharge.

Vahedi et al. (1995) derived a simple analytical model to describe power deposition in a cylindrical inductively coupled plasma source with a planar coil. The model was valid of all collisionality regimes of the plasma, i.e., with both ohmic (collisional) heating and stochastic (collisionless) heating components considered. An effective electron collision frequency with contributions from both components was devised for this purpose. From the model, it was concluded that stochastic heating had a dominant influence in power deposition for ICPs at low pressure.

In the same year, Li, Wu and Chen (1995) developed a time averaged two-dimensional fluid model for a planar coil inductive plasma source which included an electromagnetic module with self-consistent power deposition to calculate transport parameters. Some of the assumptions made for the model were negligible gas flow, Maxwellian electron energy density function (EEDF), equal ion and neutral temperature and spatially uniform neutral gas temperature and distribution. The planar spiral coil was simulated as three co-axial flat circular coils. Li et al. simulated the plasma density, electron temperature, azimuthal electric field intensity, plasma potential and ionization rate spatial profiles for the case of 500 W r.f power and 10 mTorr neutral gas pressure. The effects of gas pressure and plasma power on electron temperature and electron density were also demonstrated i.e., with the electron temperature increasing slightly with plasma power and decreasing slightly with pressure and the electron density increasing linearly with both parameters. These simulated trends were in accordance to experimentally measured results by Hopwood et al. (1993).

Gudmundsson and Lieberman (1998) calculated the effective electron collision frequency, electron density and electron temperature of planar coil argon plasma using an axis symmetric, global volume-averaged discharge model. In a global model, spatially varying experimental parameters, such as electron density and electron temperature were assumed to be of a predefined value or distribution (i.e., for simplicity). In this model, the electron density was assumed to be the average value across the chamber radius, with exception of the boundaries whereby the density values fall sharply. Three component collision frequencies, i.e., electron-neutral, electron-ion and stochastic collision frequency were used to calculate the effective electron collision frequency. Using the electron power balance equation and calculated plasma parameters, Gudmundsson et al. determined the mutual inductance, self inductance, plasma resistance and inertia inductance of the discharge as a function of skin depth and absorbed plasma power. Calculated values of induced plasma current (derived from plasma resistance) provided a reasonable estimate to experimental values measured by El-Fayoumi and Jones (1997).

El-Fayoumi and Jones (1998), also presented a comprehensive theoretical treatment of the spatial distribution of the H mode fields within a 0.56 MHz, planar coil, ICP source. The azimuthal electric, radial magnetic and axial magnetic fields were solved analytically for the cases of evacuated and plasma filled chamber with constant electron density. The case of a spatially varying electron density was also solved using the method of finite difference. Temporo-spatial magnetic field lines were visualized and compared for both measured (Figure 2.5 (a)) and simulated (Figure 2.5 (b)) fields. El-Fayoumi et al. also compared the measured and simulated phase variations at different radial distances from the chamber center. From comparisons, it was concluded that

within a factor of two, meaningful information of plasma properties can be deduced by the analysis of magnetic field data.

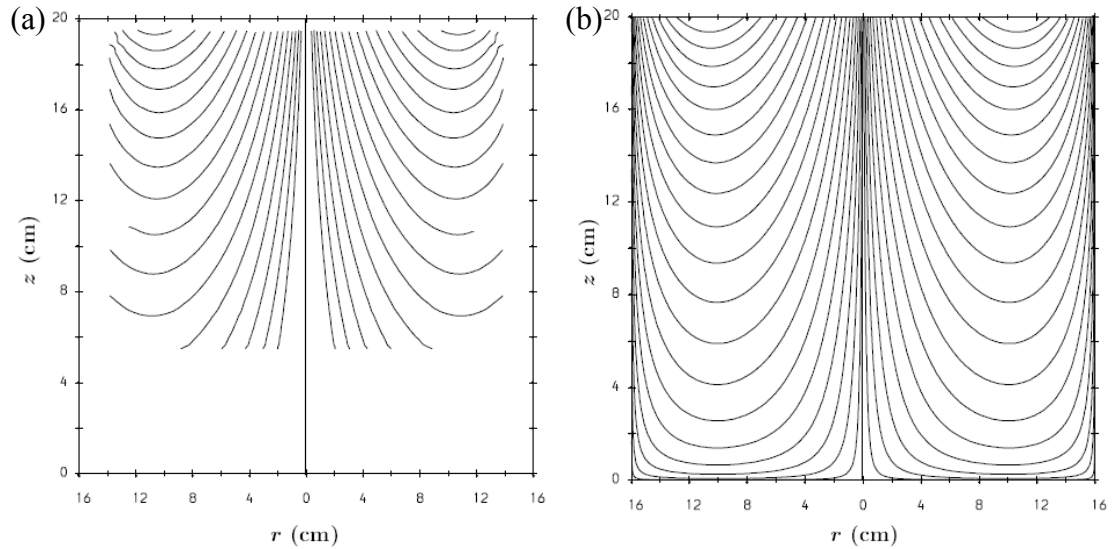


**Figure 2.5:** The (a) measured and (b) simulated magnetic field lines for an evacuated, planar coil, ICP source at 0.56 MHz (El Fayoumi & Jones, 1998).

Nanbu (2000) compiled a review article on kinetic particle simulation of low pressure, high density plasma sources which included ICPs. In the simulation, Nanbu solved the kinetic Boltzmann transport equation using the method of particle-in-cell (PIC) (Birdsall, 1991), i.e., a method in which 1000s of representative particles were generated and moved within predetermined spatial grids at discrete time steps. Displacement and velocity of the particles (by influence of the electromagnetic fields of the source) were determined using the Lorentz force equation. Collisional processes which occur during particle movement were treated using Monte Carlo (Birdsall, 1991) and direct simulation Monte Carlo schemes (Serikov, Kawamoto & Nanbu 1999); both of which were probabilistic methods of determining the type of collision (Figure 2.6).

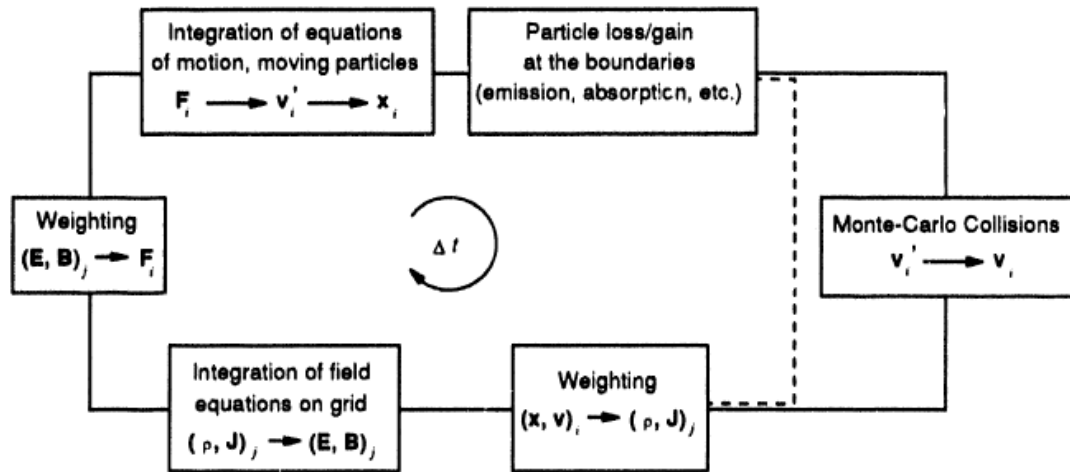


**Figure 2.6:** Example of a basic Particle in Cell-Monte Carlo Collision (PIC-MCC) algorithm. Representative particles are updated for changes in their spatial properties under the influence of an electromagnetic field and by randomized collisions at discrete time steps (Birdsall, 1991).

Collisional processes considered in Nanbu’s simulation were extensive, included were electron-molecule and ion-molecule collisions (which include elastic collisions, excitation and ionization), molecule-molecule hard sphere collisions and Coulomb collisions (electron-electron, ion-ion and ion-electron charge based influence on particle movement). Trajectory and velocity of particles were adjusted according to the collisional influences of each time step. In these simulations, were illustrated the influence of the different types of collisions on the statistical distribution of electron energy of argon plasma via electron energy distribution function (EEDF). The number density distributions of  $\text{CF}_3^+$ ,  $\text{CF}_3^-$ ,  $\text{F}^-$  and electrons of a simulated  $\text{CF}_3$  discharge were also shown.

Panagopoulos et al. (2002) developed a 3D cylindrical, finite element fluid model (MPRES-3D) to study azimuthal asymmetries in inductively coupled plasmas and its effects on ion etch uniformity in etching applications. The model was made up of several iteration modules that repeatedly compute the electromagnetic, electron energy,

particle transport, particle flux and sheath equations in a cyclical fashion till a convergence was reached. The power deposition, electrostatic potential, electron temperature, particle densities, etch rate and etch uniformity was calculable from the converged solution. Silicon wafer etching with chlorine in a planar coil reactor was simulated for four different cases, i.e., azimuthally uniform power deposition without a focus ring, azimuthally uniform power deposition with a focus ring, non-uniform power deposition without a focus ring and non-uniform power deposition with a focus ring. The power deposition profiles,  $\text{Cl}^+$  densities and Cl densities were compared at 14 cm from the wafer plane and at the wafer plane. The etch rate distributions were also compared. It was found that when the etching was ion driven, etch uniformity was strongly dependent on the power deposition profile. For the cases with uniform power deposition, however, asymmetric pumping (of discharge gas) became a more prominent factor for etch uniformity. The cases simulated with a focus ring had significantly reduced azimuthal non-uniformities compared to the cases without.

Nam and Economou (2004) developed a two dimensional self consistent fluid model for the miniaturized inductively coupled plasma (mICP) presented by Hopwood, Minayeva and Yin (2000). The chamber was 5 mm in radius and 6 mm in length with a planar coil of diameter of 5 mm. The equations of plasma power deposition, electron temperature and particle species were solved for 370-770 mTorr argon pressure and 0-1.3 W r.f. power at 450 MHz. The plasma electrons in the model were assumed to be Maxwellian and the plasma sheath was not taken into consideration. The simulated electron temperature distribution was found to peak at the power deposition region near the coil. Warm electrons were also observed to persist outside the deposition region due to the high thermal conductivity of the plasma area. Nam et al. also noted that Langmuir probe measurements would be challenging due to the strong ion density gradients seen

in the simulation. Comparisons between experimental and theoretical results for ion and electron density and temperature were of reasonable agreement.

Takao et al. (2010) developed a two-dimensional axis-symmetric PIC-MCC model to simulate the same mICP source developed by Hopwood, Minayeva and Yin (2000). Two types of power deposition schemes (i.e., collisional and kinetic) were used to simulate coupling between the r.f. fields and the plasma. The collisional scheme used the cold electron approximation and the electron velocity distribution to solve plasma power deposition whereas the kinetic scheme used the current density calculated directly from particle trajectories to solve plasma power deposition. Calculations were performed at 370-770 mTorr pressure at the rf frequency of 450 MHz for powers below 3.5 W. Results were compared to the experimental data measured by Hopwood et al. and the fluid model developed by Nam and Economou (2004). The spatial plasma density distribution of the simulation was found to be close to the Nam and Economou fluid model in which steep gradient densities were obtained. Takao et al. also found that the plasma sheath was non-negligible in simulation and sheath thickness was almost 10% of the simulated reactor length. The electron energy density distribution of the plasma was non-Maxwellian throughout the entire plasma region with depletion at higher electron energies due to inelastic collisions. Non-consideration of the sheath and assumption of Maxwellian electrons in the Nam and Economou fluid model showed electron temperature distribution that was different from the Takao et al.'s PIC-MCC model. Pressure dependence of the plasma density also showed different tendency between the collisional and kinetic schemes in the PIC-MCC model with the collisional scheme showing decrease of plasma density and the kinetic scheme showing increase of plasma density with increasing pressure. The collisional scheme did not reflect the trend shown in experiment and this was attributed by Takao et al. to be due to the inadequacy

of the collisional model which did not consider the effects of non-collisional heating processes.

The chronological development of ICP simulation and theory (as detailed in this section) is summarized in Table 2.1.

**Table 2.1:** Chronological summary of the theoretical development and simulation of electrodeless discharges and ICPs.

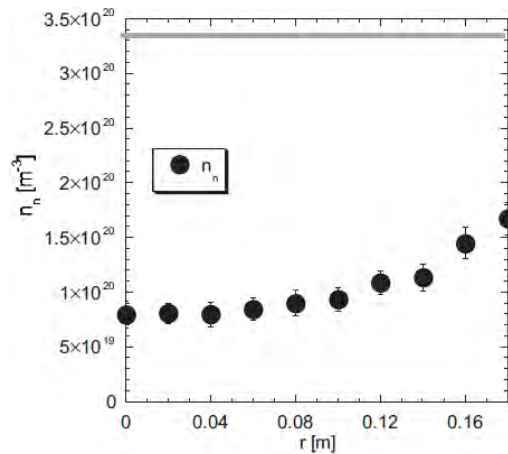
Research (Year)	Configuration	Model (Type)	Motivation
<b>Thomson (1927)</b>	Infinitely long cylindrical tube with helical coil (inductive fields)	Solenoid model (Analytical)	Development of new inductive discharge theory based on electromagnetic induction
<b>Thomson (1930)</b>	Cylindrical tube with external electrodes (capacitive fields)	Parallel plate model (Analytical)	Study of the conditions required to sustain an inductive discharge
<b>Townsend (1932)</b>	Spherical bulb/infinitely long cylindrical tube between two parallel plate electrodes	Parallel plate model (Analytical)	Development of new inductive discharge theory based on capacitive fields
<b>Kunz (1932)</b>	Infinitely long cylindrical tube with external electrodes (both inductive and capacitive fields)	Circuit model (Analytical)	Development of new circuit theory to derive inductive discharge properties
<b>Eckert (1962)</b>	Infinitely long, coaxial, cylindrical discharge tube and coil with circular cross-sections	ICP diffusion theory model (Analytical)	Development of Schottky diffusion theory (electron loss mechanism) for an inductive discharge
<b>Henriksen et al. (1971)</b>	Infinitely long, cylindrical discharge tube within an infinitely long coil	1D H mode EM field model (Analytical)	Development of electromagnetic field model with complex (previously assumed as real) plasma conductivity
<b>Vahedi et al. (1995)</b>	Planar coil ICP system seeded with Ar gas	2D Power deposition model with effective collision frequency (Analytical)	Development of power deposition model with effective collision frequency valid for both collisional and collisionless plasma regimes
<b>Li et al. (1995)</b>	Planar coil ICP system seeded with Ar and O <sub>2</sub> gases and Ar/CF <sub>4</sub> /O <sub>2</sub> gas mixture	Self consistent, time-averaged 2D fluid (Analytical)	Development of a 2D fluid model to simulate plasma transport properties valid at a specific pressure range

Table 2.1, continued...

Research (Year)	Configuration	Model (Type)	Motivation
<b>Gudmundsson &amp; Lieberman (1998)</b>	Planar coil ICP system seeded with Ar gas	Global model and transformer circuit model with effective collision frequency (Analytical)	Development of a global (volume-averaged) model and transformer (circuit) model; in which calculations were comparable to measured values.
<b>El-Fayoumi &amp; Jones (1998)</b>	Planar coil ICP system seeded with Ar gas	2D H mode EM field models (Analytical and Numerical)	Derivation of the analytical and numerical electromagnetic fields for H mode inductive discharge
<b>El-Fayoumi et al. (1998)</b>	Planar coil ICP system seeded with Ar gas	Power balance model and 2D E mode EM field model (Analytical)	Derivation of the power balance equations for calculation of the working path of an inductive discharge and description of discharge hysteresis between E-H mode transitions
<b>Turner &amp; Lieberman (1999)</b>	Planar coil ICP system seeded with Ar gas	Non-linear power balance model (Analytical)	Derivation of non-linear power balance factors contributing to E-H mode transition hysteresis in an inductive discharge
<b>Nambu (2000)</b>	High density, low pressure systems including ICPs; various atomic and molecular gases for specific calculations.	2D PIC-MCC model (Numerical)	Review of development of 2D numerical model for prediction of spatial properties of the inductive discharge including kinetic and collision theory
<b>Nam &amp; Economou (2004)</b>	Miniature ICP (mICP) with planar coil source and seeded with Ar gas	2D self-consistent fluid model (Analytical)	Development of 2D analytical fluid model for a miniaturized ICP system
<b>Takao et al. (2010)</b>	Miniature ICP (mICP) with planar coil source and seeded with Ar gas	2D PIC-MCC model (Numerical)	Development of 2D numerical model for a miniaturized ICP system

### 2.3. Measurement of Neutral Gas Heating and the Effects of Neutral Gas Depletion

The heating of neutrals in non-thermal plasmas is a recognized and well documented phenomenon especially in high density discharges such as ICPs. In plasma applications for material processing, the knowledge of neutral heating effects on plasma dynamics is essential for process control and reproducibility. A particularly non-negligible effect of neutral gas heating is the phenomenon of neutral gas depletion, in which the neutral density at the most intensely hot region of the discharge is lower compared to the surrounding region (O'Connell et al., 2008 and Shimada, Tynan & Cattolica, 2007); producing a well-type profile across the chamber radius (Figure 2.7).



**Figure 2.7:** Measured neutral gas density,  $n_n$  ( $m^{-3}$ ) (black circles) versus radius,  $r$  (m) of an ICP reactor operating at 10 mTorr argon pressure and 2000 W power. Neutral gas depletion was seen nearing the discharge center at  $r = 0$  m. Grey line shows the initial neutral gas density before discharge ignition (Shimada, Tynan & Cattolica, 2007).

Various techniques have been used to measure neutral gas heating in plasmas. Davis and Gottscho (1983) measured the temperatures of radicals, ions and neutrals in  $CCl_4$ , 98%  $CCl_4$ /2%  $N_2$  and  $N_2$  capacitive discharges. Through the  $CCl_4$  discharge, the rotational and vibrational temperatures of  $CCl$  radicals were measured using laser induced fluorescence (LIF). The rotational temperature distribution of the  $CCl$  radicals was found to be always 400 K colder than the vibrational temperature distribution. Davis et al. also measured the rotational temperature of the  $CCl$  radicals (through the

98% CCl<sub>4</sub>/2% N<sub>2</sub> discharge) and N<sub>2</sub> ions and neutrals (through the N<sub>2</sub> discharge) using the then novel technique of actinometry optical emission spectroscopy (AOES). Comparisons between measured rotational temperatures for LIF and AOES were of general agreement, however, AOES was found to be less viable when measurements were made close to surfaces. At 19 mm axial distance from the lower chamber electrode, the measured rotational temperatures for CCl radicals were 535 ± 25 K and 570 ± 30 K for LIF and AOES techniques, respectively

In 1987, Wormhoudt, Stanton, Richards and Sawin (1987) first introduced the use of a tunable diode laser technique, i.e., tunable diode laser absorption spectroscopy (TDLAS), to measure the neutral gas temperatures and atomic chlorine concentrations in a chlorine (Cl<sub>2</sub>) glow discharge. The infrared transition used for measurement was between the <sup>2</sup>P<sub>1/2</sub> ← <sup>2</sup>P<sub>3/2</sub> spin orbit levels and occurred at 11.33 μm wavelength. The measured atomic chlorine translational temperature was 770 ± 100 K and was consistent with measured rotational temperature found via AOES with nitrogen seed gas (95% chlorine/5% nitrogen). Atomic chlorine concentration was shown to increase with power (0-100 W) and pressure (200-800 mTorr) with the measured chlorine fractions in the discharge being between 3-8% or (1.8-6.6) × 10<sup>14</sup> cm<sup>-3</sup>.

Hopwood and Asmussen (1991) measured the neutral gas temperatures in a 2.45 GHz, multipolar electron cyclotron resonance plasma source seeded with argon and helium gases. Spectroscopic equipment which included an optical fiber probe, a Fabry-Perot interferometer, a ramp generator, a photomultiplier tube and a monochromator were used for this purpose. The argon and helium emission line profiles at 549.6 nm and 501.6 nm, respectively were measured and deconvolved with instrumental broadening which was determined using the 480.7 nm emission of a 150 W, 0.67 mTorr and 10

sccm xenon ECR discharge. The effects of Zeeman splitting were also compensated in the calculation to reveal constant Doppler broadening (widths) across the radius of the plasma. Neutral gas heating of argon at 0.77 mTorr was found to increase from 300 K to 500 K when microwave power was increased from 80 to 330 W. Both helium and argon neutral gas temperatures were shown to decrease as the neutral mean path increases which, according to Hopwood et al. indicates that the gases may be heated by ion-neutral collisional processes.

In a theoretical study, Fruchtman et al. (2005) investigated the impact of neutral gas depletion in the enhancement of plasma transport by self-consistently solving the pressure balance equations of plasma and neutral gas. Several parameters, including electron temperature, rate of ionization and plasma density were also derived analytically and visualized. It was found that the occurrence of neutral depletion in simulation also lead to non-linear enhancement of plasma transport. This was attributed to increased ionization and energy coupling in the region of interest. The enhancement of plasma transport also lead to unexpected decrease in plasma density despite increase in plasma power. In 2007, Liard et al. (2007) further extended the 2005 Fruchtman model by self consistently incorporating the effects of neutral gas heating. With neutral gas heating, stronger depletion was observed due to enhanced plasma transport to the walls, i.e., larger plasma flux leaving the discharge at a given plasma density.

Also in 2005, Abdel-Rahman et al. used the Abel inversion of Fulcher line intensities from OES to measure the phase and space resolved rotational temperatures of a hydrogen, planar coil RF ICP with the consideration of cascading effects of higher level molecular transitions. The rotational temperatures for different input powers and operational modes of the discharge were characterized and compared at the pressure of

15 Pa. Cross-checking with linewidth measurements of translational (i.e., neutral gas) temperature showed agreement. With the inclusion of cascading, it was found that neutral gas temperatures within the coil axis could reach up to 650 K for the input power of 350 W. Changes in these elevated temperatures were small throughout the r.f. cycle; especially in comparison to an r.f. capacitively coupled plasma.

Shimada, Tynan and Cattolica (2007) measured the radial neutral gas temperature, electron density, neutral gas pressure and total gas pressure profiles for pure N<sub>2</sub>, He/5%N<sub>2</sub> and Ar/5%N<sub>2</sub> plasmas in an ICP reactor at  $\leq 10$  mTorr pressure. A radial optical probe with a small light dump was used to measure the radial neutral gas temperature via AOES. From measurements, a significant rise of neutral gas temperature from room temperature, i.e., 600-900 K was observed for the three cases. Neutral gas density at the central region of the chamber was found to be reduced by the factor of 2-4 in the presence of the plasma (Figure 2.7). This depletion of neutrals was attributed by Shimada et al. to the electron pressure in high density plasma which was comparable to neutral gas pressure. Also in high density plasmas, the effects of neutral gas heating become significant and affect neutral gas density. By correcting the effects of thermal transpiration (which was neglected in previously published results, i.e., Tynan, 1999 and Yun, Taylor and Tynan, 2000) Shimada et al. found that the measured total gas pressure remained uniform across the chamber radius despite variations in neutral gas pressure.

O'Connell et al. (2008) investigated the neutral gas depletion mechanism in an inductively coupled, magnetic neutral loop argon plasma at different pressure regimes. In a magnetic neutral loop configuration, the inductive coil is designed to create a neutral field region in which the plasma is generated; providing higher plasma

ionization and uniformity for material processing purposes (Gans et al., 2007 and Uchida & Hamaguchi, 2008). Using the method of laser induced fluorescence (LIF), O'Connell et al. deduced the gas temperature of the argon plasma from the Doppler profile of the 772.38 nm line absorbed by argon metastable atoms (Figure 2.8 (a)).

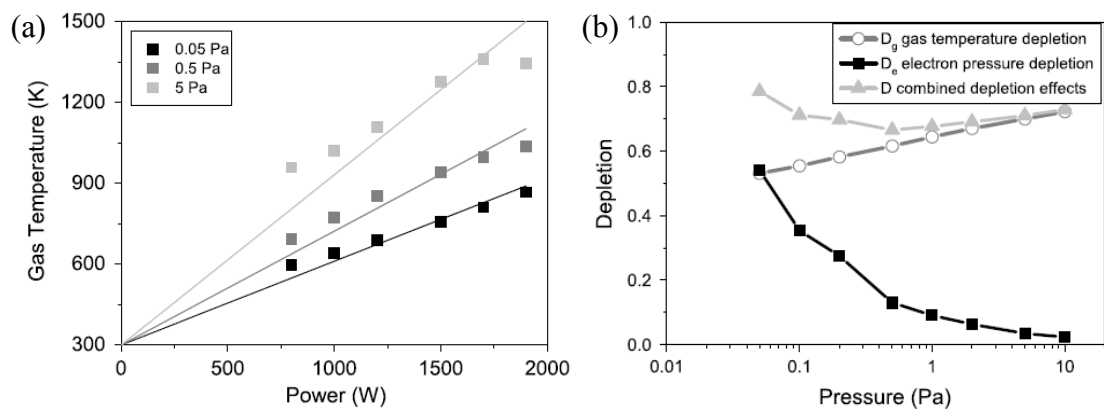


**Figure 2.8:** Graphs show (a) measured neutral gas temperature with increasing power at 0.05, 0.5 and 5 Pa and (b) measured contribution of electron pressure and gas temperature towards neutral gas depletion with increasing chamber pressure at 1000 W. Depletion of neutrals due to gas temperature becomes increasingly important as chamber pressure was increased (O'Connell et al., 2008).

Measurement of radially resolved electron density and temperature were done via Langmuir probe in the neutral loop plane. From measurements, it was observed that at pressures below 0.1 Pa, a relatively high degree of plasma ionization (above 1%) resulted in electron pressures exceeding neutral gas pressure, i.e., neutral gas depletion (Figure 2.8 (b)). This non-uniformity in plasma ionization rates produced a neutral depletion profile which peaked in the neutral loop region. At higher pressures (above 10 Pa) ionization rates were relatively low ( $<10^{-3}$ ), however, neutral gas depletion was still observed due to neutral gas heating i.e., with gas temperatures in the neutral loop region reaching close to 1500 K (Figure 2.8 (a)).

Crintea et al. (2009) introduced a novel optical emission spectroscopy (OES) technique for determination of electron temperature and plasma densities in low

pressure argon discharges. The technique was based on measurement of line ratios in argon and a collisional-radiative model (CRM) which includes metastable transport. Validation of the technique was made by comparison via simultaneous measurement obtained with Thomson scattering. Investigations were made using a 13.56 MHz, planar coil, inductively coupled neutral loop discharge (NLD) over the argon pressure range of 0.05-5 Pa and r.f. power was varied between 1-2kW. At low pressures, the EEDFs obtained by Thomson scattering were clearly Maxwellian. However, as pressure was increased, an enhancement of the energetic electron tail of the EEDF was observed. When compared to the OES measurement, electron temperature and plasma densities were in excellent agreement particularly if neutral gas depletion was included in the CRM, i.e., via increased neutral gas temperature and electron pressure in simulation. At pressures below 1 Pa and r.f. powers above 1 kW, electron pressure was the dominant depletion mechanism, whereby, electron pressure exceeded over 3 times the neutral gas pressure and the ionization degree approached 7%. At pressure above 1 Pa, neutral gas depletion was dominated by gas heating.

Fruchtman and Rax (2010) showed in their theoretical study that at plasma conditions where thermalized neutral atoms were in a sufficiently collisionless environment, an alternative phenomenon known as neutral gas repletion occurs instead of the expected neutral gas depletion. In neutral gas repletion, the neutral gas density increases instead of decreasing in the region where plasma ionization was highest. The phenomenon was attributed to the higher neutral gas inertia which dominates over collisional drag in a collisionless environment. In more typical cases where collisional drag was higher than neutral gas inertia, neutral gas depletion was observed. Fruchtman et al. in their work also identified a dimensionless parameter (i.e., proportional to the

ratio of plasma density and neutral gas density) that if larger or smaller than a critical value was able to predict the occurrence of neutral repletion or depletion.

Song, Lee and Chung (2011) characterized the properties of a low pressure, inductively coupled nitrogen-argon plasma using a combination of Langmuir probe and AOES. The plasma was characterized at the pressure range of 1-30 mTorr and applied r.f. power of 200-600 W. The actinometer used for AOES measurements was argon gas. Electron energy probability function, electron density and electron temperature were measured using an r.f. compensated Langmuir probe. The percentage of argon gas was varied between 5%-80% and its effects on plasma density, electron temperature and the dissociation fraction of nitrogen were observed. From experiments, it was found that as the percentage of argon increased, the dissociation fraction of nitrogen also increased. This was attributed to the increase in Penning excitation of the nitrogen atoms and the Penning dissociation of nitrogen molecules due to increased presence of argon metastables. Also, with increased argon percentage, the electron density was found to increase and electron temperature to slightly decrease. Song et al. further calculated the rotational and vibrational temperatures of  $N_2^+$  and  $N_2$  using the  $N_2^+$  first negative system  $B^2 \Sigma_u^+(v') \rightarrow X^2 \Sigma_g^+(v'')$  and  $N_2$  second positive system  $C^3 \Pi_u(v') \rightarrow B^3 \Pi_g(v'')$  from the molecular optical emission spectrum wavelength of 300-400 nm. The rotational temperatures and vibrational temperatures at 1.4 mTorr pressure were derived to be between 300-500 K and 8500-16500 K, respectively; with both values increasing with argon percentage.

Li et al. (2011) investigated the dependence of neutral gas temperature on gas pressure and r.f. power for argon and nitrogen inductively coupled plasmas using actinometry optical emission spectroscopy (AOES). For the argon plasma, 5% nitrogen

gas was added to the total gas flow as an actinometer. The highest neutral gas temperature measured for argon plasma was 1850 K at 1 Torr pressure and 600 W r.f. power (Figure 2.9 (a)).

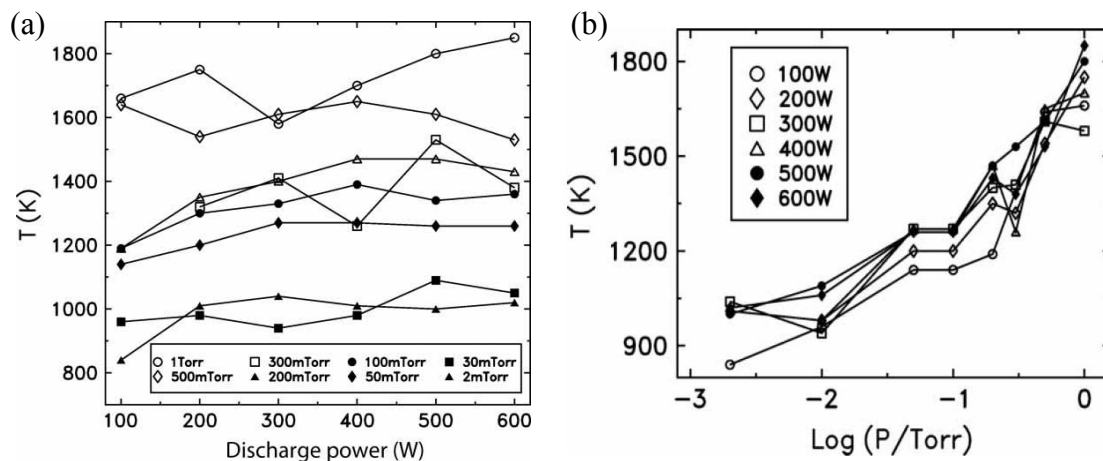


**Figure 2.9:** Measured neutral gas temperature versus (a) discharge power and (b) logarithm of pressure for an argon discharge using AOES. The highest neutral gas temperature obtained was 1850 K at 600 W and 1 Torr (Li et al., 2011).

The measured neutral gas temperature for argon (at H mode) was observed to vary almost linearly with the logarithm of gas pressure (2 mTorr-1 Torr) but vary only slightly within the r.f. power range (100-600 W) (Figure 2.9 (b)). E to H mode transition occurred during the increase of gas pressure for the nitrogen plasma which resulted in the sudden increase of measured values of neutral gas temperature. However, once in H mode, neutral gas temperatures for nitrogen plasma varied linearly with pressure as seen in argon plasma.

## CHAPTER 3: METHODOLOGY

### 3.0. Experimental Setup

A cylindrical stainless steel chamber of 0.29 m diameter and 0.30 m height was used to generate the plasma for experiments (Figure 3.1). A 0.20 m diameter and 0.01 m thick quartz dielectric plate is placed at the bottom of the chamber to allow transmission of the fields from the source. A total of twelve NW50 ports (four ports at each of the three levels) are located at the sides of the chamber for insertion of probes, vacuum pump fittings and gas inlet fittings. The chamber was pumped down using a KYKY FB450A turbo-molecular pump backed with an Edwards E2M18 rotary pump. A 6 turn planar coil of 0.09 m diameter is connected to a T&C Power Conversion AG0613 13.56 MHz 600 W r.f. power supply and is used to generate the plasma. A 7:1 step-down transformer was used to reduce the 50  $\Omega$  source impedance to the range of the plasma impedance ( $\sim 1 \Omega$ ) which was fine tuned using a variable air capacitor to match the plasma impedance. The primary discharge gas for the experiments, i.e., pure argon (99.999%) was seeded through a molecular sieve (to remove moisture) before being introduced into the system. The gas flow is controlled by two Dwyer GFC-2014 mass flow controllers. Gas pressure measurements are made using an APG100-XLC Pirani gauge. Chamber pressure was set by adjusting the flow rate of the mass flow controllers. For actinometrical measurement of neutral gas temperature, a secondary gas, nitrogen is added to the plasma in minuscule amounts (<5%). This gas is also flowed through an additional direct reading flow meter (Gilmont, EW-03232-23) and a series of needle valves for finer adjustment of the amount required.

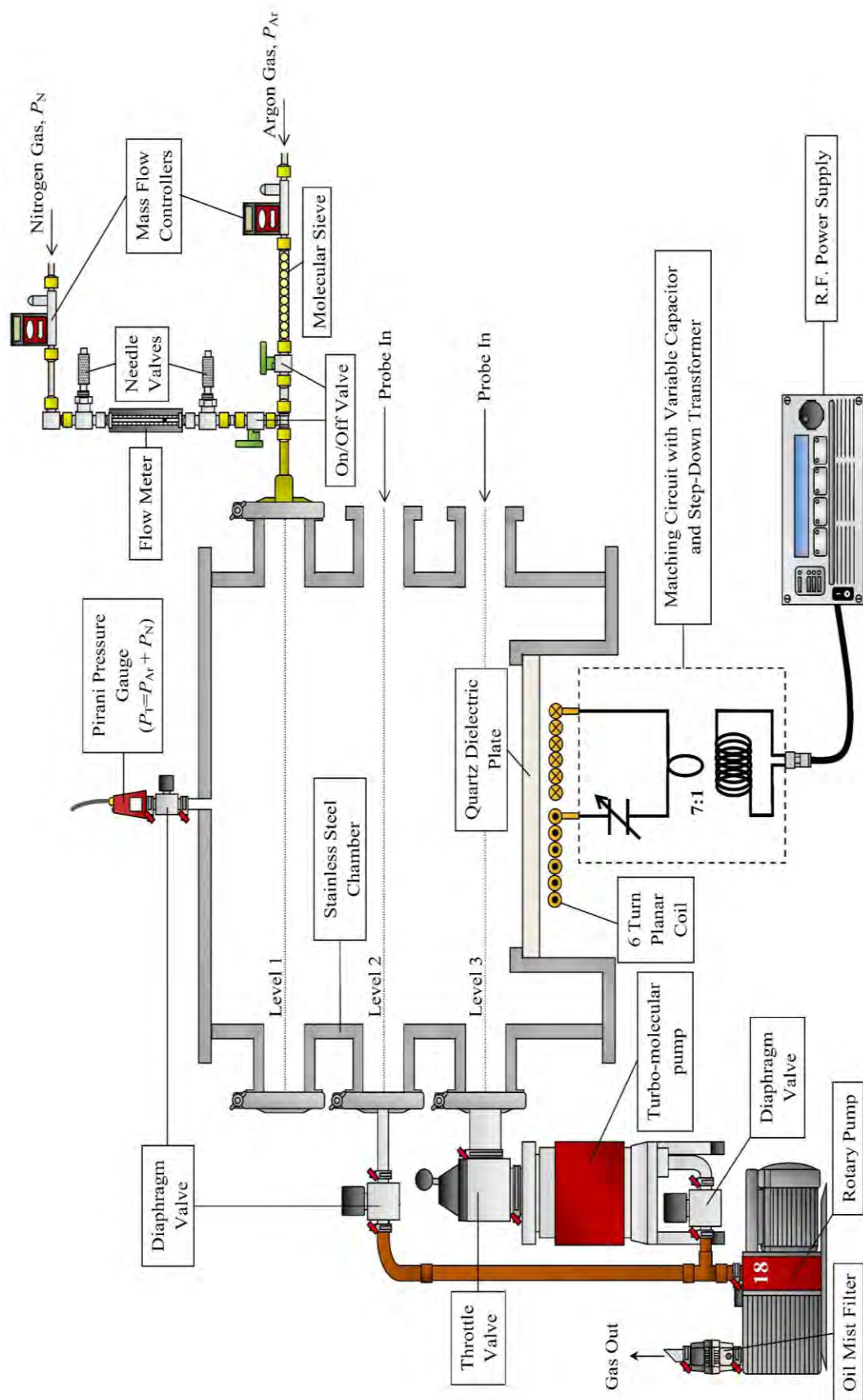


**Figure 3.1:** Inductively Coupled Plasma (ICP) setup used for experiments.

### 3.1. Langmuir Probe Setup

A laboratory r.f. compensated Langmuir probe (Figure 3.2(a)) based on the design by Chen (Chen, 2009) is used to measure the electrical characteristics of the plasma. The probe tip comprises of a tungsten wire of 0.5 mm diameter and 2.90 mm exposed length with a cylindrical collection area of 4.76 mm<sup>2</sup> (Figure 3.2 (b)). The tungsten wire is housed in a thin walled alumina tube of 0.7 mm diameter and is spaced with a wire spacer to ensure minimal electrical contact between the exposed probe tip and any conductive coatings that may deposit on the outer alumina tubing. (Lim, 2010). The probe tip was attached (via copper joint) to an LC resonant filtering circuit (Gagné & Cantin, 1972, Chabert & Braithwaite, 2011) which was used for r.f. noise compensation. The LC filter is designed to filter out signals at the self-resonant frequencies of 13.58 MHz and 27.04 MHz which are the fundamental and second harmonics of the applied drive frequency. An RG402 coaxial microwave cable is then used to transmit the filtered signal to the other end of the probe which was soldered to a BNC connector. The entire probe is sheathed by an outer alumina tubing; with the end near the probe tip covered with a Teflon insert. R.f. shielded coaxial cables were used to transmit the probe signals to the diagnostic setup for analysis. The probe's ground reference point for measurement of plasma parameters was taken to be the chamber ground. The probe was mounted into a specifically made probe housing and holder which is attached to a Huntington L-2111-6-SF vernier linear positioner to enable radially resolved measurements at millimeter precision.<sup>1</sup>

<sup>1</sup> Constraints by the positions of the available chamber diagnostic ports and by the Langmuir probe holder only allows for measurement at specific axial distances, i.e., 0.032 m, 0.060 cm and 0.114 m from the dielectric plate. For correlation in simulation, these axial distances will also be used for measurement with other probes.

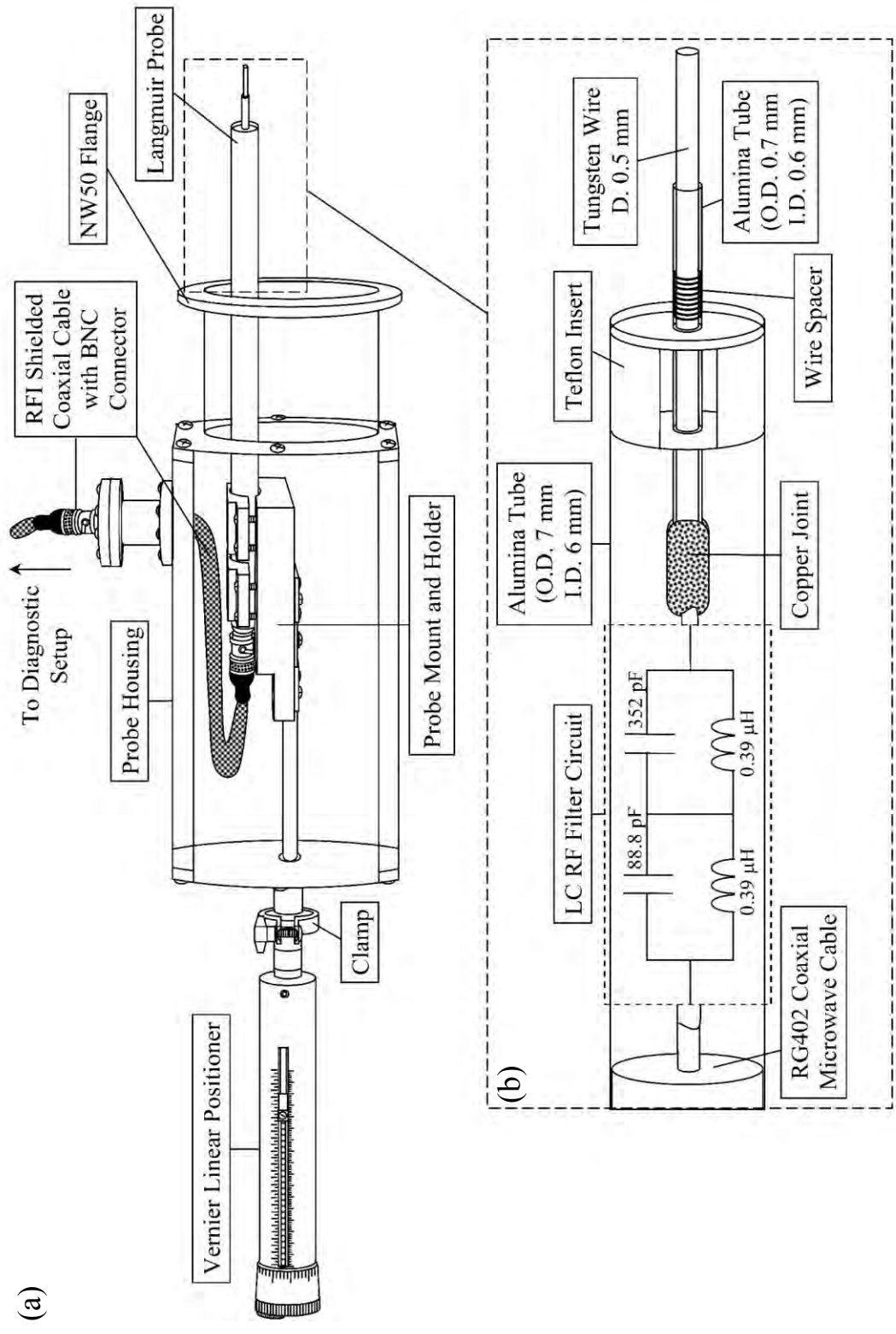


**Figure 3.2:** Langmuir probe and mount schematics.

### 3.1.1. Langmuir Probe Diagnostics Setup

To obtain the probe's current signal, a triangular bias voltage of  $-60$  to  $60$  V at  $16.1$  Hz frequency was swept into the probe using a Kepco BOP 100-1M,  $100$  W bipolar operational amplifier/power supply (Figure 3.3). The bias frequency and voltage profile was set using an Aim-TTi TG120  $20$  MHz function generator connected to the programmable inputs of the Kepco unit. The probe bias frequency is typically set at a low frequency to avoid errors from probe heating and stray capacitances from the probe circuit (Chen, 2003). Current signal from the probe is calculated from the current feedback voltage across a current monitoring resistor,  $R_1$  of suitable value ( $10$ ,  $100$  or  $1000 \Omega$ ). The value of the resistor is selected such that the probe bias voltage remains stiff, i.e., minimal loading effect (Lim, 2010). For the measured discharges,  $R_1$  was set at  $10 \Omega$ . The feedback voltage is passed through a unity gain isolation amplifier to isolate the diagnostic equipment from damaging electrical static and signal noise by the discharge. Both probe voltage and current signals are filtered by two RC low pass filters before being measured by a Tektronix TDS-2014 oscilloscope. Measurements were made for 3 axial distances above the dielectric plate, i.e., at  $0.032$  m,  $0.060$  m and  $0.114$  m at  $180$  W r.f. power and  $0.03$ ,  $0.07$  and  $0.2$  mbar argon pressure.

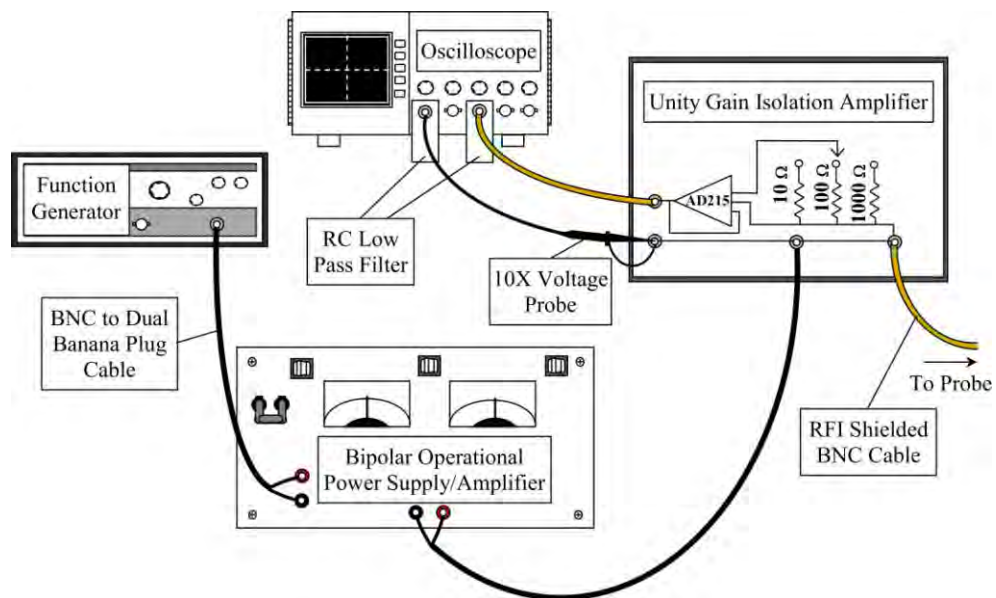


**Figure 3.3:** Langmuir probe diagnostics setup.

### 3.1.2. Langmuir Probe Theory and Analysis

A measured Langmuir probe  $I$ - $V$  signal is shown in Figure 3.4.

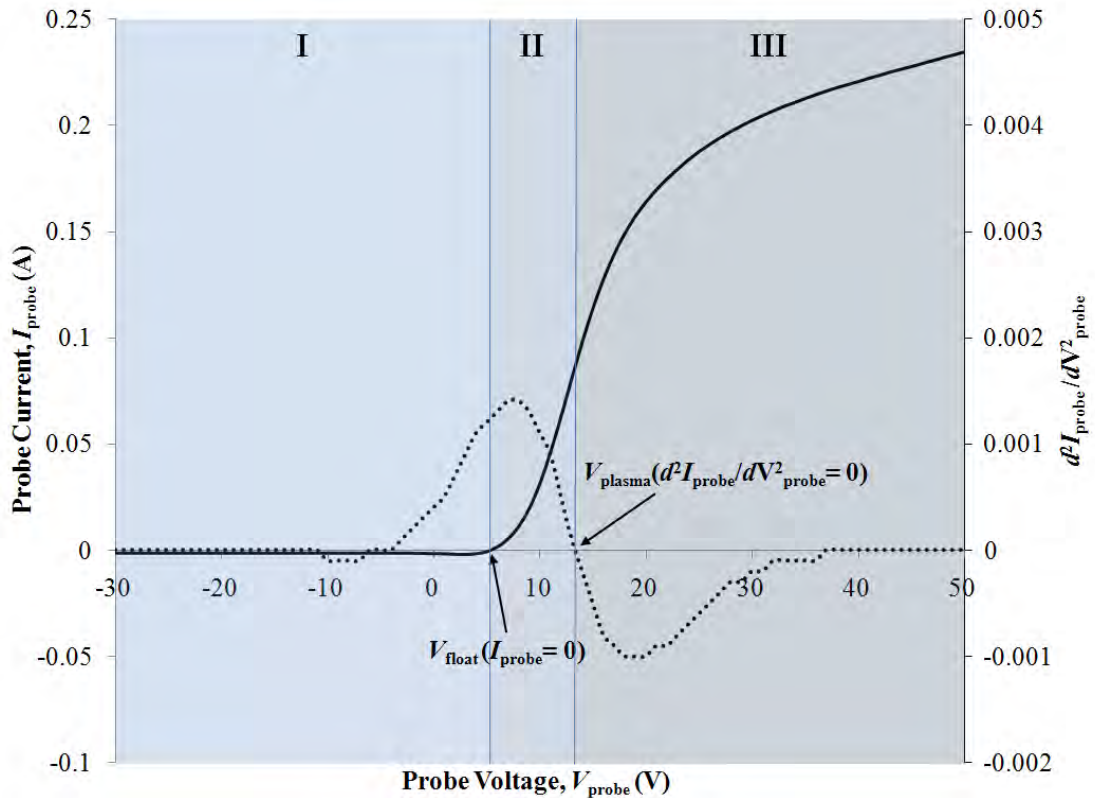


**Figure 3.4:** Measured Langmuir probe  $I$ - $V$  signal and differential curve ( $d^2I_{\text{probe}}/dV^2_{\text{probe}}$ ) at 0.032 m axial distance for 0.2 mbar pressure and 180 W r.f. power. **I** represents the ion saturation region, **II** represents the electron retardation region and **III** represents the electron saturation region. Measurement was taken at the plasma center ( $R = 0$  m).

The curve can be divided to three regions of interest namely the ion saturation region (**I**), the electron retardation region (**II**) and the electron saturation region (**III**) (Chen, 1965). In the ion saturation region (**I**), the probe bias voltage is highly negative such that it attracts only ions to its surface and thus, the resultant current is mainly due to ions. The limiting probe ion current or ion saturation current,  $I_{\text{ion,sat}}$  can be estimated from this region. In the electron retardation region (**II**), the electrons begin to be attracted and contribute to the probe current. The region starts with the floating potential,  $V_{\text{float}}$  or the potential at which the ion and electron fluxes are equal and the resultant probe current is zero ( $I_{\text{probe}} = 0$ ). As the probe bias voltage is increased from  $V_{\text{float}}$ , more electrons are attracted to the probe surface starting from highly energetic

electrons to lower energy electrons. The resultant probe current is an increasing contribution of electron current and reduced contribution of ion current. The region ends at the plasma potential,  $V_{\text{plasma}}$ , which is the potential at which the lowest energy electrons are not repelled from the probe. From the values of  $V_{\text{float}}$  and  $V_{\text{plasma}}$ , electron parameters such as electron density,  $n_e$ , electron temperature,  $T_e$ , Debye length,  $\lambda_D$  and electron energy distribution function (EEDF) can be derived. Past the electron retardation region is the electron saturation region (**III**). At this region the bias voltage of the probe attracts only electrons and even low energy ions are repelled from the probe surface. Here, the current is mainly the result of electrons and the electron limiting current or electron saturation current,  $I_{\text{elec,sat}}$  can be determined.

There are several theories available for calculation of plasma parameters. These include the orbital motion limited (OML) theory (Mott-Smith & Langmuir, 1926), the Allen-Boyd-Reynolds (ABR) theory (Allen, Boyd & Reynolds, 1957 and Chen, 1965) and the Bernstein-Rabinowitz-Laframboise (BRL) theory (Laframboise, 1966). Differences between these theories lie mainly in the derivation of the ion current based on assumptions made on ion and sheath properties. Since the  $I$ - $V$  signal of the probe is a combination of both electron and ion currents, proper treatment of the ion current is important to avoid over or under estimation of plasma parameters (Chen, 2003).

Selection of the appropriate theory can be done by estimating the current collection regime of the Langmuir probe during discharge conditions used in experiment (Maurice, 2003, Behlman, 2009 and Conde, 2011). The current collection regime is determined by the collisionality and relative thickness of the probe sheath and is defined using three parameters, i.e., probe radius,  $R_{\text{probe}}$ , sheath width,  $l_s$  and particle mean free path,  $\lambda_{\text{mfp}}$  (Figure 3.5).

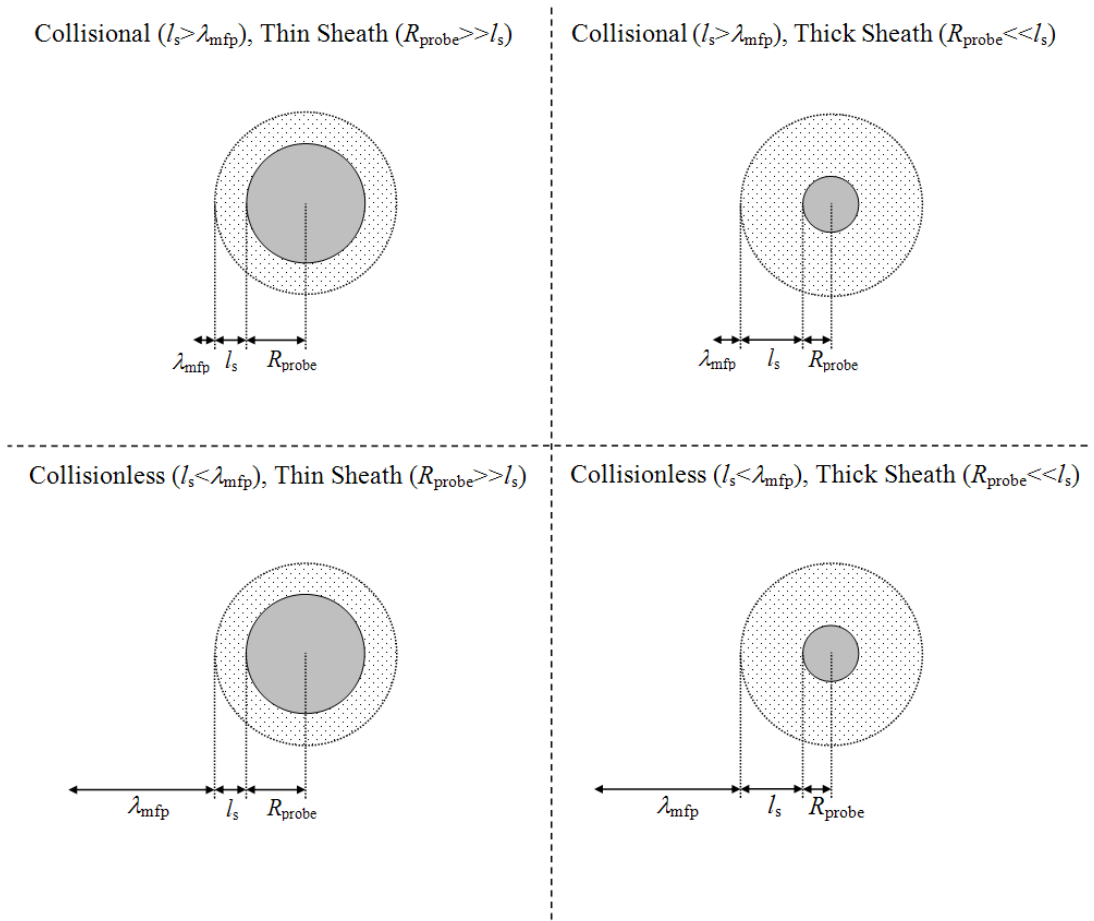


**Figure 3.5:** The four different current collection regimes for a Langmuir probe (Maurice, 2003).

A thin or thick probe sheath regime is deduced by comparing the probe sheath thickness,  $l_s$  with the probe radius,  $R_{probe}$ , i.e.,  $l_s \ll R_{probe}$  and  $l_s \gg R_{probe}$  for thin and thick sheath, respectively. On the other hand, sheath collisionality in experiment conditions can be determined by comparing  $l_s$  to the mean free path,  $\lambda_{mfp}$  of important particle interactions near the probe sheath including electron-neutral mean free path,  $\lambda_{en}$  ion-neutral mean free path,  $\lambda_{in}$  and ion-ion mean free path,  $\lambda_{ii}$ . If  $l_s < \lambda_{mfp}$ , the sheath is considered to be collisionless, else if  $l_s > \lambda_{mfp}$ , the sheath is seen as collisional. The probe sheath thickness,  $l_s$  for regime determination can be generally approximated by using Child-Langmuir relation (Lieberman & Lichtenberg, 2005 and Chabert & Braithwaite, 2011), i.e.,

$$l_s \approx \lambda_D \left( \frac{V_s}{T_e} \right)^{3/4}. \quad (3.1.1)$$

Here,  $V_s$  is the potential difference of the plasma sheath in V and  $T_e$  is the electron temperature in eV. The Debye length,  $\lambda_D$  (in m) is given by,

$$\lambda_D = 7.43 \sqrt{\frac{T_e}{n_{e, \text{cm}}}}, \quad (3.1.2)$$

where,  $n_{e, \text{cm}}$  is the electron density in  $\text{cm}^{-3}$ . To estimate the mean free paths  $\lambda_{\text{en}}$ ,  $\lambda_{\text{in}}$  and  $\lambda_{\text{ii}}$ , the following equations were used (Lieberman & Lichtenberg, 2005 and Maurice, 2003),

$$\lambda_{\text{en}} = \left( \frac{1}{n_g \sigma_{\text{en}}} \right), \quad (3.1.3)$$

$$\lambda_{\text{in}} = \left( \frac{1}{n_g \sigma_{\text{in}}} \right), \quad (3.1.4)$$

and

$$\lambda_{\text{ii}} = \frac{2.8 \times 10^{17} T_i^2}{n_e \ln \Lambda}, \quad (3.1.5)$$

where,  $n_g$  is the neutral gas density in  $\text{m}^{-3}$ ,  $\sigma_{\text{en}}$  and  $\sigma_{\text{in}}$  are the electron-neutral total collision cross section and ion-neutral scattering cross section, respectively in  $\text{m}^2$ ,  $T_i$  is the ion temperature in eV,  $n_e$  is the electron density in  $\text{m}^{-3}$  and  $\ln \Lambda$  is the Coulomb logarithm.  $n_g$  is calculated by using ideal gas law, i.e.,

$$n_g = \frac{P}{k_B T_n}. \quad (3.1.6)$$

where,  $P$  is the filling pressure in Pa,  $T_n$  is the neutral gas temperature in K and  $k_B$  is Boltzmann's constant in  $\text{JK}^{-1}$ . The Coulomb logarithm is given by (Book, 1990),

$$\ln \Lambda = 23 - \ln \frac{n_e^{1/2} T_e^{-3/2}}{100} . \quad (3.1.7)$$

For the present experimental setup, the current collection regime was determined by using the values in Table 3.1. The ions were assumed to be at low energy with the ion temperature,  $T_i = 0.1$  eV and the corresponding ion-neutral collision cross section,  $\sigma_{in} = 1.57 \times 10^{-18}$  (Phelps, 1991). The electron-neutral total collision cross section,  $\sigma_{en}$  is taken as  $\sim 10^{-19} \text{ m}^{-2}$  (Hayashi, 1981). The electron density,  $n_e$  and electron temperature,  $T_e$  were taken to be  $\sim 10^{17} \text{ m}^{-3}$  and  $\sim 2.5$  eV based on values reported by previous works and texts (Hopwood et al., 1992, Ostrikov et al. 2002, Godyak, Piejak & Alexandrovich, 2002, Lieberman & Lichtenberg, 2005, Chabert & Braitewaite, 2011). Plasma sheath potential,  $V_s$  is estimated by taking the sum of the measured bias potential at which the ion current saturates,  $V_{ion,sat}$  and the plasma potential,  $V_{plasma}$ , i.e.,  $V_s = V_{ion,sat} + V_{plasma}$ . The neutral gas temperature,  $T_n$  was taken from measurement by AOES technique detailed in Section 3.4.

**Table 3.1:** List of parameters used to determine the probe collection regime.

Argon Pressure, $P$ (mbar)	0.03	0.07	0.2
Neutral Gas Temperature, $T_n$ (K)	380	630	800
Plasma Sheath Potential, $V_s$ , V	35	45	50
Probe Radius, $R_{probe}$ ( $\mu\text{m}$ )	250	250	250
Plasma Sheath Width, $l_s$ , ( $\mu\text{m}$ )	269	325	351
Electron-neutral Mean Free Path, $\lambda_{en}$ ( $\mu\text{m}$ )	17480	12420	5520
Ion-neutral Mean Free Path, $\lambda_{in}$ ( $\mu\text{m}$ )	1113	791	352
Ion-ion Mean Free Path, $\lambda_{ii}$ ( $\mu\text{m}$ )	2976	2976	2976

For the range of pressures used in experiment, the probe sheath was found to be thick ( $l_s > R_{\text{probe}}$ ) and collisionless ( $l_s < \lambda_{\text{mfp}}$ ). Based on the probe collection regime, the orbital motion limited (OML) theory was found to be most suitable for calculation of plasma parameters. The plasma potential,  $V_p$  is first determined by taking the crossing point of the second derivative of the probe  $I$ - $V$  curve with zero, i.e.  $d^2I/dV^2 = 0$ . This technique allows for more accurate determination of  $V_p$  without the ambiguity of approximate methods. The floating potential,  $V_f$  is determined by taking the potential at which  $I = 0$ . As previously mentioned, probe current,  $I_{\text{probe}}$ , is the sum of the ion current,  $I_{\text{ion}}$  and the electron current,  $I_{\text{elec}}$ , i.e.,  $I_{\text{probe}} = I_{\text{ion}} + I_{\text{elec}}$ . Thus, before calculation of electron parameters,  $I_{\text{ion}}$  has to be first subtracted from  $I_{\text{probe}}$  to obtain  $I_{\text{elec}}$  across the signal range. A linear extrapolation from the ion saturation region is used as the estimation of  $I_{\text{ion}}$  for subtraction (Chen, 2003).

The electron temperature,  $T_e$  and electron density,  $n_e$  is subsequently calculated using the following equations (Maurice, 2003 and Chen, 2009):

$$T_e = \frac{\int_{V_f}^{V_p} I_e(V) dV}{I_e(V_p)} \quad (3.1.8)$$

and

$$n_e = \frac{I_e(V_p)}{A_p} \left( \frac{2\pi m_e}{e^2 k_B T_e} \right)^{1/2}. \quad (3.1.9)$$

Here,  $I_e(V)$  and  $I_e(V_p)$  are the electron current and the electron current at the plasma potential, respectively, in A.  $A_p$  is the probe collection area in  $\text{m}^2$ ,  $m_e$  is the mass of electrons in kg,  $T_e$  is the electron temperature in K and  $e$  is the electronic charge in C. The electron energy distribution function,  $f(\varepsilon)$  or EEDF provides important information

of the energy distribution of electrons at a particular position from which the collisional processes involving the particles can be deduced.  $\varepsilon$  is the electron energy between  $V = 0$  to  $V = V_p$ , in eV. Assuming that in the electron retardation region, the second derivative of the I-V curve is equal to the second derivative of the electron current (i.e., the second derivative of the ion current is negligible), the EEDF can be calculated by using the Druyvesteyn expression (Godyak, Piejak & Alexandrovich, 2002 and Magnus & Gudmundsson, 2008),

$$f(\varepsilon) = \frac{2I_e''}{e^{3/2}A_p}(2m_eV)^{1/2} . \quad (3.1.10)$$

The EEDF can also alternately be used to calculate the electron density,  $n_e$  ( $m^{-3}$ ) and effective electron temperature,  $T_{e,\text{eff}}$  (eV) using,

$$n_e = \int_0^\infty f(\varepsilon)d\varepsilon \quad (3.1.11)$$

and

$$T_{e,\text{eff}} = \frac{2}{3}\langle\varepsilon\rangle . \quad (3.1.12)$$

Here,  $\langle\varepsilon\rangle$  is the average electron energy in eV which can be found by using,

$$\langle\varepsilon\rangle = \frac{\int_0^\infty f(\varepsilon)\varepsilon d\varepsilon}{n_e} . \quad (3.1.13)$$

To calculate plasma parameters from the current-voltage characteristics a MATLAB code was written (see Appendix A). The electron density and electron temperature were calculated using both Maxwellian distribution assumption and EEDF methods.

### 3.2. Magnetic Probe Setup

Electrostatic noise compensated, center-tapped, axial and radial magnetic probes (Chakrabarty, 2006) were constructed to measure the radially resolved magnetic field distributions in the plasma (Figure 3.6(a)). Each probe (pick-up coil) was made using two 0.25 mm diameter copper wires which were wound together and grounded at opposing ends (Figure 3.6 (b)) on a small quartz tube of 2 mm in diameter and 5 mm length. The ends of the windings are twisted and the wires are run through a 48 cm long copper tube of 3.3 mm diameter which is attached to a cylindrical copper housing that holds two BNC connectors. The copper housing and tubing are ensured to be properly sealed together with copper foil tape to minimize pickup of stray r.f. signals. The ends of the wires were soldered to two BNC connectors. The axial probe solenoid is perpendicular to the copper tube ( $z$ -direction), whereas the radial probe solenoid is parallel ( $r$ -direction), i.e., (Figure 3.6 (c)). A port attachment with two fixed Pyrex tubes was fitted to the chamber for shielding of the magnetic probe during radially resolved measurements of the plasma. Measurements were made at 0.032 m and 0.060 m axial distances above the dielectric plate for 180 W r.f. power and 0.03, 0.07 and 0.2 mbar argon pressures. Simultaneous measurements of coil current and voltage were also made during the measurement of the fields with the respective probes (probe details in Section 3.3). Results were collected via Tektronix TDS-2014 oscilloscope.

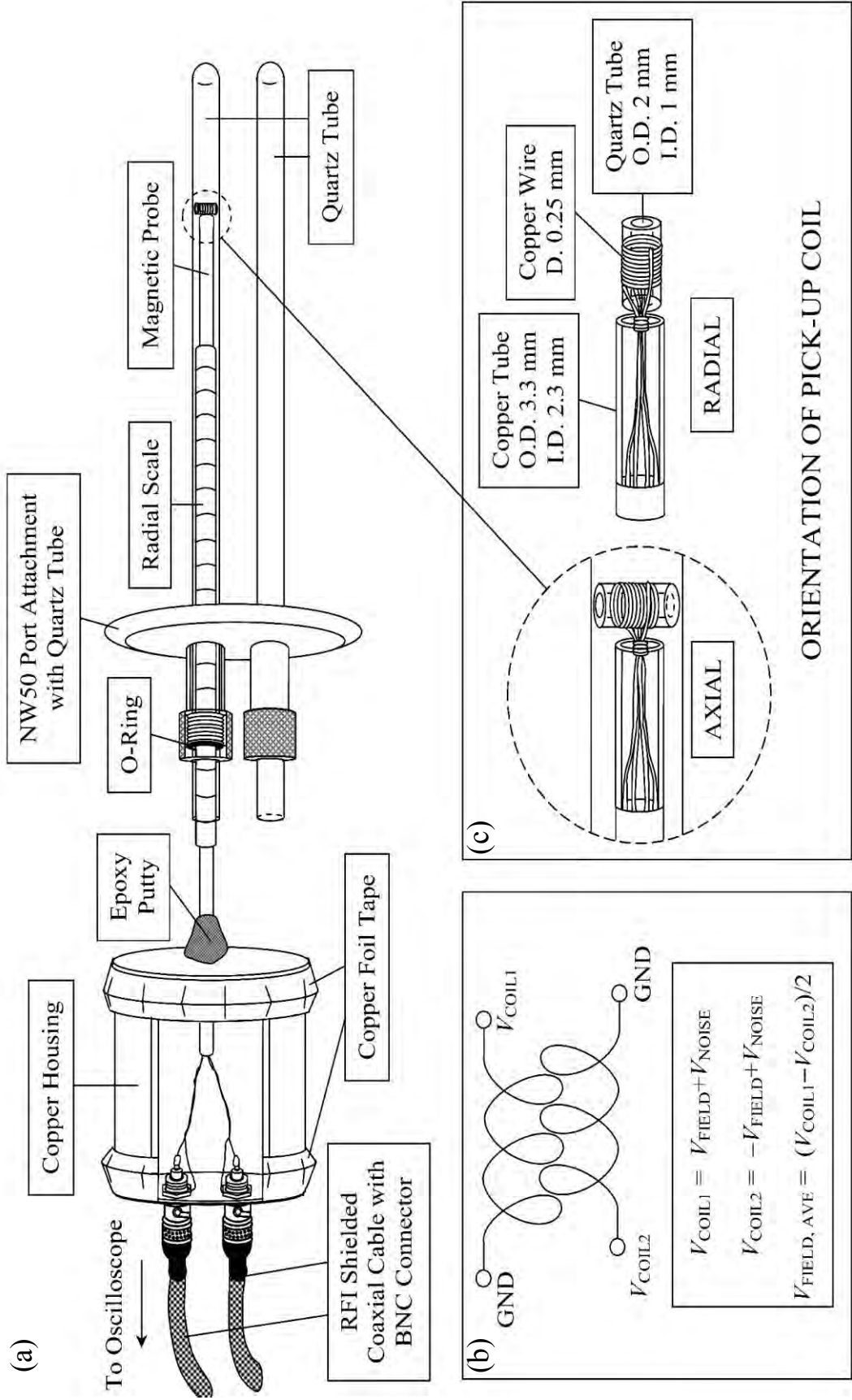


**Figure 3.6:** Magnetic probe schematics and circuit.

### 3.2.1. Probe Theory and Analysis

The typical voltage signals measured from the two coil windings (i.e.,  $V_{\text{COIL1}}$  and  $V_{\text{COIL2}}$  in Figure 3.6 (b), via the oscilloscope channels CH3 and CH4 would be sinusoidal and at opposing polarities (Figure 3.7). Random and non-periodic electrostatic noise,  $V_{\text{NOISE}}$ , from the acquired coil signals are compensated by taking the difference of  $V_{\text{COIL1}}$  and  $V_{\text{COIL2}}$ . The oscilloscope MATH function was used to calculate the difference, i.e.,  $V_{\text{MATH}} = V_{\text{CH3}} - V_{\text{CH4}} = V_{\text{COIL1}} - V_{\text{COIL2}}$  from which the average magnetic field voltage,  $V_{\text{FIELD, AVE}}$  can be obtained.

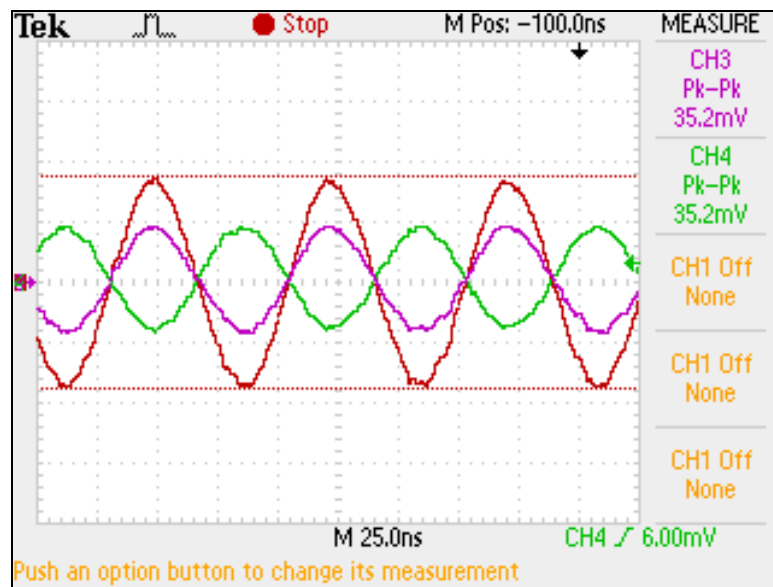


**Figure 3.7:** Oscilloscope screen capture for the axial magnetic probe at 0.032 m axial distance, 0.07 mbar argon pressure and 180 W r.f. power. Measurement was taken at the plasma center ( $R = 0$  m).

Before use in experiment, the probes are calibrated against a standard device, i.e., a laboratory Helmholtz coil, of radius,  $R_{\text{H}} = 0.046$  m and coil windings,  $N_{\text{H}} = 2$ . In a separate setup, the Helmholtz coil is connected to the AG0613 r.f. source and input power is varied from 0-50 W at 5 W intervals. The current through the device is measured using a Pearson 4100 current probe. The peak magnetic field through the Helmholtz coil,  $B_{\text{H, PEAK}}$  is given by,

$$B_{H, \text{PEAK}} = \left(\frac{4}{5}\right)^{3/2} \frac{\mu_o N_H I_{H, \text{PEAK}}}{R_H}, \quad (3.2.1)$$

where,  $I_{H, \text{PEAK}}$  is the peak Hemholtz coil current in A. For direct determination of the axial and radial magnetic fields from the measured peak differential voltage  $V_{\text{MATH, PEAK}}$ , the linear fitting,

$$B_{H, \text{PEAK}} = m_H V_{\text{MATH, PEAK}} + C_H \quad (3.2.2)$$

is used, yielding the calibration curves shown in Figure 3.8. Here,  $m_H$  and  $C_H$  are the probe calibration constants in  $\text{TV}^{-1}$  and V, respectively. The fitted calibration constants are  $m_H = (4.53 \pm 0.04) \times 10^{-5} \text{ TV}^{-1}$  and  $C_H = (4 \pm 2) \times 10^{-7} \text{ V}$  for the axial probe and  $m_H = (6.27 \pm 0.04) \times 10^{-5} \text{ TV}^{-1}$  and  $C_H = (1.0 \pm 0.1) \times 10^{-6} \text{ V}$  for the radial probe.

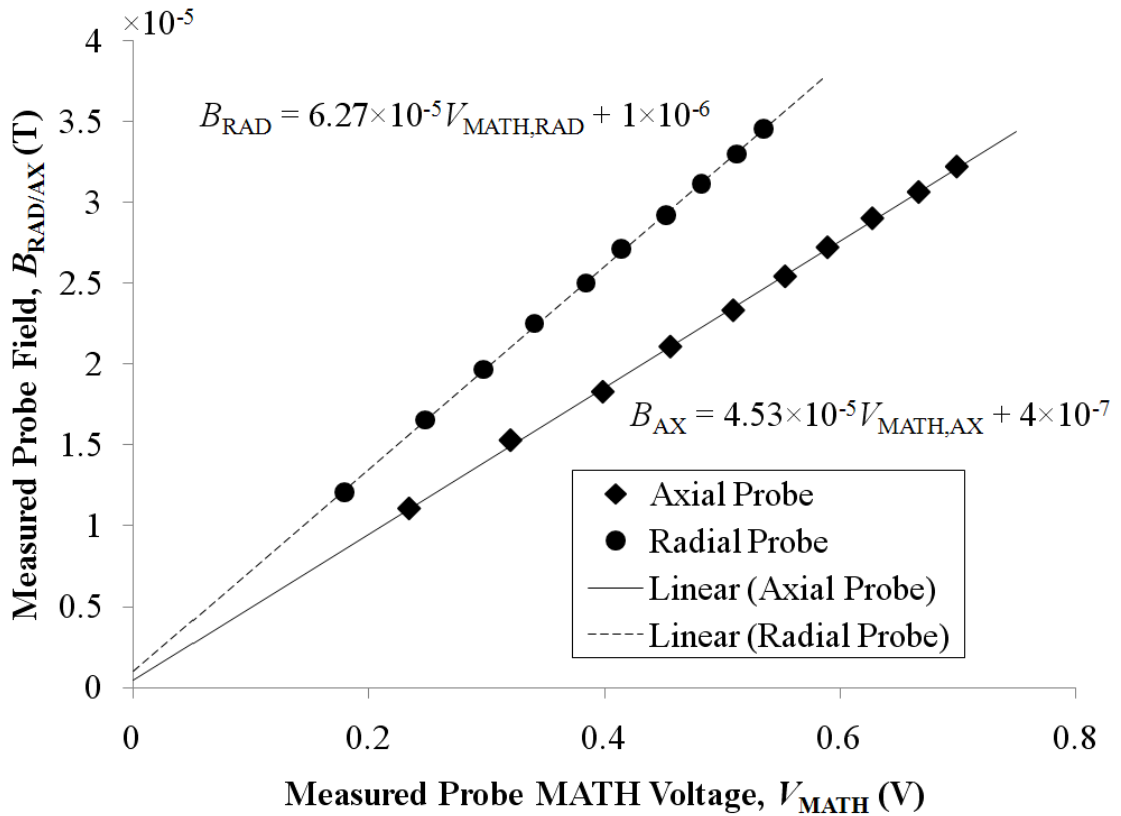


**Figure 3.8:** Axial and radial magnetic probe calibration curves.

### 3.3. Current and Voltage Probes

R.f. current passing through the planar coil was measured using a Pearson model 6595 (0.5 V/A, 100 Hz-150 MHz) current probe. Voltage is measured using a Tektronix model P6015A (1000X, 3.0 pF, 100 M $\Omega$ ) voltage probe. The average inductance of the coil was calculated from the measured values (Figure 3.9) using (El-Fayoumi, Jones & Turner 1998),

$$L = I_{p, \text{evac}} \omega / V_{p, \text{evac}} \quad (3.3.1)$$

whereby,  $\omega$  is the drive frequency and  $I_{p, \text{evac}}$  and  $V_{p, \text{evac}}$  are the measured peak coil current and  $V_{p, \text{evac}}$  is the measured peak coil voltage for an evacuated chamber. The average inductance was found to be  $(1.201 \pm 0.006) \times 10^{-6}$  H.

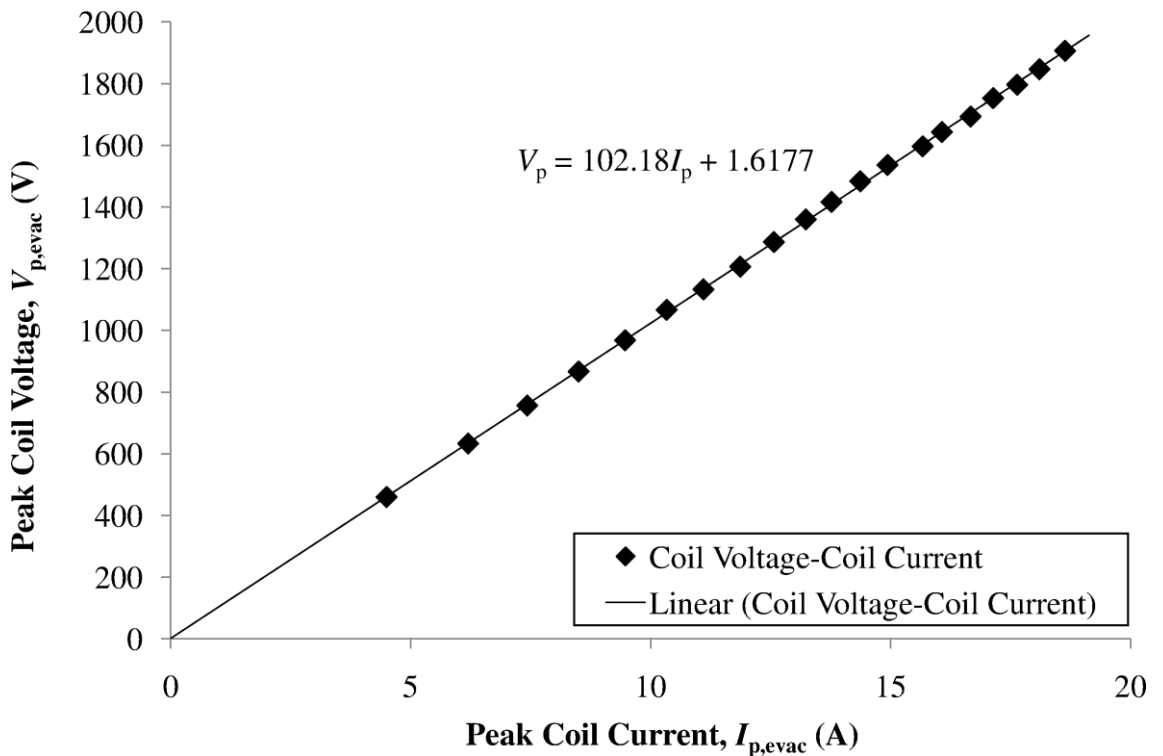


**Figure 3.9:** Measured peak planar coil voltage,  $V_{p, \text{evac}}$  (V) versus peak planar coil current,  $I_{p, \text{evac}}$  (A) at evacuated condition.

Using the current probe, measurement of the peak E to H mode transition coil currents (H mode transition current),  $I_{tr}$  and the peak H to E mode transition coil currents (H mode maintenance current),  $I_{mt}$  were made for the discharge at the argon pressures of 0.02-0.2 mbar.  $I_{tr}$  is measured at the threshold point before the discharge transition from E to H mode, when power is gradually increased; whereas,  $I_{mt}$  is measured at the threshold point before the transition from H to E mode, when power is gradually decreased.

### 3.4. Actinometry Optical Emission Spectroscopy (AOES) Setup

For actinometry measurement of neutral gas temperature an Ocean Optics HR4000 spectrometer was used. The unit consists of a collimating lens (Figure 3.10 (b)), a multimode fiber optic cable (400  $\mu\text{m}$ , UV/SR-VIS, High OH content optimized for 200-1100 nm range), a spectrometer with 10  $\mu\text{m}$  slit aperture and an USB interface cable. The spectrometer has a resolution of 0.5 nm and measures a range of 200-660 nm at 0.13 nm intervals. Spectral measurement was obtained using the SpectraSuite software. The fiber optic cable was mounted onto a modified travelling microscope stand and was aligned using an alignment laser such that the collected column of light is parallel to the radial plane of the chamber (Figure 3.10(a)). The level and adjustment knobs on the microscope (for radial-axial-depth translation) were used to adjust the fiber to the required position. Once the microscope was positioned, metal blocks were affixed around the setup to keep it in place during handling. For actinometric studies, nitrogen gas was seeded into the background argon gas at  $\leq 5\%$  total gas pressure. The emission spectra was measured at 0.032 m and 0.060 m axial distances above the dielectric plate for 0-200 W r.f. power and 0.03, 0.05, 0.07, 0.1 and 0.2 mbar total pressure (Ar/N<sub>2</sub> admixture).<sup>1</sup> An average of 20 data sets is taken for each pressure and power.

<sup>1</sup> Measurements using the AOES technique in this work would be mainly used as a reference to determine the range of neutral gas temperatures that would be suitable for simulation; without direct comparison to the measured properties of pure argon discharge by other probes.

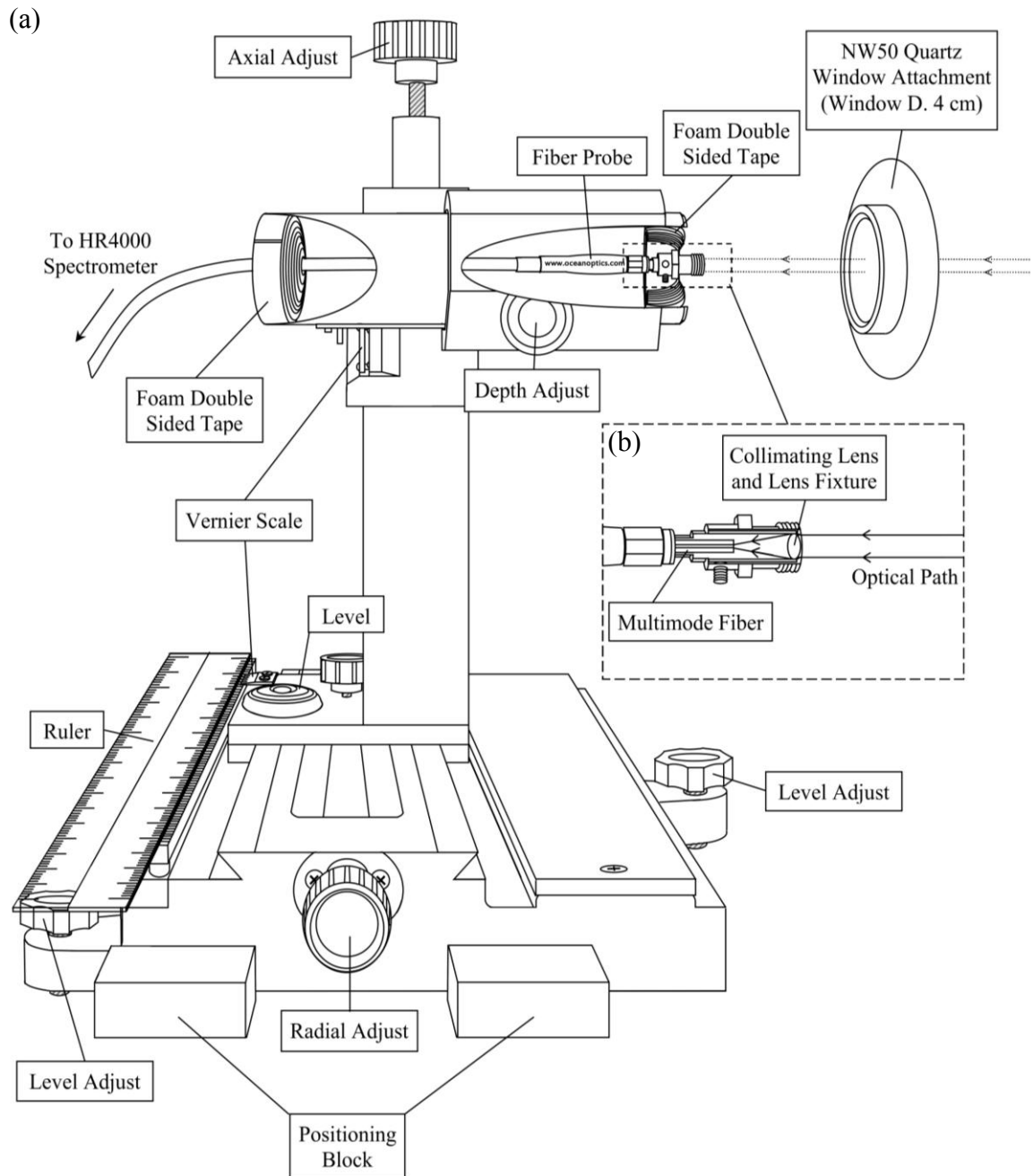


**Figure 3.10:** AOES probe and mount schematics.

### 3.4.1. AOES Theory and Analysis

Actinometric optical emission spectroscopy (AOES) is a method used to measure plasma parameters by studying the emission properties of a seeded probe gas, i.e., an actinometer. The actinometer is seeded in miniscule amounts (<5%) to minimize interaction with the measured discharge properties (Davis & Gottscho, 1983,

Wormhoudt et al., 1987, Donnelly & Malyshev, 2000, Shimada, Tynan & Cattolica, 2007, Li et al., 2011).

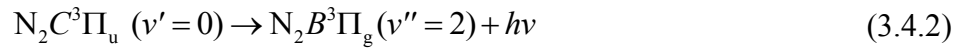
A widely measured parameter via this technique is the neutral gas temperature of the plasma. In the present experiment, the argon plasma is seeded with nitrogen gas (actinometer) at less than 5% of the total pressure and the nitrogen emission peaks are obtained (Donnelly & Malyshev, 2000). Neutral gas temperature for the discharge is calculated based on the following assumptions (Cruden et al., 2002 and Shimada, 2006):

- i. The vibro-rotational ground state temperature of the nitrogen emission peaks,  $T_{N_2,rot}$  is analogous (or equilibrated) to the translational temperature of the nitrogen neutrals,  $T_{N_2}$ , i.e.,  $T_{N_2,rot} \equiv T_{N_2}$ .
- ii. The population of the vibro-rotational ground state species for the nitrogen emission peaks is in thermal equilibrium.
- iii. The nitrogen neutral gas temperature,  $T_{N_2}$  is equal and representative of the plasma neutral gas temperature,  $T_n$ .

The vibro-rotational ground state temperature of nitrogen is calculated by taking an appropriate nitrogen emission peak from the measured spectra and retrofitting it with a synthetic spectrum obtained from theory. Criteria for selection of an emission peak are as follows:

- i. The peak should involve a ground state transitions that would represent the ground state temperature of nitrogen molecules.
- ii. The peak should be of resolvable intensity and free from peak impurities due to overlapping emissions that would affect the accuracy of the fit (Li, 2006).

In this study, the 0-2 vibrational emission peak from the nitrogen second positive system was used (Donnelly & Malyshev, 2000, Shimada, Tynan & Cattolica, 2007, Li et al., 2011), i.e.,



The emission peaks for the nitrogen second positive system are the result of excitation of neutral nitrogen molecules by low energy thermal electrons (2-3 eV) from the  $N_2 X^1 \Sigma_g^+$  ground state to the  $N_2 C^3 \Pi_u$  state and subsequent photon emission during de-excitation to the  $N_2 B^3 \Pi_g$  state. Thus, the emission peaks in the second positive system would give direct representation of the ground state vibro-rotational temperature of the molecules. The 0-2 vibrational emission peak was chosen due to not having any overlap impurities and being of resolvable intensity (Fig 3.11).

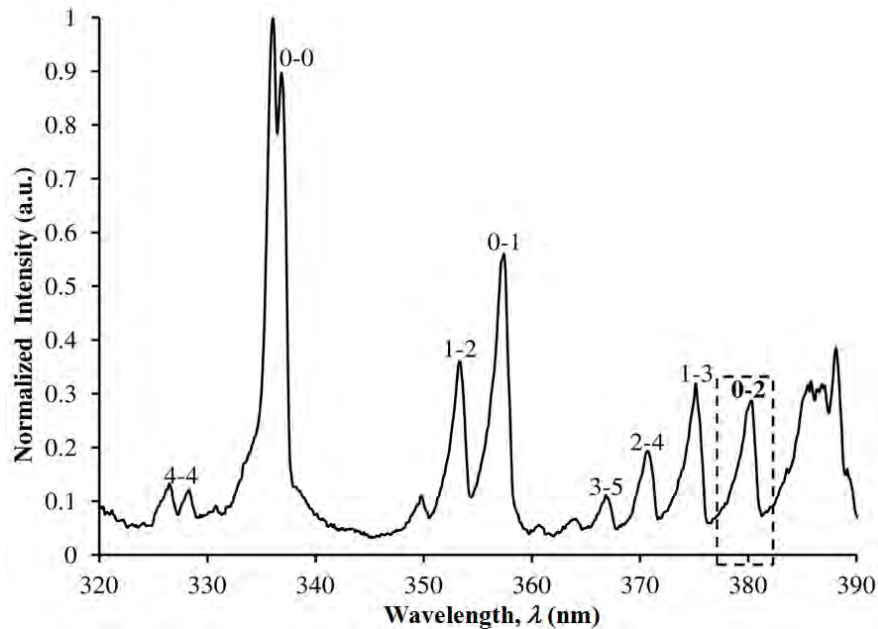


**Figure 3.11:** Measured H mode Ar/N<sub>2</sub> emission spectra showing the nitrogen second positive system ( $N_2 C^3 \Pi_u - N_2 B^3 \Pi_g$ ) at 0.05 mbar pressure (~95% Ar/~5% N<sub>2</sub>) and 200 W r.f. power. The chosen peak for simulation (0-2) is indicated.

To calculate the neutral gas temperature, the theoretical vibro-rotational spectral lines have to be determined and matched with experimental measurement. There are 3 steps involved (Shimada, 2006 and Li, 2006):

- i. To calculate all possible quantum spectral line positions and intensities as prescribed by atomic/molecular physics theory.
- ii. To convolve the discrete spectral lines with instrumental broadening to form a continuous spectrum similar to that of experimental measurement.
- iii. To retrofit the continuous theoretical spectrum with measured experimental spectrum using minimum chi squared ( $\chi^2$ ) analysis by varying rotational temperature (higher rotational temperature results in overall increased spectral broadening) and finding the minimum  $\chi^2$  value.

The synthetic vibro-rotational nitrogen emission peak for fitting with experiment is calculated using the atomic and molecular quantum theory found in Herzberg (1950), Kovac (1969) and Hollas (2004). A vibrational emission peak for an electronic state transition (e.g.,  $N_2C^3\Pi_u \rightarrow N_2B^3\Pi_g$ ) is made up of many discretized rotational emissions of which its line positions can be expressed as,

$$\lambda_i(\nu', \nu'', J', J'') = \frac{1}{\nu_i(\nu', \nu'', J', J'')n_{\text{air}}}, \quad (3.4.3)$$

where,  $n_{\text{air}}$  is the refractive index of air,  $\nu_i$  is the transitional vibro-rotational wavenumber of the spectral line in  $\text{cm}^{-1}$ ,  $\nu$  is the vibrational quantum number and  $J$  is the rotational quantum number. The notations ' and '' represent the upper and lower transition states, respectively, i.e., for the 0-2 vibrational emission peak, the upper state ( $N_2C^3\Pi_u$ ) vibrational quantum number,  $\nu' = 0$  and the lower state ( $N_2B^3\Pi_g$ ) vibrational

quantum number,  $v'' = 2$ . The transitional vibro-rotational wavenumber  $\nu_i$  is derived from the total internal energy of a molecule and can be written as,

$$\nu_i = T'_{\text{elec}} - T''_{\text{elec}} + G'(v') - G''(v'') + F'_{v'}(J') - F''_{v''}(J'') \quad (3.4.4)$$

where,  $T_{\text{elec}}$ ,  $G(v)$  and  $F_v(J)$  are the electronic, vibrational and rotational terms respectively.  $G(v)$  and  $F_v(J)$  are given by a series,

$$G(v) = \omega_e(v + \frac{1}{2}) - \omega_e x_e(v + \frac{1}{2})^2 - \omega_e y_e(v + \frac{1}{2})^3 + \dots \quad (3.4.5)$$

and

$$F_v(J) = B_v J(J+1) - D_v J^2(J+1)^2 \dots \quad (3.4.6)$$

with,

$$B_v = B_e - \alpha_e(v + \frac{1}{2}) \dots, \quad (3.4.7)$$

$$D_v = D_e + \beta_e(v + \frac{1}{2}) \dots, \quad (3.4.8)$$

and

$$D_e = \frac{4B_e^3}{\omega_e^2}. \quad (3.4.9)$$

$\omega_e$ ,  $\omega_e x_e$  and  $\omega_e y_e$ ,  $B_e$ ,  $\alpha_e$  and  $\beta_e$  are the vibrational and rotational constants in  $\text{cm}^{-1}$  for the  $\text{N}_2\text{C}^3\Pi_u$  and  $\text{N}_2\text{B}^3\Pi_g$  states. A list of measured values for the required terms and constants is given in Table 3.2.

**Table 3.2:** List of rotational constants required for simulation of  $\text{N}_2\text{C}^3\Pi_u$ - $\text{N}_2\text{B}^3\Pi_g$  state transition (Huber & Herzberg, 1979, pp. 418-420).

$\text{N}_2$ Transition States	$T_{\text{elec}}$	$\omega_e$	$\omega_e x_e$	$\omega_e y_e$	$B_e$	$\alpha_e$	$\beta_e$
$\text{N}_2\text{C}^3\Pi_u$ (Upper, ')	89136.88	2047.17	28.445	2.0883	1.8247	0.01868	$3.2 \times 10^{-7}$
$\text{N}_2\text{B}^3\Pi_g$ (Lower, ")	59619.35	1733.39	14.122	-0.0569	1.6374	0.0179	$3.0 \times 10^{-8}$

For a single vibrational emission peak,  $T'_{\text{elec}} - T''_{\text{elec}} + G'(v') - G''(v'')$  is constant and can be represented as,

$$\overline{\nu_{v'v''}} = T'_{\text{elec}} - T''_{\text{elec}} + G'(v') - G''(v''), \quad (3.4.10)$$

thus,

$$\nu_i = \overline{\nu_{v'v''}} + F'_{v'}(J') - F''_{v''}(J''). \quad (3.4.11)$$

In quantum theory, the selection rules for rotational transitions would only allow for the difference between upper and lower rotational quantum numbers, i.e.,  $\Delta J = J' - J''$  to be +1, 0 or -1. This would result in 3 transition branches for,  $\nu_i$  which are noted as  $i = R$  ( $J' - J'' = +1$ ),  $Q$  ( $J' - J'' = 0$ ) and  $P$  ( $J' - J'' = -1$ ) transitions, i.e.,

$$\nu_R = \overline{\nu_{v'v''}} + F'_{v'}(J+1) - F''_{v''}(J), \quad J = 0, 1, 2, \dots \quad (3.4.12)$$

$$\nu_Q = \overline{\nu_{v'v''}} + F'_{v'}(J) - F''_{v''}(J), \quad J=1, 2, 3... \quad (3.4.13)$$

$$\nu_P = \overline{\nu_{v'v''}} + F'_{v'}(J-1) - F''_{v''}(J), \quad J=1, 2, 3... \quad (3.4.14)$$

An important consideration for better fitting of the synthetic spectra with the measured spectra is the rotational emissions from transitions between degenerate states. The  $^3\Pi$  state applying Hund's case (a) can be split into three degenerate states from which the rotational terms are expressed as,

$$^3\Pi_0 : F_v(J) = B_v[J(J+1)] - D_v J^2 (J+1)^2 + \dots, \quad J=0,1,2,... \quad (3.4.15)$$

$$^3\Pi_1 : F_v(J) = B_v[J(J+1)-1] - D_v J^2 (J+1)^2 + \dots (+A), \quad J=1,2,3,... \quad (3.4.16)$$

$$^3\Pi_2 : F_v(J) = B_v[J(J+1)-4] - D_v J^2 (J+1)^2 + \dots (+4A), \quad J=2,3,4,... \quad (3.4.17)$$

whereby,  $A = 42.24 \text{ cm}^{-1}$  (Herzberg, 1950) is a rotational constant. In the simulation of the  $\text{N}_2\text{C}^3\Pi_u \rightarrow \text{N}_2\text{B}^3\Pi_g$  synthetic spectra, the major  $^3\Pi_0-^3\Pi_0$ ,  $^3\Pi_1-^3\Pi_1$  and  $^3\Pi_2-^3\Pi_2$  degenerate transitions were considered.

For each rotational line position, the corresponding line intensity was calculated using the following equation,

$$I(J', T_{\text{N}_2, \text{rot}}) = C_{\text{spec}} S_J(J') \exp\left(\frac{-hcF_v(J')}{k_B T_{\text{N}_2, \text{rot}}}\right), \quad (3.4.18)$$

where,  $C_{\text{spec}}$  is a constant dependent on spectroscopic parameters,  $S_J$  is the line strength,  $h$  is Planck's constant in  $\text{Js}^{-1}$ ,  $c$  is the speed of light in  $\text{cms}^{-1}$ ,  $F_v(J)$  is the upper state rotational term in  $\text{cm}^{-1}$ ,  $k_B$  is the Boltzmann constant in  $\text{JK}^{-1}$  and  $T_{N_2, \text{rot}}$  is the rotational temperature of nitrogen in K. The exact value of constant  $C_{\text{spec}}$  is not important for this analysis as only the relative normalized intensities are used for comparison (i.e.,  $C_{\text{spec}}$  is taken as 1). The line strength  $S_J$  is calculated for the three rotational branches  $i = \text{R, P, Q}$  and the corresponding  ${}^3\Pi$  degenerate state transitions using the Honl-London formulae for Hund's case (a) in Table 3.3.

**Table 3.3:** Lists the line strength equations of the  ${}^3\Pi$  degenerate state transitions for the rotational branches R, Q and P (Kovac, 1969).

Rotational Branches	${}^3\Pi$ Degenerate State Transitions		
	${}^3\Pi_0 - {}^3\Pi_0$	${}^3\Pi_1 - {}^3\Pi_1$	${}^3\Pi_2 - {}^3\Pi_2$
R ( $J' - J'' = +1$ )	$S_J = J'$	$S_J = \frac{J'^2 - 1}{J'}$	$S_J = \frac{J'^2 - 4}{J'}$
Q ( $J' - J'' = 0$ )	$S_J = 0$	$S_J = \frac{(2J'+1)}{J'(J'+1)}$	$S_J = \frac{4(2J'+1)}{J'(J'+1)}$
P ( $J' - J'' = -1$ )	$S_J = J'+1$	$S_J = \frac{(J'+1)^2 - 1}{J'+1}$	$S_J = \frac{(J'+1)^2 - 4}{J'+1}$

Line positions and intensities were calculated for  $J = 0-50$ . A total of 328 rotational transition lines were calculated including degenerate transitions and branch transitions (i.e., R<sub>0</sub>, R<sub>1</sub>, R<sub>2</sub>, Q<sub>0</sub>, Q<sub>1</sub>, Q<sub>2</sub>, P<sub>0</sub>, P<sub>1</sub>, P<sub>2</sub>) to form the discrete synthetic spectrum for the 0-2 vibrational emission peak (Figure 3.12).

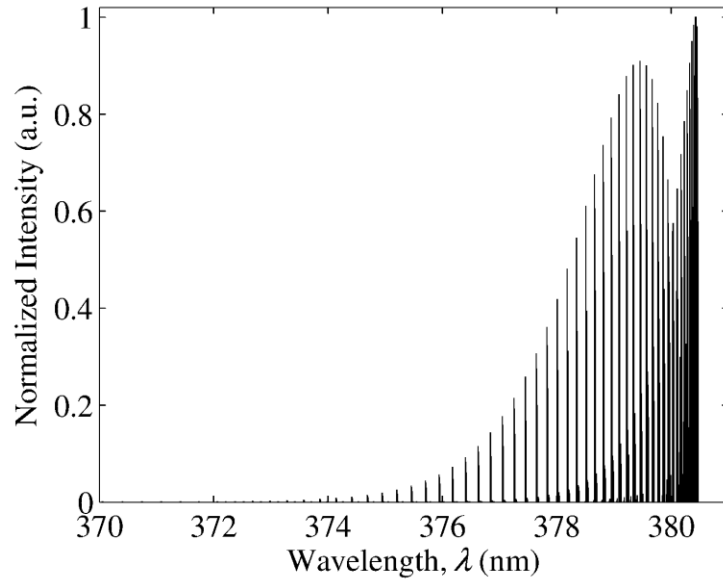


**Figure 3.12:** Discrete synthetic spectrum for the 0-2 vibrational emission peak of the nitrogen second positive system  $N_2C^3\Pi_u \rightarrow N_2B^3\Pi_g$  at  $T_n = 550$  K.

Before measurement of the discharge emission spectrum, the spectrometer was calibrated with a mercury-vapour lamp to account for systematic errors. Wavelengths of the emission peaks measured from the lamp,  $\lambda_{\text{exp}}$  were plotted with the wavelengths of the standard Hg lines,  $\lambda_{\text{calib}}$  (Sansonet & Martin, 2005) and were linearly fitted, i.e.  $\lambda_{\text{calib}} = m_{\text{OES}}\lambda_{\text{exp}} + C_{\text{OES}}$  as shown in Figure 3.13.

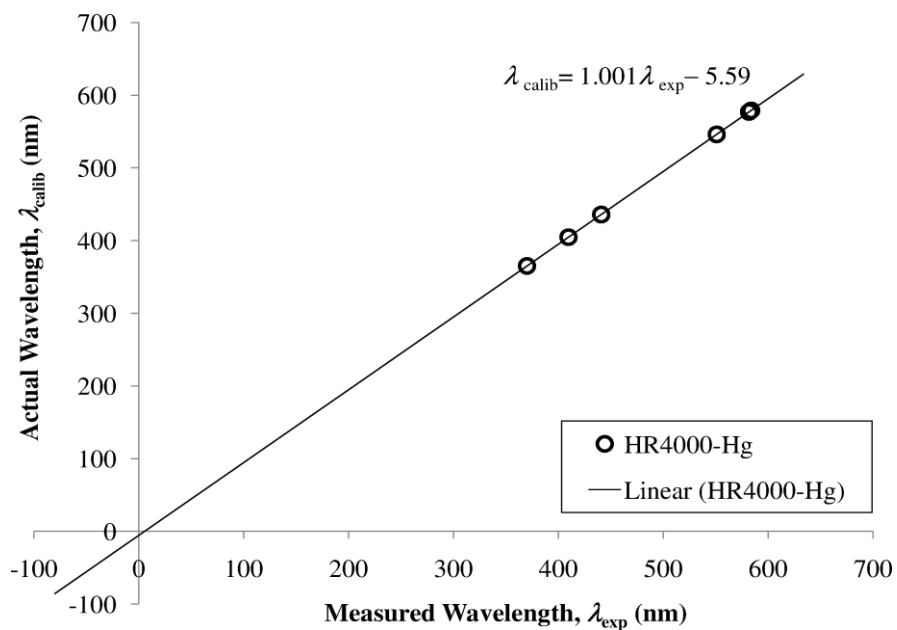


**Figure 3.13:** Calibration curve for the HR4000 spectrometer.

From the linear fit,  $\lambda_{\text{exp}}$  deviates from  $\lambda_{\text{calib}}$  by  $C_{\text{OES}} = (-5.59 \pm 0.03)$  nm. The calibrated wavelength is used in place of measured wavelength values in subsequent fittings and analysis.

The ability of the spectrometer to resolve different wavelengths of emission is limited by several mechanical factors, namely, diffraction by the spectrometer grating, dispersion by mirrors, CCD resolution, alignment and refractive errors etc. Thus, measurement of emissions (especially standard lamp emissions) is not perfectly discrete and typically includes a certain degree of spectral broadening known as instrumental broadening. For our analysis, instrumental broadening must be added to the theoretical (discrete) spectrum to properly emulate the measured spectra. To simulate instrumental broadening at the wavelength of interest, the nearest wavelength emission (435.8 nm) from a standard mercury lamp is fitted with a Voigt profile. The Voigt profile is a composite function that features both Lorentzian and Gaussian broadening mechanisms and is widely used for spectral fitting analysis. In normalized form, it is given by (Whiting, 1968),

$$f_v(\lambda) = \frac{I(\lambda)}{I(\lambda_{\text{peak}})} = \frac{2\lambda_{\text{peak}}}{\pi w_l} \int_{-\infty}^{\infty} \frac{\exp[-2.772 \frac{\lambda_{\text{peak}}^2}{w_g^2} \left(\frac{v_{\text{ave}}}{c}\right)^2] d\left(\frac{v_{\text{ave}}}{c}\right)}{1 + \frac{4}{w_l^2} \left[ (\lambda - \lambda_{\text{peak}}) - \lambda_{\text{peak}} \left(\frac{v_{\text{ave}}}{c}\right) \right]^2} \quad (3.4.19)$$

Here,  $I(\lambda_{\text{peak}})$  is the peak intensity at peak wavelength,  $\lambda_{\text{peak}}$ ,  $I(\lambda)$  is the intensity at wavelength  $\lambda$ ,  $w_l$  is the Lorentzian full width half maximum (FWHM),  $w_g$  is the Gaussian FWHM,  $v_{\text{ave}}$  is the average velocity of molecules contributing to the peak in  $\text{ms}^{-1}$  and  $c$  is the speed of light in  $\text{ms}^{-1}$ . Units for  $\lambda$ ,  $w_l$  and  $w_g$  are in nm. Adjustment of

the Lorentzian and Gaussian FWHMs broadens the Voigt profile according to the respective functions. Due to the numerous fittings at various wavelengths required for simulation, computation of the exact Voigt profile would be time consuming. Thus an approximation (Whiting, 1968) with less than 5% error was used, i.e.,

$$f(\lambda) = \frac{I(\lambda)}{I(\lambda_{\text{peak}})} = \left[1 - \frac{w_l}{w_v}\right] \exp\left[-2.772\left(\frac{\lambda - \lambda_{\text{peak}}}{w_v}\right)^2\right] + \left[\frac{w_l}{w_v}\right] \frac{1}{1 + 4\left(\frac{\lambda - \lambda_{\text{peak}}}{w_v}\right)^2} \dots$$

$$+ 0.016 \left[1 - \frac{w_l}{w_v}\right] \left[\frac{w_l}{w_v}\right] \left(\exp\left[-0.4\left(\frac{\lambda - \lambda_{\text{peak}}}{w_v}\right)^{2.25}\right] - \frac{10}{10 + \left(\frac{\lambda - \lambda_{\text{peak}}}{w_v}\right)^{2.25}}\right) \quad (3.4.20)$$

whereby,  $w_v$  is the Voigt FWHM given by,

$$w_v = \frac{w_l}{2} + \sqrt{\left(\frac{w_l^2}{4} + w_g^2\right)} \quad (3.4.21)$$

An example of a Voigt profile fitted to the Hg peak at 435.8 nm is given in Figure 3.14.

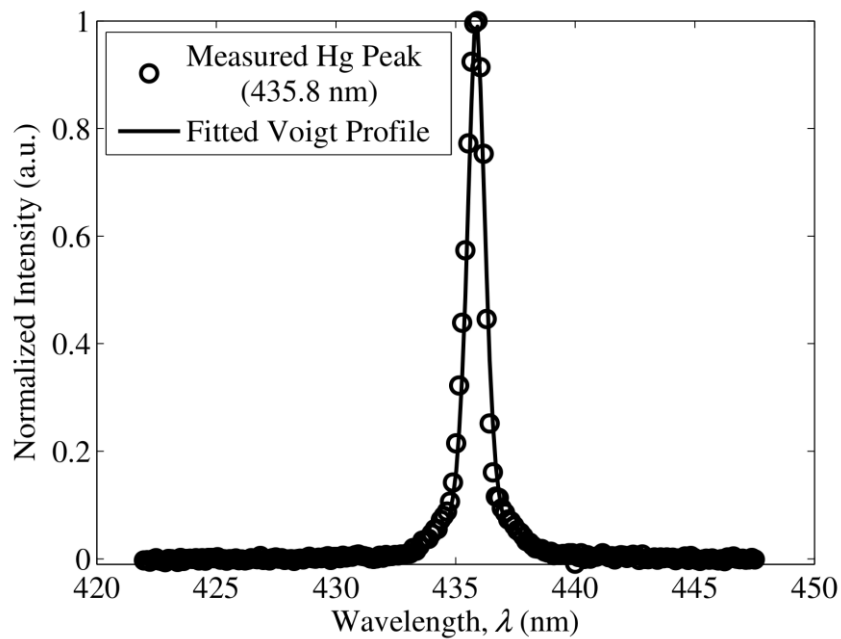


**Figure 3.14:** Voigt profile fitted to the measured Hg peak at 435.8 nm.

From the fitting of measured data,  $w_l$ ,  $w_g$  and  $w_v$  were found to be 0.5 nm, 0.6 nm and 0.9 nm, respectively. These values were used to simulate instrumental broadening for all the discrete rotational emissions of the synthetic spectra. To incorporate the broadening, the method of convolution was used, i.e.,

$$I_{\text{conv}}(\lambda) = \int_{-\infty}^{\infty} I(\lambda') \cdot f(\lambda - \lambda') d\lambda' \quad (3.4.22)$$

Here,  $I_{\text{conv}}(\lambda)$  is the convoluted intensity at wavelength  $\lambda$ ,  $I(\lambda')$  is the intensity at the integration wavelength  $\lambda'$  and  $f(\lambda - \lambda')$  is the Voigt profile with peak wavelength  $\lambda$  at displacement  $\lambda'$ . The result of convolution on the synthetic spectra is demonstrated in Figure 3.15.

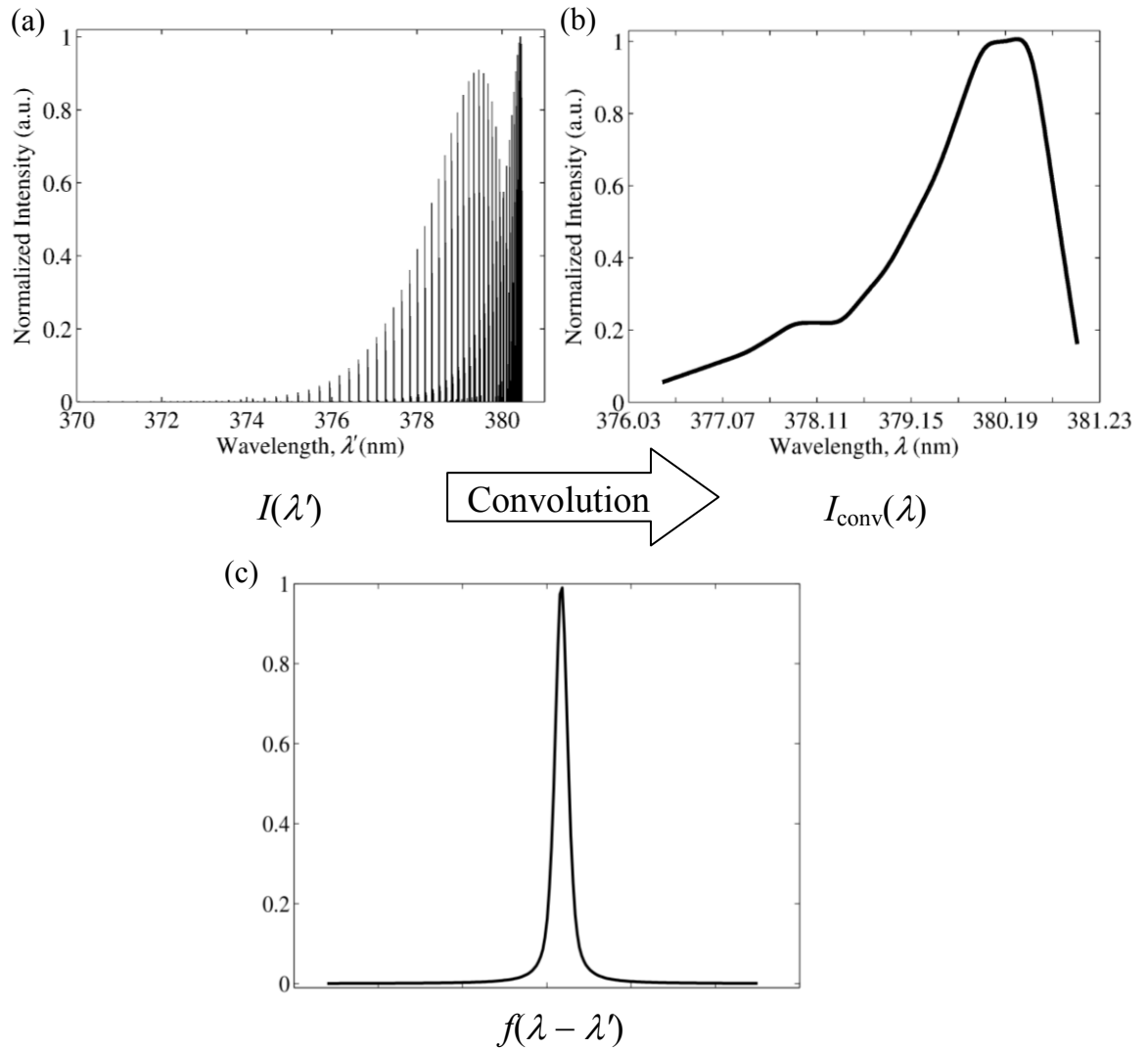


**Figure 3.15:** The discrete synthetic spectra (a) is convolved with instrumental broadening (c) via Voigt function resulting in the convolved synthetic spectrum (b). The convolved synthetic spectrum takes the shape of the experimentally measured 0-2 vibro-rotational peak seen in Figure 3.11.

The convolved synthetic spectrum is calculated for the rotational temperatures between 250-1500 K at 50 K intervals and statistically fitted with the measured spectra using the following steps:

- i. Background emission (vertical displacement) from the measured spectra is first removed to avoid overestimation of the neutral gas temperature.
- ii. The spectrum wavelength range was next divided into equally spaced bins of size of  $4 \times \text{Measured Interval} = 4 \times 0.13 \text{ nm} = 0.52 \text{ nm}$ . This roughly corresponds to the spectrometer resolution of 0.5 nm. A total number of 10 bins were obtained.

- iii. The data points for the convolved and measured spectrum were then interpolated so that the new point values coincide with the center wavelength of the selected bins, i.e., Figure 3.16.

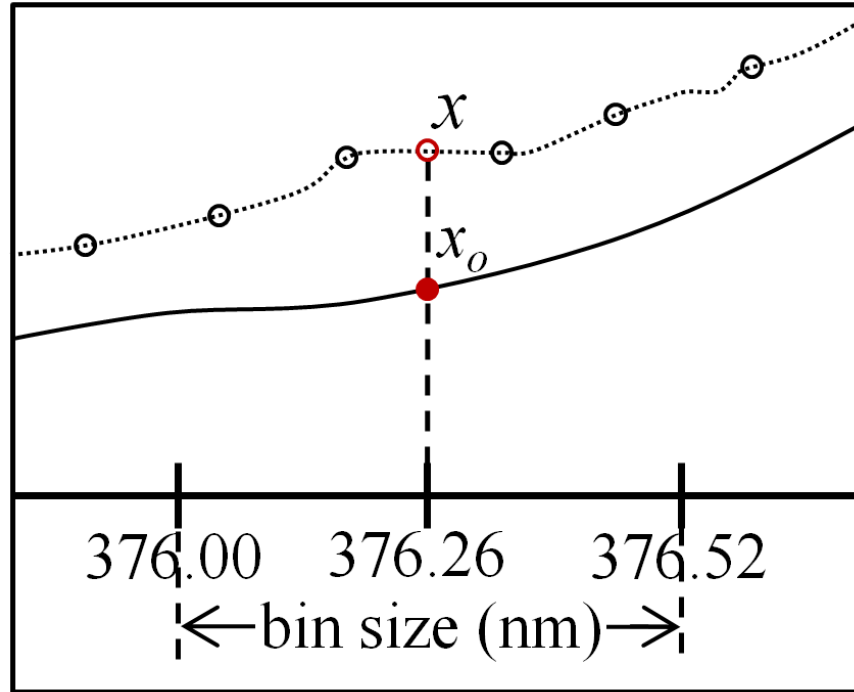


**Figure 3.16:** Demonstration of the measured spectrum intensity,  $x$  and convolved spectrum intensity,  $x_o$ ; interpolated to coincide with the central bin wavelength.

- iv. The neutral gas temperature is next estimated using the minimum  $\chi^2$  squared technique, i.e. (Li, 2006),

$$\chi^2 = \frac{\sum_{i=1}^N P_{\text{line}} (x - x_o)^2}{N_{\text{bin}} (N_{\text{bin}} - 1)} \quad (3.4.23)$$

Here,  $N$  is the total number of bins,  $x$  is the measured spectrum intensity and  $x_o$  is the synthetic spectrum intensity at the same wavelength as  $x$ .  $P_{\text{line}}$  is the probability (weight) of discrete lines in each bin which is given by,

$$P_{\text{line}} = \frac{\text{Number of Discrete Lines in Bin}}{\text{Total Number of Discrete Lines in Spectra (328)}} \quad (3.4.24)$$

The vibro-rotational temperature at which the  $\chi^2$  value is minimum, is taken as the estimated neutral gas temperature of the plasma. Example of a fitted spectrum and  $\chi^2$  plot are shown in Figure 3.17.

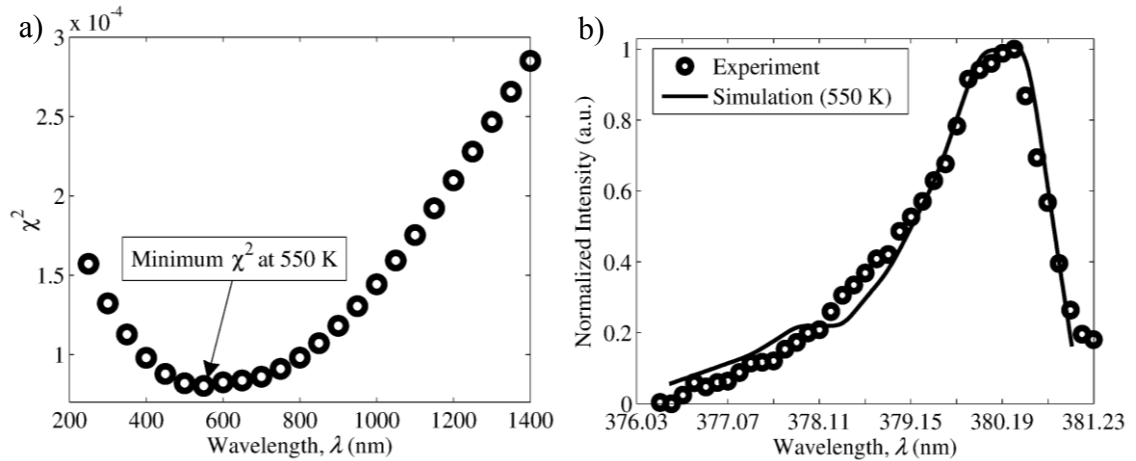


**Figure 3.17:** (a)  $\chi^2$  plot showing minimum fitting value at 550 K (b) Experimental 0-2 vibro-rotational peak at 0.05 mbar Ar/N<sub>2</sub> pressure and 200 W r.f. power fitted with the convolved synthetic spectrum at 550 K.

In this case, the minimum  $\chi^2$  value was found when the experimental spectrum was fitted with the convolved synthetic spectrum at the vibro-rotational temperature of 550 K. Thus, the neutral gas temperature,  $T_n$  of the Ar/N<sub>2</sub> discharge at 0.05 mbar pressure and 200 W and r.f. power using the actinometric technique is estimated to be 550 K.

Two MATLAB codes (see Appendix B) were written to process the measured data. The first code calculates the discrete synthetic spectrum for the vibro-rotational temperatures for 250-1500 K at 50 K intervals and convolves the spectrum with instrumental broadening. The second code fits the convolved spectrum with the measured data using minimum  $\chi^2$  statistical analysis.

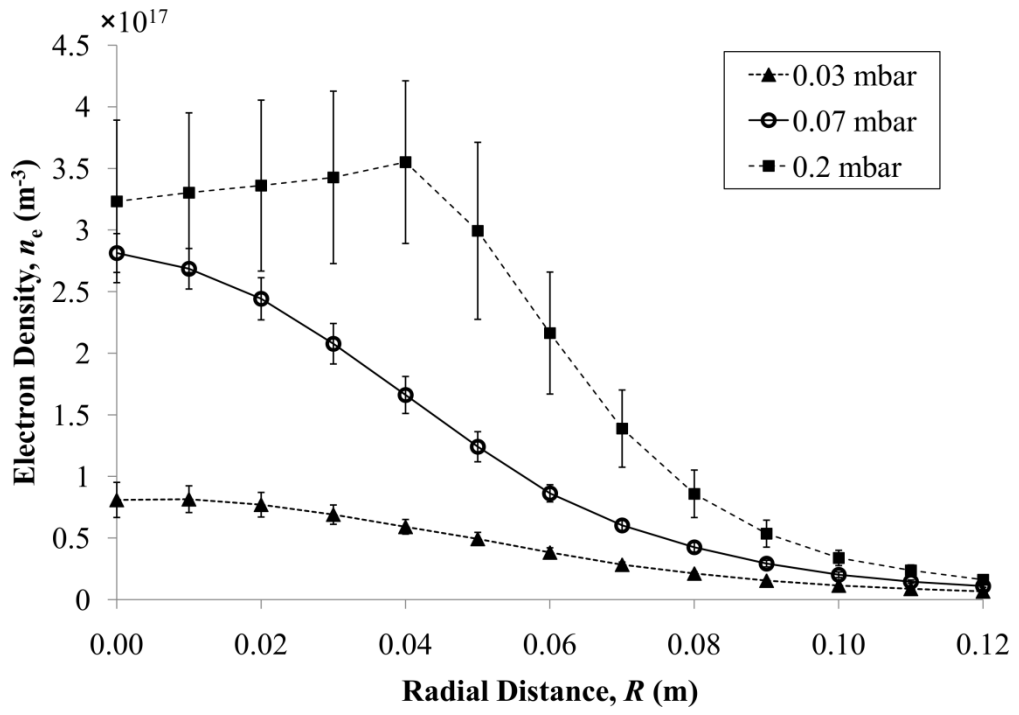
## CHAPTER 4: RESULTS AND DISCUSSION - EXPERIMENT

### 4.0. Measurement of Discharge Electrical Characteristics

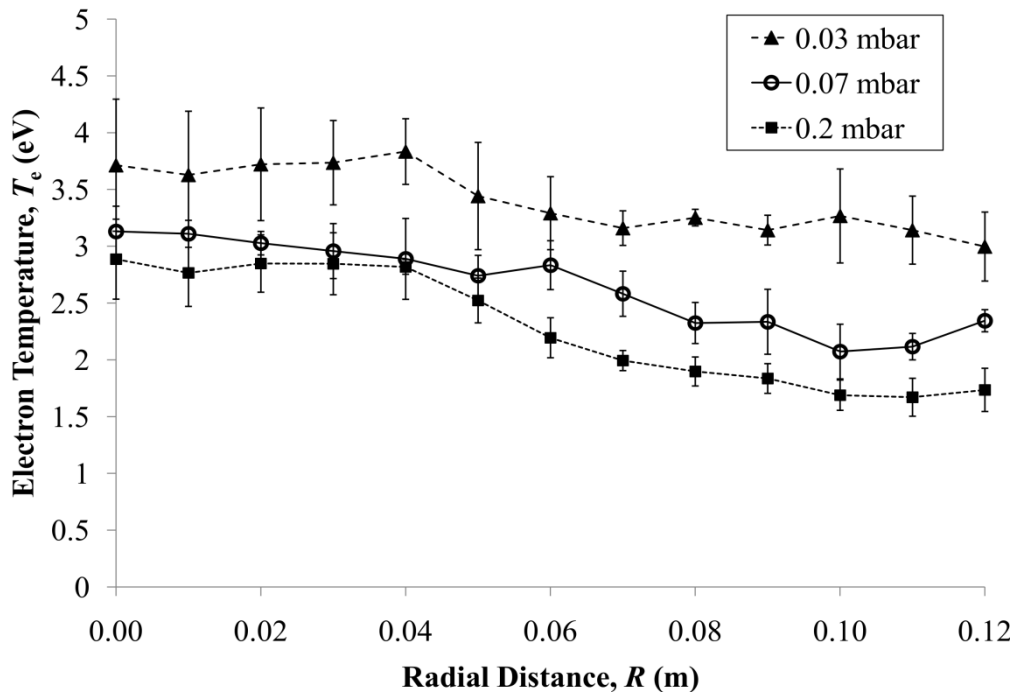
Measurement of discharge electrical characteristics is divided to two parts. The first part shows the measured radial distributions of electron density and electron temperature at different pressures and axial distances above the dielectric plate. These measurements are fitted into 2D Gaussian based distributions and subsequently used in predictive electromagnetic simulation (Chapter 6, Section 6.0.1). The second part shows the measured electron probability distribution function (EEDF) which is parametrically fitted with Maxwellian and Druyvesteyn distributions to provide a guided assumption of the distribution to be used for simulation.

#### 4.0.1. Electron Density, $n_e$ and Electron Temperature, $T_e$

Figures 4.1, 4.2 and 4.3 show the radial distributions of the (i) electron densities,  $n_e$  and (ii) electron temperatures,  $T_e$  for three argon pressures (0.03 mbar, 0.07 mbar and 0.2 mbar) measured at 0.032 m, 0.060 m and 0.114 m axial distances above the dielectric plate, respectively. R.f. power was set at 180 W. The label suffixes 'a' and 'b' (e.g. Figure 4.1a) denote the Maxwellian and EEDF calculation methods, respectively.

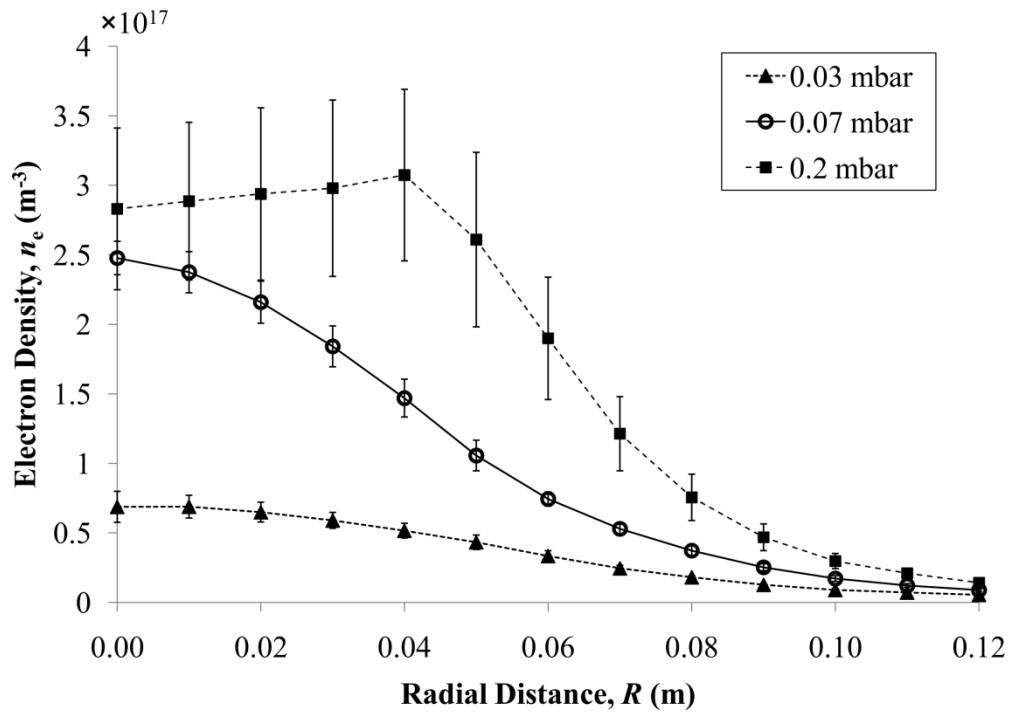


(i)

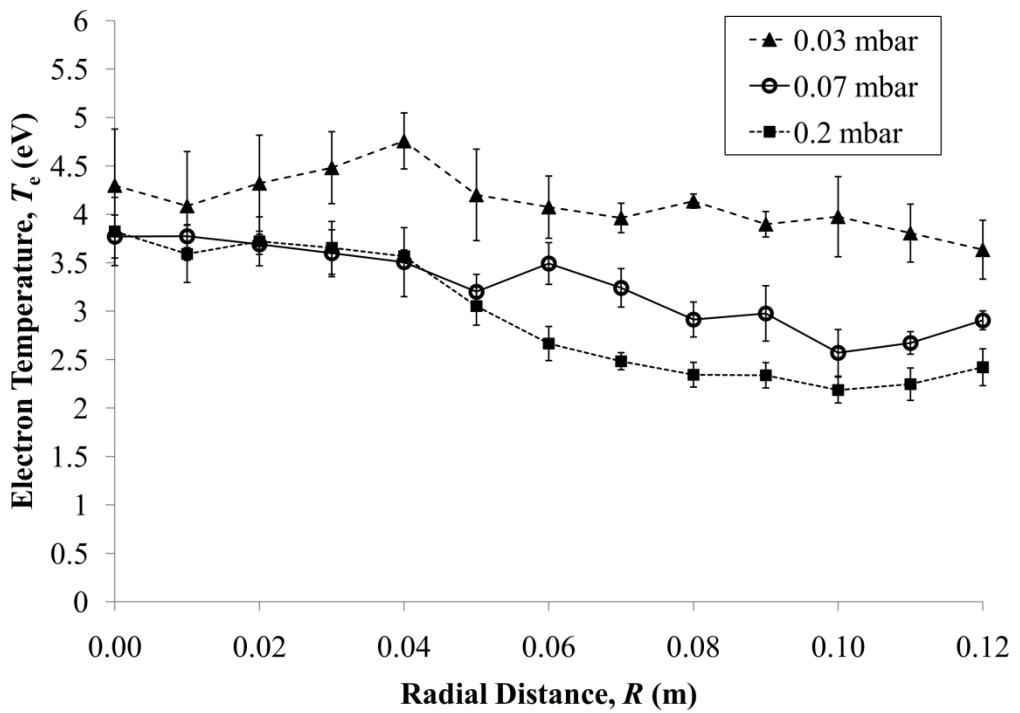


(ii)

**Figure 4.1a:** Maxwellian (i) electron density,  $n_e$  and (ii) electron temperature,  $T_e$  measured at 0.032 m distance above the dielectric plate for 0.03, 0.07 and 0.2 mbar argon pressures. R.f. power was set at 180 W.

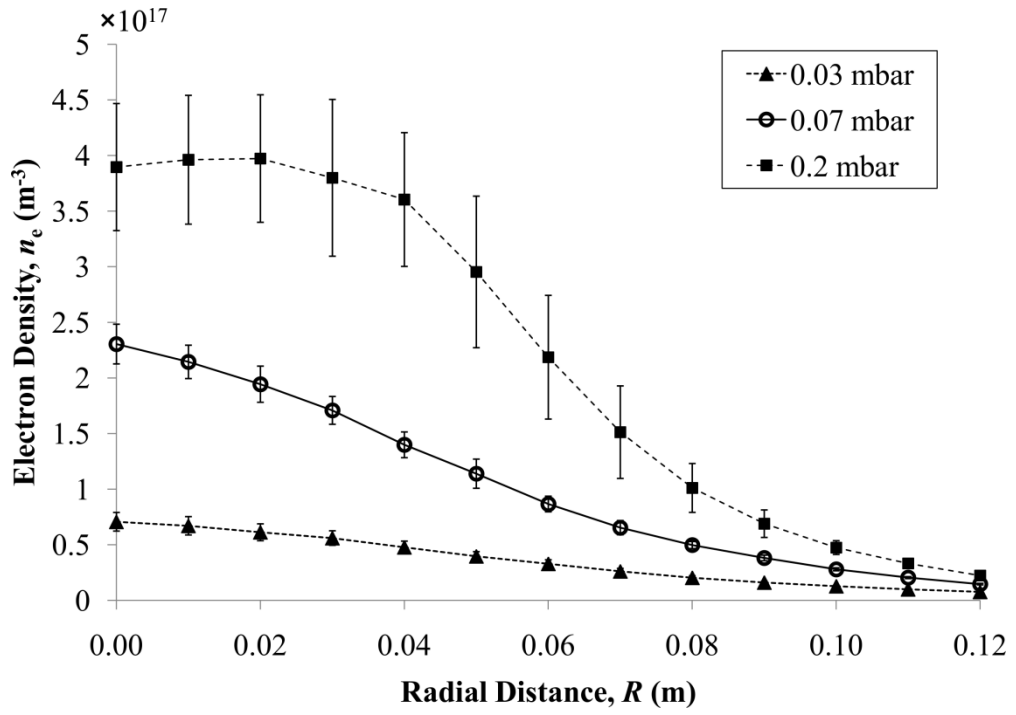


(i)

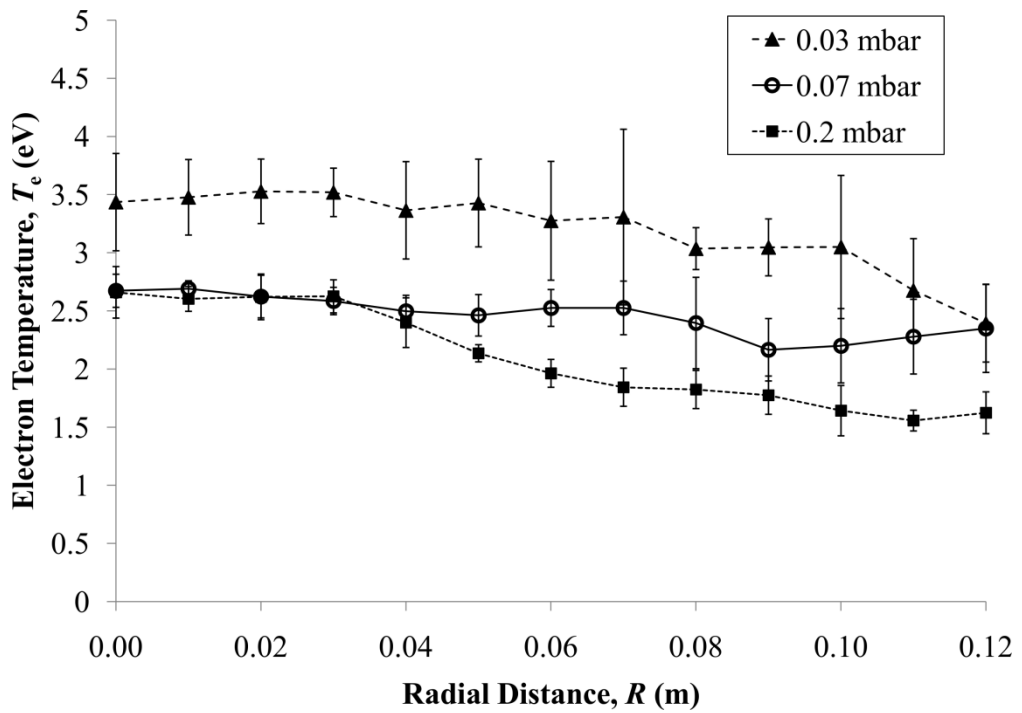


(ii)

**Figure 4.1b:** EEDF (i) electron density,  $n_e$  and (ii) electron temperature,  $T_e$  measured at 0.032 m distance above the dielectric plate for 0.03, 0.07 and 0.2 mbar argon pressures. R.f. power was set at 180 W.

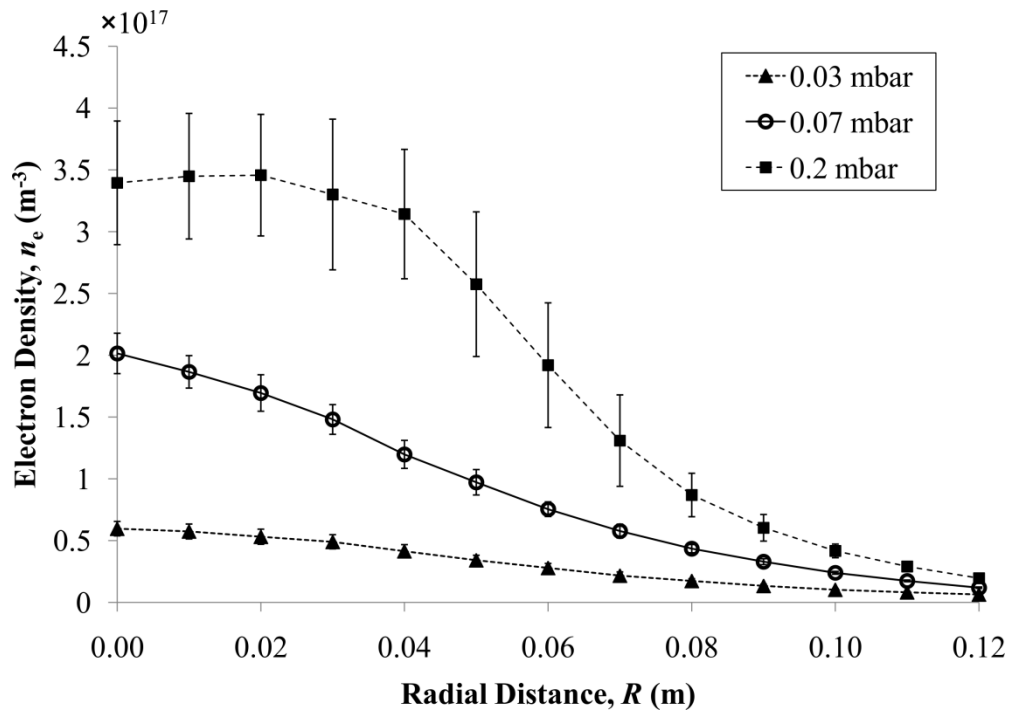


(i)

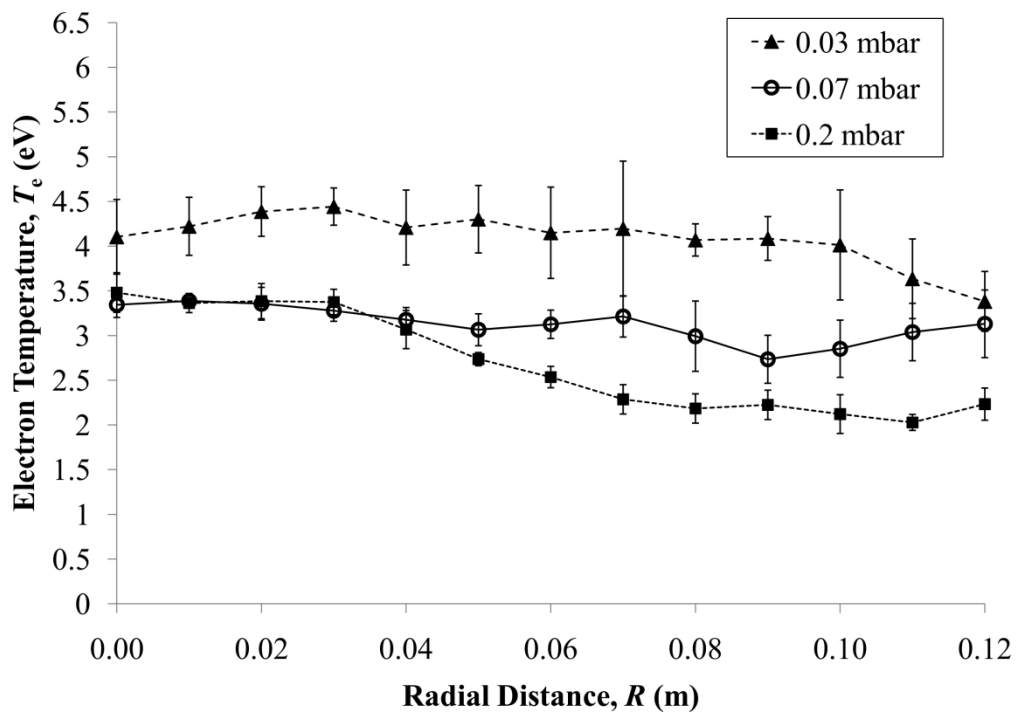


(ii)

**Figure 4.2a:** Maxwellian (i) electron density,  $n_e$  and (ii) electron temperature,  $T_e$  measured at 0.060 m distance above the dielectric plate for 0.03, 0.07 and 0.2 mbar argon pressures. R.f. power was set at 180 W.

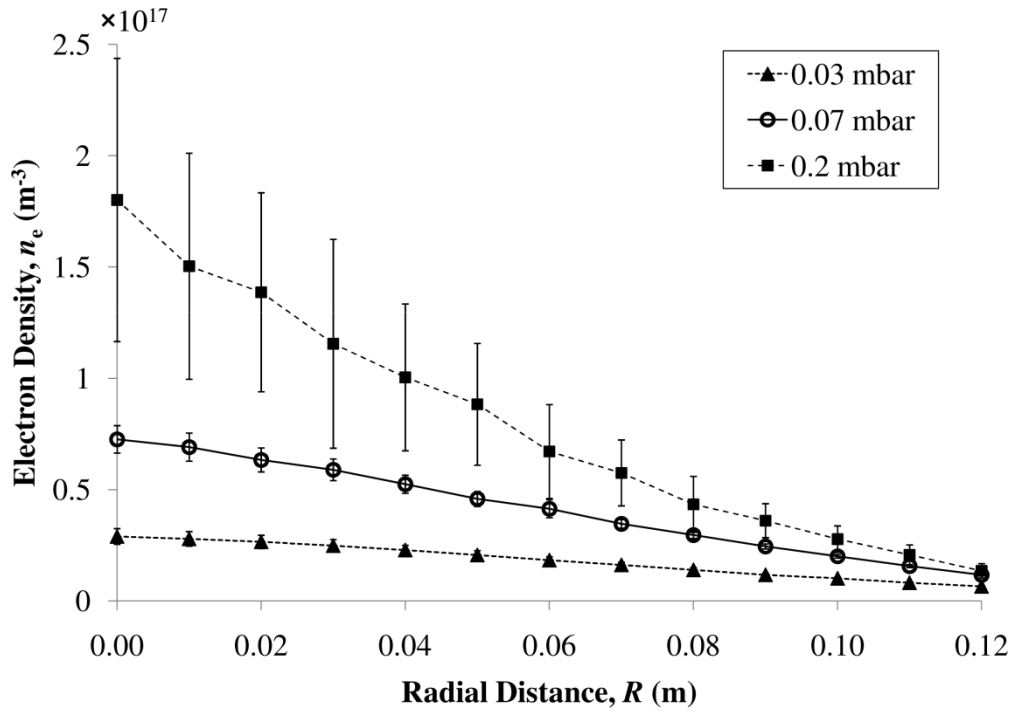


(i)

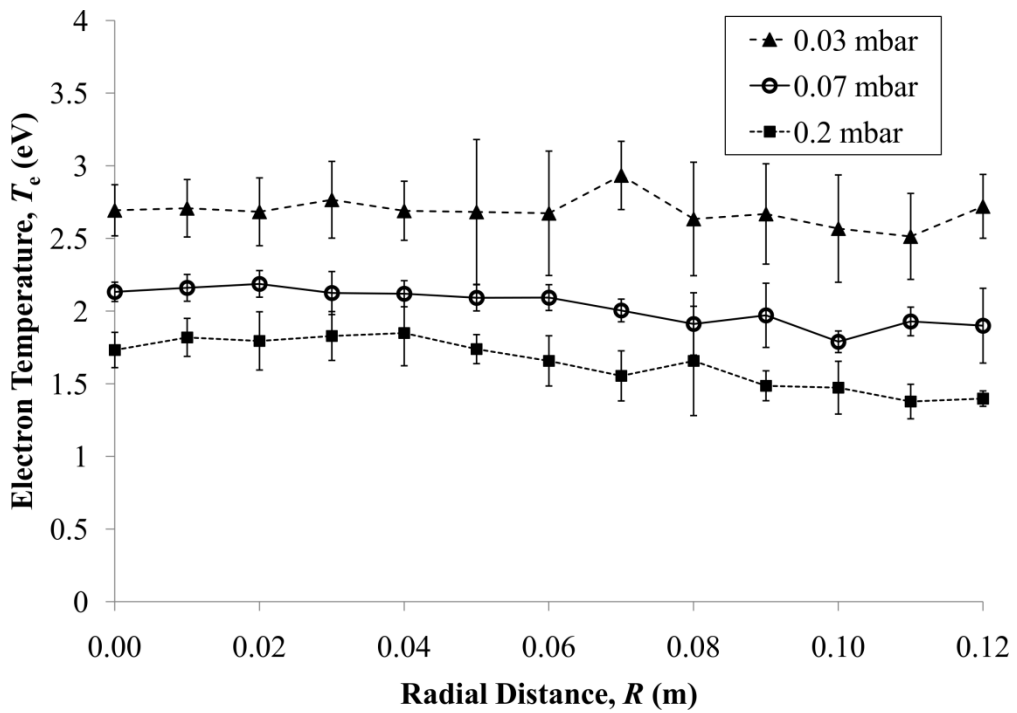


(ii)

**Figure 4.2b:** EEDF (i) electron density,  $n_e$  and (ii) electron temperature,  $T_e$  measured at 0.060 m distance above the dielectric plate for 0.03, 0.07 and 0.2 mbar argon pressures. R.f. power was set at 180 W.

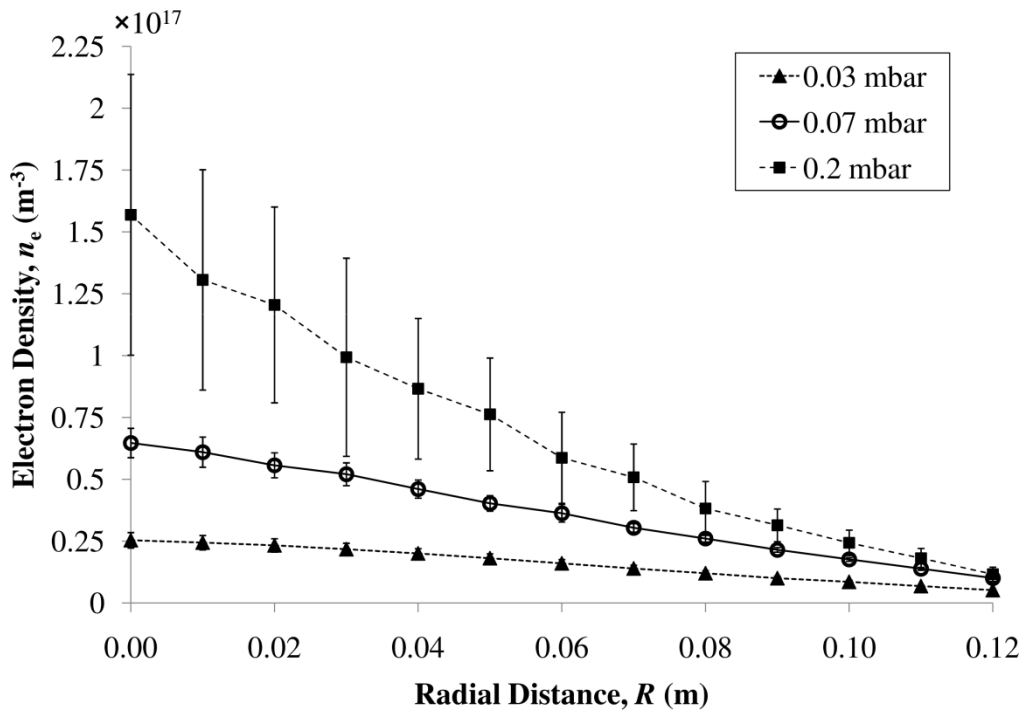


(i)

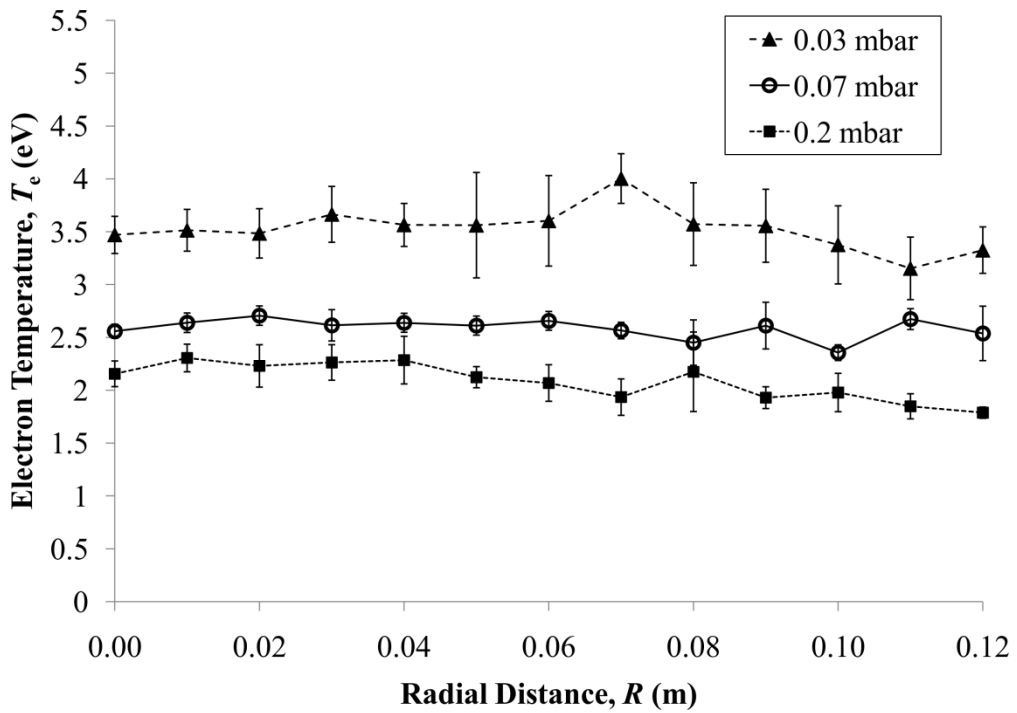


(ii)

**Figure 4.3a:** Maxwellian (i) electron density,  $n_e$  and (ii) electron temperature,  $T_e$  measured at 0.114 m distance above the dielectric plate for 0.03, 0.07 and 0.2 mbar argon pressures. R.f. power was set at 180 W.



(i)



(ii)

**Figure 4.3b:** EEDF (i) electron density,  $n_e$  and (ii) electron temperature,  $T_e$  measured at 0.114 m distance above the dielectric plate for 0.03, 0.07 and 0.2 mbar argon pressures. R.f. power was set at 180 W.

Higher values of  $n_e$  and lower values of  $T_e$  were obtained using the Maxwellian method in comparison to the EEDF method; with discrepancies between calculated values for both methods within the error bar limits. At 0.2 mbar argon pressure, the measured deviation for  $n_e$  is seen to be larger in comparison to 0.07 mbar and 0.03 mbar. This can be attributed to probe signal fluctuations caused by the gradual increase of neutral gas temperature during the course of measurement. It was found that for higher pressures, it takes longer time for the neutrals at H mode to thermally equilibrate.

An increase in  $n_e$  was observed for all radial positions with the increase of pressure from 0.03 mbar to 0.2 mbar; with marked increase of  $n_e$  seen near the coil region ( $R < 0.05$  m) for 0.2 mbar argon pressure. The maximum Maxwellian and EEDF electron densities obtained were  $(4.0 \pm 0.6) \times 10^{17} \text{ m}^{-3}$  and  $(3.5 \pm 0.5) \times 10^{17} \text{ m}^{-3}$ , respectively for 0.02 mbar pressure at 0.060 m axial distance above the dielectric plate. The range of electron densities obtained were  $(0.065 \pm 0.004)$ - $(4.0 \pm 0.6) \times 10^{17} \text{ m}^{-3}$  for the Maxwellian method and  $(0.052 \pm 0.004)$ - $(3.5 \pm 0.5) \times 10^{17} \text{ m}^{-3}$  for the EEDF method. There are several interesting observations that were made for the measured  $n_e$  distributions with axial distance:

- i. At increasing pressure (for the same r.f. power), the discharge becomes increasingly denser, especially near the coil region. When pressure is increased, more argon particles enter the chamber and interact with (absorb) the source field. This increases the number of ionizing collisions in the discharge and increases the plasma collision frequency; which is important for sustaining the discharge at higher densities. The resulting increase in electron density occurs mostly at the region where the r.f. field is strongest, forming the observed distributions. Further validation can be made by the simulation results for the total absorbed electron power,  $P_{\text{abs}}$  (Chapter 6, Section 6.0.2, Table 6.2); whereby,

for measured parameters at 180 W input r.f. power,  $P_{\text{abs}}$  increases with argon pressure.

- ii. The electron density of the discharge is typically expected to decrease with reduced proximity from the source magnetic field. However, for the pressure of 0.2 mbar,  $n_e$  at 0.060 m from the dielectric plate is higher than  $n_e$  at 0.032 m from the dielectric plate; which is especially prominent near the coil region. This phenomenon has been reported in El-Fayoumi and Jones (1998) and Stittsworth and Wendt (1996), whereby, there is a displacement between the power deposition of the source field (which is near the dielectric plate) and toroidal region of maximum electron density (which forms at a higher axial plane). El-Fayoumi and Jones has explained this as being due to the mean free path of the ionized electrons being sufficiently long ( $\sim 5$  cm for  $T_e \approx 3$  eV) which allows for travel to the region of maximum electron density. However, it is also possible that neutral gas heating in the discharge would contribute to the displacement of the electrons. According to Liard et al. (2007), heating of the neutral gas at the high density regions of the discharge would cause an enhancement in transport of plasma particles via temperature gradient; pushing the particles away from the discharge source (hotter region) towards the chamber walls (colder region). The resulting steady state flux of the moving particles and background heating would together form the observed displacement of the region of maximum electron density. This is further confirmed by the fact that the displacement only occurs at the pressure in which the measured neutral gas temperature is highest ( $\sim 800$  K for 0.2 mbar as compared to  $\sim 350$  K and  $\sim 600$  K for 0.03 mbar and 0.07 mbar, respectively; Section 4.3).

- iii. The radial distribution of  $n_e$  (i) near the coil region for 0.2 mbar at 0.032 m distance above dielectric plate (Figures 4.1a and 4.1b) does not follow the other distribution trends (maximum  $n_e$  at  $R = 0$ );  $n_e$  increases from the chamber center to the coil edge. This (as in (ii)) can be explained by the effect of neutral gas heating which causes a temperature gradient that pushes the plasma particles away from the discharge center and towards the edge of the coil.

The measured  $T_e$  of the discharge generally decreases with increasing pressure for all radial and axial positions and has a tapered distribution across the chamber radius, with an increased number of higher energy electrons occurring near the coil region; especially at 0.2 mbar argon pressure. This can be attributed to the increase in electron collision frequency with pressure which reduces the free mean path of the electrons and thus, reduces the kinetic energy accumulated by the electrons ( $\equiv T_e$ ). Due to the added effect of neutral gas heating, the collision frequency near the discharge center would be comparatively lower than the collision frequency at the coil edge, which results in the observed increase in higher energy electrons in the coil region. The range of values measured for  $T_e$  were  $(1.38 \pm 0.08)$ - $(3.8 \pm 0.2)$  eV using the Maxwellian method and  $(1.78 \pm 0.05)$ - $(4.8 \pm 0.3)$  eV using the EEDF method.

#### **4.0.2. Electron Energy Probability Function (EEDF)**

It is typical that the EEDF of the discharge,  $f(\varepsilon)$ , be parametrically fitted with known distribution trends, i.e., Maxwellian and Druyvestyeyn, to determine a suitable approximation for use in predictive simulation. For this purpose, the EEDF is converted to a convenient form which is the electron energy probability function,  $g(\varepsilon)$  or EEPF, i.e.,

$$g(\varepsilon) = \varepsilon^{-1/2} f(\varepsilon) \quad (4.0.1)$$

Using the EEPF, the semi-logarithmic plots of the Maxwellian and Druyvestyen distributions with energy,  $\varepsilon$  are reduced to linear and quadratic functions, respectively; thus, simplifying the fitting process (Godyak, Piejak & Alexandrovich, 2002). These two distributions, after reduction, can be expressed as,

$$\ln(\text{EEPF}) = \alpha_p \varepsilon^y + \beta_p \quad (4.0.2)$$

Here,  $\alpha_p$  and  $\beta_p$  are the fitting constants for the argon pressure,  $P$ . The constant,  $y = 1$  for the Maxwellian distribution and  $y = 2$  for the Druyvestyen distribution.

Figures 4.4, 4.5 and 4.6 show the measured electron energy probability functions (EEPF) at the discharge center ( $R = 0$ ) for 0.03, 0.07 and 0.2 mbar argon pressure at 0.032 m, 0.060 m and 0.114 m distance above the dielectric plate, respectively. R.f. power was set to 180 W. The values used for  $\alpha_p$  and  $\beta_p$  fitting parameters given in the figures.

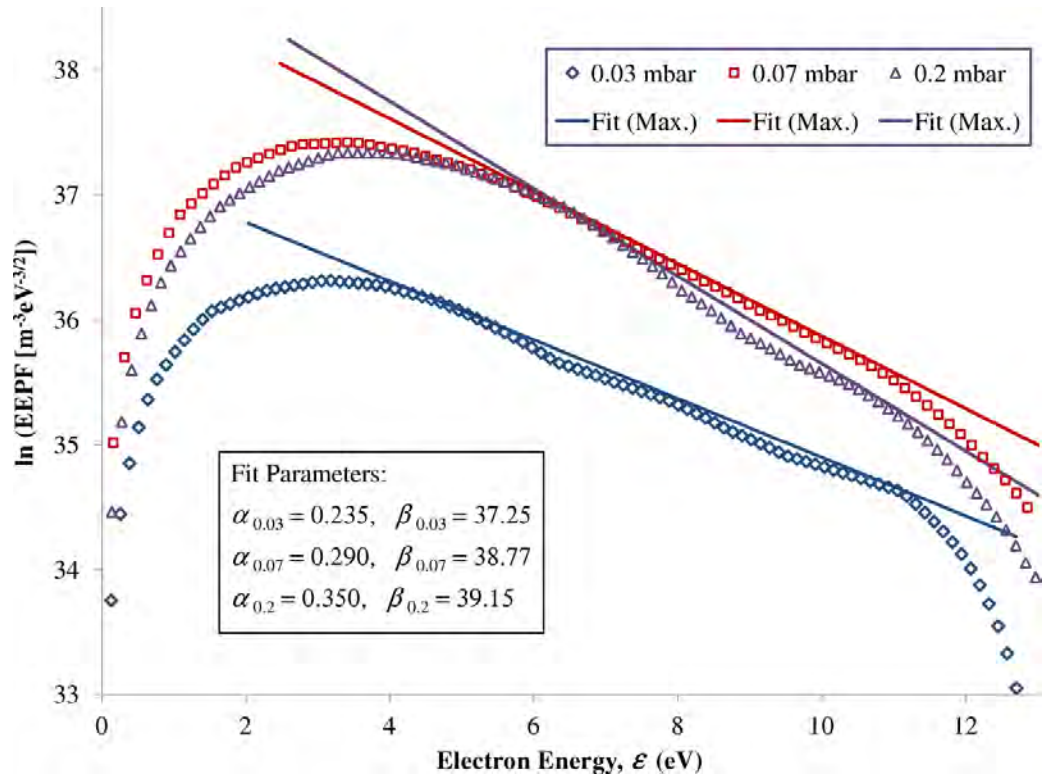


**Figure 4.4:** Electron energy probability function (EEPF) at 0.032 m distance above the dielectric plate for 0.03, 0.07 and 0.2 mbar argon pressures with corresponding parametric fit. R. f. power was at 180 W.

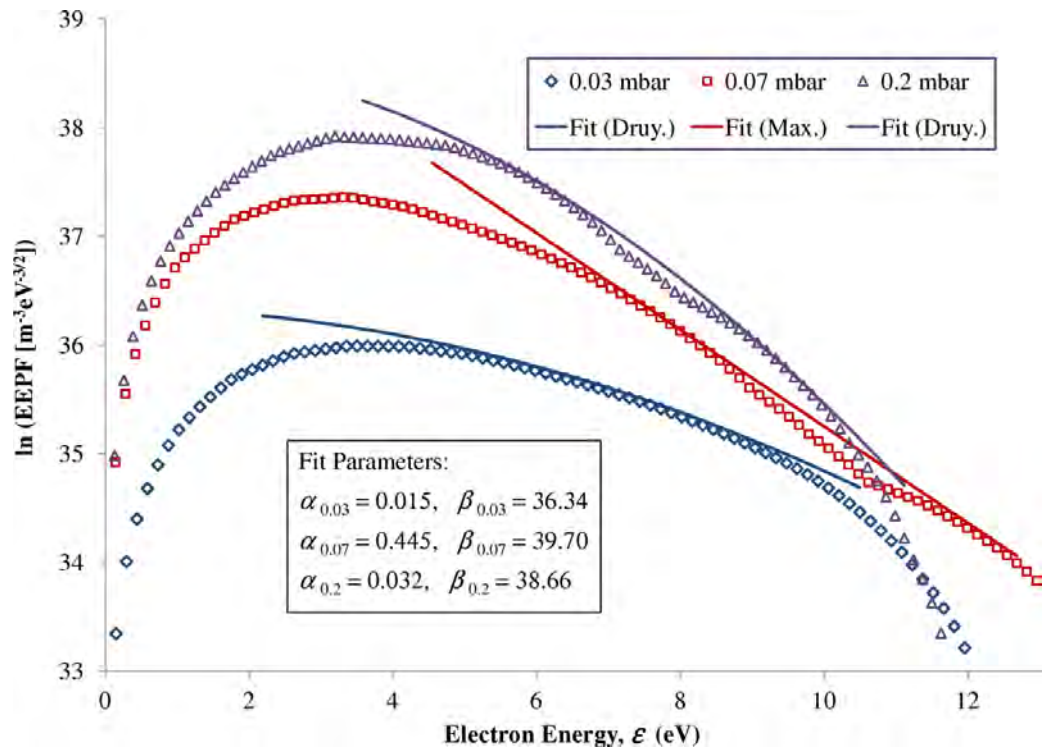


**Figure 4.5:** Electron energy probability function (EEPF) at 0.060 m distance above the dielectric plate for 0.03, 0.07 and 0.2 mbar argon pressures with corresponding parametric fit. R. f. power was at 180 W.

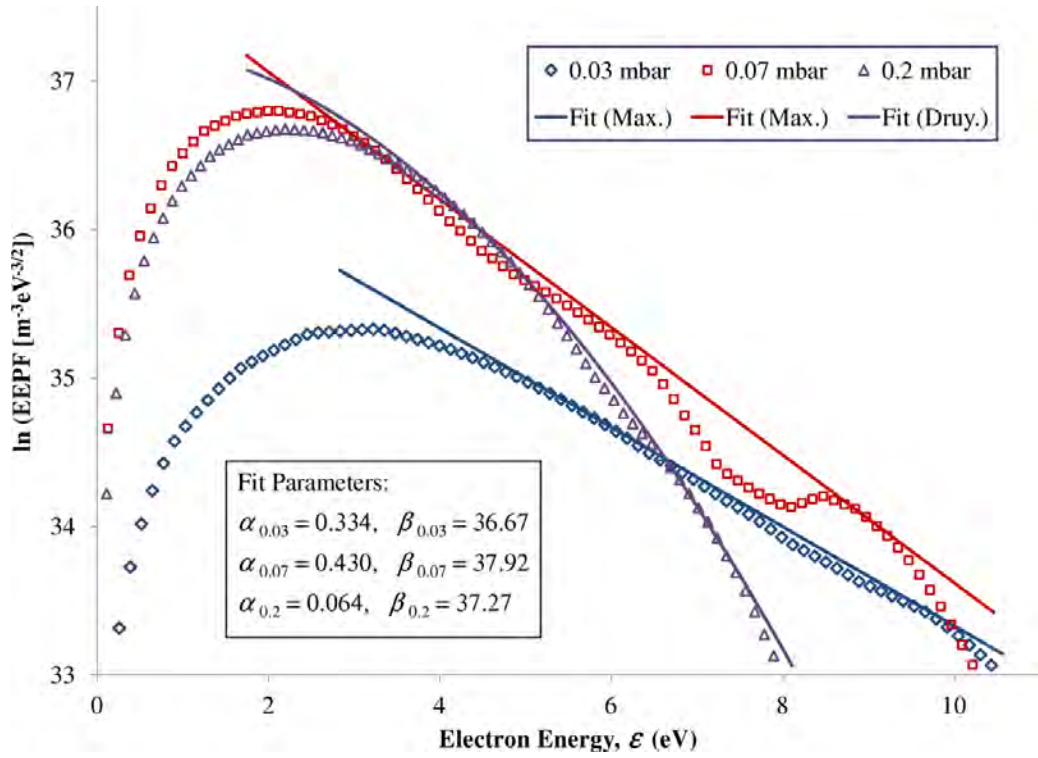


**Figure 4.6:** Electron energy probability function (EEPF) at 0.114 m distance above the dielectric plate for 0.03, 0.07 and 0.2 mbar argon pressures with corresponding parametric fit. R. f. power was at 180 W.

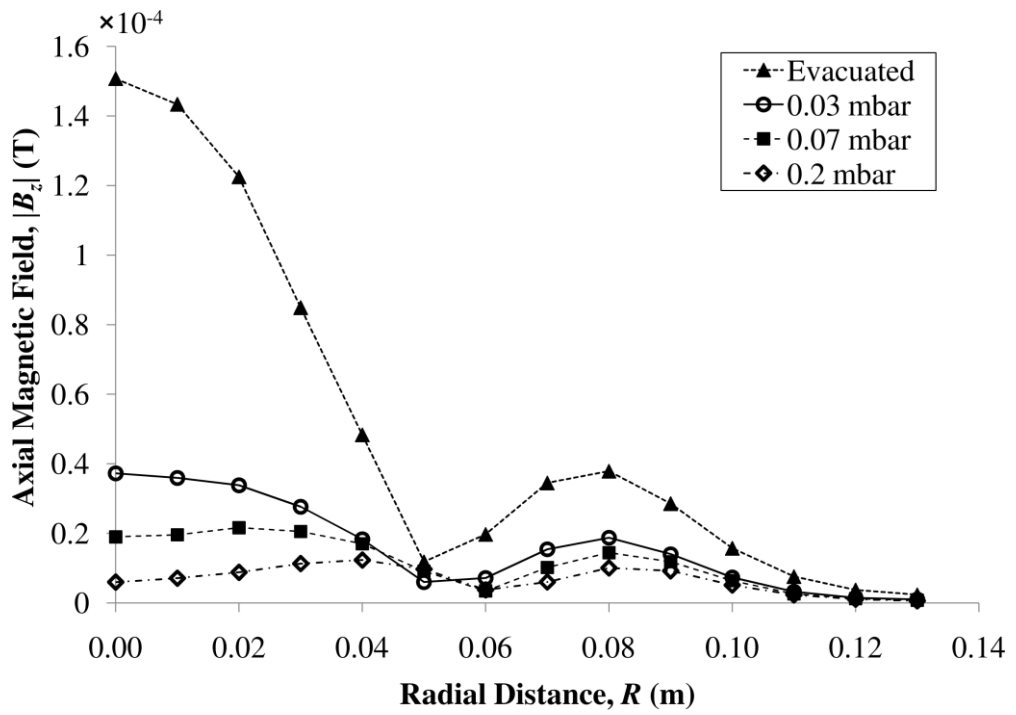
The measured EEPF distributions are similar to those reported by Lim (2010) for the same system; with most probable electron energy occurring within the range of 2-4 eV for all axial distances from the coil. Attempts of parametric fitting of the EEPFs with Maxwellian and Druyvesteyn functions indicated Maxwellian-like trends; although the exact measured EEPFs have more complex distributions. For simplicity of the simulations presented in Chapter 5 and 6, the EEDFs used in calculation of effective collision frequency,  $\nu_{\text{eff}}$  were approximated as Maxwellian.

## **4.1. Measurement of Discharge Magnetic Fields**

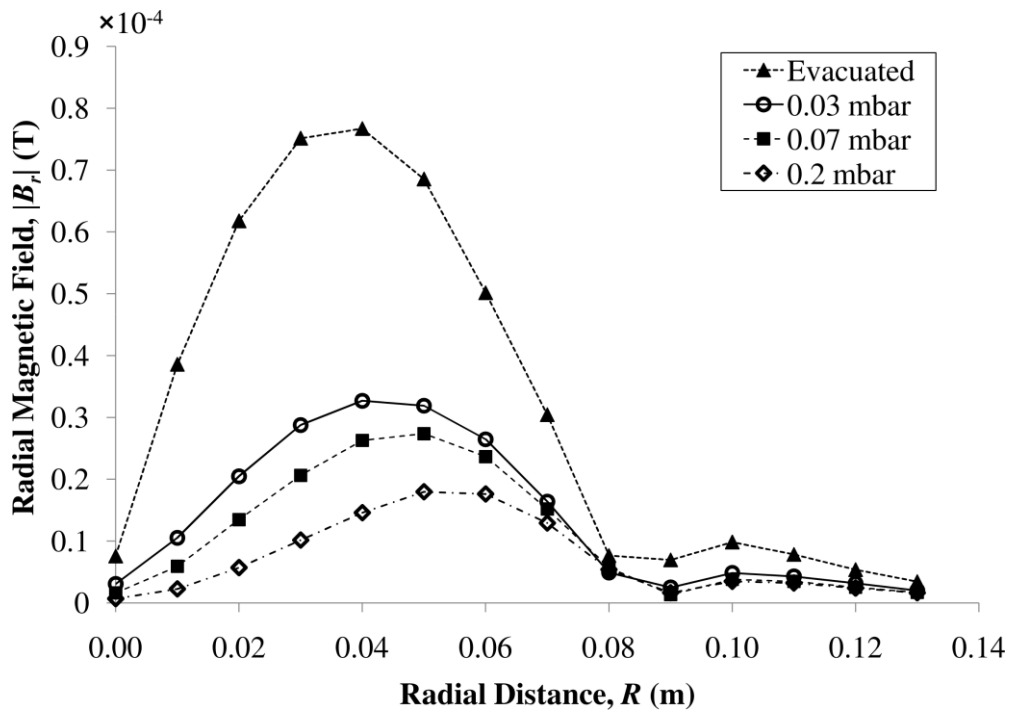
The absolute magnitudes of the axial and radial magnetic fields were measured at different pressures and distances above the dielectric plate; with and without the presence of the plasma. Results for the fields in the presence of the plasma were used for comparison with the fields calculated by predictive electromagnetic simulation (Chapter 6, Section 6.0.4).

### **4.1.1. Absolute Axial, $|B_z|$ and Radial, $|B_r|$ Magnetic Fields**

Figures 4.7 and 4.8 depict the measured absolute magnitudes of the (i) axial,  $|B_z|$  and (ii) radial,  $|B_r|$  magnetic fields at evacuated condition (without plasma) ( $P < 10^{-3}$  mbar) and at 0.03 mbar, 0.07 mbar and 0.2 mbar argon pressure for 0.032 m and 0.060 m axial distances above the dielectric plate, respectively. R.f. power was set at 180 W.

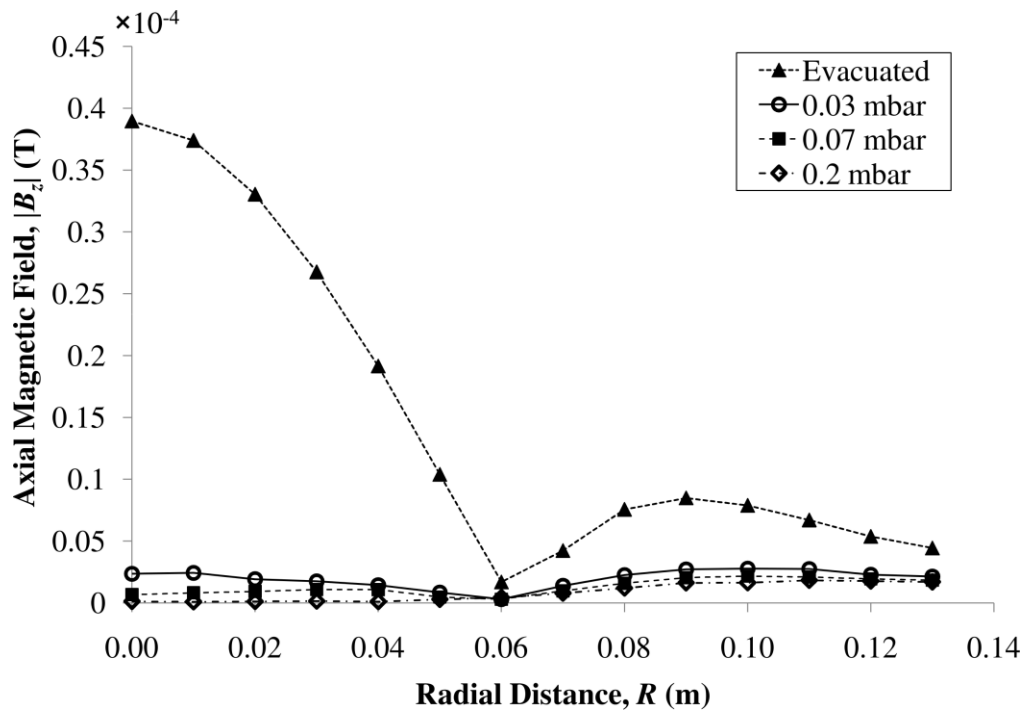


(i)

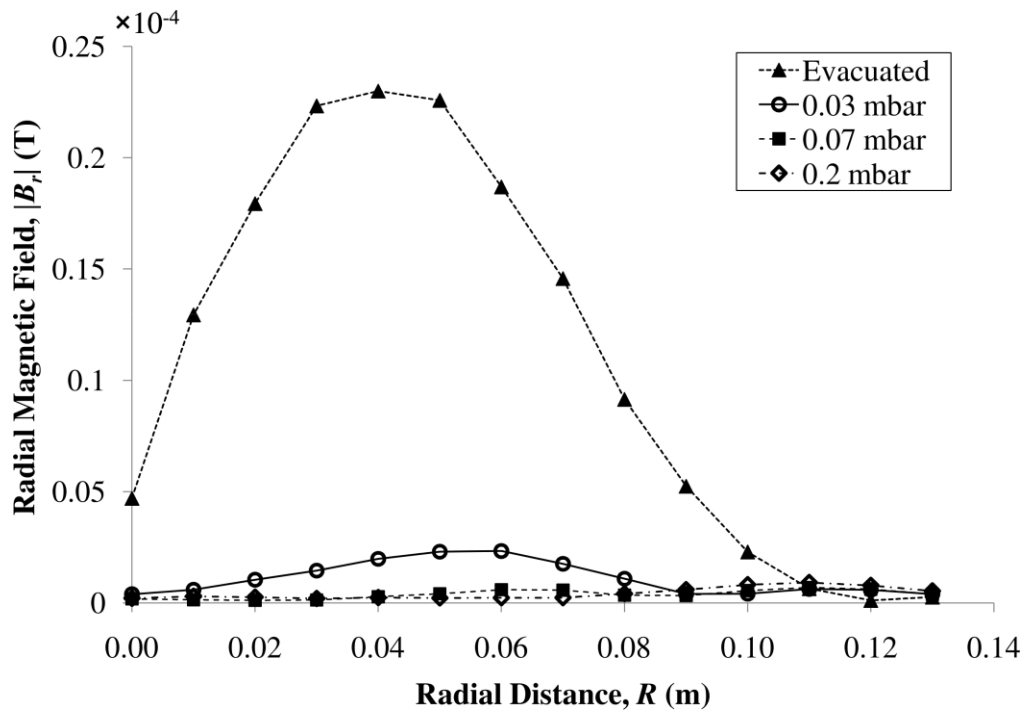


(ii)

**Figure 4.7:** Measured absolute magnitudes of the (i) axial and (ii) radial magnetic fields at 0.032 m distance above the dielectric plate for evacuated, 0.03 mbar, 0.07 mbar and 0.2 mbar argon pressures. R.f. power was set at 180 W.



(i)



(ii)

**Figure 4.8:** Measured absolute magnitudes of the (i) axial and (ii) radial magnetic fields at 0.060 m distance above the dielectric plate for evacuated, 0.03 mbar, 0.07 mbar and 0.2 mbar argon pressures. R.f. power was set at 180 W.

When the chamber is evacuated (without plasma), the measured axial and radial magnetic fields gave the highest magnitudes with  $(1.507 \pm 0.005) \times 10^{-4}$  T and  $(7.67 \pm 0.01) \times 10^{-5}$  T, respectively for 0.032 m and  $(3.90 \pm 0.02) \times 10^{-5}$  T and  $(2.30 \pm 0.03) \times 10^{-5}$  T, respectively for 0.060 m. The peak coil current,  $I_p$  obtained when measuring the magnetic fields were  $(19.2 \pm 0.2)$  A at evacuated condition,  $(14.4 \pm 0.2)$  A at 0.03 mbar,  $(14.2 \pm 0.2)$  A at 0.07 mbar and  $(13.4 \pm 0.2)$  at 0.2 mbar.

Increased suppression of the magnetic field magnitudes was seen as pressure was increased for both the axial and radial magnetic fields at both distances above the dielectric plate; indicating increased utilization of the magnetic fields by the plasma. With increase of pressure, it is also noted that a trough is formed in both the axial and radial magnetic field magnitudes within the coil region ( $R < 0.05$  m), whereby the magnetic fields near the center of the chamber is more highly utilized. This is consistent with the trends seen in the electron density in Figures 4.1 and 4.2 at which the discharge becomes more confined to the coil region and less diffused as pressure is increased. Beyond the coil region ( $R > 0.05$  m), the field is to be out of phase and is negative (when plotted as absolute values, the field is positive and inverted). This is mainly due to the geometry of the chamber in which the coil, chamber and dielectric diameters are different.

#### **4.2. Measurement of Peak Coil Transition and Maintenance Currents**

The H mode peak coil transition and maintenance currents were measured for a range of argon pressures. These values were compared with predictive simulation of the currents using the power deposition model (Chapter 6, Section 6.1).

#### 4.2.1. H Mode Peak Transition, $I_{tr}$ and Maintenance, $I_{mt}$ Currents

Figure 4.9 shows the measured H mode peak coil transition current (E to H mode transition),  $I_{tr}$  and H mode peak coil maintenance current (H to E mode transition),  $I_{mt}$  for the argon pressure range of 0.02-0.3 mbar.

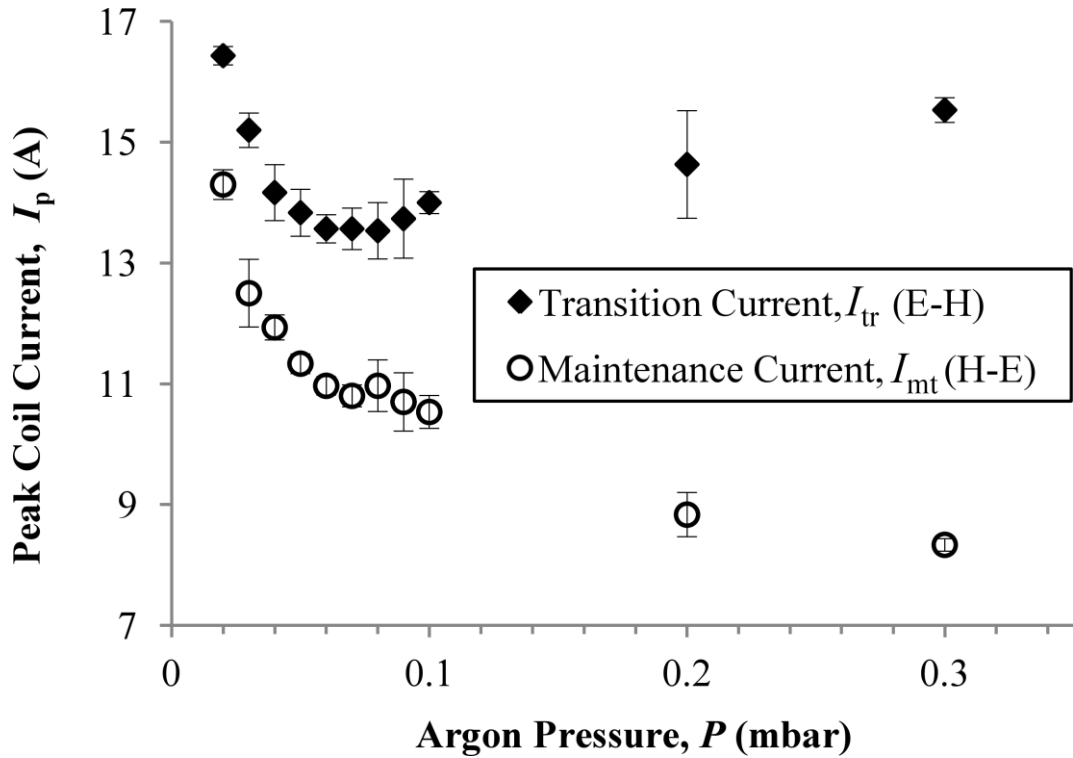


**Figure 4.9:** Measured H mode peak coil transition current,  $I_{tr}$  (E-H) and H mode peak coil maintenance current,  $I_{mt}$  (H-E) for 0.02-0.2 mbar argon pressure.

At lower pressures, higher coil current is required to initiate a transition from E mode to H mode discharge i.e.,  $(16.4 \pm 0.2)$  A at 0.02 mbar. As pressure is increased,  $I_{tr}$  decreases to a minimum value of  $(13.5 \pm 0.5)$  A at 0.08 mbar before increasing to  $(15.5 \pm 0.2)$  A at 0.3 mbar. This is attributed to the power coupling of source fields which has been shown to be most efficient when the ratio of effective collision frequency to drive frequency,  $\nu_{eff}/\omega \approx 1$  (Piejak, Godyak & Alexandrovich, 1992 and El-Fayoumi, Jones & Turner, 1998). From simulation of  $I_{tr}$  with neutral gas heating (i.e.,

Section 6.1.2.),  $\nu_{\text{eff}}/\omega \approx 1$  is found near the measured argon pressure range of 0.07-0.08 mbar; at which least current is required to initiate a transition to H mode.

In the case of  $I_{\text{mt}}$ , higher values are also required to maintain the discharge in H mode operation at low pressures, i.e.,  $(14.3 \pm 0.2)$  A at 0.02 mbar. As pressure is increased,  $I_{\text{mt}}$  decreases to  $(8.3 \pm 0.1)$  A at 0.3 mbar. The increasing deviation between  $I_{\text{tr}}$  and  $I_{\text{mt}}$  with increasing pressure indicates the more prominent effect of hysteresis in the working path of the system. The effect of hysteresis is more thoroughly discussed in Chapter 6. Several factors can be attributed to the lower  $I_{\text{mt}}$  requirement for the discharge at higher pressures:

- i. At higher pressures, the electron density of the H mode discharge is higher. Multi-step ionization (i.e., ionization of the neutrals through intermediate excitation states) becomes the primary process of conversion of absorbed excited state energy over radiative de-excitation processes (Turner and Lieberman, 1999). Thus, more energy from the excitation collisions that occur in the discharge contributes toward the ionization of particles, allowing for maintenance of the H mode discharge at lower currents.
- ii. At higher pressures, there are also more plasma particles that are present in the chamber. The increase in collision frequency of these particles would also result in more ionizing collisions, which allows for maintenance of the H mode discharge at lower currents.
- iii. The neutral gas temperature of the discharge is also seen to increase (in reference to Section 4.3) at higher pressure. This may result in the neutral particles being more readily ionized due to more of the background particles having higher

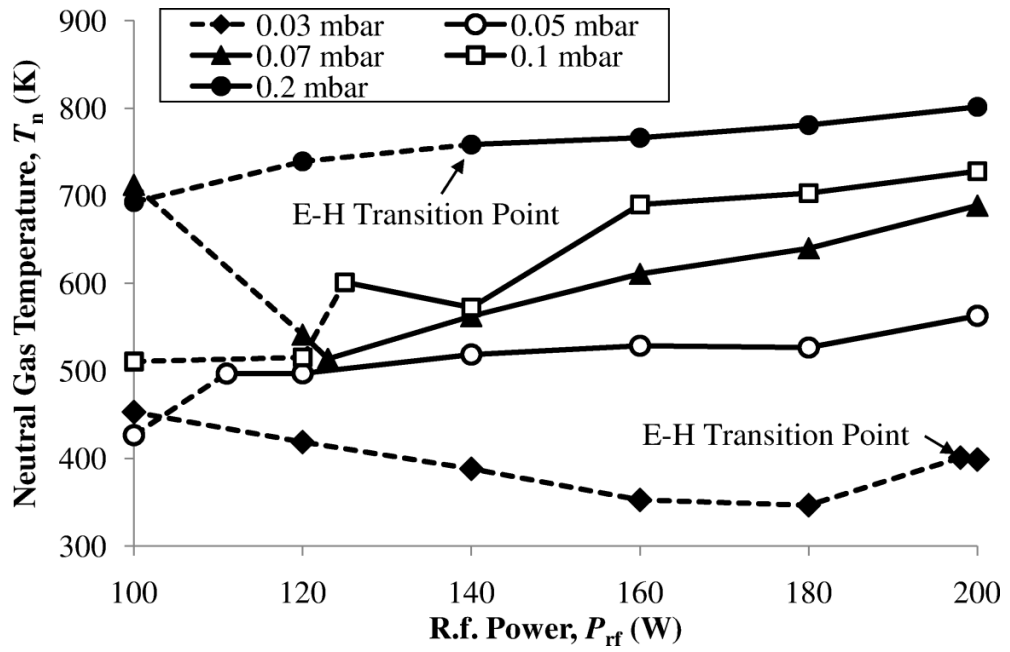
kinetic energies. This may have some contribution in enabling the sustenance of the H mode discharge at lower currents for higher pressures.

### **4.3. Measurement of Discharge Neutral Gas Temperature via AOES**

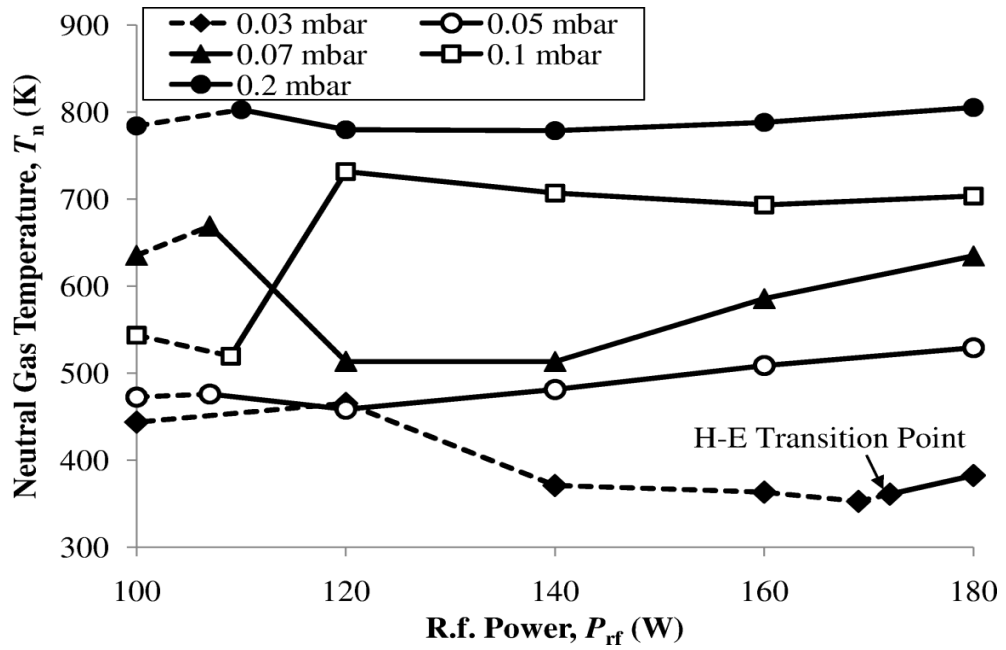
Using the AOES technique, the neutral gas temperature of the discharge was measured at different pressures and distances above the dielectric plate for increasing and decreasing input r.f. powers. Results from measurement were taken as reference for the predictive simulations found in Chapter 6.

#### **4.3.1. Measured Neutral Gas Temperature, $T_n$**

Figure 4.10 and 4.11 shows the measured neutral gas temperatures,  $T_n$  at 0.03, 0.05, 0.07, 0.1 and 0.2 mbar Ar/N<sub>2</sub> pressure for (i) increasing and (ii) decreasing r.f. power at 0.032 m and 0.060 m axial distance above the dielectric plate, respectively.

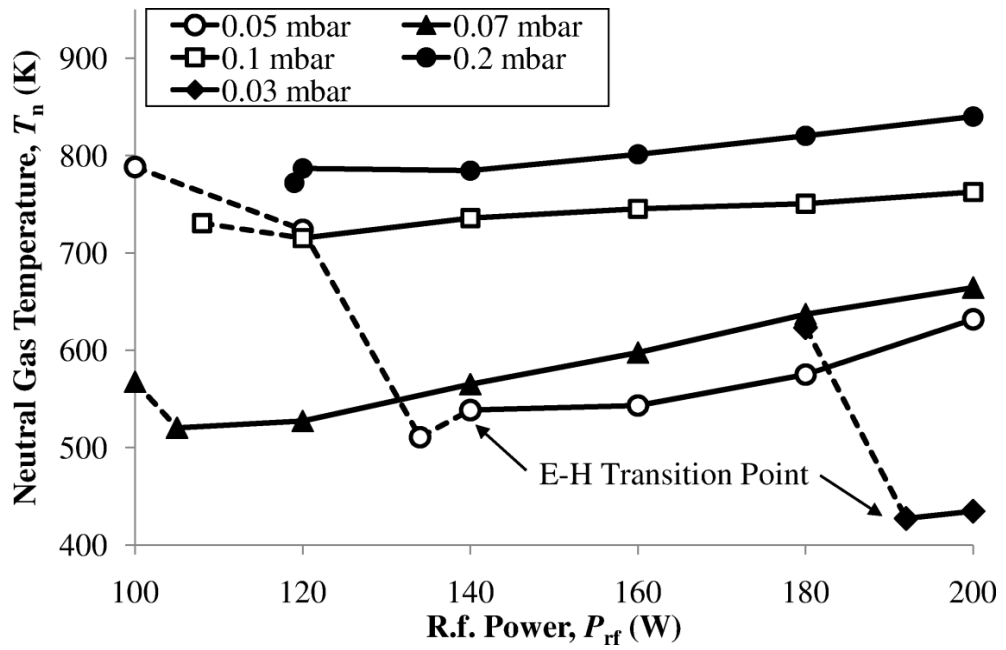


(i)

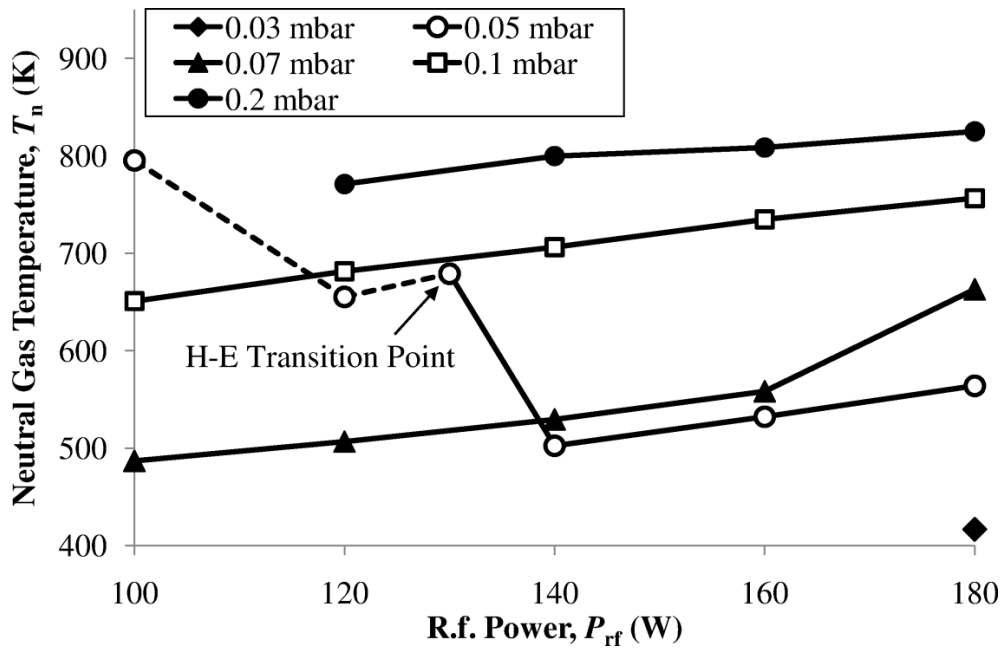


(ii)

**Figure 4.10:** Measured neutral gas temperature,  $T_n$  at 0.03, 0.05, 0.07, 0.1 and 0.2 mbar Ar/N<sub>2</sub> pressures for (i) increasing and (ii) decreasing r.f. power. Measurement was made at 0.032 m distance above the dielectric plate.



(i)



(ii)

**Figure 4.11:** Measured neutral gas temperature,  $T_n$  at 0.03, 0.05, 0.07, 0.1 and 0.2 mbar Ar/N<sub>2</sub> pressures for (i) increasing and (ii) decreasing r.f. power. Measurement was made at 0.060 m distance above the dielectric plate.

The dashed lines on the plots represent the discharge at E mode state, whereas, the solid lines represent the discharge in H mode state. The mode transition point is the point between the dashed and solid lines.  $T_n$  measured in E mode state had higher errors on average (i.e., 10-20 % error for the discharge in E mode compared to 5-12 % error in H mode) due to the lower definitions of the fitted peak, especially for 0.060 m distance above the dielectric plate. At certain powers,  $T_n$  was not measured due to the reference peak being not of resolvable intensity.

With r.f. power and distance above the dielectric plate,  $T_n$  is seen to have little variation; within the bounds of measured error. With increase in gas pressure, however,  $T_n$  becomes markedly increased. These observed trends are explained as follows:

- i. As Ar/N<sub>2</sub> pressure is increased at a fixed input r.f. power, more energy is coupled into the plasma. This is demonstrated by calculations tabulated in Chapter 6, Section 6.0.2, Table 6.2, whereby, absorbed electron power,  $P_{\text{abs}}$  is higher at higher pressure,  $P$  for the same input r.f. power of 180 W. With increased power coupled into the discharge, electron density and ion density increases. Because of the presence of more charged and neutral particles within the same volume for higher pressure, the collision frequency of the plasma particles increases. Transfer of kinetic energy from charged particles to neutral particles is increased via charge transfer collision of energetic ions with neutrals and de-excitation collision of ions by electrons (Lieberman & Lichtenberg, 2005). This raises the number of thermalized neutrals within the plasma, thus, increasing  $T_n$ .
- ii. With collisional processes between charged and neutral particles limited by the collision frequency which is correlated with Ar/N<sub>2</sub> pressure (as mentioned in the

previous point, i.), variation of r.f. power does not significantly affect  $T_n$ ; due to the limited energy transfer from charged particles to the neutrals.

- iii. The convection of thermalized neutrals from "hotter" plasma regions (i.e., nearer to the source field, where the discharge is more intense) to colder regions (away from the source field) would mean that the particles would also be distributed to regions further from the source (noted in Section 4.0.1 for electron density). Thus, at the measured axial distances of 0.032 m and 0.060 m,  $T_n$  does not show significant variation beyond the discrepancy obtained in measurement.

For increasing r.f. power at H mode and 0.032 m plate distance, values of  $T_n$  ranged from  $(350 \pm 30)$  K at 0.03 mbar to  $(800 \pm 20)$  K at 0.2 mbar. For decreasing r.f. power at H mode and 0.032 m plate distance, values of  $T_n$  were from  $(380 \pm 10)$  K at 0.03 mbar to  $(810 \pm 20)$  K at 0.2 mbar. In the case of increasing r.f. power at H mode and 0.060 m plate distance, values for  $T_n$  ranged from  $(430 \pm 20)$  K at 0.03 mbar to  $(840 \pm 30)$  K at 0.2 mbar. For decreasing r.f. power at H mode and 0.060 m plate distance, values for  $T_n$  were from  $(420 \pm 20)$  K at 0.03 mbar to  $(830 \pm 30)$  K at 0.2 mbar. These values of  $T_n$  will be used as a reference range for the simulations shown in Chapter 6.

## CHAPTER 5: SIMULATION

### 5.0. Electromagnetic Field Model

Simulation of the E mode and H mode electromagnetic fields used in this work (Sections 5.1, 5.2, 5.3 and 5.4) is based on the field theory derived by El-Fayoumi et al. (El-Fayoumi, 1996; El-Fayoumi & Jones, 1998; El-Fayoumi, Jones & Turner, 1998). To obtain a more accurate representation of the laboratory ICP reactor fields, certain aspects of the original model were improved. These include:

- i. Modifications of the model field grid to more closely resemble the actual dimensions of the laboratory reactor.
- ii. Independent adjustment of radius of the planar coil source, quartz dielectric plate and chamber.
- iii. Extended calculation of the collision frequency parameter; accounting for the effects of important collisional processes.
- iv. Spatially resolved plasma parameters such as electron density, electron temperature and neutral gas temperature; which interact with the fields.

The E mode and H mode electromagnetic fields in the laboratory ICP reactor are modeled in cylindrical coordinates  $(r, \theta, z)$  with the following measured dimensions: radius of the 6-turn planar coil,  $a = 0.045$  m; radius of the 0.010 m thick quartz dielectric plate,  $d = 0.100$  m; inner radius of chamber,  $b = 0.145$  m; full inner height of chamber,  $H = 0.304$  m; effective height of chamber,  $L = 0.218$  m; height of indented

cylinder,  $M = 0.099$  m; edge width of indented cylinder,  $W = 0.026$  m; and total thickness of coil-chamber spacing,  $D = 0.024$  m. The axial coordinate,  $z$ , begins (i.e.,  $z = 0$ ) at the chamber lid and the radial coordinate,  $r$ , begins (i.e.,  $r = 0$ ) at the center axis of the chamber (Figure 5.1).

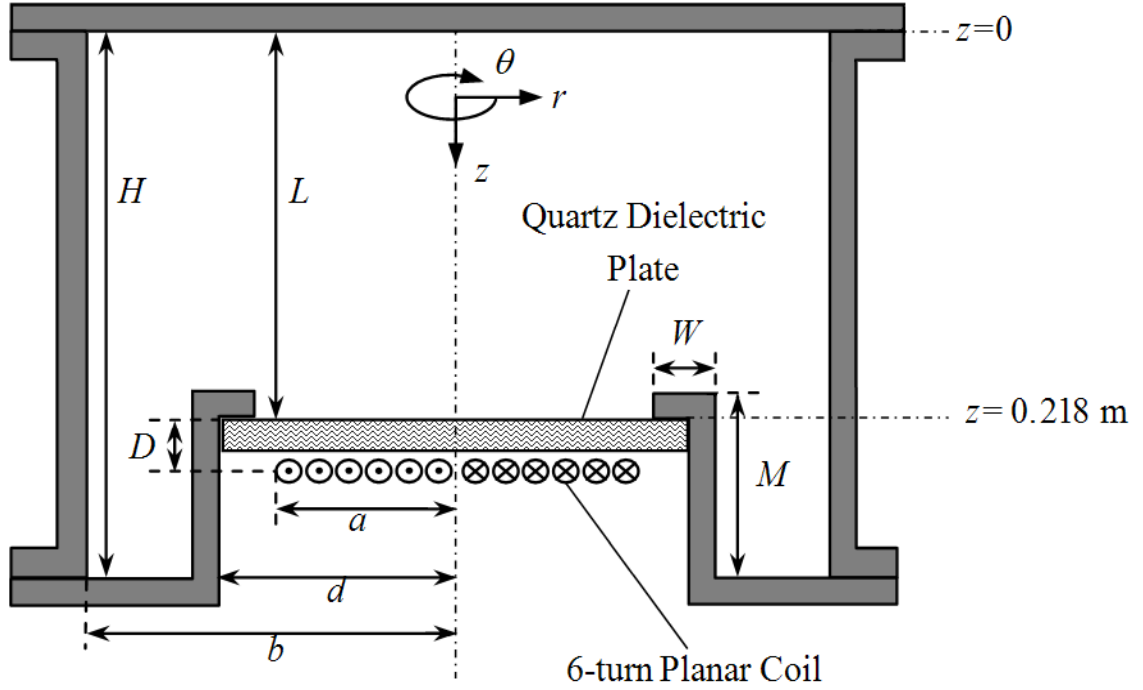


**Figure 5.1:** Numerical model diagram of the laboratory ICP reactor.

Starting from the standard Maxwell's equations (Sadiku, 2001, pp. 384-385), i.e.,

$$\nabla \times \mathcal{E}(r, \theta, z, t) = -\frac{\partial \mathcal{B}(r, \theta, z, t)}{\partial t}, \quad (5.0.1)$$

$$\nabla \cdot \mathcal{E}(r, \theta, z, t) = \frac{\rho}{\epsilon_0}, \quad (5.0.2)$$

$$\nabla \times \mathcal{B}(r, \theta, z, t) = \mu_0 \left( \mathcal{J}(r, \theta, z, t) + \epsilon_0 \frac{\partial \mathcal{E}(r, \theta, z, t)}{\partial t} \right), \quad (5.0.3)$$

and

$$\nabla \cdot \mathcal{B}(r, \theta, z, t) = 0, \quad (5.0.4)$$

the following assumptions were applied:

- i. The reactor is azimuthally symmetric, thus, the fields only vary in the  $-r$  and  $-z$  directions.
- ii. The plasma mainly consists of low energy electrons and the immobile ions thus, satisfying the local Ohm's Law equation,

$$\mathcal{E}(r, \theta, z, t) = \frac{m_e}{n_e e^2} \left( \nu \mathcal{J}(r, \theta, z, t) + \frac{\partial \mathcal{J}(r, \theta, z, t)}{\partial t} \right), \quad (5.0.5)$$

where,  $m_e$  is the electronic mass in kg,  $e$  is the electronic charge in C,  $n_e$  is the electron density in  $\text{m}^{-3}$  and  $\nu$  is the electron collision frequency in  $\text{s}^{-1}$ .

- iii. For free space, the charge density term,  $\rho = 0$ , thus, reducing Eq. (5.0.2) to,

$$\nabla \cdot \mathcal{E}(r, \theta, z, t) = 0. \quad (5.0.6)$$

- iv. The steady state temporal term of the r.f. field is represented by  $\exp(j\omega t)$ , where  $\omega$  is the r.f. angular frequency (rad/s), i.e.,  $\omega = 2\pi \times 13.56 \text{ MHz}$ .

Here,  $\mathcal{E}$ ,  $\mathcal{B}$  and  $\mathcal{J}$  are the time varying electric field in  $\text{Vm}^{-1}$ , magnetic field in T and current density in  $\text{Am}^{-2}$ , respectively.  $\mu_0$  is the free space permeability in  $\text{Hm}^{-1}$  and  $\epsilon_0$  is

the free space permittivity in  $\text{Fm}^{-1}$ . With these assumptions, Eqs. (5.0.1-5.0.5) can be subsequently simplified as,

$$\nabla \times \mathbf{E}(r, z) = -j\omega \mathbf{B}(r, z) , \quad (5.0.7)$$

$$\nabla \cdot \mathbf{E}(r, z) = 0 , \quad (5.0.8)$$

$$\nabla \times \mathbf{B}(r, z) = \mu_0 \mathbf{J}(r, z) + j\varepsilon_0 \mu_0 \omega \mathbf{E}(r, z) , \quad (5.0.9)$$

$$\nabla \cdot \mathbf{B}(r, z) = 0 , \quad (5.0.10)$$

and

$$\mathbf{J}(r, z) = \frac{\varepsilon_0 \omega_p^2}{\nu + j\omega} \mathbf{E}(r, z) , \quad (5.0.11)$$

$\omega_p$  is the plasma frequency in  $\text{s}^{-1}$  and is given by,

$$\omega_p = \left( \frac{n_e e^2}{\varepsilon_0 m_e} \right)^{1/2} . \quad (5.0.12)$$

The equations were solved both analytically and numerically for the H mode fields with the initial field values for boundary convergence of the numerical solution being analytically derived. Analytical E mode fields were also derived for use in the power balance model in Section 5.4. Solutions for each of the fields are addressed separately in the following sections.

### 5.1. Analytical H mode fields

To solve for the analytical H mode fields from Eqs. (5.0.7-5.0.12), further assumptions and boundary conditions were applied:

- a) The displacement current term in Eq. (5.0.9) is neglected (i.e.,  $j\epsilon_0\mu_0\omega\mathbf{E}(r,z) = 0$ ). This is due to the higher free excitation wavelength ( $\sim 22$  m for 13.56 MHz) as compared to the chamber dimensions. Eq. (5.0.9) then reduces to,

$$\nabla \times \mathbf{B}(r, z) = \mu_0 \mathbf{J}(r, z) . \quad (5.1.1)$$

- b) The planar coil is assumed to be an infinitesimally thin disc of moving uniform charge and has a surface current density of,

$$K_\theta = \frac{NI_p}{a} , \quad (5.1.2)$$

where  $I_p$  is the peak coil current in A,  $N$  is the number of turns in the coil and  $a$  is the coil radius in m.

- c) The chamber is a simple azimuthally symmetric cylinder of radius,  $b$  and effective height,  $L$  with a coil radius of  $a$ . The coil-chamber spacing is  $D$  (Figure 5.2).

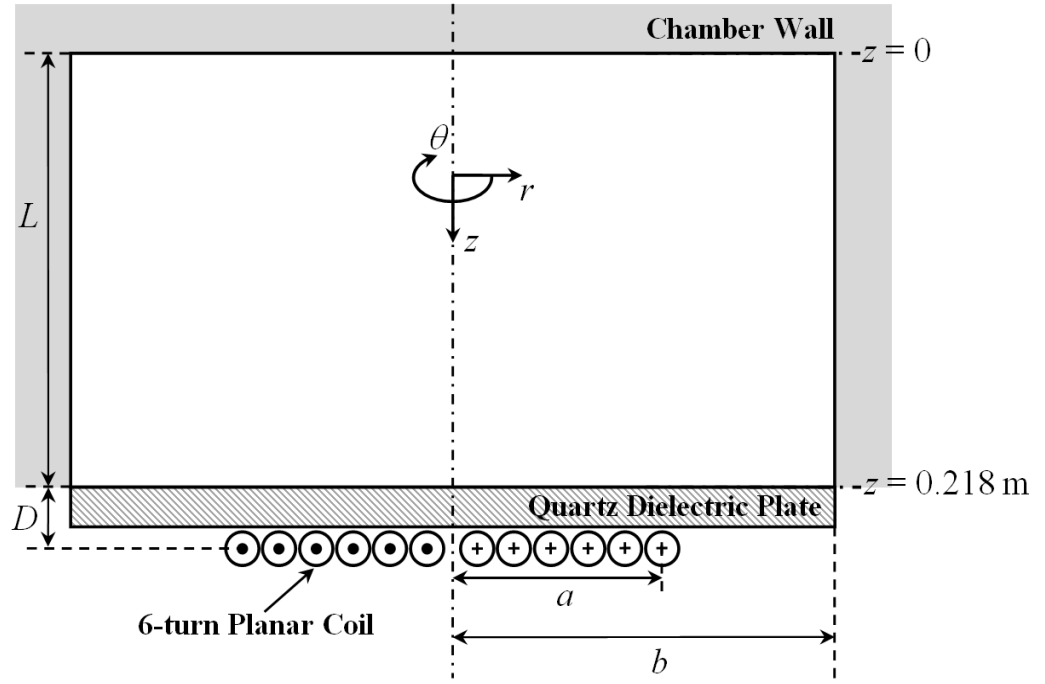


**Figure 5.2:** Analytical model diagram of the laboratory ICP reactor.

- d) The chamber (from boundaries  $-b < r < b$  and  $0 < z < L$ ) has a uniform electron density,  $n_e$ , collision frequency,  $\nu$  and electron temperature,  $T_e$ . Externally, these parameters are equal to zero.
- e) At the boundaries between the quartz plate and the plasma, the tangential electric fields and tangential and normal magnetic fields are continuous.
- f) At the boundaries between the chamber walls and the plasma, the tangential electric fields and normal magnetic fields are equal to zero.

By taking the curl of Eq. (5.0.7) and by further substitutions of Eqs. (5.0.11) and (5.1.1), we arrive at the following key expressions,

$$\nabla \times \mathbf{E}(r, z) = -j\omega \mathbf{B}(r, z) \quad (5.1.3)$$

and

$$\nabla \times \nabla \times \mathbf{E}(r, z) = - \left( \frac{\mu_0 \epsilon_0 \omega_p^2}{1 - j\nu/\omega} \right) \mathbf{E}(r, z) . \quad (5.1.4)$$

The term  $\mu_0 \epsilon_0 \omega_p^2 / (1 - j\nu/\omega)$  in Eq. (5.1.4) represents the quantified interaction between the electromagnetic fields and plasma and is more conveniently expressed as the spatial conductivity parameter,  $\alpha^2$ , i.e.,

$$\alpha^2 = \frac{\mu_0 n_e e^2}{m_e [1 - j\nu/\omega]} . \quad (5.1.5)$$

Calculation of  $\alpha^2$  can be made by taking the average values of  $n_e$  and  $\nu$ . Details of finding  $\nu$  (i.e.,  $\nu_{\text{eff}}$ ) is discussed in the Section 5.2.1. With  $\alpha^2$  defined as in Eq. (5.1.5), Eq. (5.1.4) can be simplified to,

$$\nabla \times \nabla \times \mathbf{E}(r, z) = -\alpha^2 \mathbf{E}(r, z) . \quad (5.1.6)$$

Due to azimuthal symmetry of the chamber, the solution to the H mode electromagnetic fields would only have the scalar azimuthal electric field,  $E_\theta$  component, i.e.,  $\mathbf{E} = [0, E_\theta, 0]$  and the scalar radial magnetic field,  $B_r$  and axial magnetic field,  $B_z$  components,  $\mathbf{B} = [B_r, 0, B_z]$ . In component form, Eqs. (5.1.3) and (5.1.4) can be rewritten as,

$$\frac{1}{r} \frac{\partial}{\partial r} \left( r \frac{\partial E_{\theta}}{\partial r} \right) - \frac{E_{\theta}}{r^2} + \frac{\partial^2 E_{\theta}}{\partial z^2} = \alpha^2 E_{\theta} , \quad (5.1.7)$$

$$B_r = -\frac{j}{\omega} \frac{\partial E_{\theta}}{\partial z} , \quad (5.1.8)$$

and

$$B_z = \frac{j}{\omega} \frac{1}{r} \left( \frac{\partial(rE_{\theta})}{\partial r} \right) . \quad (5.1.9)$$

for  $0 \leq z \leq L + D$ .

### 5.1.1. Separation of Variables Method for the H mode Fields

To solve the field Eqs. (5.1.7-5.1.9), the separation of variables method is used (Boas, 1983, pp. 558-562; Kreyszig, 2011, pp. 593-597; Sadiku, 2009). In this method, a multivariable function is split and solved as separate single variable functions which are bridged together using an introduced expression known as a separation constant. For the present case, the multivariable azimuthal electric field,  $E_{\theta}(r, z)$  is defined to be the product of two single variable functions,  $R(r)$  and  $Z(z)$ , i.e.,

$$E_{\theta} = Z(z)R(r) . \quad (5.1.10)$$

The defined Eq. (5.1.10) is next substituted into Eq. (5.1.7) yielding,

$$\frac{1}{R(r)} \left( \frac{1}{r} \frac{\partial R(r)}{\partial r} + \frac{\partial^2 R(r)}{\partial r^2} - \frac{R(r)}{r^2} - \alpha^2 R(r) \right) + \frac{1}{Z(z)} \frac{\partial^2 Z(z)}{\partial z^2} = 0 . \quad (5.1.11)$$

By introducing a separation constant,  $k^2$ , Eq. (5.1.11) is separated into two equations, i.e.,

$$\frac{1}{R(r)} \left( \frac{1}{r} \frac{\partial R(r)}{\partial r} + \frac{\partial^2 R(r)}{\partial r^2} - \frac{R(r)}{r^2} - \alpha^2 R(r) \right) = -k^2 \quad (5.1.12)$$

and

$$\frac{1}{Z(z)} \frac{\partial^2 Z(z)}{\partial z^2} = k^2 . \quad (5.1.13)$$

Rearranging Eqs. (5.1.12) and (5.1.13) to be representative of closed-form solutions, we arrive at,

$$r^2 \frac{\partial^2 R(r)}{\partial r^2} + r \frac{\partial R(r)}{\partial r} + [\lambda^2 r^2 - 1] R(r) = 0 , \quad (5.1.14)$$

and

$$\frac{\partial^2 Z(z)}{\partial z^2} = k^2 Z(z) . \quad (5.1.15)$$

Here,  $\lambda^2$  and  $k^2$  are separation constants and are related by,

$$k^2 = \lambda^2 + \alpha^2 . \quad (5.1.16)$$

Looking at the boundary conditions b) to f) in Section 5.1, we are able to deduce several important relations for the component fields:

- i. At the plane of the coil ( $z = L + D$ ), the total radial magnetic field emitted by an infinitesimally thin disc of surface current density,  $K_\theta$  is given by,

$$B_r(r, L + D)_- - B_r(r, L + D)_+ = \mu_0 K_\theta \quad , \quad (5.1.17)$$

where,  $B_r(r, L + D)_-$  and  $B_r(r, L + D)_+$  are the radial magnetic field emissions below and above the plane of the coil. Taking point that  $B_r(r, L + D)_- = -B_r(r, L + D)_+$ , the radial magnetic field traversing into the plasma at the coil plane can be deduced as,

$$B_r = \begin{cases} -\frac{\mu_0 K_\theta}{2} & 0 \leq r \leq a \\ 0 & a < r \leq b \end{cases} \quad (5.1.18)$$

or in relation to Eq. (5.1.8)

$$\left. \frac{\partial E_\theta}{\partial z} \right|_{z=L+D} = \begin{cases} -\frac{j\omega\mu_0 K_\theta}{2} & 0 \leq r \leq a \\ 0 & a < r \leq b \end{cases} \quad (5.1.19)$$

Here,  $a$  is the radius of the coil and  $b$  is the radius of the chamber.

- ii. The tangential electric field and tangential and normal magnetic field components between the quartz plate and plasma would be continuous; giving the following relations:

$$E_{\theta}(r, L_{+}) = E_{\theta}(r, L_{-}) . \quad (5.1.20)$$

$$B_r(r, L_{+}) = B_r(r, L_{-}) , \quad (5.1.21)$$

and

$$B_z(r, L_{+}) = B_z(r, L_{-}) . \quad (5.1.22)$$

In terms of the azimuthal electric field, Eqs. (5.1.21) and (5.1.22) are written, respectively as,

$$\left. \frac{\partial E_{\theta}}{\partial z} \right|_{z=L_{+}} = \left. \frac{\partial E_{\theta}}{\partial z} \right|_{z=L_{-}} \quad (5.1.23)$$

and

$$\left. \frac{1}{r} \frac{\partial r E_{\theta}}{\partial r} \right|_{z=L_{+}} = \left. \frac{1}{r} \frac{\partial r E_{\theta}}{\partial r} \right|_{z=L_{-}} . \quad (5.1.24)$$

iii. The tangential electric field and normal magnetic field components at the chamber walls are zero, yielding,

$$E_{\theta}(b, z) = 0 , \quad (5.1.25)$$

$$B_r(b, z) = 0 , \quad (5.1.26)$$

$$E_{\theta}(r, 0) = 0 \quad (5.1.27)$$

and

$$B_z(r, 0) = 0 . \quad (5.1.28)$$

iv. The spatial conductivity parameter  $\alpha^2 = 0$  for  $L < z < L + D$ .

From the deduced field boundaries i.-iv., the general solutions for Eqs. (5.1.10), (5.1.14) and (5.1.15) are determined as,

$$R(r) = A_1 J_1(\lambda r) , \quad (5.1.29)$$

$$Z(z) = B_1 \sinh(kz) , \quad (5.1.30)$$

and

$$E_\theta = A \sinh(kz) J_1(\lambda r) , \quad (5.1.31)$$

for  $0 \leq z \leq L$ ,

and

$$R(r) = A_2 J_1(\lambda r) , \quad (5.1.32)$$

$$Z(z) = B_2 \exp(\lambda z) + C_2 \exp(-\lambda z) , \quad (5.1.33)$$

and

$$E_\theta = [B \exp(\lambda z) + C \exp(-\lambda z)] J_1(\lambda r) , \quad (5.1.34)$$

for  $L < z \leq L + D$ .

Here,  $A$ ,  $B$  and  $C$  in Eqs. (5.1.31) and (5.1.34) are boundary constants to be defined and  $A = A_1 B_1$ ,  $B = A_2 B_2$  and  $C = A_2 C_2$ . To obtain the radial magnetic field,  $B_r$  and axial

magnetic field,  $B_z$  (as per Eqs. (5.1.8) and (5.1.9)), Eqs. (5.1.31) and (5.1.34) are differentiated, i.e.,

$$B_r(r, z) = \begin{cases} -\frac{j}{\omega} Ak \cosh(kz) J_1(\lambda r) & 0 \leq z \leq L \\ -\frac{j}{\omega} [C \exp(\lambda z) - B \exp(-\lambda z)] \lambda J_1(\lambda r) & L < z \leq L + D \end{cases} \quad (5.1.35)$$

$$B_z(r, z) = \begin{cases} \frac{j}{\omega} A \lambda \sinh(kz) J_0(\lambda r) & 0 \leq z \leq L \\ \frac{j}{\omega} [B \exp(-\lambda z) + C \exp(\lambda z)] \lambda J_0(\lambda r) & L < z \leq L + D \end{cases} \quad (5.1.36)$$

It is noted that in Eq. (5.1.25),  $E_0(b, z) = 0$  at the radial boundaries of the chamber.

Thus, in obtaining a valid solution for the value of  $\lambda$ , the Bessel function  $n^{\text{th}}$  root,  $\mu_n$  (which forms a set of eigen values) has to be a multiple of the chamber radius,  $b$ , i.e.,

$$\lambda_n b = \mu_n \quad (5.1.37)$$

or

$$\lambda_n = \frac{\mu_n}{b} . \quad (5.1.38)$$

Consequently, we get  $k$  as,

$$k_n = \sqrt{\lambda_n^2 + \alpha^2} . \quad (5.1.39)$$

The form of the differential Eqs. (5.1.14) and (5.1.15) is generally the form of the Sturm-Liouville problem in which the solution constitutes the sum of a set of orthogonal

eigen functions (Herman, 2008, Atkinson & Mingarelli, 2011). Hence, the full solution for the H mode fields can be appropriately written as the eigen function series,

$$E_{\theta}(r, z) = \begin{cases} \sum_{n=1}^{\infty} A_n \sinh(k_n z) J_1(\lambda_n r) & 0 \leq z \leq L \\ \sum_{n=1}^{\infty} [B_n \exp(-\lambda_n z) + C_n \exp(\lambda_n z)] J_1(\lambda_n r) & L < z \leq L + D \end{cases} \quad (5.1.40)$$

$$B_r(r, z) = \begin{cases} -\frac{j}{\omega} \sum_{n=1}^{\infty} A_n k_n \cosh(k_n z) J_1(\lambda_n r) & 0 \leq z \leq L \\ -\frac{j}{\omega} \sum_{n=1}^{\infty} [C_n \exp(\lambda_n z) - B_n \exp(-\lambda_n z)] \lambda_n J_1(\lambda_n r) & L < z \leq L + D \end{cases} \quad (5.1.41)$$

$$B_z(r, z) = \begin{cases} \frac{j}{\omega} \sum_{n=1}^{\infty} A_n \lambda_n \sinh(k_n z) J_0(\lambda_n r) & 0 \leq z \leq L \\ \frac{j}{\omega} \sum_{n=1}^{\infty} [B_n \exp(-\lambda_n z) + C_n \exp(\lambda_n z)] \lambda_n J_0(\lambda_n r) & L < z \leq L + D \end{cases} \quad (5.1.42)$$

### 5.1.2. Solving for H mode Boundary Constants

The next step is to derive closed form expressions for the boundary constants  $A_n$ ,  $B_n$  and  $C_n$ . Using the boundary conditions at the coil-chamber boundary,  $L$ , as given by Eqs. (5.1.20) and (5.1.21), we are able to obtain the following simultaneous equations for derivation:

$$A_n \sinh(k_n L) = B_n \exp(-\lambda_n L) + C_n \exp(\lambda_n L) , \quad (5.1.43)$$

and

$$A_n k_n \cosh(k_n L) = -\lambda_n [B_n \exp(-\lambda_n L) - C_n \exp(\lambda_n L)] . \quad (5.1.44)$$

For a more convenient solution, it would be apt to define an additional constant,

$$v_n = C_n \exp(\lambda_n (L + D)) - B_n \exp(-\lambda_n (L + D)) . \quad (5.1.45)$$

From simultaneous solving of Eqs. (5.1.43), (5.1.44) and (5.1.45) for  $A_n$ ,  $B_n$  and  $C_n$ , we finally get,

$$A_n = \frac{v_n \lambda_n}{\lambda_n \sinh(\lambda_n D) \sinh(k_n L) + k_n \cosh(\lambda_n D) \cosh(k_n L)} , \quad (5.1.46)$$

$$B_n = \frac{A_n}{2\lambda_n} e^{\lambda_n L} [\lambda_n \sinh(k_n L) - k_n \cosh(k_n L)] , \quad (5.1.47)$$

$$C_n = \frac{A_n}{2\lambda_n} e^{-\lambda_n L} [\lambda_n \sinh(k_n L) + k_n \cosh(k_n L)] . \quad (5.1.48)$$

To complete the solution set for the H mode fields, an independent expression for the constant  $v_n$  is required. By replacing the field boundary condition at  $(L + D)$  given in Eq. (5.1.19) and the constant  $v_n$  defined in Eq. (5.1.45) into Eq. (5.1.41), we get the piecewise continuous relationship,

$$\sum_{n=1}^{\infty} v_n \lambda_n J_1(\lambda_n r) = \begin{cases} -\frac{j\omega\mu_0 K_\theta}{2} & 0 \leq r \leq a \\ 0 & a < r \leq b \end{cases} \quad (5.1.49)$$

Multiplying both sides of Eq. (5.1.49) with the eigen function  $rJ_1(\lambda_n r)$  and by integration across the chamber radius,  $0 \leq r \leq b$ ; due to orthogonality of the Sturm-Liouville problem, we would subsequently get the equation,

$$v_n \lambda_n \int_0^b r J_1^2(\lambda_n r) dr = -\frac{j\omega\mu_0 K_\theta}{2} \int_0^a r J_1(\lambda_n r) dr, \quad (5.1.50)$$

and thus, the solution for  $v_n$ , i.e.,

$$v_n = -\frac{j\omega\mu_0 K_\theta}{2} \frac{\int_0^a r J_1(\lambda_n r) dr}{\lambda_n \int_0^b r J_1^2(\lambda_n r) dr}. \quad (5.1.51)$$

Using the Bessel function identity for orthogonality (Boas, 1983, pp. 522-524) in Eq. (5.1.48), i.e.,

$$\int_0^b r J_p(\lambda_n r) J_p(\lambda_n r) dr = \frac{b^2}{2} J_{p+1}^2(\lambda_n b) = \frac{b^2}{2} J_{p-1}^2(\lambda_n b) = \frac{b^2}{2} J_p'^2(\lambda_n b), \quad (5.1.52)$$

in which,  $p$  is the Bessel function order;  $v_n$  is then simplified to,

$$v_n = -j\omega\mu_0 K_\theta \frac{\int_0^a r J_1(\lambda_n r) dr}{\lambda_n b^2 J_1^2(\lambda_n b)}. \quad (5.1.53)$$

The analytical solutions and corresponding derived constants for the H mode fields for the ICP chamber of height,  $L$  and radius,  $b$  with the coil radius,  $a$  and the coil-chamber distance,  $D$  can be summarized as the following equation set:

$$E_{\theta}(r, z) = \begin{cases} \sum_{n=1}^{\infty} A_n \sinh(k_n z) J_1(\lambda_n r) & 0 \leq z \leq L \\ \sum_{n=1}^{\infty} [B_n \exp(-\lambda_n z) + C_n \exp(\lambda_n z)] J_1(\lambda_n r) & L < z \leq L + D \end{cases} \quad (5.1.54a)$$

$$B_r(r, z) = \begin{cases} -\frac{j}{\omega} \sum_{n=1}^{\infty} A_n k_n \cosh(k_n z) J_1(\lambda_n r) & 0 \leq z \leq L \\ -\frac{j}{\omega} \sum_{n=1}^{\infty} [C_n \exp(\lambda_n z) - B_n \exp(-\lambda_n z)] \lambda_n J_1(\lambda_n r) & L < z \leq L + D \end{cases} \quad (5.1.54b)$$

$$B_z(r, z) = \begin{cases} \frac{j}{\omega} \sum_{n=1}^{\infty} A_n \lambda_n \sinh(k_n z) J_0(\lambda_n r) & 0 \leq z \leq L \\ \frac{j}{\omega} \sum_{n=1}^{\infty} [B_n \exp(-\lambda_n z) + C_n \exp(\lambda_n z)] \lambda_n J_0(\lambda_n r) & L < z \leq L + D \end{cases} \quad (5.1.54c)$$

$$k_n = \sqrt{\lambda_n^2 + \alpha^2} \quad (5.1.51d) \quad ; \lambda_n = \frac{\mu_n}{b} \quad (5.1.54e)$$

$$v_n = -j\omega\mu_0 K_{\theta} \frac{\int_0^a r J_1(\lambda_n r) dr}{\lambda_n b^2 J_1^2(\lambda_n b)} \quad (5.1.54f)$$

$$A_n = \frac{v_n \lambda_n}{\lambda_n \sinh(\lambda_n D) \sinh(k_n L) + k_n \cosh(\lambda_n D) \cosh(k_n L)} \quad (5.1.54g)$$

$$B_n = \frac{A_n}{2\lambda_n} \exp(\lambda_n L) [\lambda_n \sinh(k_n L) - k_n \cosh(k_n L)] \quad (5.1.54h)$$

$$C_n = \frac{A_n}{2\lambda_n} \exp(-\lambda_n L) [\lambda_n \sinh(k_n L) + k_n \cosh(k_n L)] \quad (5.1.54i)$$

A MATLAB code for solving the analytical H mode fields (equation set (5.1.54)) can be found in Appendix C.

## 5.2. Numerical H mode fields

The numerical H mode fields are solved using Eqs. (5.1.7-5.1.9) with the finite difference method (Sadiku, 2009; Zhou, 1993; Salon & Chari, 2000). One of the advantages of solving the fields numerically is the ability to input spatially resolved ( $-r$  and  $-z$  varying) plasma parameters such as electron density,  $n_e(r, z)$ , electron temperature,  $T_e(r, z)$  and neutral gas temperature,  $T_n(r, z)$  which will give a better theoretical visualization of the electromagnetic fields in the laboratory reactor. The actual chamber dimensions can also be straightforwardly modeled by this method.

In the finite difference method, the plasma chamber is divided into a 2 dimensional grid of equally spaced cells with a radial spacing,  $\Delta r$  and axial spacing,  $\Delta z$ .  $\Delta r$  and  $\Delta z$  are chosen to be small enough such that,

$$\frac{E_{\theta, n+1, m} - E_{\theta, n-1, m}}{2\Delta r} \approx \frac{\partial E_\theta}{\partial r}, \quad (5.2.1)$$

$$\frac{E_{\theta, n+1, m} - 2E_{\theta, n, m} + E_{\theta, n-1, m}}{(\Delta r)^2} \approx \frac{\partial^2 E_\theta}{\partial r^2}, \quad (5.2.2)$$

$$\frac{E_{\theta,n,m+1} - E_{\theta,n,m-1}}{2\Delta z} \approx \frac{\partial E_{\theta}}{\partial z} , \quad (5.2.3)$$

and

$$\frac{E_{\theta,n,m+1} - 2E_{\theta,n,m} + E_{\theta,n,m-1}}{(\Delta z)^2} \approx \frac{\partial^2 E_{\theta}}{\partial z^2} . \quad (5.2.4)$$

Here, the  $n$  and  $m$  subscripts represent the radial and axial positions of the calculated field points on the grid. Rewriting Eqs. (5.1.7-5.1.9) in finite difference notation, we get,

$$\begin{aligned} \frac{1}{r_{n,m}} \frac{E_{\theta,n+1,m} - E_{\theta,n,m-1}}{2\Delta r} + \frac{E_{\theta,n+1,m} - 2E_{\theta,n,m} + E_{\theta,n-1,m}}{(\Delta r)^2} - \frac{E_{\theta,n,m}}{r_{n,m}^2} \\ + \frac{E_{\theta,n,m+1} - 2E_{\theta,n,m} + E_{\theta,n,m-1}}{(\Delta z)^2} = \alpha_{n,m}^2(r, z) E_{\theta,n,m} , \end{aligned} \quad (5.2.5)$$

$$B_{r,n,m} = -\frac{j}{\omega} \frac{E_{\theta,n,m+1} - E_{\theta,n,m-1}}{2\Delta z} , \quad (5.2.6)$$

and

$$B_{z,n,m} = \frac{j}{\omega} \frac{1}{r_{n,m}} \left( \frac{r_{n+1,m} E_{\theta,n+1,m} - r_{n-1,m} E_{\theta,n-1,m}}{2\Delta r} \right) . \quad (5.2.7)$$

$\alpha_{n,m}^2(r, z)$  represents the radially and axially resolved spatial conductivity parameter for the grid position  $(n, m)$ . To avoid singularity for Eqs. (5.2.5) and (5.2.7) as  $r$  approaches zero, i.e.,  $r \rightarrow 0$ , L'Hôpital's rule was applied to Eqs. (5.1.7) and (5.1.9) for calculations at  $r = 0$ , yielding the reduced finite difference solutions,

$$\frac{3}{2} \left( \frac{E_{\theta,n+1,m} - 2E_{\theta,n,m} + E_{\theta,n-1,m}}{(\Delta r)^2} \right) \quad (5.2.8)$$

$$+ \frac{E_{\theta,n,m+1} - 2E_{\theta,n,m} + E_{\theta,n,m-1}}{(\Delta z)^2} = \alpha_{n,m}^2(r, z) E_{\theta,n,m} \ ,$$

and

$$B_{z,n,m} = \frac{2j}{\omega} \left( \frac{E_{\theta,n+1,m} - 2E_{\theta,n,m} + E_{\theta,n-1,m}}{(\Delta r)^2} \right) . \quad (5.2.9)$$

In a spatially resolved form, the spatial conductivity parameter is represented by a spatially varying electron density,  $n_e(r, z)$  and effective collision frequency,  $\nu_{\text{eff}}(r, z)$  i.e.,

$$\alpha^2(r, z) = \frac{\mu_0 n_e(r, z) e^2}{m_e [1 - j\nu_{\text{eff}}(r, z)/\omega]} . \quad (5.2.10)$$

### 5.2.1 Calculation of Effective Collision Frequency, $\nu_{\text{eff}}(r, z)$

The effective electron collision frequency,  $\nu_{\text{eff}}(r, z)$  consists of the sum of most frequent particle collisions occurring in the plasma. For the present setup, the sum of the three largest collision frequencies were used to estimate  $\nu_{\text{eff}}(r, z)$ , i.e., the electron neutral collision frequency,  $\nu_{\text{en}}$ , electron ion collision frequency,  $\nu_{\text{ei}}$ , and stochastic collision frequency,  $\nu_{\text{st}}$  (Gudmundsson & Lieberman, 1998; Maurice, 2003, pp. 74-75).  $\nu_{\text{eff}}(r, z)$  is thus, denoted as,

$$\nu_{\text{eff}}(r, z) = \nu_{\text{en}} + \nu_{\text{ei}} + \nu_{\text{st}} \quad (5.2.11)$$

The electron-neutral collision frequency,  $\nu_{\text{en}}$  is obtained from the integral between the argon atom collision frequency and EEDF, i.e. (Lister, Li & Godyak, 1996),

$$\nu_{\text{en}} + j\omega_{\text{eff}} = -\frac{3}{2} \left[ \int_0^{\infty} \frac{\varepsilon^{3/2}}{\nu_c(\varepsilon) + j\omega} \frac{df(\varepsilon)}{d\varepsilon} d\varepsilon \right]^{-1}, \quad (5.2.12)$$

with  $\varepsilon$  being the electron energy in J,  $\omega_{\text{eff}}$  being the effective drive frequency in Hz,  $\nu_c(\varepsilon)$  is the collision frequency term for argon gas and  $f(\varepsilon)$  is the EEDF. For simplicity of calculation, a Maxwellian EEDF is used and is defined as,

$$f(\varepsilon) = \frac{2}{\sqrt{\pi}} \frac{1}{(eT_e(r, z))^{3/2}} \exp\left[-\frac{\varepsilon}{T_e(r, z)}\right] \quad (5.2.13)$$

where,  $T_e(r, z)$  is the electron temperature in eV. The collision frequency term,  $\nu_c(\varepsilon)$  of argon gas is given by,

$$\nu_c(\varepsilon) = n_g(r, z) \sigma_c(\varepsilon) \sqrt{\frac{2e\varepsilon}{m_e}} \quad (5.2.14)$$

Here,  $n_g(r, z)$  is the neutral gas density of the plasma in  $\text{m}^{-3}$  and  $\sigma_c(\varepsilon)$  is the collision cross section of argon gas in  $\text{m}^2$  taken from Hayashi (1981); Appendix E, Table E.1.  $n_g(r, z)$  for this model is deduced from the ideal gas law,

$$n_g(r, z) = (P - p_e - p_i) / k_B T_n(r, z) \approx P / k_B T_n(r, z). \quad (5.2.15)$$

$P$ ,  $p_i$  and  $p_e$  are the argon filling pressure, ion pressure and electron pressure, respectively in Pa,  $k_B$  is the Boltzmann constant in  $\text{JK}^{-1}$  and  $T_n(r, z)$  is the neutral gas

temperature in K.  $p_i$  and  $p_e$  have negligible effects at our range of interest ( $P \gg p_{i,e}$ ) and  $n_g(r, z)$  can be directly calculated from  $P$ .

The electron-ion collision frequency,  $\nu_{ei}$  is calculated using the Coulomb logarithm and is expressed as (Gudmundsson & Lieberman, 1998),

$$\nu_{ei} = \frac{n_e(r, z)e^4 \ln \Lambda}{4\pi\epsilon_0^2 m_e^{1/2} (eT_e(r, z))^{3/2}}, \quad (5.2.16)$$

with the Coulomb logarithm as defined in Chapter 3, Section 3.1.2, Eq. (3.1.7).

To account for the anomalous skin effect of the spatially inhomogeneous r.f. field, the stochastic collision frequency,  $\nu_{st}$  is included.  $\nu_{st}$  is derived from the average thermal velocity of the electrons and the anomalous skin depth of the r.f. fields and is expressed as (Vahedi et al., 1995),

$$\nu_{st} \approx \frac{1}{4} \frac{\bar{v}_e}{\delta}, \quad (5.2.17)$$

$\bar{v}_e$  denotes the average electron velocity, which in the Maxwellian case is,

$$\bar{v}_e = \left( \frac{8eT_e(r, z)}{\pi m_e} \right)^{1/2}, \quad (5.2.18)$$

in  $\text{ms}^{-1}$ .  $\delta$  is the anomalous skin depth approximated by,

$$\delta = \left( \frac{c}{\omega_p(r, z)} \right) \left( \frac{\bar{\nu}_e \omega_p(r, z)}{2c\omega} \right)^{1/3}, \quad (5.2.19)$$

with  $\omega_p(r, z)$  being the plasma angular frequency given in Eq. (5.0.12) calculated with the spatially varying electron density,  $n_e(r, z)$ . In the case of the analytical H mode fields,  $\nu (= \nu_{\text{eff}})$  is calculated using the measured spatially averaged values of  $n_e$ ,  $T_e$  and  $T_n$ .

### 5.2.2. Five Point Stencil Algorithm

The spatially varying H mode electromagnetic fields were solved using a 5 point stencil algorithm (Sadiku, 2009, p. 123) with  $\Delta r$  and  $\Delta z$  equally spaced at 0.001 m. In a 5 point stencil, the adjacent field values of grid position  $(m, n + 1)$ ,  $(m, n - 1)$ ,  $(m + 1, n)$  and  $(m - 1, n)$  are required to calculate a new updated field value for grid position  $(m, n)$  which will be used for the next iteration (Figure 5.3).

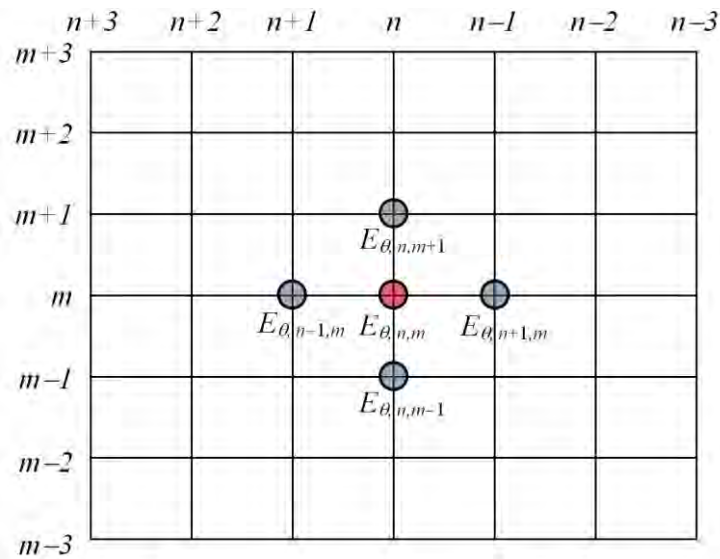


**Figure 5.3:** The five point stencil algorithm illustrated. The field values at the four adjacent (blue) grid points are used to calculate the new field value for the center (red) grid point.

This cycle of calculations are repeated until the field values remain unchanged between successive iterations within an acceptable magnitude of error, i.e. convergence. The calculations are bounded within the chamber dimensions using the following boundary conditions:

- i. The walls of the chamber are assumed to be infinitely conducting, such that all fields at the walls are equal to zero.
- ii. The radial magnetic fields at the coil surface ( $L + D$ ) for the coil radius of  $-a \leq r \leq a$  is constant and is given by,

$$B_r = -\frac{\mu_0 K_\theta}{2} . \quad (5.2.20)$$

A flowchart of the program algorithm is shown in Figure 5.4.

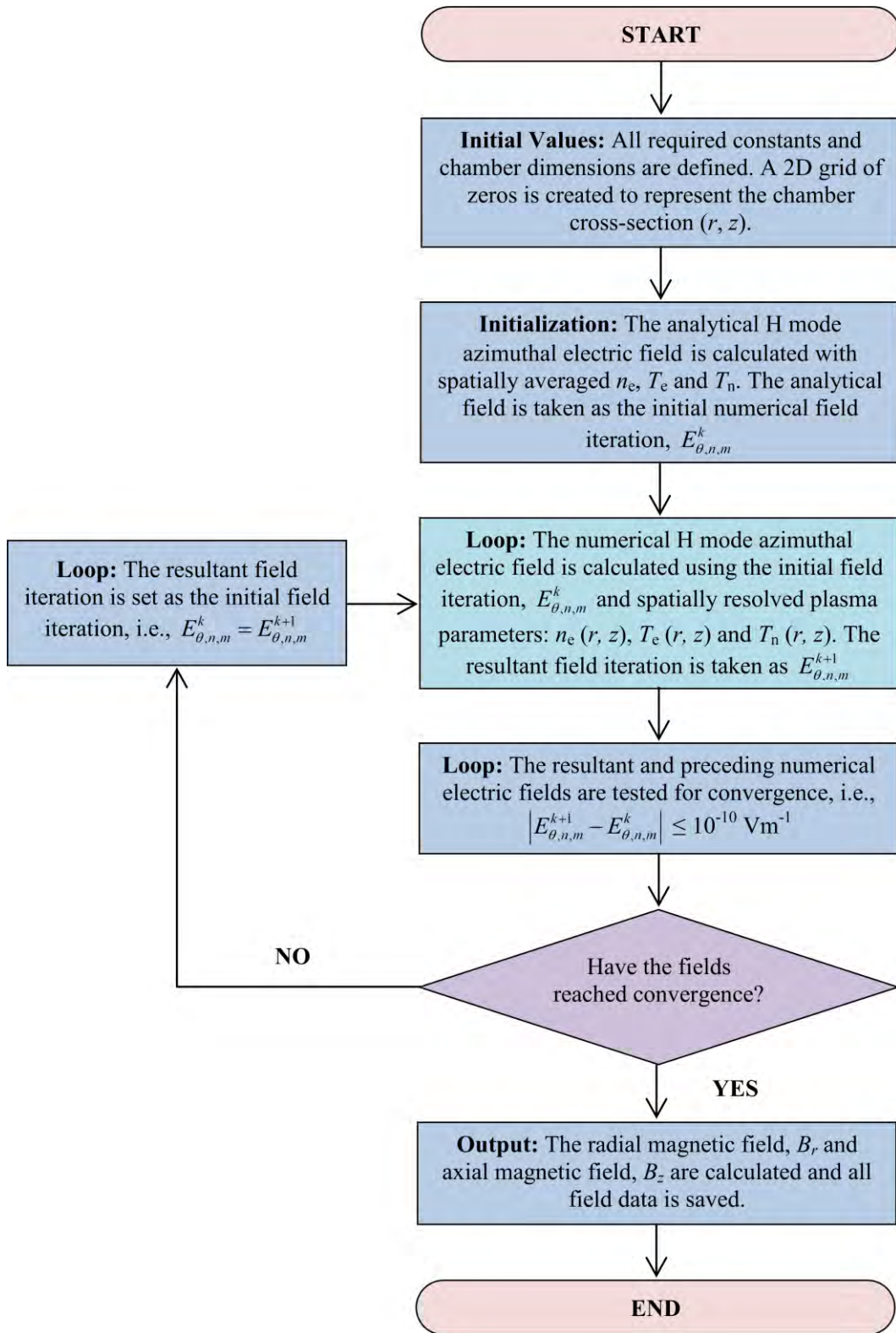


**Figure 5.4:** Program flowchart for the numerical H mode fields.

The initial field values used to start the simulation was calculated from the analytical H mode solutions in the equation set (5.1.54) using spatially averaged  $n_e$ ,  $T_e$  and  $T_n$  within the range of measured values. The exact values  $n_e$ ,  $T_e$  and  $T_n$  are not essential for

accuracy, however, closer estimates to expected values would yield faster convergence. The convergence point for the algorithm is set at a maximum deviation of  $10^{-10}$  T between successive iterations.

### 5.3. Analytical E mode fields

For deriving the analytical E mode fields, a similar set of assumptions and boundary conditions as the H mode fields were applied to Eqs. (5.0.7-5.0.12):

- a) The coil (at  $-a \leq r \leq a$ ) is assumed to be an infinitely thin disc with an uniform radial electric field,  $E_o$  of magnitude,

$$E_o = \frac{V_p}{a} . \quad (5.3.1)$$

where  $V_p$  is the peak coil current in V and  $a$  is the coil radius in m.

- b) The chamber is an azimuthally symmetric cylinder of radius,  $b$  and effective height,  $L$  with a coil radius of  $a$ . The coil-chamber spacing is  $D$ .
- c) The chamber (from boundaries  $-b < r < b$  and  $0 < z < L$ ) has a uniform electron density,  $n_e$ , collision frequency,  $\nu$  and electron temperature,  $T_e$ . Externally, these parameters are equal to zero.
- d) At the boundaries between the chamber walls and the plasma, the normal magnetic fields and tangential electric fields are equal to zero.

- e) At the boundaries between the quartz plate and the plasma, the normal magnetic fields and tangential electric fields are continuous.

Due to the assumption of azimuthal symmetry for the chamber, the solutions for the E mode fields would be limited to the radial and axial electric field components, i.e.,  $\mathbf{E} = [E_r, 0, E_z]$  and azimuthal magnetic field component, i.e.,  $\mathbf{B} = [0, B_\theta, 0]$ . Thus, the displacement current term  $j\varepsilon_0\mu_0\omega\mathbf{E}(r,z)$  in Eq. (5.0.9) for the E mode fields is not ignored due to the presence of a time varying electric field through the dielectric plate.

By substitution of Eq. (5.0.11) into Eq. (5.0.9), we get,

$$\nabla \times \mathbf{B}(r, z) = \frac{j\omega}{c^2} \left( 1 - \frac{\left( \omega_p^2 / \omega^2 \right)}{1 - j\nu/\omega} \right) \mathbf{E}(r, z), \quad (5.3.2)$$

in which the term  $1 - \left( \omega_p^2 / \omega^2 \right) / (1 - j\nu/\omega)$  represents the permittivity of the plasma medium,  $\varepsilon_p$ . Eq. (5.3.2) can be thus, simplified as,

$$\nabla \times \mathbf{B}(r, z) = \frac{j\omega}{c^2} \varepsilon_p \mathbf{E}(r, z), \quad (5.3.3)$$

where,  $c (= \sqrt{1/\mu_0\varepsilon_0})$  is the speed of light in  $\text{ms}^{-1}$ .

For the E mode fields inside the dielectric quartz plate ( $L < z \leq L + D$ ) the plasma permittivity term,  $\varepsilon_p$  in Eq. (5.3.3) is replaced by the dielectric constant,  $\varepsilon_r$ . This yields a field equation set for two boundaries, i.e.,

$$\nabla \times \mathbf{B}(r, z) = \begin{cases} \frac{j\omega}{c^2} \varepsilon_p \mathbf{E}(r, z) & 0 \leq z \leq L \\ \frac{j\omega}{c^2} \varepsilon_r \mathbf{E}(r, z) & L < z \leq L + D \end{cases} \quad (5.3.4)$$

For the quartz plate used in the laboratory reactor, the dielectric constant,  $\varepsilon_r = 3.8$ . Next, by taking the curl of the equation set (5.3.4) and substituting the field Eq. (5.0.7), we obtain the simplified single term magnetic field expressions,

$$\nabla \times \nabla \times \mathbf{B}(r, z) = \begin{cases} \varepsilon_p \frac{\omega^2}{c^2} \mathbf{B}(r, z) & 0 \leq z \leq L \\ \varepsilon_r \frac{\omega^2}{c^2} \mathbf{B}(r, z) & L < z \leq L + D \end{cases} \quad (5.3.5)$$

For solving Eqs. (5.3.4) and (5.3.5) for only the electromagnetic field components and taking into account the assumption of azimuthal symmetry (boundary condition b)), we subsequently arrive at the following set of scalar equations:

$$\frac{1}{r} \frac{\partial}{\partial r} \left( r \frac{\partial B_\theta}{\partial r} \right) - \frac{B_\theta}{r^2} + \frac{\partial^2 B_\theta}{\partial z^2} = -\varepsilon_p \left( \frac{\omega}{c} \right)^2 B_\theta, \quad (5.3.6)$$

$$E_r = \frac{jc^2}{\omega \varepsilon_p} \frac{\partial B_\theta}{\partial z}, \quad (5.3.7)$$

and

$$E_z = -\frac{jc^2}{\omega \varepsilon_p} \frac{1}{r} \left( \frac{\partial(rB_\theta)}{\partial r} \right). \quad (5.3.8)$$

for  $0 \leq z \leq L$ ;

$$\frac{1}{r} \frac{\partial}{\partial r} \left( r \frac{\partial B_\theta}{\partial r} \right) - \frac{B_\theta}{r^2} + \frac{\partial^2 B_\theta}{\partial z^2} = -\epsilon_r \left( \frac{\omega}{c} \right)^2 B_\theta, \quad (5.3.9)$$

$$E_r = \frac{jc^2}{\omega\epsilon_r} \frac{\partial B_\theta}{\partial z}, \quad (5.3.10)$$

and

$$E_z = -\frac{jc^2}{\omega\epsilon_r} \frac{1}{r} \left( \frac{\partial(rB_\theta)}{\partial r} \right). \quad (5.3.11)$$

for  $L < z \leq L + D$ .

### 5.3.1. Separation of Variables Method for the E mode Fields

As with the H mode fields in Section 5.1.1, the separation of variables method is used to solve field Eqs. (5.3.6-5.3.11). The boundary conditions a)-e) in Section 5.3 would yield the following relations for the component E mode fields:

- i. At the plane of the coil ( $z = L + D$ ), the radial electric field is given by,

$$E_r = \begin{cases} E_o = \frac{V_p}{a} & 0 \leq r \leq a \\ 0 & a < r \leq b \end{cases} \quad (5.3.12)$$

- ii. The tangential electric field and normal magnetic field between the quartz plate and plasma would be continuous, thus,

$$E_r(r, L_+) = E_r(r, L_-) , \quad (5.3.13)$$

iii. At the chamber boundaries, applying boundary condition d), we get,

$$E_z(b, z) = 0 , \quad (5.3.14)$$

and

$$E_r(r, 0) = 0 . \quad (5.3.15)$$

For the axial electric field at the boundary between the plasma and the dielectric plate,  $E_z(r, L)$ , an additional relationship,

$$\varepsilon_p E_z(r, L_+) = \varepsilon_r E_z(r, L_-) , \quad (5.3.16)$$

is also introduced. The electric fields  $E_z(r, L_+)$  and  $E_z(r, L_-)$  given in Eq. (5.3.16) are discontinuous. This accounts for the abrupt change between media (plasma-dielectric plate) of the traversing electric fields.

Solving for the E mode fields with the same steps shown in Section 5.1.1, we get,

$$B_\theta(r, z) = \begin{cases} D \cosh(qz) J_1(\lambda r) & 0 \leq z \leq L \\ [E \exp(sz) + F \exp(-sz)] J_1(\lambda r) & L < z \leq L + D \end{cases} \quad (5.3.17)$$

$$E_r(r, z) = \begin{cases} \frac{jc^2}{\omega \varepsilon_p} q D \sinh(qz) J_1(\lambda r) & 0 \leq z \leq L \\ \frac{jc^2}{\omega \varepsilon_r} s [E \exp(sz) - F \exp(-sz)] J_1(\lambda r) & L < z \leq L + D \end{cases} \quad (5.3.18)$$

and

$$E_r(r, z) = \begin{cases} \frac{-jc^2}{\omega\epsilon_p} \lambda D \cosh(qz) J_0(\lambda r) & 0 \leq z \leq L \\ \frac{-jc^2}{\omega\epsilon_r} \lambda [E \exp(sz) + F \exp(-sz)] J_0(\lambda r) & L < z \leq L + D \end{cases} \quad (5.3.19)$$

Here,  $\lambda$ ,  $q$  and  $s$  are the separation constants related by,

$$q^2 = \lambda^2 - \epsilon_p \left( \frac{\omega}{c} \right)^2, \quad (5.3.20)$$

and

$$s^2 = \lambda^2 - \epsilon_r \left( \frac{\omega}{c} \right)^2. \quad (5.3.21)$$

$D$ ,  $E$  and  $F$  are constants to be defined.

If applying the boundary condition for the radial walls of the chamber (Eq. (5.3.14)) to Eqs. (5.3.17-5.3.21), i.e.,  $E_z(b, z) = 0$ , a valid solution can only be obtained if  $J_0(\lambda b) = 0$ . Thus, it can be deduced that the separation constant,  $\lambda$  would be a solution set consisting of the ratios of the eigen Bessel function roots,  $\mu_n$  and the chamber radius, i.e.,

$$\lambda_n = \frac{\mu_n}{b}. \quad (5.3.22)$$

Rewriting Eqs. (5.3.17-5.3.19) as a sum of the set of orthogonal eigen functions with the deduction given in Eq. (5.3.22), we subsequently get,

$$B_{\theta}(r, z) = \begin{cases} \sum_{n=1}^{\infty} D_n \cosh(q_n z) J_1(\lambda_n r) & 0 \leq z \leq L \\ \sum_{n=1}^{\infty} [E_n \exp(s_n z) + F_n \exp(-s_n z)] J_1(\lambda_n r) & L < z \leq L + D \end{cases} \quad (5.3.23)$$

$$E_r(r, z) = \begin{cases} \frac{j c^2}{\omega \varepsilon_p} \sum_{n=1}^{\infty} q_n D_n \sinh(q_n z) J_1(\lambda_n r) & 0 \leq z \leq L \\ \frac{j c^2}{\omega \varepsilon_r} \sum_{n=1}^{\infty} s_n [E_n \exp(s_n z) - F_n \exp(-s_n z)] J_1(\lambda_n r) & L < z \leq L + D \end{cases} \quad (5.3.24)$$

and

$$E_z(r, z) = \begin{cases} \frac{-j c^2}{\omega \varepsilon_p} \sum_{n=1}^{\infty} \lambda_n D_n \cosh(q_n z) J_0(\lambda_n r) & 0 \leq z \leq L \\ \frac{-j c^2}{\omega \varepsilon_r} \sum_{n=1}^{\infty} \lambda_n [E_n \exp(s_n z) + F_n \exp(-s_n z)] J_0(\lambda_n r) & L < z \leq L + D \end{cases} \quad (5.3.25)$$

with,

$$q_n^2 = \lambda_n^2 - \varepsilon_p \left( \frac{\omega}{c} \right)^2 \quad (5.3.26)$$

and

$$s_n^2 = \lambda_n^2 - \varepsilon_r \left( \frac{\omega}{c} \right)^2 . \quad (5.3.27)$$

### 5.3.2. Solving for E mode Boundary Constants

The expressions for the solution of boundary constants  $D_n$ ,  $E_n$  and  $F_n$  are determined by taking the field relationships given in Eqs. (5.3.13) and (5.3.16), i.e.,

$$D_n \cosh(q_n L) = E_n \exp(s_n L) + F_n \exp(-s_n L) \quad (5.3.28)$$

and

$$\varepsilon_r q_n D_n \sinh(q_n L) = \varepsilon_p s_n [E_n \exp(s_n L) - F_n \exp(-s_n L)] . \quad (5.3.29)$$

For the convenience of solving  $D_n$ ,  $E_n$  and  $F_n$  using simultaneous equations, an additional constant,  $u_n$  is introduced:

$$u_n = E_n \exp(s_n (L + D)) - F_n \exp(-s_n (L + D)) . \quad (5.3.30)$$

With subsequent replacement in Eqs. (5.3.28) and (5.3.29), yield the solutions,

$$D_n = \frac{u_n \varepsilon_p s_n}{\varepsilon_p s_n \cosh(q_n L) \sinh(s_n D) + \varepsilon_r q_n \sinh(q_n L) \cosh(s_n D)} , \quad (5.3.31)$$

$$E_n = \frac{D_n}{2\varepsilon_p s_n} \exp(-s_n L) [\varepsilon_p s_n \cosh(q_n L) + \varepsilon_r q_n \sinh(q_n L)] , \quad (5.3.32)$$

and

$$F_n = \frac{D_n}{2\varepsilon_p s_n} \exp(s_n L) [\varepsilon_p s_n \cosh(q_n L) - \varepsilon_r q_n \sinh(q_n L)] \quad (5.3.33)$$

At the plane of the coil ( $L + D$ ), the radial electric field,  $E_r(r, L + D)$  can be expressed in terms of  $u_n$  as,

$$E_r(r, L + D) = \frac{j\omega c^2}{\omega \varepsilon_r} \sum_{n=1}^{\infty} s_n u_n J_1(\lambda_n r) \quad (5.3.34)$$

Applying the boundary conditions given by the piecewise continuous Eq. (5.3.12) from the chamber center to the coil radius,  $a$  and chamber radius,  $b$ , to Eq. (5.3.34), we get,

$$\frac{j\omega c^2}{\omega \varepsilon_r} \sum_{n=1}^{\infty} s_n u_n J_1(\lambda_n r) = \begin{cases} E_0 & 0 \leq r \leq a \\ 0 & a < r \leq b \end{cases} \quad (5.3.35)$$

To obtain a calculable expression for  $u_n$ , Eq. (5.3.35) is first multiplied with  $r$  and differentiated. This yields the following equation,

$$\frac{j\omega c^2}{\omega \varepsilon_r} \sum_{n=1}^{\infty} s_n u_n \lambda_n r J_0(\lambda_n r) = \begin{cases} E_0 & 0 \leq r \leq a \\ 0 & a < r \leq b \end{cases} \quad (5.3.36)$$

Next, by multiplying both sides of the equation with  $J_0(\lambda_n r)$  and integrating across the chamber radius  $0 \leq r \leq b$  (with the orthogonal properties Sturm-Liouville problem), we eventually get,

$$\frac{j c^2 s_n u_n \lambda_n}{\omega \varepsilon_r} \int_0^b r J_0^2(\lambda_n r) dr = E_o \int_0^a J_0(\lambda_n r) dr \quad , \quad (5.3.37)$$

which can be rewritten as,

$$u_n = - \frac{j \omega \varepsilon_r E_o \int_0^a J_0(\lambda_n r) dr}{c^2 s_n \lambda_n \int_0^b r J_0^2(\lambda_n r) dr} \quad . \quad (5.3.38)$$

Eq. (5.3.38) can be further simplified with Bessel function identity given in Eq. (5.1.52), yielding,

$$u_n = - \frac{2 j \omega \varepsilon_r E_o \int_0^a J_0(\lambda_n r) dr}{b^2 c^2 s_n \lambda_n J_1^2(\lambda_n b)} \quad . \quad (5.3.39)$$

The analytical solutions and corresponding derived constants for the E mode fields for the ICP chamber (height,  $L$ ; radius,  $b$ ; coil radius,  $a$  and the coil-chamber distance,  $D$ ) can be summarized as the following equation set:

$$B_\theta(r, z) = \begin{cases} \sum_{n=1}^{\infty} D_n \cosh(q_n z) J_1(\lambda_n r) & 0 \leq z \leq L \\ \sum_{n=1}^{\infty} [E_n \exp(s_n z) + F_n \exp(-s_n z)] J_1(\lambda_n r) & L < z \leq L + D \end{cases} \quad (5.3.40a)$$

$$E_r(r, z) = \begin{cases} \frac{jc^2}{\omega\epsilon_p} \sum_{n=1}^{\infty} D_n q_n \sinh(q_n z) J_1(\lambda_n r) & 0 \leq z \leq L \\ \frac{jc^2}{\omega\epsilon_r} \sum_{n=1}^{\infty} [E_n \exp(s_n z) - F_n \exp(-s_n z)] s_n J_1(\lambda_n r) & L < z \leq L + D \end{cases} \quad (5.3.40b)$$

$$E_z(r, z) = \begin{cases} -\frac{jc^2}{\omega\epsilon_p} \sum_{n=1}^{\infty} D_n \lambda_n \cosh(q_n z) J_0(\lambda_n r) & 0 \leq z \leq L \\ -\frac{jc^2}{\omega\epsilon_r} \sum_{n=1}^{\infty} [E_n \exp(s_n z) + F_n \exp(-s_n z)] \lambda_n J_0(\lambda_n r) & L < z \leq L + D \end{cases} \quad (5.3.40c)$$

$$q_n^2 = \lambda_n^2 - \epsilon_p \left( \frac{\omega}{c} \right)^2 \quad (5.3.40d) \quad ; \quad s_n^2 = \lambda_n^2 - \epsilon_r \left( \frac{\omega}{c} \right)^2 \quad (5.3.40e)$$

$$\lambda_n = \frac{\mu_n}{b} \quad (5.3.40f)$$

$$u_n = -\frac{2j\omega\epsilon_r E_0 \int_0^a J_0(\lambda_n r) dr}{b^2 c^2 s_n \lambda_n J_1^2(\lambda_n b)} \quad (5.3.40g)$$

$$D_n = \frac{u_n \epsilon_p s_n}{\epsilon_p s_n \cosh(q_n L) \sinh(s_n D) + \epsilon_r q_n \sinh(q_n L) \cosh(s_n D)} \quad (5.3.40h)$$

$$E_n = \frac{D_n}{2\epsilon_p s_n} \exp(-s_n L) [\epsilon_p s_n \cosh(q_n L) + \epsilon_r q_n \sinh(q_n L)] \quad (5.3.40i)$$

$$F_n = \frac{D_n}{2\epsilon_p s_n} \exp(s_n L) [\epsilon_p s_n \cosh(q_n L) - \epsilon_r q_n \sinh(q_n L)] \quad (5.3.40j)$$

## 5.4. Power Balance Model

The power balance model simulates the operating conditions of the ICP system (as observed in experiments) as the function of input power, coil current and electron density. The power balance model enables better understanding of the effects of input parameters on plasma characteristics including the prediction of transition points between the E and H modes of the plasma and the hysteresis effect in mode transition. In a low temperature discharge, the stability of an operating condition is theorized to be the points of equilibrium between the total absorbed electron power,  $P_{\text{abs}}$  and the electron power loss,  $P_{\text{loss}}$  (Cunge et al., 1999; El-Fayoumi, Jones & Turner, 1998; Turner & Lieberman, 1999); with both being non-linear functions of electron density.

### 5.4.1. Absorbed Electron Power, $P_{\text{abs}}$

The total absorbed electron power,  $P_{\text{abs}}$  is defined as the sum of the component powers that contribute to the generation and heating of plasma electrons. In this model, the H mode field power,  $P_{\text{h}}$ , the E mode field power,  $P_{\text{e}}$  and power from stochastic heating of plasma capacitive sheath,  $P_{\text{stoc}}$  is considered for  $P_{\text{abs}}$  (El-Fayoumi, Jones & Turner, 1998), i.e.,

$$P_{\text{abs}} = P_{\text{h}} + P_{\text{e}} + P_{\text{stoc}} \quad . \quad (5.4.1)$$

To calculate the absorbed power contributions from the H mode ( $P_{\text{h}}$ ) and E mode ( $P_{\text{e}}$ ) fields, the time-averaged Poynting vector,  $\mathcal{P}_{\text{ave}}$ , given by (Sadiku, 2001, p. 438),

$$\mathcal{P}_{\text{ave}} = 1/2\mu_0 \text{Re} (\mathbf{E} \times \mathbf{B}^*) \quad , \quad (5.4.2)$$

is integrated over the induction coil area,  $d\mathbf{S} = 2\pi r(-\hat{z})dr$  at the coil surface,  $z = L + D$ .

Here,  $\mathbf{B}^*$  and  $\hat{z}$  are the complex conjugate of the magnetic field and the unit vector for the axial coordinate, respectively. For  $P_h$ , the derivation is as follows:

$$\begin{aligned}
P_h &= \int_{-a}^a \mathcal{P}_{\text{ave}} \cdot d\mathbf{S} \\
&= \text{Re} \left[ \frac{1}{2\mu_0} \int_0^a (\mathbf{E} \times \mathbf{B}^*) \cdot d\mathbf{S} \right] \\
&= \text{Re} \left\{ \frac{1}{2\mu_0} \int_0^a [E_\theta(r, L + D)B_r^*(r, L + D)] \hat{z} \cdot 2\pi r(-\hat{z})dr \right\}
\end{aligned} \tag{5.4.3}$$

$$P_h = \text{Re} \left\{ \frac{\pi}{\mu_0} \int_0^a r [E_\theta(r, L + D)_+ B_r^*(r, L + D)_+ - E_\theta(r, L + D)_- B_r^*(r, L + D)_-] dr \right\}$$

Recognizing that  $E_\theta(r, L + D)_- = E_\theta(r, L + D)_+$  for an infinitesimally thin disc of uniform  $K_\theta$  and by replacing the complex conjugate of the radial magnetic field,  $B_r^*$  with the boundary  $K_\theta$  relationship given in Eq. (5.1.17), the expression for  $P_h$  can be shortened to,

$$P_h = \text{Re}(-\pi K_\theta \int_0^a r E_\theta(r, L + D) dr) . \tag{5.4.4}$$

Using the steps shown in (5.4.2),  $P_e$  can be similarly derived as,

$$P_e = \text{Re} \left[ -\frac{2\pi}{\mu_0} \int_0^a r E_r(r, L + D) B_\theta^*(r, L + D) dr \right] . \tag{5.4.5}$$

Here,  $B_\theta^*$  is the complex conjugate of the azimuthal magnetic field. By replacing the radial electric field,  $E_r$  with the given boundary value,  $E_0$  in Eq. (5.3.12),  $P_e$  can be simplified to,

$$P_e = \text{Re}\left(-\frac{2\pi}{\mu_0} E_0 \int_0^a r B_\theta^*(r, L+D) dr\right) . \quad (5.4.6)$$

At lower r.f. powers (in which capacitive coupling is dominant), the plasma sheath formed near the dielectric quartz plate is large enough such that significant source power (i.e., especially that of the inductive fields) is damped from being absorbed by the plasma electrons. To simulate this sheathing effect, a simplified, time-averaged capacitive sheath thickness,  $S$  is added to the coil-chamber distance,  $D$  when calculating  $P_h$  and  $P_e$ ; making the effective distance for field power as,  $(L + D + S)$ .  $S$  is derived from Child's Law for a collisionless capacitive sheath which is shown in detail by Lieberman and Lichtenberg (2005). It is expressed as:

$$S = \frac{1}{a} \int_0^a \frac{5J_s^3(r)}{12e^2\omega^3\epsilon_0 n_e^2 T_e} dr . \quad (5.4.7)$$

$J_s$  is represents the first harmonic component of current density through the sheath and is defined by,

$$J_s^2(r) \approx 1.73e\epsilon_0\omega^2 n_e (T_e V_s(r))^{1/2} , \quad (5.4.8)$$

where,  $V_s(r)$  is the first harmonic component of voltage across the plasma sheath at the coil-dielectric interface. The subsequent harmonics for the current density and voltage are not considered due to the negligible contribution in derivation. For the planar coil,

$$V_s(r) = \frac{V_p}{a} r \quad . \quad (5.4.9)$$

In addition to the power absorbed from the H mode and E mode fields, incident electrons may also be heated (via acceleration) by the fields of the oscillating capacitive plasma sheath. Power gained by the plasma electrons in this manner is known as stochastic power.  $P_{\text{stoc}}$ . For a single capacitive sheath in which the motion of oscillation is slower than the thermal velocity of the electrons,  $P_{\text{stoc}}$  is approximated by,

$$P_{\text{stoc}} \approx 0.9\pi\epsilon_0\omega^2 \left( \frac{m_e T_e}{e} \right)^{1/2} \int_0^a r V_s(r) dr \quad . \quad (5.4.10)$$

#### 5.4.2. Electron Power Loss, $P_{\text{loss}}$

Electron power loss in an ICP is primarily due to the energy dissipated for the sustenance and creation of ion-electron pairs in the discharge. In simplified derivations, this power dissipation,  $P_{\text{loss}}$  is directly proportional to the electron density,  $n_e$  (i.e.,  $P_{\text{loss}} \propto n_e$ ). However, in order to successfully simulate the operating conditions seen in a laboratory plasma system, non-linearities in the power loss curve have to be taken into consideration. For this simulation, the contribution of electron-electron collisions or Coulomb collisions is considered; with the transition from Druyvestyeyn to Maxwellian electron energy density function (EEDF) being representative of the non-linearity in the electron power loss. This equation for  $P_{\text{loss}}$  can be written as (Turner & Lieberman, 1999),

$$P_{\text{loss}} = n_e u_B A_{\text{eff}} \varepsilon_T \left( \frac{\varepsilon_{\text{cD}}}{\varepsilon_{\text{cM}}} \right)^{1/(1+C_{\text{D-M}} n_e / n_g)} \quad (5.4.11)$$

where,  $u_B$  is the Bohm velocity in  $\text{ms}^{-1}$ ; given by,

$$u_B = (eT_e / M_{\text{Ar}})^{1/2} \quad (5.4.12)$$

with,  $M_{\text{Ar}}$  being the argon ion mass in kg and  $T_e$  the electron temperature in eV.  $A_{\text{eff}}$  is the effective surface area for particle loss in the reactor in  $\text{m}^2$  and  $\varepsilon_T$  is the total energy lost per electron-ion pair created by the discharge in J. Both equations and terms required for calculation of  $A_{\text{eff}}$  and  $\varepsilon_T$  are obtained from Lieberman and Lichtenberg (2005) (pp. 81, 330-336).  $A_{\text{eff}}$  for a simple cylindrical chamber defined as,

$$A_{\text{eff}} = 2\pi b(bh_l + Lh_r) . \quad (5.4.13)$$

Here,  $h_l$  and  $h_r$  are the radial and axial plasma diffusion terms when approaching the sheath edge, i.e.,

$$h_l \approx 0.86(3 + L / 2\lambda_{\text{in}})^{-1/2} \quad (5.4.14)$$

and

$$h_r \approx 0.80(4 + b / \lambda_{\text{in}})^{-1/2} . \quad (5.4.15)$$

$L$ ,  $b$  and  $\lambda_{in}$  are the effective chamber height in m, chamber radius in m and ion-neutral mean free path (given by Chapter 3, Section 3.1.2, Eq. (3.1.4)) in m, respectively.

$\varepsilon_T$  (calculated in terms of eV) is defined the sum of the collisional energy loss per ion-electron pair,  $\varepsilon_c$ , the mean kinetic energy lost per ion,  $\varepsilon_i$  and the mean kinetic energy lost per electron,  $\varepsilon_e$ , i.e.,

$$\varepsilon_T(\text{eV}) = \varepsilon_c + \varepsilon_i + \varepsilon_e . \quad (5.4.16)$$

For argon plasma, the kinetic energy lost per ion and per electron is approximated by,  $\varepsilon_i \approx 5.2T_e$  and  $\varepsilon_e \approx 2T_e$ , respectively. The collisional energy loss per ion-electron pair,  $\varepsilon_c$ , itself comprises of the total collisional losses due to ionization, excitation and elastic scattering of electrons with neutrals. It is expressed as,

$$\varepsilon_c = \varepsilon_{iz} + \frac{K_{ex}}{K_{iz}} \varepsilon_{ex} + \frac{K_{el}}{K_{iz}} \frac{3m_e}{M_{Ar}} T_e . \quad (5.4.17)$$

Here,  $\varepsilon_{iz}$  (= 15.76 eV) is the argon ionization threshold energy and  $\varepsilon_{ex}$  (= 12.14 eV) is the argon excitation threshold energy.  $K_{iz}$ ,  $K_{ex}$  and  $K_{el}$  are the argon ionization, excitation and elastic scattering rate constants ( $\text{m}^3\text{s}^{-1}$ ) given respectively by,

$$K_{iz} = 2.34 \times 10^{-14} T_e^{0.59} \exp(-17.44/T_e) , \quad (5.4.18)$$

$$K_{ex} = 2.48 \times 10^{-14} T_e^{0.33} \exp(-12.78/T_e) , \quad (5.4.19)$$

and

$$K_{el} = 2.336 \times 10^{-14} T_e^{1.609} \exp(0.0618 \ln(T_e)^2 - 0.1171 \ln(T_e)^3) \quad . \quad (5.4.20)$$

respectively. The term  $(\varepsilon_{cD}/\varepsilon_{cM})^{1/(1 + C_{D-M} n_e/n_g)}$  in Eq. (5.4.11) accounts for the non-linear effect of transition in electron energy distribution function (EEDF) from Druyvesteyn to Maxwellian when approaching higher electron densities. The exponential factor  $C_{D-M}$ , adjusts for the experimental discrepancy (due to random and systematic errors) of the transition point between Druyvesteyn and Maxwellian EEDFs; which is concurrent with the transition of the discharge from E mode to H mode (Cunge, et al., 1999).  $n_g$  is the neutral gas density and is determined from Eq. (5.2.15).  $\varepsilon_{cD}/\varepsilon_{cM}$  is the ratio of the Druyvesteyn and Maxwellian electron-electron collision energy loss factors which is approximated as,

$$\frac{\varepsilon_{cD}}{\varepsilon_{cM}} \approx 1.27 + \frac{9.73}{T_e} \quad . \quad (5.4.21)$$

A MATLAB code for solving the power balance model can be found in Appendix D.

## CHAPTER 6: RESULTS AND DISCUSSION - SIMULATION

### 6.0. Predictive Simulation of the Discharge Magnetic Fields

The absolute magnitudes of the axial,  $|B_z|$  and radial,  $|B_r|$  magnetic fields at 0.032 m distance above the dielectric plate for 0.03, 0.07 and 0.2 mbar argon pressure were simulated using the numerical H mode model detailed in Chapter 5, Section 5.2. Initial values for the model were calculated from the analytical H mode model derived in Chapter 5, Section 5.1. The required spatially resolved electron density,  $n_e(r, z)$  and electron temperature,  $T_e(r, z)$  were empirically fitted. The spatially resolved neutral gas temperature  $T_n(r, z)$ , on the other hand, was heuristically fitted in simulation to give the closest agreement with measured fields at 0.032 m distance above the dielectric plate and at 180 W r. f. power. For comparison, the magnetic fields were also simulated using two spatially averaged neutral gas temperatures,  $T_{n,ave}$ ; one set at room temperature (300 K) and the other from AOES measurement.<sup>1</sup>

#### 6.0.1. Empirical Fitting of the Spatially Resolved Electron Density, $n_e(r, z)$ and Spatially Resolved Electron Temperature, $T_e(r, z)$

The spatially resolved electron density,  $n_e(r, z)$  and the spatially resolved electron temperature,  $T_e(r, z)$  required for Eqs. (5.2.10-5.2.13) and Eqs. (5.2.15-5.2.19) were empirically fitted from the measured Maxwellian values at 0.032, 0.060 and 0.114 m axial distance above the dielectric plate and at 0.03, 0.07 and 0.2 mbar argon pressure (Chapter 4, Figures 4.1a, 4.2a and 4.3a) using the following modified Gaussian distributions:

<sup>1</sup> Results in this section comprises of edited and revised material that has been published in Jayapalan and Chin (2014). The thesis author is the primary author and investigator for the paper.

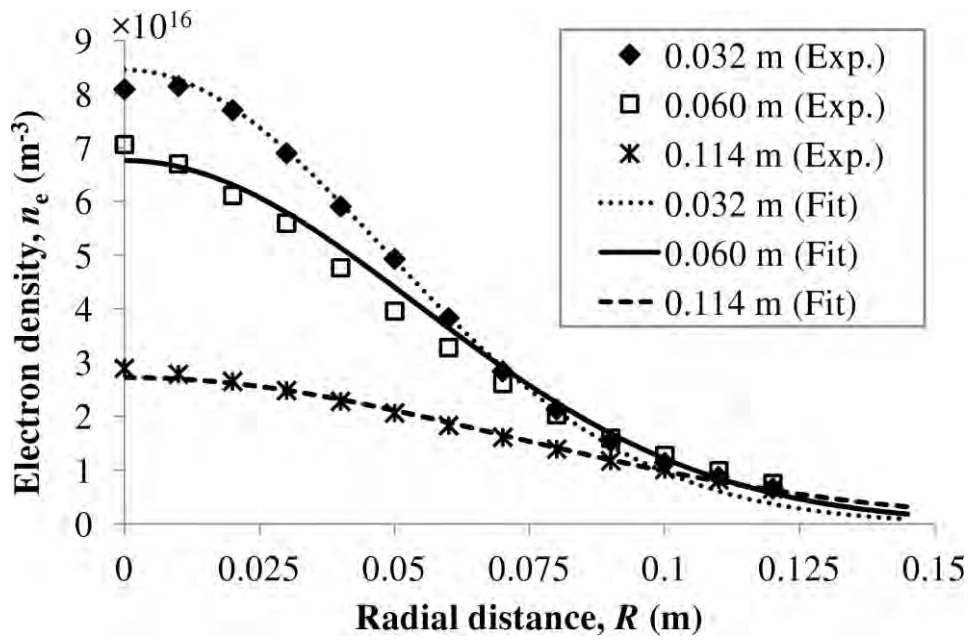
$$n_e(r, z) = n_{e, \text{peak}} \exp\left(-\left(\frac{r}{2\sigma_{r, n_e}}\right)^2 - \left(\frac{(L-z)}{2\sigma_{z, n_e}}\right)^2\right) \quad (6.0.1)$$

and

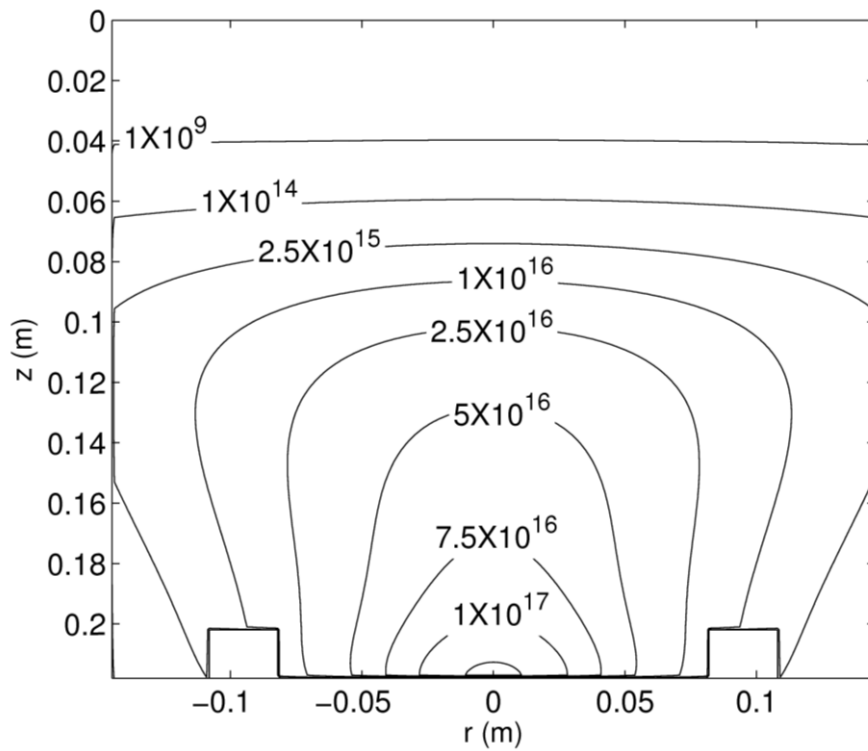
$$T_e(r, z) = T_{e, \text{peak}} \exp\left(-\left(\frac{r}{2\sigma_{r, T_e}}\right)^2 - \left(\frac{(L-z)}{2\sigma_{z, T_e}}\right)^2\right). \quad (6.0.2)$$

Here,  $n_{e, \text{peak}}$  is the fitted peak electron density in  $\text{m}^{-3}$ ,  $T_{e, \text{peak}}$  is the fitted peak electron temperature in eV,  $\sigma_{r, n_e}$  is the radial fitting parameter for electron density,  $\sigma_{z, n_e}$  is the axial fitting parameter for electron density,  $\sigma_{r, T_e}$  is the radial fitting parameter for electron temperature and  $\sigma_{z, T_e}$  is the axial fitting parameter for electron temperature.  $r$  is the radial coordinate in m,  $z$  is the axial coordinate in m and  $L$  is the effective chamber height in m. The term  $(L - z)$  denotes the distance above the dielectric plate. The values and equations for  $\sigma_{r, n_e}$ ,  $\sigma_{r, T_e}$ ,  $\sigma_{z, n_e}$  and  $\sigma_{z, T_e}$  fitted at the different argon pressures are listed in Appendix F, Tables F.1 and F.2.

The resultant (i) empirical fitment at 0.032 m, 0.060 m and 0.114 m above the dielectric plate and the corresponding spatially resolved (ii) modeled 2D contour plot are shown in Figures 6.1 for  $n_e(r, z)$  and Figure 6.2 for  $T_e(r, z)$ . The suffixes a, b and c in the figure labels (e.g., Figure 6.1a) indicate the argon pressures at 0.03, 0.07 and 0.2 mbar, respectively. The modeled 2D contour plots adequately represent the trends observed in experimental measurement; with the  $n_e(r, z)$  plots showing increased density within the coil region as pressure is increased. The  $T_e(r, z)$  plots, on the other hand, depict tapered distribution trends with higher electron temperature near the coil region and close to the dielectric plate.

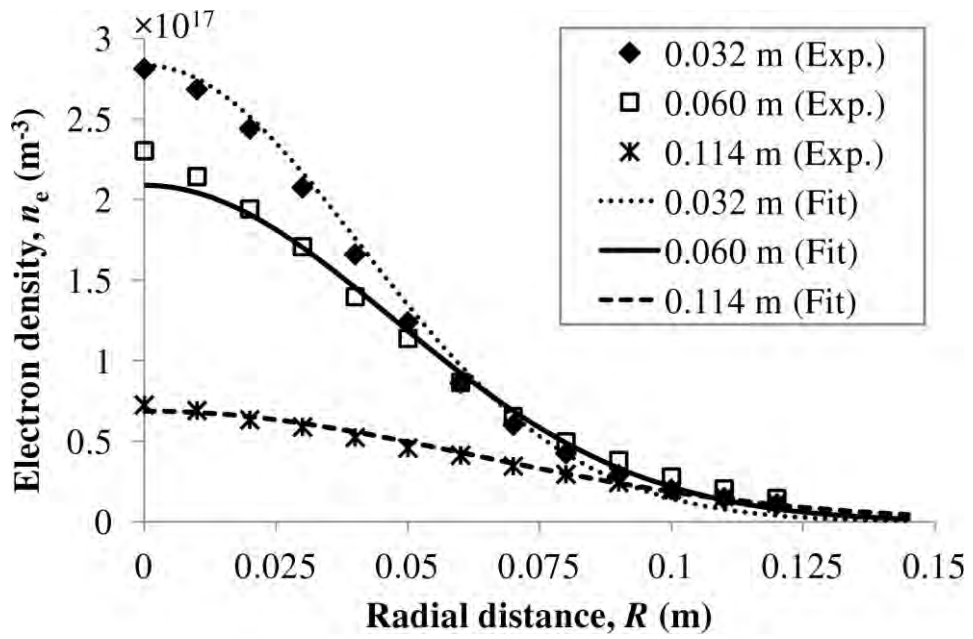


(i)

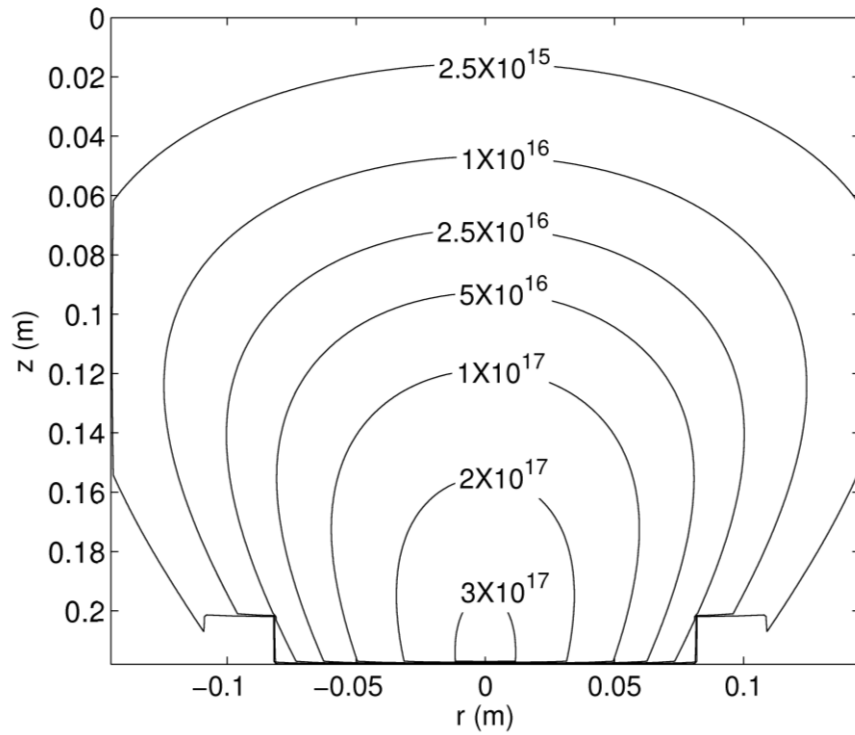


(ii)

**Figure 6.1a:** Empirically fitted 2D Gaussian based distribution of electron density  $n_e(r, z)$  used for the magnetic field simulation at 0.03 mbar argon pressure and 180 W r. f. power. (i) Fitment with measured values at 0.032 m, 0.060 m and 0.114 m distance above the dielectric plate. (ii) Modeled 2D contour plot (labels in  $\text{m}^{-3}$ ).

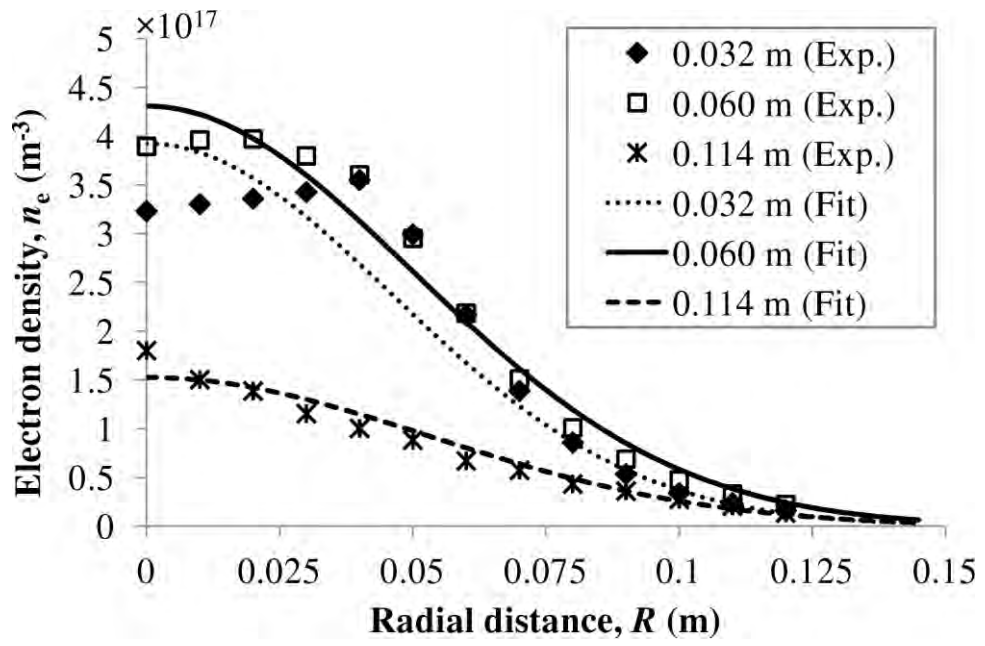


(i)

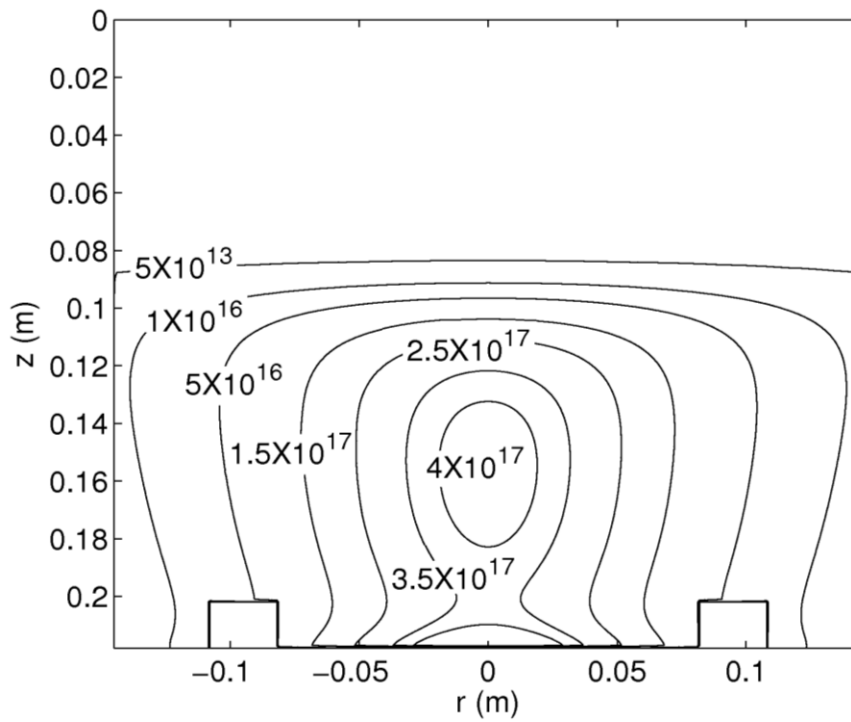


(ii)

**Figure 6.1b:** Empirically fitted 2D Gaussian based distribution of electron density  $n_e(r, z)$  used for the magnetic field simulation at 0.07 mbar argon pressure and 180 W r. f. power. (i) Fitment with measured values at 0.032 m, 0.060 m and 0.114 m distance above the dielectric plate. (ii) Modeled 2D contour plot (labels in  $\text{m}^{-3}$ ).

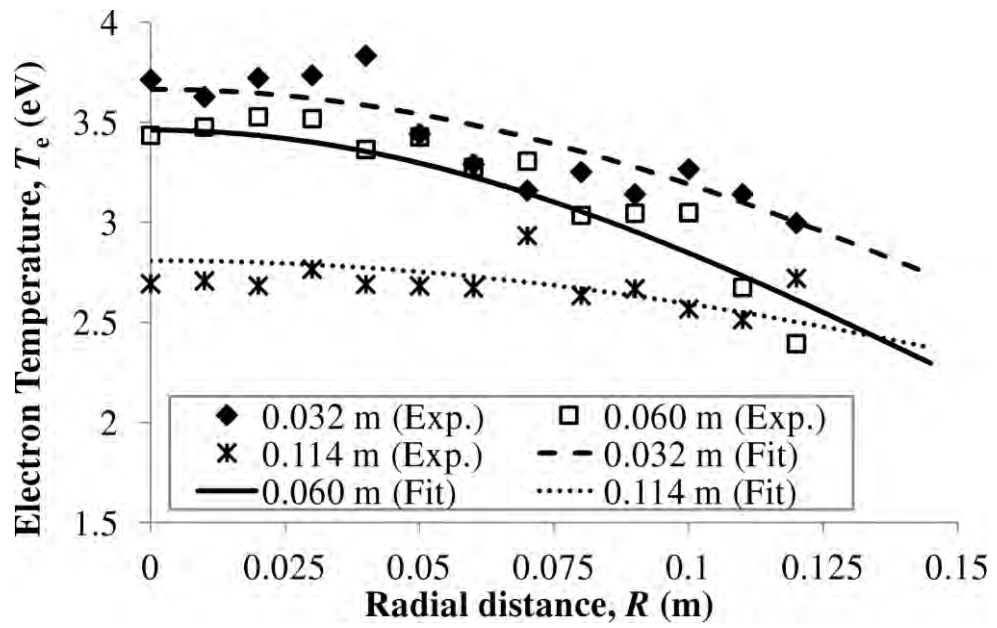


(i)

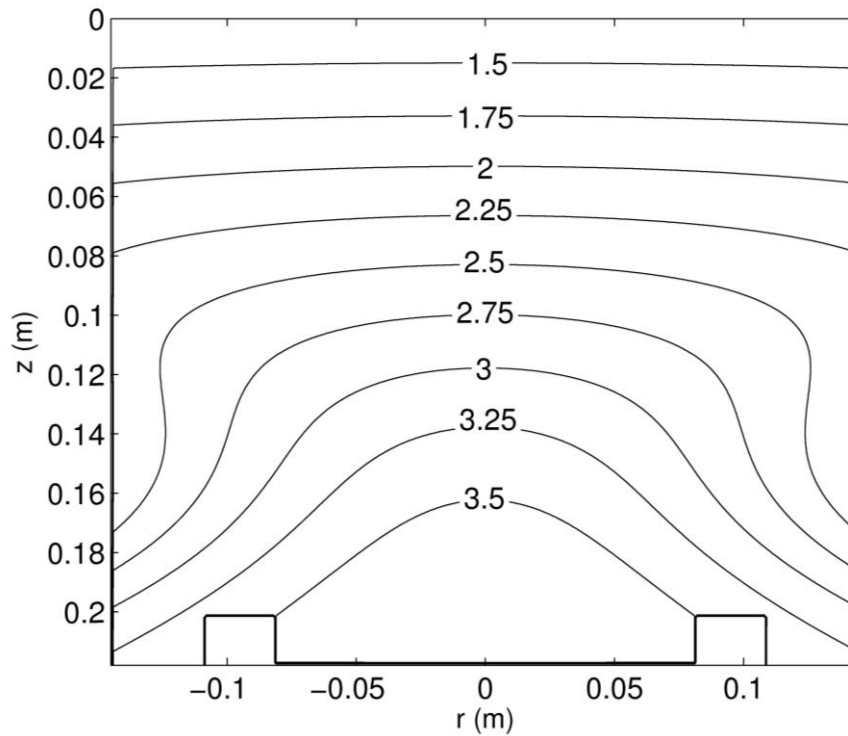


(ii)

**Figure 6.1c:** Empirically fitted 2D Gaussian based distribution of electron density  $n_e(r, z)$  used for the magnetic field simulation at 0.2 mbar argon pressure and 180 W r. f. power. (i) Fitment with measured values at 0.032 m, 0.060 m and 0.114 m distance above the dielectric plate. (ii) Modeled 2D contour plot (labels in  $\text{m}^{-3}$ ).

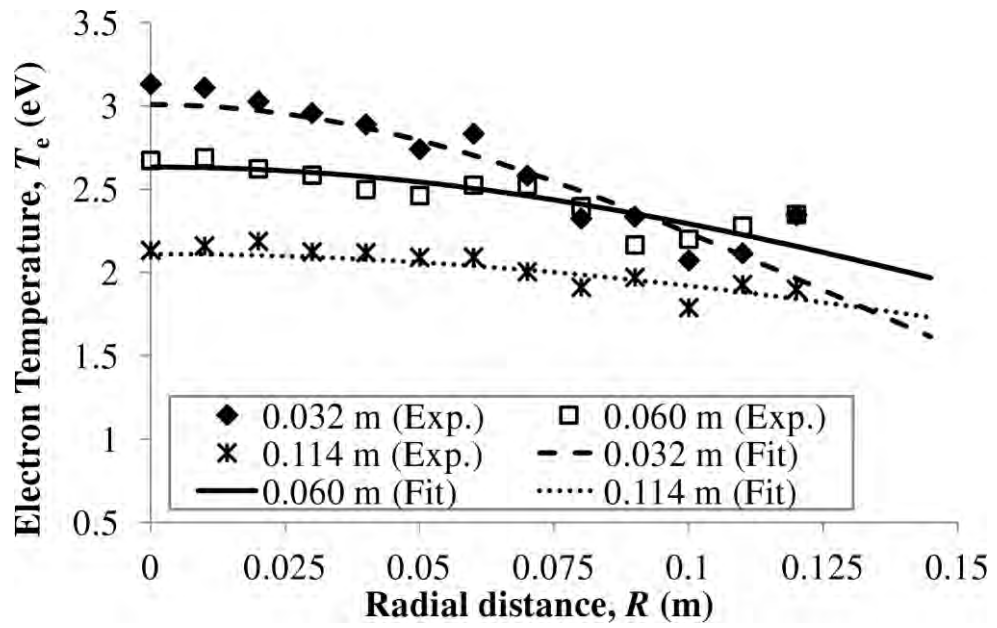


(i)

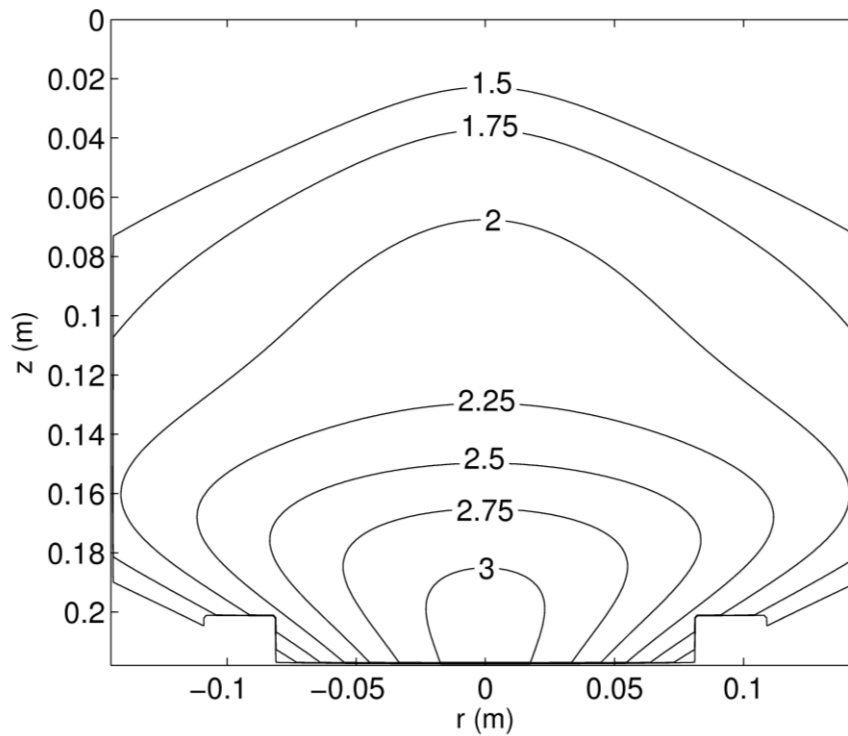


(ii)

**Figure 6.2a:** Empirically fitted 2D Gaussian based distribution of electron temperature  $T_e(r, z)$  used for the magnetic field simulation at 0.03 mbar argon pressure and 180 W r. f. power. (i) Fitment with measured values at 0.032 m, 0.060 m and 0.114 m distance above the dielectric plate. (ii) Modeled 2D contour plot (labels in eV).

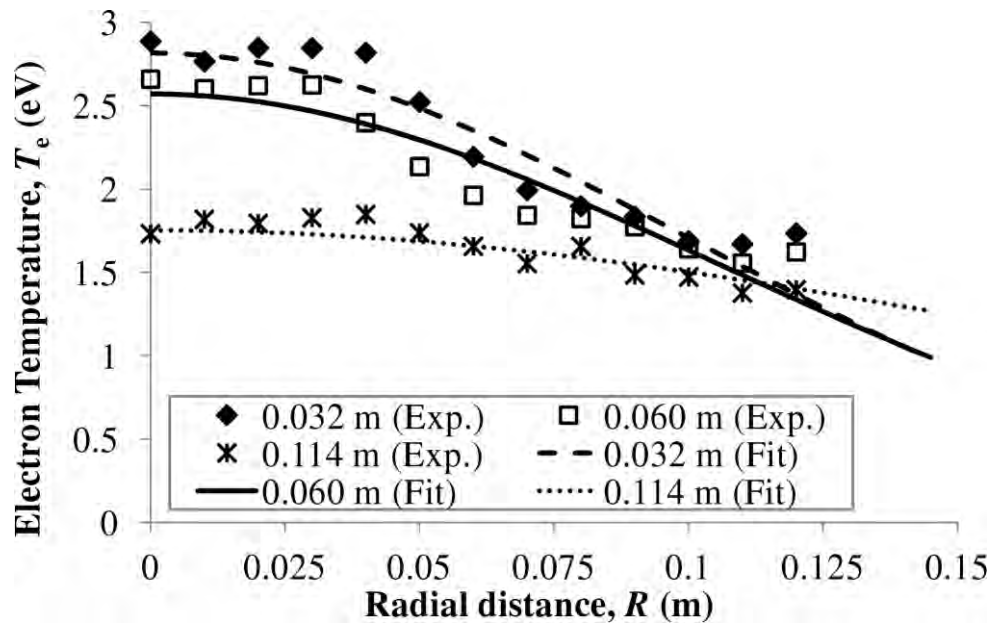


(i)

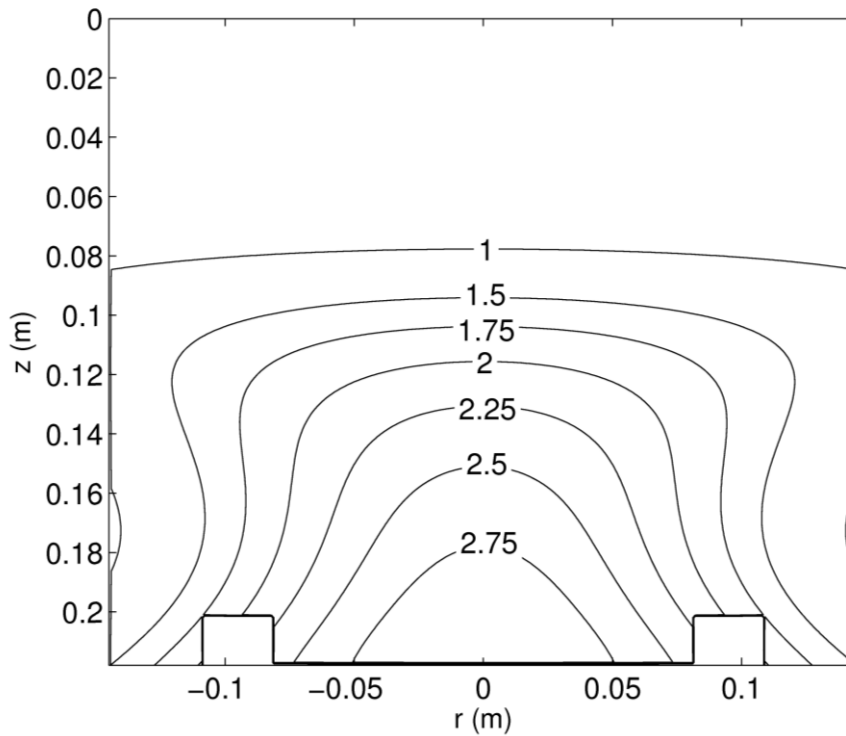


(ii)

**Figure 6.2b:** Empirically fitted 2D Gaussian based distribution of electron temperature  $T_e(r, z)$  used for the magnetic field simulation at 0.07 mbar argon pressure and 180 W r. f. power. (i) Fitment with measured values at 0.032 m, 0.060 m and 0.114 m distance above the dielectric plate. (ii) Modeled 2D contour plot (labels in eV).



(i)



(ii)

**Figure 6.2c:** Empirically fitted 2D Gaussian based distribution of electron temperature  $T_e(r, z)$  used for the magnetic field simulation at 0.2 mbar argon pressure and 180 W r. f. power. (i) Fitment with measured values at 0.032 m, 0.060 m and 0.114 m distance above the dielectric plate. (ii) Modeled 2D contour plot (labels in eV).

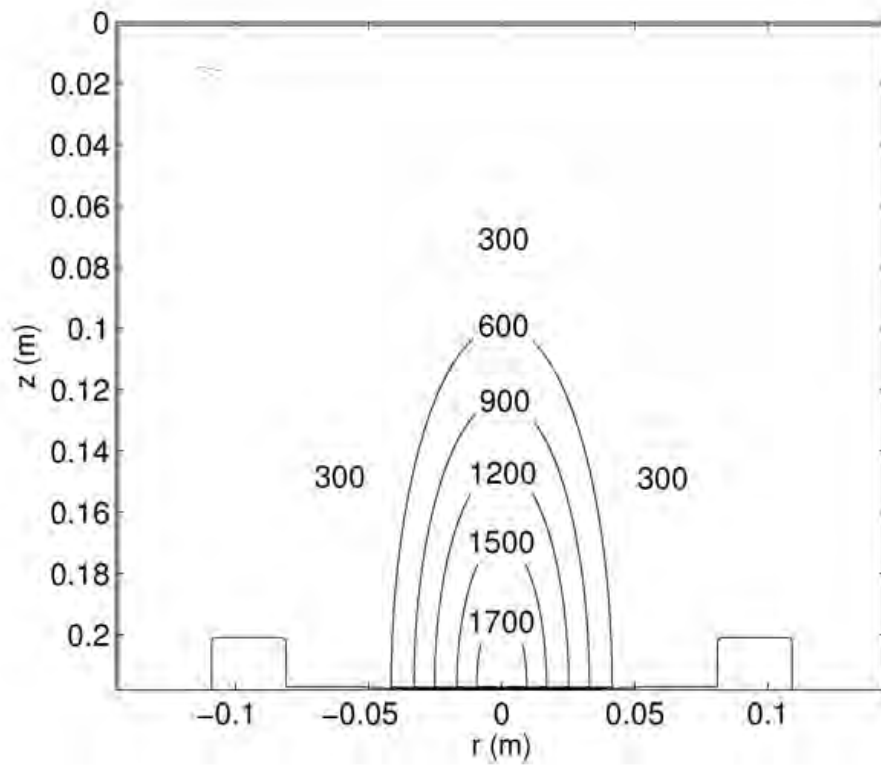
### 6.0.2. Heuristic fitting of the Spatially Resolved Neutral Gas Temperature, $T_n(r, z)$

Using the similar modified Gaussian function in Section 6.0.1, the spatially resolved neutral gas temperature,  $T_n(r, z)$  was heuristically fitted in simulation to values that give the closest agreement to the measured magnetic fields at 0.032 m axial distance above the dielectric plate and 180 W r. f. power. The function can be written as,

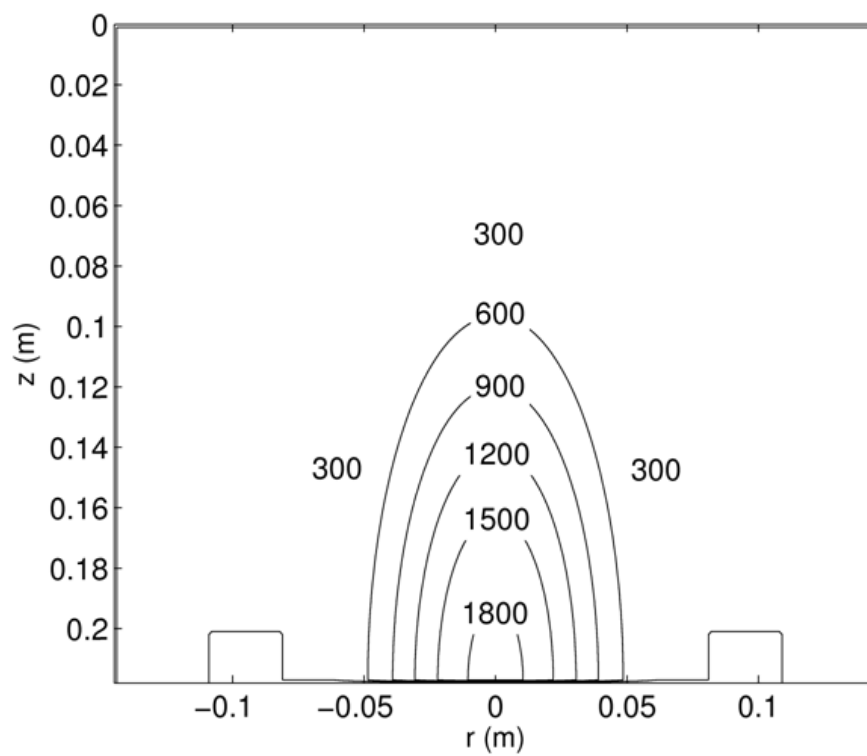
$$T_n(r, z) = T_{n, \text{peak}} \exp \left( - \left( \frac{r}{2\sigma_{r, T_n}} \right)^2 - \left( \frac{(L-z)}{2\sigma_{z, T_n}} \right)^2 \right), \quad (6.0.3)$$

where,  $T_{n, \text{peak}}$  is the fitted peak neutral gas temperature in K,  $\sigma_{r, T_n}$  is the radial fitting parameter for neutral gas temperature and  $\sigma_{z, T_n}$  is the axial fitting parameter for neutral gas temperature. Values for  $\sigma_{r, T_n}$  and  $\sigma_{z, T_n}$  for different argon pressures simulated are given in Appendix F, Table F.3.

The 2D contour plots of the heuristic  $T_n(r, z)$  fits that gave the best agreement with measured values for 0.03, 0.07 and 0.2 mbar argon pressures are shown in Figures 6.3 (a), 6.3 (b) and 6.3 (c), respectively. The fitted peak temperatures,  $T_{n, \text{peak}}$  were in the range of 1800-2300 K; values which may be considered high if compared with other reported works (Table 6.1). The distribution of  $T_n(r, z)$  was observed to peak at the center of the chamber above the dielectric plate; tapering off gradually at the axial direction and rapidly towards the edge of the coil at all pressures. Heating of the neutrals (i.e.,  $T_n(r, z) > 300$  K) for all pressures was mostly confined within the coil region, with increase in distribution temperature as argon pressure was increased.



(a)



(b)

Figure 6.3, continued...

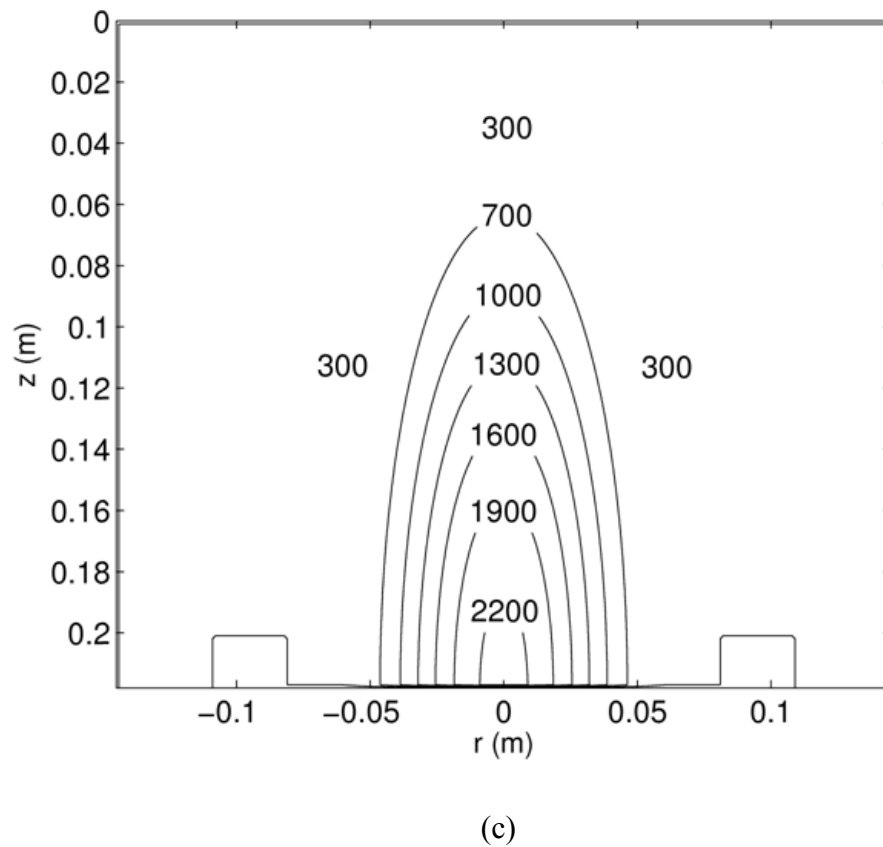


Figure 6.3: Heuristically fitted 2D contour plot for spatially resolved neutral gas temperature,  $T_n(r, z)$  at (a) 0.03 mbar (b) 0.07 mbar and (c) 0.2 mbar argon pressure. Labeled temperatures are in K.

**Table 6.1:** Comparison of parameters of present setup with other reported works of similar ICPs.

Parameters	Present Setup	Ostrikov et al. (2002)	Hebner (1996)	Sadeghi et al, (1997)	Shimada et al. (2007, 2008)	Li et al. (2011)
Pressure $P$ (mbar)	0.07	0.04	0.04	0.05	0.01	0.07
$n_e$ ( $m^{-3}$ )	$10^{17}$	$10^{17}$	$10^{17}$	-	$10^{17}$	$10^{17}$
$T_e$ (eV)	2.0-3.1	2.0-2.1	-	-	2.5	-
Measured $T_n$ (K)	630	543	1100	650	-	1200
Radial range of $T_n$ (K)	300-1900	-	-	-	600-900	-
Coil radius, $a$ (m) * <i>helical coil</i>	0.045	0.160	0.055	*0.050	*0.055	0.104
Chamber inner radius, $b$ (m)	0.145	0.160	0.065	0.075	0.175	0.104
Axial distance from dielectric plate, $(L - z)$ (m)	0.032	0.060	0.016	-	0.160	-
Power (W)	180	612.4	200	400	2000	200
Surface power density, r. f. power / coil area ( $Wm^{-2}$ )	2.82	0.76	2.10	-	-	0.59
r. f. Frequency (MHz)	13.56	0.46	13.56	13.56	13.56	13.56

These observations can be justified by the following points:

- i. The surface power density ( $2.82 Wm^{-2}$ ) is higher for the present setup as compared to the other works due to smaller coil dimensions, i.e., coil radius  $\sim 0.045$  m whereas, chamber radius  $\sim 0.145$  m. This translates to more concentrated heating of the plasma particles by the source power over a smaller chamber volume, which subsequently results in increased localized thermalization of the neutral particles. Other comparative systems have larger coils (at equal diameters with the chamber) which would attribute to a lower surface power density at the same power. Thus, the power deposited by the

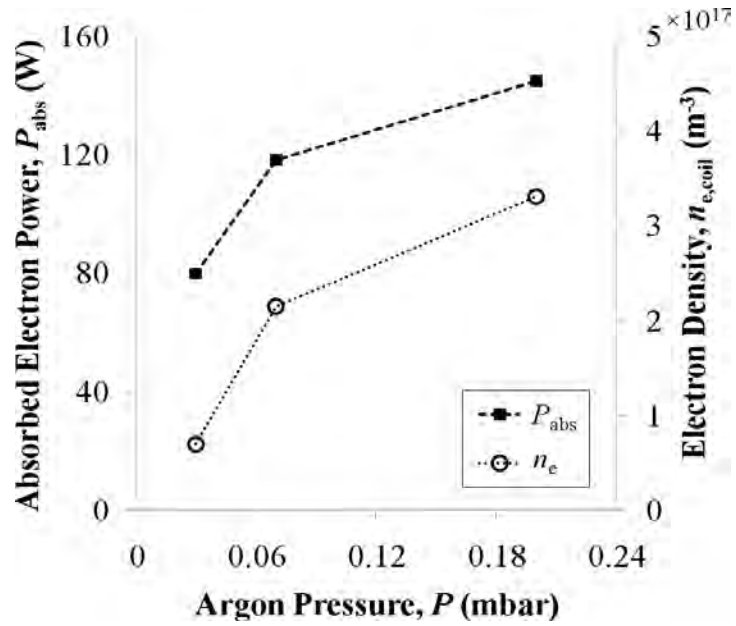
inductive coils into these systems would be distributed in a wider area and the consequential effect of neutral gas heating would be less.

- ii. The trend of the spatial distributions obtained (i.e., in which the neutral gas is the hottest at the center above the dielectric plate and tapers off rapidly at the axial direction and towards the edge of the coil) is valid and has been reported in measurement by Shimada, Tynan and Cattolica, 2007.
- iii. The increase in neutral gas heating with argon pressure is attributed to increased r. f. power coupling from the source coil to the plasma particles with pressure. To demonstrate this, it would be convenient to first tabulate the relevant power balance parameters; derived from the theoretical equations in Chapter 5, Sections 5.2.1 and 5.4. The effective collision frequency,  $\nu_{\text{eff}}$  and the total absorbed electron power,  $P_{\text{abs}}$  were calculated for the fitted argon pressures,  $P$  using the measured peak coil current,  $I_p$ , the measured average electron density,  $n_{\text{e,coil}}$  and electron temperature,  $T_{\text{e,coil}}$  across the coil radius (for 180 W input r.f. power) and the set peak neutral gas temperature,  $T_{\text{n,peak}}$  (Table 6.2).

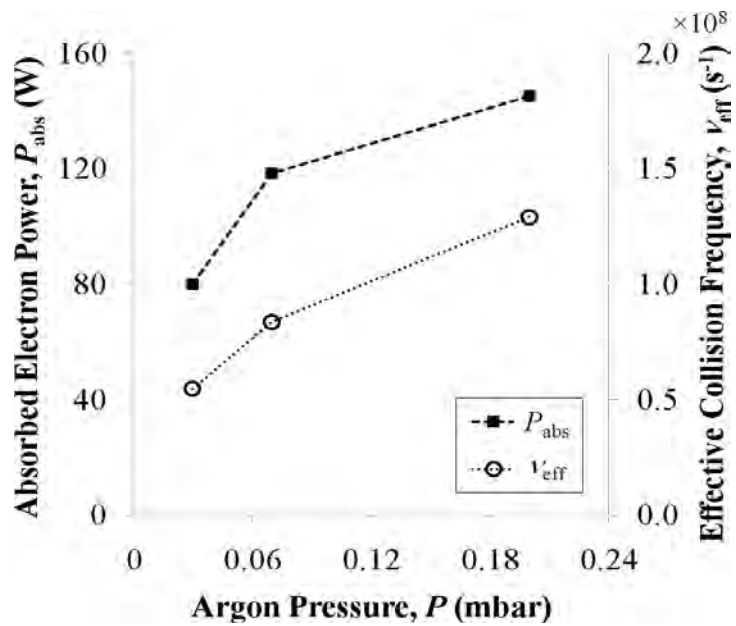
**Table 6.2:** Calculated values for effective collision frequency,  $\nu_{\text{eff}}$  and total absorbed electron power,  $P_{\text{abs}}$  with measured average coil electron density,  $n_{\text{e,coil}}$ , average coil electron temperature,  $T_{\text{e,coil}}$  and peak coil current,  $I_p$  (for 180 W input r.f. power) and set peak neutral gas temperature,  $T_{\text{n,peak}}$  at 0.03, 0.07 and 0.2 mbar argon pressure.

Argon Pressure, $P$ (mbar)	$n_{\text{e, coil}} \text{ (m}^{-3}\text{)}$	$T_{\text{e, coil}} \text{ (eV)}$	$I_p \text{ (A)}$	$T_{\text{n,peak}} \text{ (K)}$	$\nu_{\text{eff}} \text{ (s}^{-1}\text{)}$	$P_{\text{abs}} \text{ (W)}$
0.03	$6.95 \times 10^{16}$	3.68	14.8	1800	$5.46 \times 10^7$	79.9
0.07	$2.15 \times 10^{17}$	2.97	14.2	1900	$8.35 \times 10^7$	118.2
0.2	$3.31 \times 10^{17}$	2.78	13.8	2300	$1.29 \times 10^8$	145.0

With the data presented in Table 6.2, the trends of  $P_{\text{abs}}$ ,  $n_{\text{e,coil}}$  and  $\nu_{\text{eff}}$  with argon pressure are plotted and shown in Figure 6.4.



(a)



(b)

**Figure 6.4:** Calculated absorbed electron power,  $P_{\text{abs}}$  with (a) average measured electron density within the coil radius,  $n_{\text{e,coil}}$  ( $\text{m}^{-3}$ ) and (b) calculated effective collision frequency,  $\nu_{\text{eff}}$  versus argon pressure.

From Figure 6.4, it is observed that  $P_{\text{abs}}$  increases non-linearly with argon pressure, i.e., from 79.9 W at 0.03 mbar to 145.0 W at 0.2 mbar. With increase

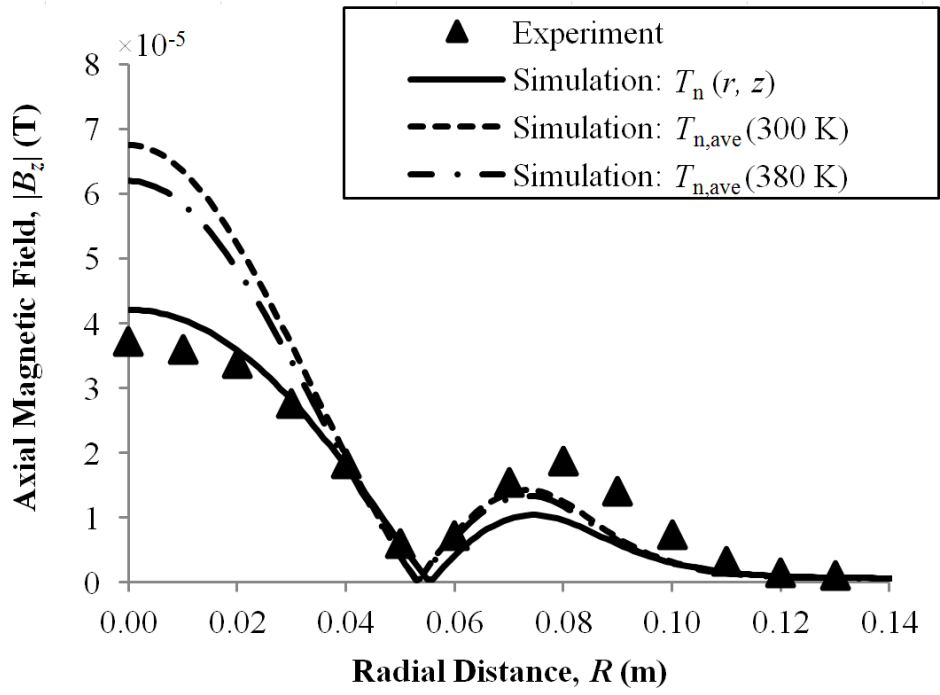
in  $P_{\text{abs}}$ ,  $n_{\text{e,coil}}$  also becomes higher (Figure 6.4 (a)). Higher  $n_{\text{e,coil}}$  at higher pressures would mean that there is higher number of ions available within the coil region for heating by the oscillating r. f. fields (Shimada, Tynan & Cattolica, 2008). These accelerated ions are highly energized and can reach very high temperatures (Hebner, 1996). Since effective collision frequency also increases with pressure (Figure 6.4 (b)), more of these highly energized ions would be converted into thermalized neutrals via de-excitation with electrons and elastic or charge transfer collisions with other neutrals (Lieberman & Lichtenberg, 2005). Hence, the increase in formation thermalized neutrals would contribute to the increase in neutral gas heating with pressure; as seen in fitment.

### **6.0.3. Spatially averaged neutral gas temperatures, $T_{\text{n,ave}}$**

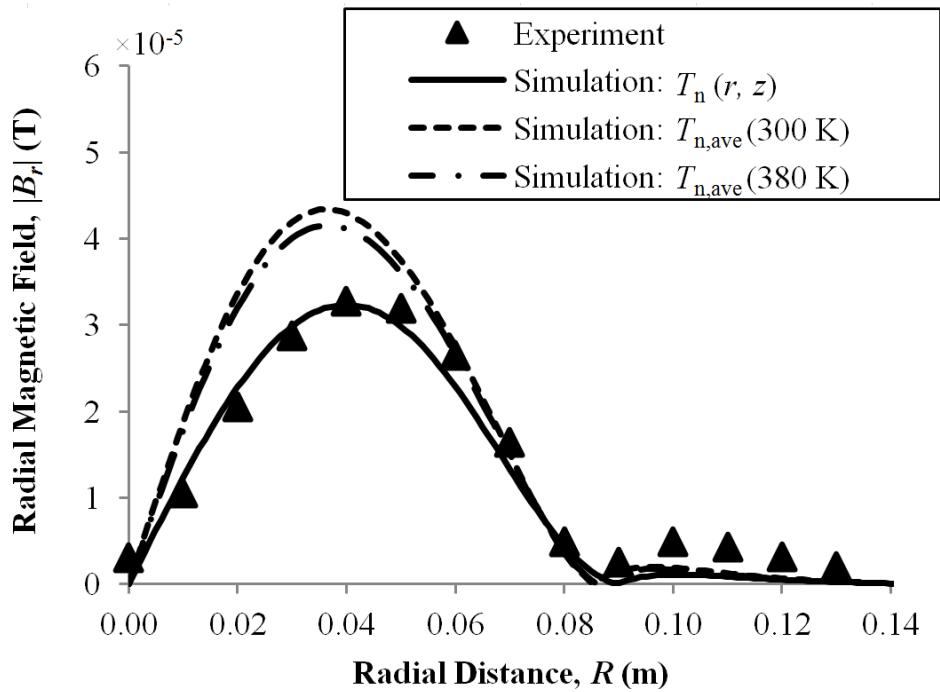
For comparison with simulations using  $T_{\text{n}}(r, z)$ , the magnetic fields were also calculated with spatially averaged neutral gas temperature values,  $T_{\text{n,ave}}$ .  $T_{\text{n,ave}}$  was set at both room temperature ( $T_{\text{n,ave}} = 300$  K) and measured temperature. The measured values used for simulation were 380, 630 and 800 K for 0.03, 0.07 and 0.2 mbar argon pressure, respectively; corresponding to the results at 0.032 m axial distance obtained from Chapter 4, Section 4.3.1, Figure 4.10.

### **6.0.4. Comparison of Measured and Simulated Magnetic Fields**

Measured axial and radial magnetic fields are compared to simulated values for 0.03, 0.07 and 0.2 mbar argon pressures at 0.032 m above the dielectric plate as shown in Figures 6.5a, 6.5b and 6.5c. At 180 W r. f. power, the measured peak coil currents,  $I_{\text{p}}$  were 14.4 A for 0.03 mbar, 14.2 A for 0.07 mbar and 13.4 A for 0.2 mbar; values that were used for simulation.

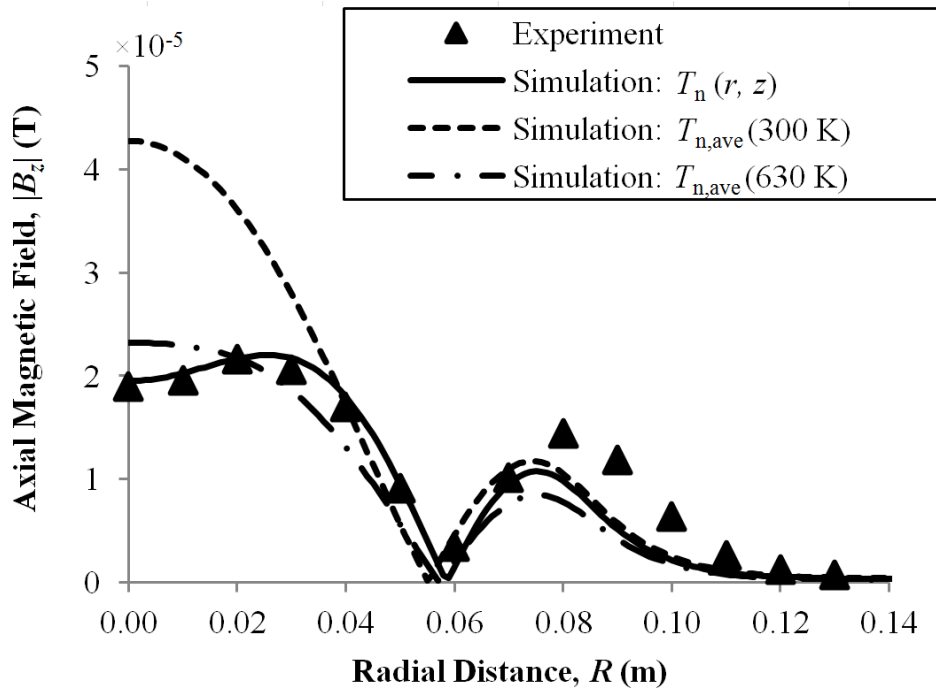


(i)

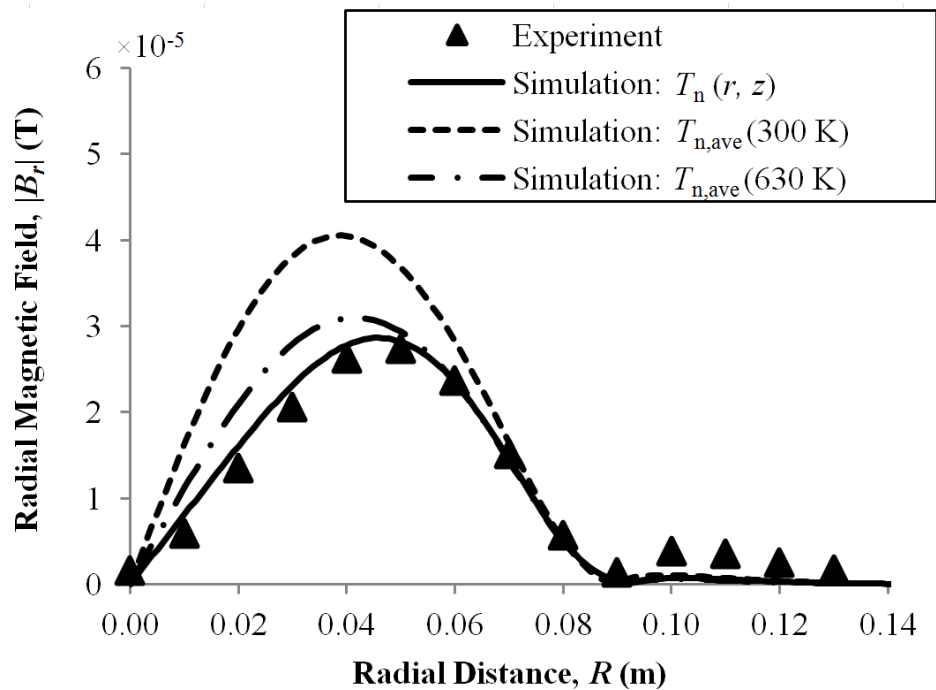


(ii)

**Figure 6.5a:** Measured and simulated (i) axial magnetic fields,  $|\text{Re}(B_z)|$  and (ii) radial magnetic fields,  $|\text{Re}(B_r)|$  versus radial distance,  $R$  for 0.03 mbar argon pressure at 0.032 m distance above the dielectric plate. R.f. input power was 180 W and  $I_p=14.4$  A.

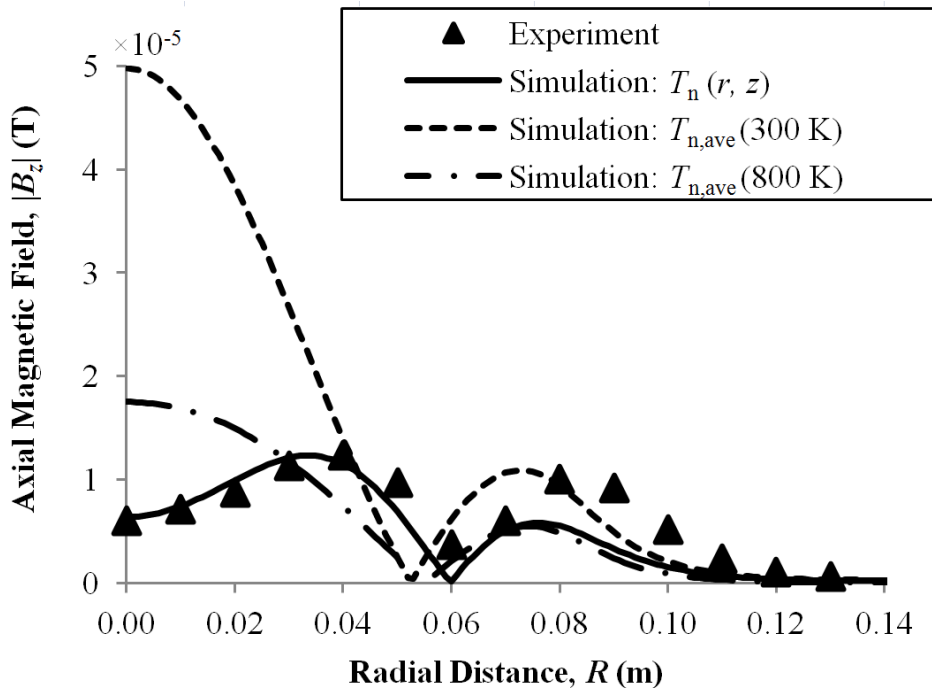


(i)

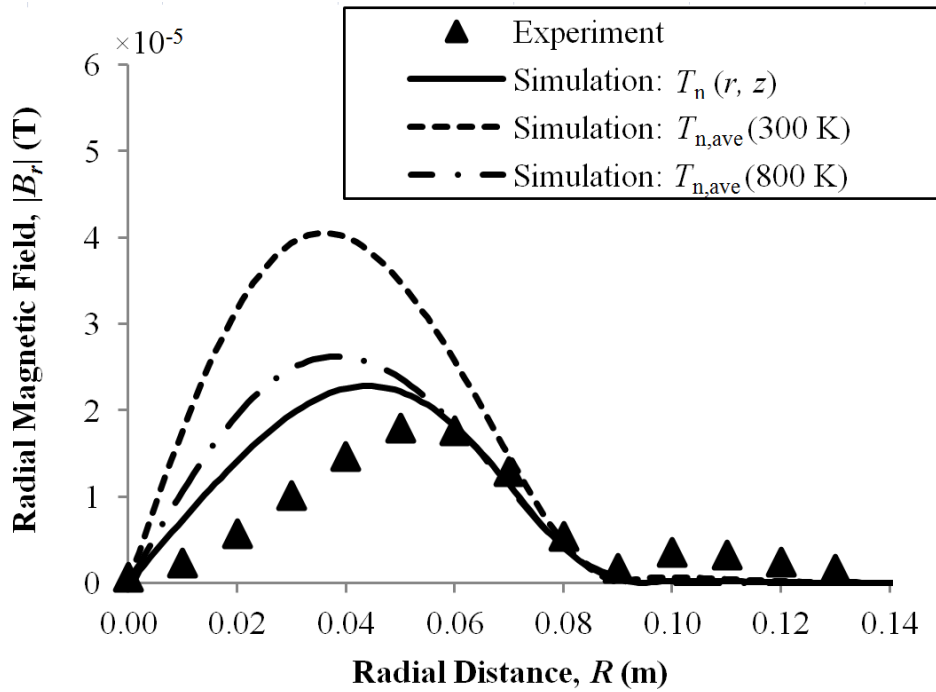


(ii)

**Figure 6.5b:** Measured and simulated (i) axial magnetic fields,  $|\text{Re}(B_z)|$  and (ii) radial magnetic fields,  $|\text{Re}(B_r)|$  versus radial distance,  $R$  for 0.07 mbar argon pressure at 0.032 m distance above the dielectric plate. R.f. input power was 180 W and  $I_p=14.2$  A.



(i)



(ii)

**Figure 6.5c:** Measured and simulated (i) axial magnetic fields,  $|\text{Re}(B_z)|$  and (ii) radial magnetic fields,  $|\text{Re}(B_r)|$  versus radial distance,  $R$  for 0.2 mbar argon pressure at 0.032 m distance above the dielectric plate. R.f. input power was 180 W and  $I_p=13.4$  A.

The simulated fields were computed using neutral gas temperature that was spatially resolved,  $T_n(r, z)$  and its spatially averaged values  $T_{n,ave}$  at room and measured temperature. Suppression of the magnetic fields (especially at the centre axis of the chamber, i.e.,  $R = 0$  m) is seen to progressively increase with chamber pressure and is especially prominent at 0.07 mbar and 0.2 mbar. This suppression trend is only sufficiently matched by the simulation with the spatially resolved neutral gas temperature,  $T_n(r, z)$  and not the spatially averaged neutral temperatures,  $T_{n,ave}$ .

The mechanism of the suppression of the magnetic fields can be explained as follows. When the discharge is initiated, inductive coupling would result in ionization of the argon neutrals to form ion-electron pairs. These ion-electron pairs move freely in the plasma region and may be thermalized under the influence of the bulk ambipolar electrostatic field (Shimada, Tynan & Cattolica, 2008). Further thermalization of the charged particles also occurs via Coulomb collisions and stochastic heating by the oscillating capacitive sheath (Gudmunsson & Lieberman, 1998). Ions thermalized by these interactions (reaching temperatures of 1000-4000 K as reported by Hebner, 1996) will subsequently undergo collisional processes with electrons via de-excitation and elastic or charge transfer collisions with other neutrals, forming thermalized neutrals that increase the neutral temperature in the vicinity. These thermalized neutrals, which at the beginning, are formed mostly at the center of the discharge region would create a pressure and temperature gradient across the coil radius that would lead to convection of these particles towards the edge of the coil.

As a result of this convection, a depletion of neutral gas density will start to occur at the central region of the plasma. As this depletion profile grows, the mean free path of the plasma particles (including the neutrals) is increased, thus, allowing for more highly energetic particles to exist (Fruchtman et al., 2005). Heating of these background

particles would also generate a localized environment whereby less energy is required to sustain ion-electron pairs; increasing the utilization of the magnetic fields by the plasma (Turner & Lieberman, 1999). The depletion of neutrals at the centre of the plasma region would continue until an equilibrium state is formed between the number of available neutrals and ionization of new plasma electrons.

At higher pressures, this equilibrium state occurs at higher electron densities due to the higher number of neutrals, thus, resulting in higher utilization of the incident fields with increased suppression (Figure 6.5c). Consequently, the increased utilization of the magnetic fields in the centre reduces the skin depth in the region of effect, i.e., the coil radius. The comparative effect of neutral gas heating on the magnetic fields can be seen in Figures 6.5 whereby in the case of 300 K, the simulated fields are much higher than the experimentally measured values. This suggests that part of the energy coupled into the plasma particles has been distributed to the neutrals and hence, it is inferred that neutral gas heating plays an important role in determining the skin depth of the magnetic fields. Knowledge of the non-uniform distribution of neutral gas temperature across the chamber radius is also essential for accurate deduction of field suppression trends.

## 6.1. Predictive Simulation of H mode Transition and Maintenance Currents

The peak E to H mode transition current (H mode transition current),  $I_{tr}$  and H to E mode transition current (H mode maintenance current),  $I_{mt}$  were simulated with the power balance model detailed in Chapter 5, Section 5.4. A 3D power evolution plot detailing the effects of hysteresis in the discharge is also discussed.<sup>1</sup>

### 6.1.1. E-H mode Transition Dynamics and Hysteresis Effects in Discharge

When the absorbed electron power,  $P_{abs}$  and electron power loss,  $P_{loss}$  parameters are plotted against electron density, they intersect at certain points; in which both powers are at equilibrium ( $P_{abs} = P_{loss}$ ). These intersecting points represent the plausible operating states of the system observable in experiments. At lower electron densities, the plasma is predominantly coupled by E mode power,  $P_e$  and is at E mode state, whereas, at higher electron densities, the plasma is predominantly coupled by H mode power,  $P_h$  and is at H mode state. Plausibility of these operating points also depends on the condition of stability in which the rate of change of absorbed power with electron density must be less than rate of change of power loss with electron density, i.e.,  $\delta P_{abs}/\delta n_e < \delta P_{loss}/\delta n_e$  (Ostrikov et al., 2002 and Shamrai, Pavlenko & Taranov, 1997). An illustrative of this is seen in Figure 6.6, where points I and III represent the stable and observable H and E mode operations, respectively with  $\delta P_{abs}/\delta n_e < \delta P_{loss}/\delta n_e$  and  $P_{abs} = P_{loss}$  conditions fulfilled. Point II represents an unstable state which is not observable experimentally.

<sup>1</sup> Results in this section comprises of edited and revised material that has been published in Jayapalan and Chin (2012). The thesis author is the primary author and investigator for the paper.

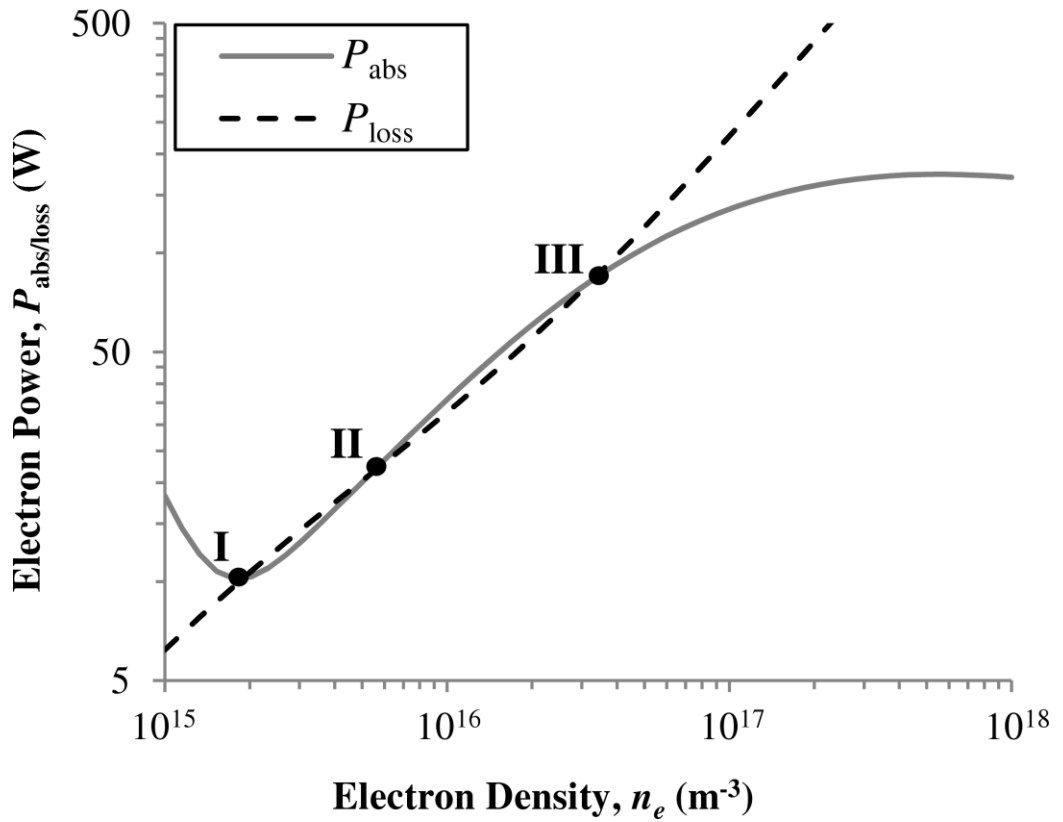


**Figure 6.6:** Simulated electron absorbed power and electron power loss versus electron density for 15 A peak r.f. coil current at 0.02 mbar argon pressure. **I**, **II**, and **III** represent the E mode, unstable operation, and H mode, respectively. Electron temperature,  $T_e$ , neutral gas temperature,  $T_n$ , and the factor  $C_{D-M}$  were set at 4.2 eV, 433 K and  $6.6 \times 10^4$ , respectively.

In order to determine the H mode transition current and H mode maintenance current, it is important to have an understanding on the mechanism of hysteresis in the ICP system. Taking the experimentally fitted case of 0.02 mbar argon pressure as an example, a 3D plot of electron power (absorbed and loss) versus peak coil current and electron density is first visualized (Figure 6.7).

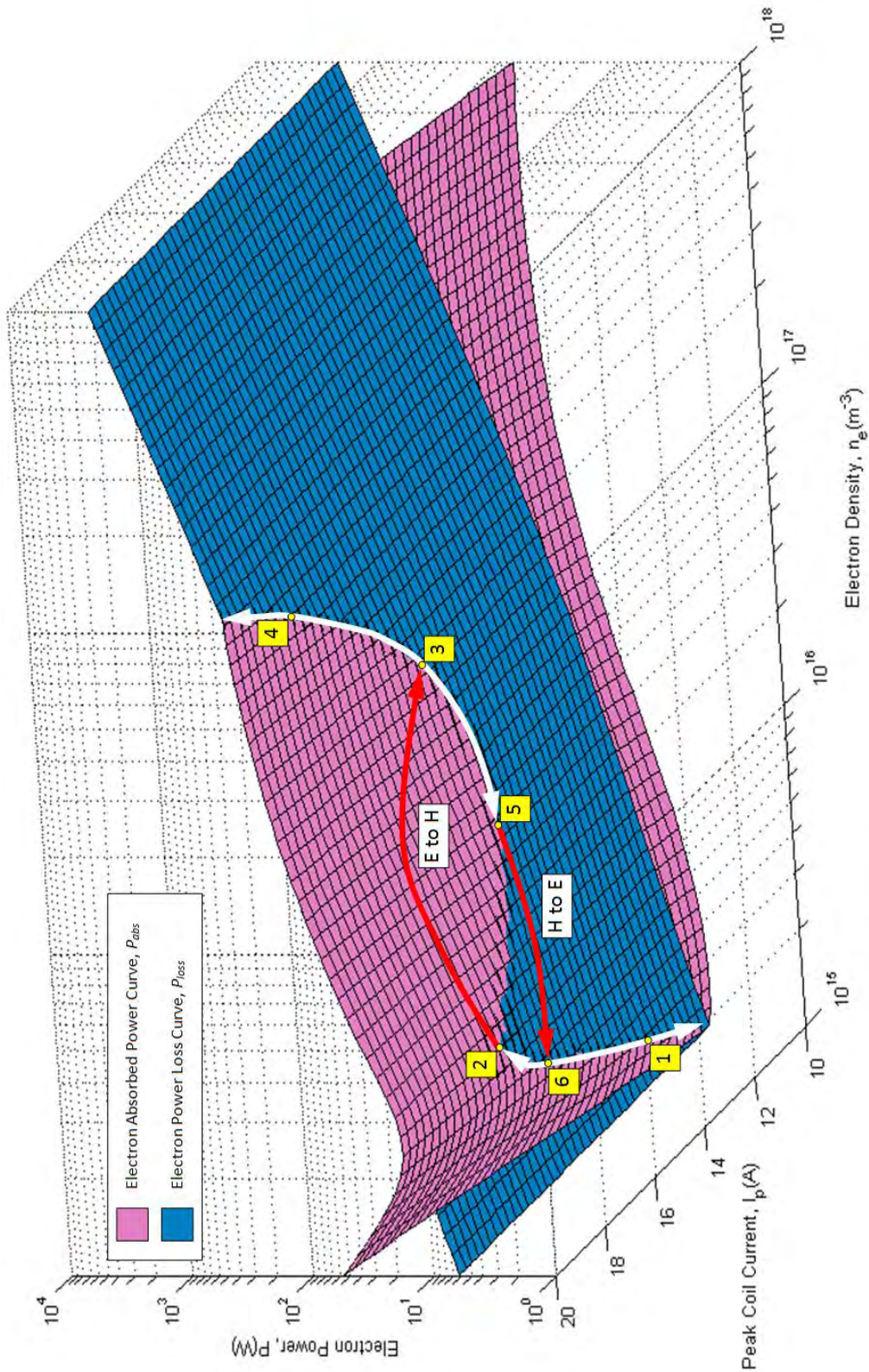


**Figure 6.7:** A 3D plot of absorbed electron power,  $P_{abs}$  (magenta surface) and electron power loss,  $P_{loss}$  (dark blue surface) versus electron density,  $n_e$  and peak coil current,  $I_p$  at 0.02 mbar argon pressure. Electron temperature,  $T_e$  was set at 4.2 eV, neutral gas temperature,  $T_n$  set at 433K and  $C_{D-M} = 6.6 \times 10^4$ . The white arrows indicate the working path of the system, whereas the red arrows indicate mode transitions.

The magenta (lighter) surface of the 3D plot represents the evolution of absorbed electron power,  $P_{\text{abs}}$  whereas dark blue (darker) surface represents the evolution of electron power loss,  $P_{\text{loss}}$ . As aforementioned, the intersections between the two surfaces represent the working path of the system. In a typical experiment, the input coil current starts at zero. As the input coil current (or r.f. power) is increased, the operating point of the system moves to point 1 (Figures 6.7 and 6.8).

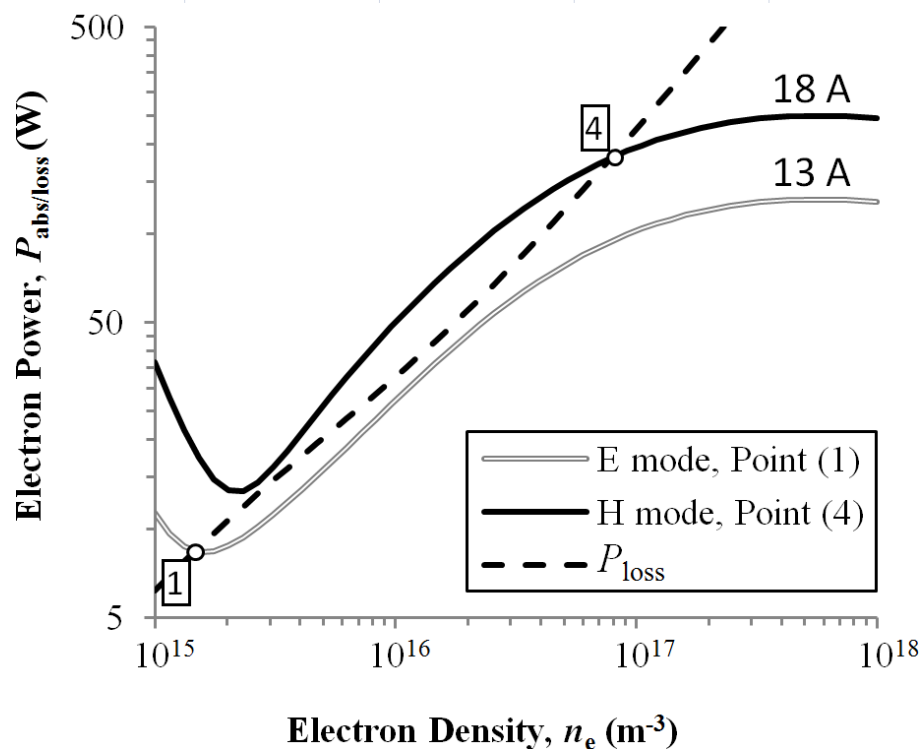


**Figure 6.8:** The simulated absorbed electron power (solid line) and power loss (dashed line) curves depicting (a) the current at which either E mode (13 A) or H mode operation (18 A) alone occurs.

At this point, the low density E mode plasma is observed (E mode was ignited before point 1 at input coil current of  $5.2 \pm 0.2$  A). A further increase in current would shift the operating point of the system to point 2. Point 2 is the threshold at which any further increase in coil current would trigger a transition from E to H mode, marking the H mode transition current (Figures 6.7 and 6.9).

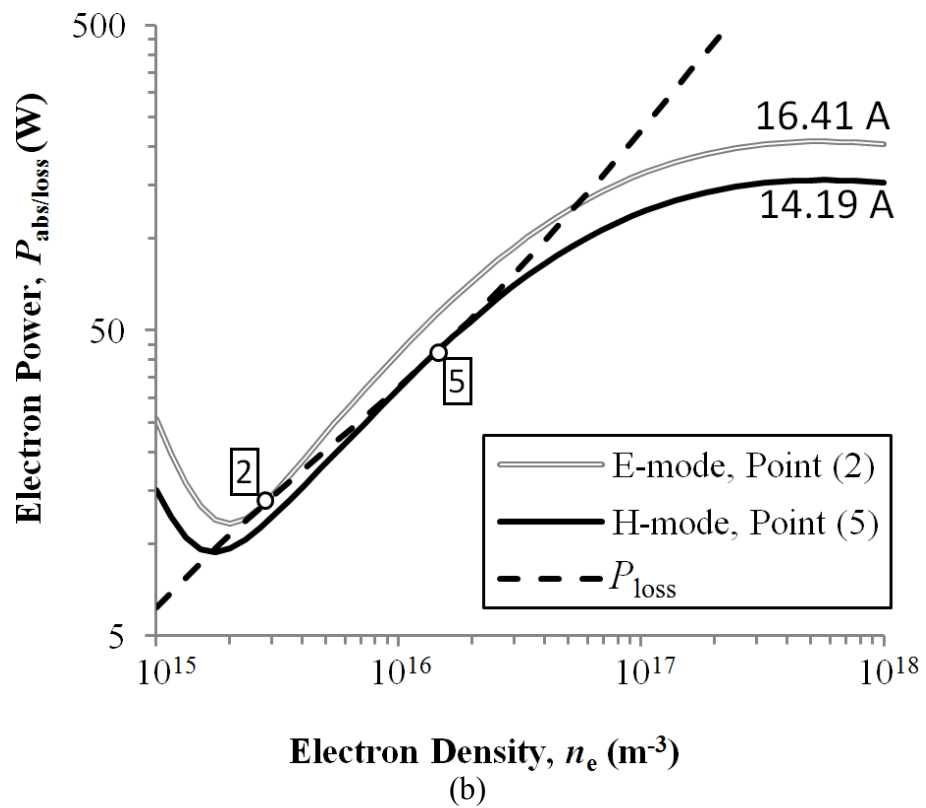


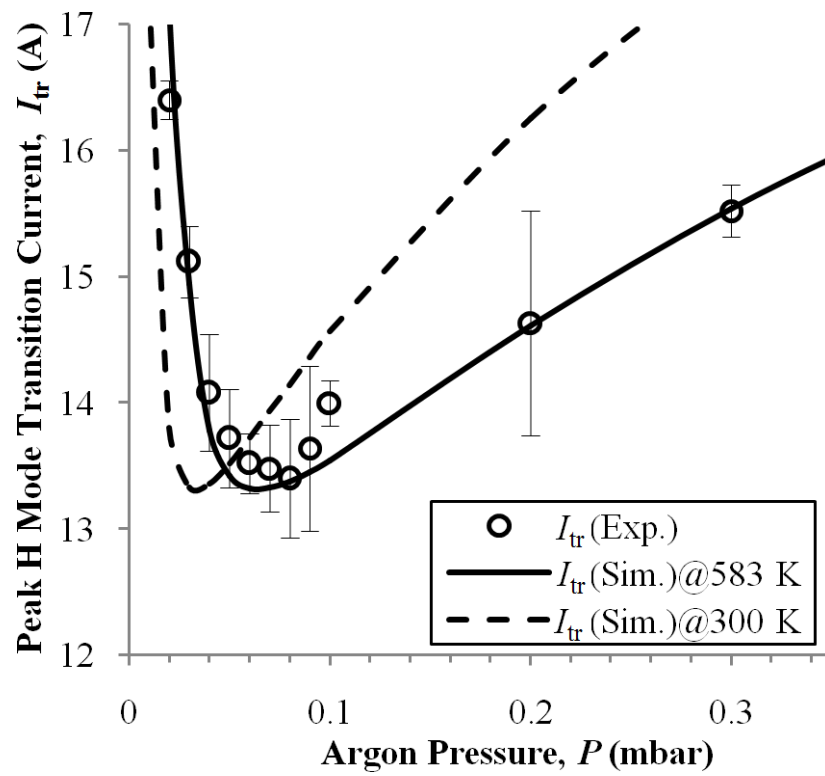
**Figure 6.9:** The simulated absorbed electron power (solid line) and power loss (dashed line) curves depicting the threshold currents for E to H (16.41 A) and H to E (14.19 A) mode transitions.

From point 2, the system jumps to point 3 which is in H mode. Point 3 is determined experimentally and is affected by the sensitivity and accuracy of the impedance matching circuit (El-Fayoumi, Jones & Turner, 1998, Cunge, et al., 1999 and Turner & Lieberman, 1999). Increase in coil current at point 3 would bring system operation to point 4 (Figures 6.7 and 6.8) which is higher density plasma in H mode. When coil current is decreased from point 4, the system follows the working H mode path until point 5. Point 5 is the threshold at which a further decrease would trigger a transition to E mode (Figures 6.7 and 6.9). This threshold point is measured as the minimum or maintenance current for H mode plasma. The disparity between transition and maintenance currents (as observed in the plot) denotes the effect of hysteresis in the working path of the system. From point 5, a decrease in coil current shifts the system operation to point 6 which is in E mode.

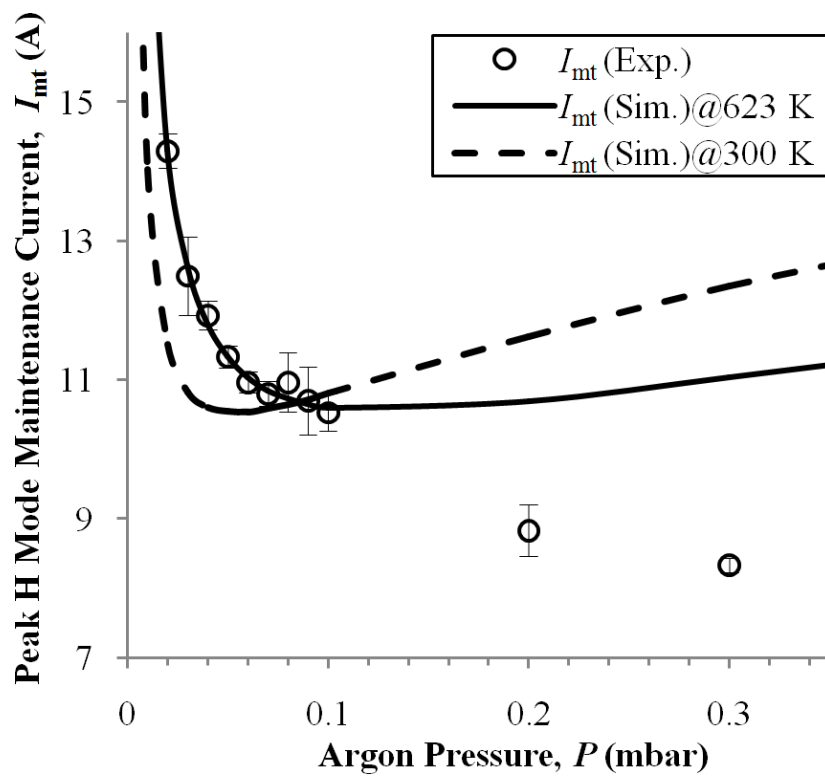
It is noted that the experimentally measured H mode transition and maintenance currents for 0.02 mbar argon pressure are  $16.4 \pm 0.1$  A and  $14.3 \pm 0.3$  A, respectively. These values are consistent with the simulated values (16.41 A and 14.19 A) presented in this example.

### **6.1.2. Comparison of Measured H mode Transition Current, $I_{tr}$ and H mode Maintenance Current, $I_{mt}$ with Simulation**

The measured H mode transition current,  $I_{tr}$  and H mode maintenance current,  $I_{mt}$  for the argon pressure range of 0.02-0.3 mbar are compared with values calculated from the power balance model in Chapter 5, Section 5.4 (Figure 6.10). The plasma parameters used in simulation of the (a)  $I_{tr}$  curve are  $T_e = 4.0$  eV,  $T_n = 583$  K and  $C_{D-M} = 8.8 \times 10^4$  whereas, for the (b)  $I_{mt}$  curve, the parameters are  $T_e = 3.0$  eV,  $T_n = 623$  K and  $C_{D-M} = 3.0 \times 10^5$ . Values for electron temperature and neutral gas temperature for both curves were fitted in simulation within the range measured at 0.032 m (nearest measured axial distance above the coil); i.e.,  $(1.7 \pm 0.1)$ - $(3.8 \pm 0.2)$  eV for  $T_e$  and  $(350 \pm 30)$ - $(810 \pm 20)$  K for  $T_n$ . The values for  $C_{D-M}$ , on the other hand, were heuristically chosen to be in the  $10^4$ - $10^5$  range such that the EEDF transition occurs near the electron densities,  $n_e \approx 10^{15}$ - $10^{16}$  m<sup>-3</sup>; consistent with reported values of mode transition point for the same system (Lim, 2010). For further comparison, simulation at room temperature ( $T_n = 300$  K) for both  $I_{tr}$  and  $I_{mt}$  curves are also shown.



(a)



(b)

**Figure 6.10:** Simulated (Sim.) and measured (Exp.) (a) H mode transition currents,  $I_{tr}$  (b) H mode maintenance currents,  $I_{mt}$  at 0.02-0.3 mbar argon pressure range.

In Figure 6.10 (a), it is observed that the simulated  $I_{tr}$  curve is well matched to the measured values when neutral gas heating is considered. At room temperature, however, the  $I_{tr}$  curve does not match. Measured  $I_{tr}$  values are higher than simulated  $I_{tr}$  values at room temperature at lower filling pressures of  $<0.06$  mbar; whereas, at higher filling pressures of  $>0.06$  mbar, the measured  $I_{tr}$  values are lower. At lower filling pressure, thermalization of the neutrals diffuses the particles in the plasma in accordance to ideal gas law (O'Connell et al., 2008, Shimada, Tynan & Cattolica, 2008). Since, the plasma is diffused, higher input current is required to generate sufficient plasma ionization and reach threshold electron density to attain H mode (Fruchtman, 2008). At higher filling pressures, the neutral gas density of the plasma has become high enough such that thermalization of the neutral particles increases the power transfer efficiency by assisting plasma collisional processes (Lieberman & Lichtenberg, 2005 and Suzuki et al., 1998). This reduces the input  $I_{tr}$  required to sustain H mode.

In Figure 6.10 (b), the simulated  $I_{mt}$  curve with neutral gas heating is well matched to the measured values at the range of and 0.02-0.1 mbar. Discrepancy between the measured  $I_{mt}$  and simulated  $I_{mt}$  curves at room temperature can also be explained in the same way as the  $I_{tr}$  curve; with thermalization of the neutrals in experiment diffusing the plasma at lower filling pressures ( $<0.09$  mbar) and assisting in plasma collision processes at higher filling pressures ( $>0.09$  mbar). The higher pressure region at which diffusion of the particles influence  $I_{mt}$  ( $\sim 0.09$  mbar) as compared to  $I_{tr}$  ( $\sim 0.06$  mbar) is due to the lower plasma density at which the H to E mode transition occurs.

The increasing deviation at higher pressures of 0.2-0.3 mbar between the simulated and experimental  $I_{mt}$  curves is suspected to be due to the non-linear effects of multistep ionization which is yet to be included in the simulation. At higher pressures, complex

ionization processes occurring from intermediary or metastable excitation states become more significant such that the total energy required to sustain the ion-electron pairs created in the discharge is further reduced, i.e., lower electron power loss (Turner & Lieberman, 1999). This effect, in part, explains the ability of the H mode discharge in experiment to be maintained at a much lower current than the values obtained by simulation.

## CHAPTER 7: SUMMARY AND CONCLUSION

### 7.0. Overview

In this study, a 13.56 MHz, 6 turn planar coil, argon inductively coupled plasma (ICP) was characterized with a combination of experimental diagnostic techniques and predictive simulation; from which the effects of neutral gas heating was observed. Summary of the results obtained are given in following sections along with key findings and suggestions for future work.

### 7.1. Experimental Characterization

Experimental characterization was done using several diagnostic probes; with each measuring different properties of the plasma. Electrical properties such as the radially resolved electron density,  $n_e$ , the radially resolved electron temperature,  $T_e$  and the electron energy distribution function, EEDF at the chamber center ( $R = 0$ ) were measured using a r.f. compensated Langmuir probe. The spatially resolved absolute axial magnetic fields,  $|B_z|$  and absolute radial magnetic fields,  $|B_r|$  were measured using two electrostatically compensated magnetic probes at the respective orientations. The peak H mode transition current,  $I_{tr}$  and peak H mode maintenance peak current,  $I_{mt}$  were measured using a current probe attached to the source coil. The neutral gas temperature,  $T_n$  of the discharge was measured via the AOES technique.

#### 7.1.1. Measurement of Electron Density, $n_e$ and Electron Temperature, $T_e$ and Electron Energy Distribution Function (EEDF)

The radially resolved electron density,  $n_e$  and electron temperature,  $T_e$  of the discharge were measured at 0.03, 0.07 and 0.2 mbar argon pressure for 0.032 m, 0.060 and 0.114 axial distances above the dielectric plate and calculated using Maxwellian and

EEDF methods. R.f. power was set at 180 W. Higher values of  $n_e$  and lower values of  $T_e$  were obtained using the Maxwellian method in comparison to the EEDF method. With increase in argon pressure for all measured radial positions,  $n_e$  increases and  $T_e$  decreases. The range of electron densities obtained were  $(0.065 \pm 0.004)-(4.0 \pm 0.6) \times 10^{17} \text{ m}^{-3}$  for the Maxwellian method and  $(0.052 \pm 0.004)-(3.5 \pm 0.5) \times 10^{17} \text{ m}^{-3}$  for the EEDF method. The range of values measured for  $T_e$ , on the other hand, were  $(1.38 \pm 0.08)-(3.8 \pm 0.2) \text{ eV}$  using the Maxwellian method and  $(1.78 \pm 0.05)-(4.8 \pm 0.3) \text{ eV}$  using the EEDF method. Several important observations were made:

- i. As argon pressure was increased, the discharge becomes increasingly denser within the coil region ( $R < 0.05 \text{ m}$ ). This was attributed to the increase in plasma collision frequency with argon particles, producing more ionizing collisions in the region where the r.f. source field was the strongest. This was further validated by the simulation results for the total absorbed electron power,  $P_{\text{abs}}$  (Chapter 6, Section 6.0.2, Table 6.2); whereby, for measured parameters at 180 W input r.f. power,  $P_{\text{abs}}$  increases with argon pressure.
- ii.  $n_e$  at 0.2 mbar did not decrease (as expected) with reduced proximity from the source r.f. field. Instead,  $n_e$  within the coil region was highest at 0.060 m axial distance above the dielectric plate. The observed displacement between power deposition of the source r.f. field and region of maximum  $n_e$  was likely to be from enhanced plasma transport due to neutral gas heating; with particles forming a steady state flux due to temperature gradient and travelling away from the source coil and towards the chamber walls.

- iii. The radial distribution of  $n_e$  at 0.2 mbar argon pressure for 0.032 m axial distance above the dielectric plate (close to the source) was higher at the edge of the coil region and did not follow the other distribution trends which peaked at  $R = 0$ . This was also attributed to enhanced plasma transport due to neutral gas heating; as plasma particles were pushed away from the discharge center towards the edge of the coil region due to temperature gradient.
  
- iv.  $T_e$  distribution for 0.2 mbar argon pressure showed increased number of higher energy electrons near the coil region. This supports the notion of neutral gas heating, which would cause the plasma collision frequency in the vicinity of effect to be comparatively less than the plasma collision frequency of the surrounding area and thus, allow for higher accumulation of electron energy via increased free mean path.

As with  $n_e$  and  $T_e$ , the EEDFs at the chamber center ( $R = 0$ ) at 0.03, 0.07 and 0.2 mbar argon pressure for 0.032 m, 0.060 and 0.114 axial distances above the dielectric plate were also calculated and parametrically fitted (as the electron energy probability function or EEPF) with defined Maxwellian or Druyvestyen functions (Table 7.1).

**Table 7.1:** EEPF fitment trends at 0.03, 0.07 and 0.2 mbar argon pressure for 0.032 m, 0.060 m and 0.114 m axial distances above the dielectric plate.

EEPF Fitment Trend		Argon Pressure, $P$ (mbar)		
		0.03	0.07	0.2
Axial Distance Above Dielectric Plate, $(L - z)$ (m)	0.032	Maxwellian	Maxwellian	Maxwellian
	0.060	Druyvestyen	Maxwellian	Druyvestyen
	0.114	Maxwellian	Maxwellian	Druyvestyen

Although the exact EEPFs had more complex distributions, fitment showed more Maxwellian-like trends. This supports the approximation of Maxwellian distribution for calculations in predictive simulation.

### 7.1.2. Measurement of Absolute Axial Magnetic Field, $|B_z|$ and Radial Magnetic Field, $|B_r|$

The radially resolved absolute magnitudes of the axial magnetic field,  $|B_z|$  and radial magnetic field,  $|B_r|$  were measured at evacuated condition (without plasma) ( $<10^{-3}$  mbar) and at 0.03 mbar, 0.07 mbar and 0.2 mbar argon pressure for 0.032 m and 0.060 m axial distances above the dielectric plate. R.f. power was set at 180 W. Measured axial and radial magnetic fields under evacuated condition exhibited the highest magnitudes with  $(1.507 \pm 0.005) \times 10^{-4}$  T and  $(7.67 \pm 0.01) \times 10^{-5}$  T, respectively for 0.032 m and  $(3.90 \pm 0.02) \times 10^{-5}$  T and  $(2.30 \pm 0.03) \times 10^{-5}$  T, respectively for 0.060 m.

$|B_z|$  and  $|B_r|$  for both axial distances above the dielectric plate were increasingly suppressed as pressure was increased; indicating increased utilization of the magnetic fields by the plasma. Within the coil region ( $R < 0.05$  m), where both  $|B_z|$  and  $|B_r|$  were

most utilized, a trough was formed with increase in pressure. This observation was consistent with the distribution trends seen in  $n_e$ .

### 7.1.3. Measurement of Peak H Mode Transition, $I_{tr}$ and H Mode Maintenance Currents, $I_{mt}$

H mode transition current (E to H mode transition current),  $I_{tr}$  and H mode maintenance current (H to E mode transition current),  $I_{mt}$  was measured for the argon pressure range of 0.02-0.3 mbar. At 0.02 mbar,  $I_{tr} = (16.4 \pm 0.2)$  A was required to initiate a transition from E mode to H mode. As pressure was increased,  $I_{tr}$  decreased to a minimum value of  $(13.5 \pm 0.5)$  A at 0.08 mbar before subsequently increasing to  $(15.5 \pm 0.2)$  A at 0.3 mbar. This is attributed to the power coupling of source fields which has been shown to be most efficient when  $\nu_{eff}/\omega \approx 1$ ; found at the simulated pressures of 0.07-0.08 mbar. For  $I_{mt}$  at 0.02 mbar,  $(14.3 \pm 0.2)$  A was required to maintain the discharge. As pressure was increased,  $I_{mt}$  decreases consistently to  $(8.3 \pm 0.1)$  A at 0.3 mbar. The effect of hysteresis in the working path of the system with pressure was seen from the increasing deviation between  $I_{tr}$  and  $I_{mt}$  values. The lower  $I_{mt}$  requirement at higher pressures was explained by the following points:

- i. At higher discharge pressures (with higher electron densities), multi-step ionization becomes the primary process of conversion of absorbed excited state energy over radiative de-excitation processes. Thus, more energy from the excitation collisions that occur contributes toward the ionization of particles, i.e., lower  $I_{mt}$ .
- ii. Increase in plasma collision frequency with pressure increases the number of ionizing collisions, allowing for lower  $I_{mt}$ .

- iii. From results in AOES measurement, the neutral gas temperature of the discharge was also seen to increase with pressure. With the background particles having higher kinetic energy, they were more readily ionized in collisional processes. This would result in lower  $I_{mt}$  with pressure.

#### **7.1.4. Measurement of Neutral Gas Temperature, $T_n$**

The neutral gas temperature,  $T_n$  was measured at 0.03, 0.05, 0.07, 0.1 and 0.2 mbar Ar/N<sub>2</sub> pressures for increasing and decreasing r.f. power steps at 0.032 m and 0.060 m axial distance above the dielectric plate. Changes in r.f. power and distances above the dielectric plate showed little variation in  $T_n$ . Significant increase in  $T_n$ , however, was observed when pressure was increased. These trends were explained by the following points:

- i. As Ar/N<sub>2</sub> pressure is increased at a fixed input r.f. power, more energy is coupled into the plasma; thus, increasing electron density and ion density. With more charged and neutral particles within the same volume, the collision frequency of the plasma particles increases. Transfer of kinetic energy from charged particles to neutral particles is increased via charge transfer collision of energetic ions with neutrals and de-excitation collision of ions by electrons; raising the number of thermalized neutrals within the plasma and increasing  $T_n$ .
- ii. With collisional processes limited by collision frequency, variation of r.f. power does not significantly affect  $T_n$ ; owing to the limited energy transfer from charged particles to the neutrals.
- iii. The convection of thermalized neutrals would mean that the particles would also be distributed to regions further from the source. Thus, at the measured axial

distances of 0.032 m and 0.060 m,  $T_n$  does not show significant variation beyond measurement discrepancy.

Results for  $T_n$  are summarized in Table 7.2.

**Table 7.2:** Measured maximum and minimum  $T_n$  for increasing and decreasing r.f. power steps and different axial distances above the dielectric plate.

Axial Distance Above the Dielectric Plate, $(L - z)$ (m)	R.f. Power Step During Measurement	Neutral Gas Temperature (K), $T_n$ @ Ar/N <sub>2</sub> Pressure (mbar)	
		Minimum	Maximum
0.032	Increasing	$(350 \pm 30)$ @ 0.03	$(800 \pm 20)$ @ 0.2
	Decreasing	$(380 \pm 10)$ @ 0.03	$(810 \pm 20)$ @ 0.2
0.060	Increasing	$(430 \pm 10)$ @ 0.03	$(840 \pm 30)$ @ 0.2
	Decreasing	$(420 \pm 20)$ @ 0.03	$(830 \pm 30)$ @ 0.2

## 7.2. Theoretical Characterization

For theoretical characterization, two predictive models (written in MATLAB) were used. The first predictive model was an electromagnetic field model that simulates the H mode wave magnetic fields of the coil at different discharge conditions. The spatially resolved electron density,  $n_e(r, z)$  and electron temperature,  $T_e(r, z)$  required for simulation were empirically fitted from experimental data. Simulations were run using various neutral gas temperature values including room temperature (300 K), uniform elevated temperatures (from measured results) and spatially resolved heuristically fitted temperature distributions. The second predictive model was a power deposition model that simulates the peak transition and maintenance H mode currents from the averaged electron density, electron temperature and neutral gas temperature near the plane of the coil. The H mode transition and maintenance currents were simulated at room temperature and at elevated neutral gas temperature. The effect of hysteresis in mode

transition of the discharge was also demonstrated using an experimentally fitted 3D power evolution plot.

### **7.2.1. Predictive Simulation of the Discharge Magnetic Fields**

The axial and radial magnetic field distributions in a 13.56 MHz 6-turn planar coil ICP reactor were predictively simulated for 0.03, 0.07, and 0.2 mbar argon pressures with the consideration of the effect of neutral gas heating. The spatially resolved electron densities,  $n_e(r, z)$  and electron temperatures,  $T_e(r, z)$  required for simulation were empirically fitted using 2D Gaussian based distributions from experimental data. Neutral heating (and depletion) were simulated by using spatially resolved neutral gas temperatures,  $T_n(r, z)$  which were heuristically fitted, modified Gaussian distributions. As a reference, simulation with spatially averaged neutral gas temperature,  $T_{n,ave}$  (including room temperature at 300 K) was also done for each pressure. The experimental fields were more sufficiently matched with the simulation using spatially resolved  $T_n(r, z)$  as compared to the simulation using uniform  $T_{n,ave}$ . This shows that neutral gas heating (and in effect, neutral gas depletion) plays an important role in determining the skin depth of the magnetic fields. Heating of the neutrals via ion-electron and ion-neutral collisional processes with the subsequent effect of neutral gas depletion results in a localized environment whereby less energy was required to sustain ion-electron pairs. This increases the utilization of the incident magnetic fields by the plasma (especially within the coil radius) and thus, reduces the skin depth of the fields.

### **7.2.2. Predictive Simulation of H mode Transition and Maintenance Currents**

Hysteresis occurring in the ICP plasma system was visualized via an experimentally matched, 3D power evolution surface plotted at 0.02 mbar argon pressure. Also, the simulation of H mode transition and maintenance currents in a 13.56 MHz laboratory 6

turn planar coil ICP reactor was done at the low pressure argon discharge range of 0.02-0.3 mbar for elevated and ambient neutral gas temperature. Experimental results were in good agreement for the range of 0.02-0.3 mbar for transition currents and 0.02-0.1 mbar for maintenance currents for the simulation that included neutral gas heating. The mismatch of the maintenance currents at 0.2 and 0.3 mbar was likely to be due to the non-linear effects of multistep ionization. When using ambient temperature, the simulations were poorly matched. It can be thus concluded that neutral gas heating plays a non-negligible role in determining the E to H and H to E mode transition points (i.e., H mode transition and maintenance currents) in an r.f. ICP system.

### **7.3. Suggestions for Future Work**

As the effects of neutral gas heating in an ICP discharge have been established, further improvements and follow-up studies can be made for better understanding of the discharge mechanism in theory and application:

(a) Spatially resolved measurement of neutral gas temperature,  $T_n(r, z)$

In the present study, the AOES technique was applied to deduce the neutral gas temperature,  $T_n$  and the spatially resolved temperature,  $T_n(r, z)$  had to be heuristically deduced. In future works, more innovative measurement methods can be developed and utilized for in situ radial measurement of  $T_n$ , e.g., with the incorporation of appropriate lenses that focus emissions from only the point of measurement or the development of specialized, inert resistance thermometers with adequate protection from the discharge oxidation to make localized measurements.

- (b) Theoretical calculation of spatially resolved neutral gas temperature,  $T_n(r, z)$  from the magnetic fields

With established methods and probes for measuring the magnetic fields and phases in the discharge, a novel theoretical derivation can be developed to back-calculate in situ  $T_n$  values at different radial positions from measured magnetic fields with the existing field simulation code.

- (c) Improvement of power balance model by inclusion of multistep ionization

The power balance model in Chapter 5, Section 5.4 can be improved by the inclusion of multistep ionization effect into the power loss equation. This may help improve predictive simulation of H mode maintenance current,  $I_{mt}$  at higher argon pressures; which was deviated in the present model.

- (d) Particle in Cell-Monte Carlo collisions (PIC-MCC) modeling of ICP particles with elevated neutral gas temperature profiles

Expansion of the present numerical field model into a self-contained PIC-MCC model would be the next step of development for simulation of ICP. The PIC-MCC model directly tracks the motion of a fixed amount of plasma particles in the reactor space for a set period of time. The particles are subject to interaction with the source field and from random (Monte Carlo) collision processes with other particles. The dynamics of the discharge particles with time at elevated neutral gas temperatures can be more thoroughly observed and may give interesting findings.

- (e) Development of material processing aspect in simulation for applications

Another aspect of simulation that can be developed from the present model is discharge interaction with substrate surfaces for material deposition or etching

applications. Together with PIC-MCC, modeling of chemical and kinetic interaction of plasma particles with substrate structures at elevated temperatures would be the first initiative of incorporation of this study into applicative material fields.

## REFERENCES

- Abdel-Rahman, M., Gans, T., Schulz-von der Gathen, V., & Döbele, H. F. (2005). Space and time resolved rotational state populations and gas temperatures in an inductively coupled hydrogen RF discharge. *Plasma Sources Science and Technology*, 14(1), 51. doi: <http://dx.doi.org/10.1088/0963-0252/14/1/007>
- Allen, J. E., Boyd, R. L. F., & Reynolds, P. (1957). The collection of positive ions by a probe immersed in a plasma. *Proceedings of the Physical Society. Section B*, 70(3), 297. doi: <http://dx.doi.org/10.1088/0370-1301/70/3/303>
- Amorim, J., Maciel, H. S., & Sudano, J. P. (1991). High-density plasma mode of an inductively coupled radio frequency discharge. *Journal of Vacuum Science & Technology B: Microelectronics and Nanometer Structures*, 9(2), 362-365. doi: <http://dx.doi.org/10.1116/1.585576>
- Atkinson, F., & Mingarelli, A. (2011). *Multiparameter Eigenvalue Problems Sturm-Liouville Theory*. Boca Raton: CRC Press.
- Babat, G. I. (1947). Electrodeless discharges and some allied problems. *Journal of the Institution of Electrical Engineers-Part III: Radio and Communication Engineering*, 94(27), 27-37.
- Behlman, N. J. (2009). *Electron Energy Distribution Measurements in the Plume Region of a Low Current Hollow Cathode*. Worcester Polytechnic Institute, Worcester.
- Bird, G. A. (1976). *Molecular Gas Dynamics*. Oxford: Clarendon Press.
- Birdsall, C. K. (1991). Particle-in-cell charged-particle simulations, plus Monte Carlo collisions with neutral atoms, PIC-MCC. *Plasma Science, IEEE Transactions on*, 19(2), 65-85. doi: <http://dx.doi.org/10.1109/27.106800>
- Birdsall, C. K., & Langdon, A. B. (1985). *Plasma Simulation via Computer Simulation*. New York: McGraw-Hill Book Company.
- Boas, M. (1983). *Mathematical Methods in the Physical Sciences. Mathematical methods in physical sciences* (2nd ed.). Hoboken: John Wiley & Sons.
- Book, D. L. (1990). *NRL Plasma Formulary. Revision* (No. NRL-PUB-177-4405). Washington, D.C.: Naval Research Lab.

- Boulos, M. I. (1976). Flow and temperature fields in the fire-ball of an inductively coupled plasma. *Plasma Science, IEEE Transactions on*, 4(1), 28-39. doi: <http://dx.doi.org/10.1109/TPS.1976.4316928>
- Chabert, P., & Braithwaite, N. (2011). *Physics of Radio-Frequency Plasmas*. Cambridge: Cambridge University Press.
- Chakrabarty, C. K. (2006). Magnetic field measurements for N<sub>2</sub> and H<sub>2</sub> discharges from a low frequency RF inductively coupled plasma source. *Measurement*, 39(8), 736-739. doi: <http://dx.doi.org/10.1016/j.measurement.2006.03.003>
- Chen, F. F. (1965). Electric Probes. In R. H. Huddlestone & S. L. Leonard (Eds.), *Plasma Diagnostic Techniques*. New York: Academic Press Inc.
- Chen, F. F. (2003). *Mini-Course on Plasma Diagnostics: Langmuir Probe Diagnostics*. Paper presented at the IEEE-ICOPS Meeting, Jeju, Korea.
- Chen, F. F. (2008). RF plasma sources for semiconductor processing. In d'Agostino, R., Favia, P., Kawai, Y., Ikegami, H., Sato, N., & Arefi-Khonsari, F. (Eds.), *Advanced Plasma Technology*. Hoboken, New Jersey: John Wiley & Sons, Inc.
- Chen, F. F. (2009). Langmuir probes in RF plasma: surprising validity of OML theory. *Plasma Sources Science and Technology*, 18(3), 035012. doi: <http://dx.doi.org/10.1088/0963-0252/18/3/035012>
- Conde, L. (2011). An introduction to Langmuir probe diagnostics of plasmas. Universidad Politécnica de Madrid.
- Crintea, D. L., Czarnetzki, U., Iordanova, S., Koleva, I., & Luggenhölscher, D. (2009). Plasma diagnostics by optical emission spectroscopy on argon and comparison with Thomson scattering. *Journal of Physics D: Applied Physics*, 42(4), 045208. doi: <http://dx.doi.org/10.1088/0022-3727/42/4/045208>
- Cruden, B. A., Rao, M., Sharma, S. P., & Meyyappan, M. (2002). Neutral gas temperature estimates in an inductively coupled CF<sub>4</sub> plasma by fitting diatomic emission spectra. *Journal of Applied Physics*, 91(11), 8955-8964. doi: <http://dx.doi.org/10.1063/1.1474614>
- Cunge, G., Crowley, B., Vender, D., & Turner, M. M. (1999). Characterization of the E to H transition in a pulsed inductively coupled plasma discharge with internal coil geometry: bi-stability and hysteresis. *Plasma Sources Science and Technology*, 8(4), 576. doi: <http://dx.doi.org/10.1088/0963-0252/8/4/309>

- Cuomo, J. J., Guarnieri, C. R., Hopwood, J. A., & Whitehair, S. J. (1994). *U.S. Patent No. 5,280,154*. Washington, DC: U.S. Patent and Trademark Office.
- Czerwiec, T., & Graves, D. B. (2004). Mode transitions in low pressure rare gas cylindrical ICP discharge studied by optical emission spectroscopy. *Journal of Physics D: Applied Physics*, 37(20), 2827. doi: <http://dx.doi.org/10.1088/0022-3727/37/20/009>
- Daltrini, A. M., Moshkalev, S. A., Morgan, T. J., Piejak, R. B., & Graham, W. G. (2008). Plasma power measurement and hysteresis in the E-H transition of a rf inductively coupled plasma system. *Applied Physics Letters*, 92(6), 061504-061504-061503. doi: <http://dx.doi.org/10.1063/1.2844885>
- Davis, G. P., & Gottscho, R. A. (1983). Measurement of spatially resolved gas-phase plasma temperatures by optical emission and laser-induced fluorescence spectroscopy. *Journal of Applied Physics*, 54(6), 3080-3086. doi: <http://dx.doi.org/10.1063/1.332514>
- Donnelly, V. M., & Malyshev, M. V. (2000). Diagnostics of inductively coupled chlorine plasmas: Measurements of the neutral gas temperature. *Applied Physics Letters*, 77(16), 2467-2469. doi: <http://dx.doi.org/10.1063/1.1318727>
- Eckert, H. U. (1962). Diffusion theory of the electrodeless ring discharge. *Journal of Applied Physics*, 33(9), 2780-2788. doi: <http://dx.doi.org/10.1063/1.1702549>
- El-Fayoumi, I. M. (1996). *The Electrical and Electromagnetic Properties of a Low Frequency, Inductively Coupled RF Plasma Source*. Flinders University of South Australia, Adelaide.
- El-Fayoumi, I. M., & Jones, I. R. (1997). Measurement of the induced plasma current in a planar coil, low-frequency, RF induction plasma source. *Plasma Sources Science and Technology*, 6(2), 201. doi: <http://dx.doi.org/10.1088/0963-0252/6/2/014>
- El-Fayoumi, I. M., & Jones, I. R. (1998). Theoretical and experimental investigations of the electromagnetic field within a planar coil, inductively coupled RF plasma source. *Plasma Sources Science and Technology*, 7(2), 162. doi: <http://dx.doi.org/10.1088/0963-0252/7/2/011>
- El-Fayoumi, I. M., Jones, I. R., & Turner, M. M. (1998). Hysteresis in the E-to H-mode transition in a planar coil, inductively coupled rf argon discharge. *Journal of Physics D: Applied Physics*, 31(21), 3082. doi: <http://dx.doi.org/10.1088/0022-3727/31/21/014>

- Fruchtman, A. (2008). Neutral depletion in a collisionless plasma. *Plasma Science, IEEE Transactions on*, 36(2), 403-413. doi: <http://dx.doi.org/10.1109/TPS.2008.918777>
- Fruchtman, A., Makrinich, G., Chabert, P., & Rax, J.-M. (2005). Enhanced plasma transport due to neutral depletion. *Physical Review Letters*, 95(11), 115002. doi: <http://dx.doi.org/10.1103/PhysRevLett.95.115002>
- Fruchtman, A., & Rax, J. M. (2010). Neutral-gas depletion and repletion in plasmas. *Physics of Plasmas*, 17, 043502. doi: <http://dx.doi.org/10.1063/1.3368041>
- Gagné, R. R. J., & Cantin, A. (1972). Investigation of an rf plasma with symmetrical and asymmetrical electrostatic probes. *Journal of Applied Physics*, 43(6), 2639-2647. doi: <http://dx.doi.org/10.1063/1.1661573>
- Gans, T., Critea, D. L., O'Connell, D., & Czarnetzki, U. (2007). A planar inductively coupled radio-frequency magnetic neutral loop discharge. *Journal of Physics D: Applied Physics*, 40(15), 4508. doi: <http://dx.doi.org/10.1088/0022-3727/40/15/021>
- Gao, F., Zhao, S.-X., Li, X.-S., & Wang, Y.-N. (2010). Effects of matching network on the hysteresis during E and H mode transitions in argon inductively coupled plasma. *Physics of Plasmas*, 17, 103507. doi: <http://dx.doi.org/10.1063/1.3496385>
- Godyak, V. A., Piejak, R. B., & Alexandrovich, B. M. (2002). Electron energy distribution function measurements and plasma parameters in inductively coupled argon plasma. *Plasma Sources Science and Technology*, 11(4), 525. doi: <http://dx.doi.org/10.1088/0963-0252/11/4/320>
- Gottscho, R. A., & Donnelly, V. M. (1984). Optical emission actinometry and spectral line shapes in rf glow discharges. *Journal of Applied Physics*, 56(2), 245-250. doi: <http://dx.doi.org/10.1063/1.333954>
- Gudmundsson, J. T., & Lieberman, M. A. (1998). Magnetic induction and plasma impedance in a planar inductive discharge. *Plasma Sources Science and Technology*, 7(2), 83. doi: <http://dx.doi.org/10.1088/0963-0252/7/2/002>
- Hash, D. B., Bose, D., Rao, M. V. V. S., Cruden, B. A., Meyyappan, M., & Sharma, S. P. (2001). Impact of gas heating in inductively coupled plasmas. *Journal of Applied Physics*, 90(5), 2148-2157. doi: <http://dx.doi.org/10.1063/1.1390503>

- Hayashi, M. (1981). *Recommended Values of Transport Cross Sections for Elastic Collision and Total Collision Cross Section of Electrons in Atomic and Molecular Gases*, IPPJ- AM-19. Nagoya.
- Hebner, G. A. (1996). Spatially resolved, excited state densities and neutral and ion temperatures in inductively coupled argon plasmas. *Journal of applied physics*, 80(5), 2624-2636. doi: <http://dx.doi.org/10.1063/1.363178>
- Henriksen, B. B., Keefer, D. R., & Clarkson, M. H. (1971). Electromagnetic field in electrodeless discharge. *Journal of Applied Physics*, 42(13), 5460-5464. doi: <http://dx.doi.org/10.1063/1.1659964>
- Herman, R., 2008. *A Second Course in Ordinary Differential Equations: Dynamical Systems and Boundary Value Problems*, Available at: [http://people.uncw.edu/hermanr/mat463/ODEBook/Book/ODE\\_Main.pdf](http://people.uncw.edu/hermanr/mat463/ODEBook/Book/ODE_Main.pdf).
- Herzberg, G. (1950). *Spectra of diatomic molecules* (2 ed. Vol. 1). New York: D. Van Nostrand Company, Inc.
- Hittorf, W. (1884). Ueber die electricitätsleitung der gase. *Annalen der Physik*, 257(1), 90-139. doi: <http://dx.doi.org/10.1002/andp.18842570105>
- Hollas, J. M. (2004). *Modern Spectroscopy* (4 ed.). Chichester, West Sussex: John Wiley & Sons.
- Hopwood, J. (1992). Review of inductively coupled plasmas for plasma processing. *Plasma Sources Science and Technology*, 1(2), 109. doi: <http://dx.doi.org/10.1088/0963-0252/1/2/006>
- Hopwood, J., & Asmussen, J. (1991). Neutral gas temperatures in a multipolar electron cyclotron resonance plasma. *Applied Physics Letters*, 58(22), 2473-2475.
- Hopwood, J., Guarnieri, C. R., Whitehair, S. J., & Cuomo, J. J. (1993). Langmuir probe measurements of a radio frequency induction plasma. *Journal of Vacuum Science & Technology A: Vacuum, Surfaces, and Films*, 11(1), 152-156. doi: <http://dx.doi.org/10.1063/1.105232>
- Hopwood, J., Minayeva, O., & Yin, Y. (2000). Fabrication and characterization of a micromachined 5 mm inductively coupled plasma generator. *Journal of Vacuum Science & Technology B: Microelectronics and Nanometer Structures*, 18(5), 2446-2451. doi: <http://dx.doi.org/10.1116/1.1288945>

- Huber, K. P., & Herzberg, G. (1979). *Constants of Diatomic Molecules*. New York: Van Nostrand Reinhold Company.
- Jayapalan, K. K., & Chin, O. H. (2012). The effects of neutral gas heating on H mode transition and maintenance currents in a 13.56 MHz planar coil inductively coupled plasma reactor. *Physics of Plasmas (1994-present)*, *19*(9), 093501. doi: <http://dx.doi.org/10.1063/1.4750055>
- Jayapalan, K. K., & Chin, O. H. (2014). Effect of neutral gas heating on the wave magnetic fields of a low pressure 13.56 MHz planar coil inductively coupled argon discharge. *Physics of Plasmas (1994-present)*, *21*(4), 043510. doi: <http://dx.doi.org/10.1063/1.4872004>
- Jones, F. L. (1953). Electrical discharges. *Reports on Progress in Physics*, *16*(1), 216. doi: <http://dx.doi.org/10.1088/0034-4885/16/1/306>
- Kaufman, M. (1976). Some Novel Diagnostic Techniques for Plasma Chemistry. *Pure and Applied Chemistry*, *48*(2), 155-161.
- Keeble, F. (1989). U. S. Patent No. 4,844,775. Washington, DC: U.S. Patent and Trademark Office.
- Keefer, D. R., Sprouse, J. A., & Loper, F. C. (1973). The Electrodeless Arc with Radial Inflow. *Plasma Science, IEEE Transactions on*, *1*(4), 71-75. doi: <http://dx.doi.org/10.1109/TPS.1973.4316116>
- Kirchner, F. (1925). Über die Glimmentladung bei schnell wechselndem Feld. *Annalen der Physik*, *382*(11), 287-301.
- Knipp, C. T., & Knipp, J. K. (1931). Electrodeless Discharge: Method of Measuring Induced Current, Variation of Current with Pressure for Various Gases. *Physical Review*, *38*(5), 948. doi: <http://dx.doi.org/10.1103/PhysRev.38.948>
- Kortshagen, U., Gibson, N. D., & Lawler, J. E. (1996). On the E-H mode transition in RF inductive discharges. *Journal of Physics D: Applied Physics*, *29*(5), 1224. doi: <http://dx.doi.org/10.1088/0022-3727/29/5/017>
- Kovács, I. (1969). *Rotational structure in the spectra of diatomic molecules*. London: Adam Hilger Ltd.

- Kreyszig, E. (2011). *Advanced Engineering Mathematics* (10th ed.). Hoboken: John Wiley & Sons.
- Kunz, J. (1932). XC. Theory of electromagnetic and electrostatic induction in electrodeless discharges. *The London, Edinburgh, and Dublin Philosophical Magazine and Journal of Science*, 13(87), 964-975.
- Laframboise, J. G. (1966). *Theory of spherical and cylindrical Langmuir probes in a collisionless, Maxwellian plasma at rest*. University of Toronto, Toronto.
- Lee, H. C., Kim, D. H., & Chung, C. W. (2013). Discharge mode transition and hysteresis in inductively coupled plasma. *Applied Physics Letters*, 102(23), 234104. doi: <http://dx.doi.org/10.1063/1.4809925>
- Li, H. (2006). *Measurements of electron energy distribution function and neutral gas temperature in an inductively coupled plasma*. University of Saskatchewan, Saskatoon.
- Li, H., Xiao, C., Zhang, E., Singh, A. K., & Hirose, A. (2011). Measurement of neutral gas temperature in inductively coupled plasmas. *Radiation Effects & Defects in Solids*, 166(6), 399-407. doi: <http://dx.doi.org/10.1080/10420150.2011.566876>
- Li, M., Wu, H.-M., & Chen, Y. (1995). Two-dimensional simulation of inductive plasma sources with self-consistent power deposition. *Plasma Science, IEEE Transactions on*, 23(4), 558-562. doi: <http://dx.doi.org/10.1109/27.467975>
- Liard, L., Raimbault, J. L., Rax, J. M., & Chabert, P. (2007). Plasma transport under neutral gas depletion conditions. *Journal of Physics D: Applied Physics*, 40(17), 5192. doi: <http://dx.doi.org/10.1088/0022-3727/40/17/026>
- Lieberman, M. A., & Lichtenberg, A. J. (2005). *Principles of Plasma Discharges and Materials Processing* (2<sup>nd</sup> ed.). Hoboken, New Jersey: John Wiley & Sons, Inc.
- Lim, A. N. (2010). *Characterization of an inductively coupled plasma produced in argon at 13.56 MHz*. University of Malaya, Kuala Lumpur.
- Lister, G. G., Li, Y.-M., & Godyak, V. A. (1996). Electrical conductivity in high-frequency plasmas. *Journal of Applied Physics*, 79(12), 8993. doi: <http://dx.doi.org/10.1063/1.362631>

- MacKinnon, K. A. (1929). LXVI. On the origin of the electrodeless discharge. *The London, Edinburgh, and Dublin Philosophical Magazine and Journal of Science*, 8(52), 605-616.
- Magnus, F., & Gudmundsson, J. T. (2008). Digital smoothing of the Langmuir probe IV characteristic. *Review of Scientific Instruments*, 79(7), 073503. doi: <http://dx.doi.org/10.1063/1.2956970>
- Maurice, C. Y. M. (2003). *Inductively Coupled Plasmas: Ion dynamics and interactions with bone tissue*. Technische Universiteit Eindhoven, Eindhoven.
- Mostaghimi, J., & Boulos, M. I. (1989). Two-dimensional electromagnetic field effects in induction plasma modelling. *Plasma chemistry and plasma processing*, 9(1), 25-44. doi: <http://dx.doi.org/10.1116/1.575936>
- Mott-Smith, H. M., & Langmuir, I. (1926). The theory of collectors in gaseous discharges. *Physical review*, 28(4), 727. doi: <http://dx.doi.org/10.1103/PhysRev.28.727>
- Nam, S. K., & Economou, D. J. (2004). Two-dimensional simulation of a miniaturized inductively coupled plasma reactor. *Journal of Applied Physics*, 95(5), 2272-2277. doi: <http://dx.doi.org/10.1063/1.1644043>
- Nanbu, K. (2000). Probability theory of electron-molecule, ion-molecule, molecule-molecule, and Coulomb collisions for particle modeling of materials processing plasmas and cases. *Plasma Science, IEEE Transactions on*, 28(3), 971-990. doi: <http://dx.doi.org/10.1109/27.887765>
- O'Connell, D., Gans, T., Crintea, D. L., Czarnetzki, U., & Sadeghi, N. (2008). Neutral gas depletion mechanisms in dense low-temperature argon plasmas. *Journal of Physics D: Applied Physics*, 41(3), 035208. doi: <http://dx.doi.org/10.1088/0022-3727/41/3/035208>
- Ogle, J. S. (1990). U. S, Patent 4,948,458. Washington, DC: U.S. Patent and Trademark Office.
- Ostrikov, K. N., Denysenko, I. B., Tsakadze, E. L., Xu, S., & Storer, R. G. (2002). Diagnostics and two-dimensional simulation of low-frequency inductively coupled plasmas with neutral gas heating and electron heat fluxes. *Journal of applied physics*, 92(9), 4935-4946. doi: <http://dx.doi.org/10.1063/1.1510598>

- Panagopoulos, T., Kim, D., Midha, V., & Economou, D. J. (2002). Three-dimensional simulation of an inductively coupled plasma reactor. *Journal of Applied Physics*, 91(5), 2687-2696. doi: <http://dx.doi.org/10.1063/1.1448673>
- Paranjpe, A. P. (1994). Modeling an inductively coupled plasma source. *Journal of Vacuum Science & Technology A*, 12(4), 1221-1228. doi: <http://dx.doi.org/10.1116/1.579299>
- Patrick, R., Bose, F., Schoenborn, P., & Toda, H. (1995). *U.S. Patent No. 5,401,350*. Washington, DC: U.S. Patent and Trademark Office.
- Phelps, A. V. (1991). Cross sections and swarm coefficients for nitrogen ions and neutrals in N<sub>2</sub> and argon ions and neutrals in Ar for energies from 0.1 eV to 10 keV. *Journal of physical and chemical reference data*, 20(3), 557-573. doi: <http://dx.doi.org/10.1063/1.555889>
- Phillips, D. M. (1976). Determination of gas temperature from unresolved bands in the spectrum from a nitrogen discharge. *Journal of Physics D: Applied Physics*, 9(3), 507. doi: <http://dx.doi.org/10.1088/0022-3727/9/3/017>
- Piejak, R. B., Godyak, V. A., & Alexandrovich, B. M. (1992). A simple analysis of an inductive RF discharge. *Plasma sources science and technology*, 1(3), 179. doi: <http://dx.doi.org/10.1088/0963-0252/1/3/006>
- Razzak, M. A., Kondo, K., Uesugi, Y., Ohno, N., & Takamura, S. (2004). Transition from electrostatic-to-electromagnetic mode in a radio-frequency Ar inductively coupled plasma in atmospheric pressure. *Journal of Applied Physics*, 95(2), 427-433. doi: <http://dx.doi.org/10.1063/1.1635650>
- Sadeghi, N., Van De Grift, M., Vender, D., Kroesen, G. M. W., & De Hoog, F. J. (1997). Transport of argon ions in an inductively coupled high-density plasma reactor. *Applied physics letters*, 70(7), 835-837. doi: <http://dx.doi.org/10.1063/1.118218>
- Sadiku, M. (2001). *Elements of Electromagnetics* (3rd ed.). New York: Oxford University Press.
- Sadiku, M. (2009). *Numerical Techniques in Electromagnetics with MATLAB* (3rd ed.). Boca Raton: CRC Press.
- Salon, S., & Chari, M. (2000). *Numerical Methods in Electromagnetism*. San Diego: Academic Press Inc.

- Sansonetti, J. E., Martin, W. C., & Young, S. L. (2005). Handbook of basic atomic spectroscopic data. *Journal of physical and chemical reference data*, 34(4), 1559-2260. doi: <http://dx.doi.org/10.1063/1.1800011>
- Schottky, W. (1924). Wandströme und Theorie der positiven Säule. *Phys. Z*, 25, 342-348.
- Serikov, V. V., Kawamoto, S., & Nanbu, K. (1999). Particle-in-cell plus direct simulation Monte Carlo (PIC-DSMC) approach for self-consistent plasma-gas simulations. *Plasma Science, IEEE Transactions on*, 27(5), 1389-1398. <http://dx.doi.org/10.1109/27.799817>
- Shamrai, K. P., Pavlenko, V. P., & Taranov, V. B. (1997). Excitation, conversion and damping of waves in a helicon plasma source driven by an  $m = 0$  antenna. *Plasma physics and controlled fusion*, 39(3), 505. doi: <http://dx.doi.org/10.1088/0741-3335/39/3/011>
- Shimada, M. (2006). *Experimental and numerical studies of neutral gas depletion in an inductively coupled plasma*. University of California, San Diego.
- Shimada, M., Tynan, G. R., & Cattolica, R. (2007). Neutral gas density depletion due to neutral gas heating and pressure balance in an inductively coupled plasma. *Plasma Sources Science and Technology*, 16(1), 193. doi: <http://dx.doi.org/10.1088/0963-0252/16/1/024>
- Shimada, M., Tynan, G. R., & Cattolica, R. (2008). Neutral depletion in inductively coupled plasmas using hybrid-type direct simulation Monte Carlo. *Journal of Applied Physics*, 103(3), 033304-033304. doi: <http://dx.doi.org/10.1063/1.2836938>
- Smith, H., Lynch, W. A., & Hilberry, N. (1931). The electrodeless discharge in mercury vapor. *Physical Review*, 37(9), 1091. doi: <http://dx.doi.org/10.1103/PhysRev.37.1091>
- Song, M. A., Lee, Y. W., & Chung, T. H. (2011). Characterization of an inductively coupled nitrogen-argon plasma by Langmuir probe combined with optical emission spectroscopy. *Physics of Plasmas*, 18(2), 023504-023512. doi: <http://dx.doi.org/10.1063/1.3554706>
- Stewart, R. A., Vitello, P., Graves, D. B., Jaeger, E. F., & Berry, L. A. (1995). Plasma uniformity in high-density inductively coupled plasma tools. *Plasma Sources Science and Technology*, 4(1), 36. doi: <http://dx.doi.org/10.1088/0963-0252/4/1/005>

- Stittsworth, J. A., & Wendt, A. E. (1996). Reactor geometry and plasma uniformity in a planar inductively coupled radio frequency argon discharge. *Plasma Sources Science and Technology*, 5(3), 429. doi: <http://dx.doi.org/10.1088/0963-0252/5/3/011>
- Stuhlman, O., & Whitaker, M. D. (1930). High Frequency Electrodeless Discharge Characteristics. *Review of Scientific Instruments*, 1(12), 772-779. doi: <http://dx.doi.org/10.1063/1.1748667>
- Suzuki, K., Nakamura, K., Ohkubo, H., & Sugai, H. (1998). Power transfer efficiency and mode jump in an inductive RF discharge. *Plasma Sources Science and Technology*, 7(1), 13. doi: <http://dx.doi.org/10.1088/0963-0252/7/1/003>
- Takao, Y., Kusaba, N., Eriguchi, K., & Ono, K. (2010). Two-dimensional particle-in-cell Monte Carlo simulation of a miniature inductively coupled plasma source. *Journal of Applied Physics*, 108(9), 093309-093308. doi: <http://dx.doi.org/10.1063/1.3506536>
- Taylor, H. E. (2001). *Inductively coupled plasma-mass spectrometry: practices and techniques*: London, England: Academic Press.
- Thomson, J. (1930). XXII. On the mechanism of the electrodeless discharge. *The London, Edinburgh, and Dublin Philosophical Magazine and Journal of Science*, 10(63), 280-291.
- Thomson, J. J. (1927). The electrodeless discharge through gases. *Proceedings of the Physical Society*, 40(1), 79. doi: <http://dx.doi.org/10.1088/0959-5309/40/1/314>
- Townsend, J. S. (1932). LXX. Electrodeless discharges. *The London, Edinburgh, and Dublin Philosophical Magazine and Journal of Science*, 13(86), 745-759.
- Townsend, J. S., & Donaldson, R. H. (1928). XVI. Electrodeless discharges. *The London, Edinburgh, and Dublin Philosophical Magazine and Journal of Science*, 5(27), 178-191.
- Turner, M. M., & Lieberman, M. A. (1999). Hysteresis and the E-to-H transition in radiofrequency inductive discharges. *Plasma Sources Science and Technology*, 8(2), 313. doi: <http://dx.doi.org/10.1088/0963-0252/8/2/312>
- Tynan, G. R. (1999). Neutral depletion and transport mechanisms in large-area high density plasma sources. *Journal of Applied Physics*, 86(10), 5356-5364. doi: <http://dx.doi.org/10.1063/1.371532>

- Uchida, T., & Hamaguchi, S. (2008). Magnetic neutral loop discharge (NLD) plasmas for surface processing. *Journal of Physics D: Applied Physics*, 41(8), 083001. doi: <http://dx.doi.org/10.1088/0022-3727/41/8/083001>
- Vahedi, V., Lieberman, M. A., DiPeso, G., Rognien, T. D., & Hewett, D. (1995). Analytic model of power deposition in inductively coupled plasma sources. *Journal of Applied Physics*, 78(3), 1446-1458. doi: <http://dx.doi.org/10.1063/1.360723>
- Whiting, E. E. (1968). An empirical approximation to the Voigt profile. *Journal of Quantitative Spectroscopy and Radiative Transfer*, 8(6), 1379-1384. doi: [http://dx.doi.org/10.1016/0022-4073\(68\)90081-2](http://dx.doi.org/10.1016/0022-4073(68)90081-2)
- Wormhoudt, J., Stanton, A. C., Richards, A. D., & Sawin, H. H. (1987). Atomic chlorine concentration and gas temperature measurements in a plasma etching reactor. *Journal of Applied Physics*, 61(1), 142-148. doi: <http://dx.doi.org/10.1063/1.338846>
- Xu, S., Ostrikov, K. N., Li, Y., Tsakadze, E. L., & Jones, I. R. (2001). Low-frequency, high-density, inductively coupled plasma sources: Operation and applications. *Physics of Plasmas*, 8(5), 2549-2557. doi: <http://dx.doi.org/10.1063/1.1343887>
- Xu, S., Ostrikov, K. N., Luo, W., & Lee, S. (2000). Hysteresis and mode transitions in a low-frequency inductively coupled plasma. *Journal of Vacuum Science & Technology A*, 18(5), 2185-2197. doi: <http://dx.doi.org/10.1116/1.1286142>
- Yun, S., Taylor, K., & Tynan, G. R. (2000). Measurement of radial neutral pressure and plasma density profiles in various plasma conditions in large-area high-density plasma sources. *Physics of Plasmas*, 7, 3448. doi: <http://dx.doi.org/10.1063/1.874209>
- Zhou, P. (1993). *Numerical Analysis of Electromagnetic Fields*. (J. Kassakian & D. H. Naunin, Eds.). New York: Springer-Verlag Berlin Heidelberg.

## APPENDIX A: LANGMUIR PROBE PARAMETRIC SOLVER

```
%%%%%%%%%%%%%%%%%%%%%%%%%%%%%%%%%%%%%%%%%%%%%%%%%%%%%%%%%%%%%%%%%%%%%%%%
%                               Probe Parameters and Common Constants                               %
%%%%%%%%%%%%%%%%%%%%%%%%%%%%%%%%%%%%%%%%%%%%%%%%%%%%%%%%%%%%%%%%%%%%%%%%

Aprobe=4.76E-6; % Probe Area (m-2)
el=1.6E-19; % Electronic Charge (C)
me=9.1E-31; % Electron Mass (kg)
k=1.38E-23; % Boltzmann Constant (J K-1)
Baseline=-2.6E-2; % Measured Baseline Without Signal

%%%%%%%%%%%%%%%%%%%%%%%%%%%%%%%%%%%%%%%%%%%%%%%%%%%%%%%%%%%%%%%%%%%%%%%%
%                               Oscilloscope Data Extraction Code                               %
%%%%%%%%%%%%%%%%%%%%%%%%%%%%%%%%%%%%%%%%%%%%%%%%%%%%%%%%%%%%%%%%%%%%%%%%

CSVCH2=dir('*CH2.csv');
CSVCH3=dir('*CH3.csv');
psize=size(CSVCH2,1);

DPACK=[];

for p=1:psize

    filenameCH2=CSVCH2(p).name;
    filenameCH3=CSVCH3(p).name;

    DSETCH2=csvread(filenameCH2,0,4);
    DSETCH3=csvread(filenameCH3,0,4);
    DSET=[DSETCH3(:,1) DSETCH2(:,1)];
    DPACK=cat(2,DPACK,DSET);

end

ParamMat=[];
EEDFMat=[];

msize=size(DPACK,2);

%%%%%%%%%%%%%%%%%%%%%%%%%%%%%%%%%%%%%%%%%%%%%%%%%%%%%%%%%%%%%%%%%%%%%%%%
%                               Calculation Loop for Each I-V Data                               %
%%%%%%%%%%%%%%%%%%%%%%%%%%%%%%%%%%%%%%%%%%%%%%%%%%%%%%%%%%%%%%%%%%%%%%%%

y=1; n=2;

for p=1:psize
```

```

%%%%%%%%%%%%%%%%%%%%%%%%%%%%%%%%%%%%%%%%%%%%%%%%%%%%%%%%%%%%%%%%%%%%%%%%
%                               Current Monitoring Resistor Select                               %
%%%%%%%%%%%%%%%%%%%%%%%%%%%%%%%%%%%%%%%%%%%%%%%%%%%%%%%%%%%%%%%%%%%%%%%%

q=2.*p-1;
filenameCH2=CSVCH2(p).name;
disp(filenameCH2);

Rinput=input('Choose Current Monitoring Resistance (1==>10 Ohm, 2==>100 Ohm
3==>1 kOhm (Default=100 Ohm)-->'); % Current Monitoring Resistance Select
(Ohm)

if Rinput==1
    PrRes=10;
    disp(PrRes);
elseif isempty(Rinput)==1 || Rinput==2
    PrRes=100;
    disp(PrRes);
elseif Rinput==3
    PrRes=1000;
    disp(PrRes);
else
    disp('Input Error')
    break
end

%%%%%%%%%%%%%%%%%%%%%%%%%%%%%%%%%%%%%%%%%%%%%%%%%%%%%%%%%%%%%%%%%%%%%%%%
%                               Data Smoothing Algorithm                               %
%%%%%%%%%%%%%%%%%%%%%%%%%%%%%%%%%%%%%%%%%%%%%%%%%%%%%%%%%%%%%%%%%%%%%%%%

inputtol=input('Input smoothing tolerance (default==1E-3)-->');

if isempty(inputtol)==1;
    inputtol=1E-3;
end

DPACK(:,q)=10.*DPACK(:,q);
DPACK(:,q+1)=DPACK(:,q+1)./PrRes-Baseline./PrRes;
smoothplot=spaps(DPACK(:,q),DPACK(:,q+1),inputtol);
smoothplotvals=fval(smoothplot,DPACK(:,q));

```

```

figure(1)

plot(DPACK(:,q),DPACK(:,q+1),'om');
xlabel('Ramp Voltage (V/V)')
ylabel('Probe Current (I/A)')

hold on

fnplt(smoothplot,'k');

hold off

Okay=input('Fit Okay? (y/n)-->');

if isempty(Okay)==1;

    Okay=1;

end

Next=2;

while Next==2

    while Okay==2

        inputtol=input('Input smoothing tolerance (default==1E-3)-->');

        if isempty(inputtol)==1;

            inputtol=1E-3;

        end

        smoothplot=spaps(DPACK(:,q),DPACK(:,q+1),inputtol);

        smoothplotvals=fnval(smoothplot,DPACK(:,q));

        figure(1);

        plot(DPACK(:,q),DPACK(:,q+1),'om');
        xlabel('Ramp Voltage (V/V)')
        ylabel('Probe Current (I/A)')

        hold on

        fnplt(smoothplot,'k');

        hold off

        Okay=input('Fit Okay? (y/n)-->');

        if isempty(Okay)==1;

            Okay=1;

        end

    end

end

%%%%%%%%%%%%%%%%%%%%%%%%%%%%%%%%%%%%%%%%%%%%%%%%%%%%%%%%%%%%%%%%%%%%%%%%%%%%%%
%                               Ion Current Calculation and Subtraction                               %
%%%%%%%%%%%%%%%%%%%%%%%%%%%%%%%%%%%%%%%%%%%%%%%%%%%%%%%%%%%%%%%%%%%%%%%%%%%%%%

if Okay==1

    Good=2;

```

```

while Good==2

figure(1);

plot(DPACK(:,q),DPACK(:,q+1),'om');
xlabel('Ramp Voltage (V/V)')
ylabel('Probe Current (I/A)')

hold on

fnplt(smoothplot,'k');

hold off

disp('Choose Ion Saturation Current Region');

[Vionpoints Iionpoints]=ginput(2);

Iionsat=fnmin(smoothplot,[Vionpoints(1,1) Vionpoints(2,1)]); % Ion
Saturation Current (A)

IonCurrentFit=polyfit(Vionpoints, Iionpoints,1);

IonCurrentVals=IonCurrentFit(1).*DPACK(:,q)+IonCurrentFit(2);

ElectronCurrent=smoothplotvals-IonCurrentVals;

figure(2)

fnplt(smoothplot,'b')

hold on

plot(DPACK(:,q),IonCurrentVals,'g');

plot(DPACK(:,q),ElectronCurrent,'k');

hold off

Good=input('Good Representation? (y/n)-->');

end

smoothplotelec=spaps(DPACK(:,q),ElectronCurrent,0);

Good=2;

%%%%%%%%%%%%%%%%%%%%%%%%%%%%%%%%%%%%%%%%%%%%%%%%%%%%%%%%%%%%%%%%%%%%%%%%
%                               Electron Saturation Current Calculation                               %
%%%%%%%%%%%%%%%%%%%%%%%%%%%%%%%%%%%%%%%%%%%%%%%%%%%%%%%%%%%%%%%%%%%%%%%%

figure(2)

fnplt(smoothplotelec,'k');

while Good==2

disp('Choose Electron Saturation Current Extrapolation Points');

[Veleepoints Ielecpoints]=ginput(2);

[IelecCoeff IelecLin]=polyfit([Veleepoints(1,1)
Veleepoints(2,1)], [fnval(smoothplotelec, Veleepoints(1,1))
fnval(smoothplotelec, Veleepoints(2,1))], 1);

IelecLinmin=polyval(IelecCoeff, DPACK(1,q));

```

```

IelecLinmax=polyval(IelecCoeff,DPACK(size(DPACK,1),q));

fnplt(smoothplotelec,'k');

hold on

plot([DPACK(1,q) Velecpoints(1,1) Velecpoints(2,1)
      DPACK(size(DPACK,1),q)], [IelecLinmin fnval(smoothplotelec,
      Velecpoints(1,1)) fnval(smoothplotelec,Velecpoints(2,
      1)) IelecLinmax], '--g')

hold off

Good=input('Good Representation? (y/n)-->');

end

Ielecsata=max(ElectronCurrent); % Electron Saturation Current by Max
Value (A)

hold on

line([min(DPACK(:,q)) max(DPACK(:,q))], [Ielecsata Ielecsata],
      'LineStyle', '--', 'Color', 'b')

hold off

%%%%%%%%%%%%%%%%%%%%%%%%%%%%%%%%%%%%%%%%%%%%%%%%%%%%%%%%%%%%%%%%%%%%%%%%
%           Plasma and Floating Potential Calculation           %
%%%%%%%%%%%%%%%%%%%%%%%%%%%%%%%%%%%%%%%%%%%%%%%%%%%%%%%%%%%%%%%%%%%%%%%%

secondarydiff=fnder(smoothplot,2);

disp('Choose Zero Point Range (Plasma Potential)');

figure(3);

fnplt(secondarydiff,'b');
xlabel('Ramp Voltage (V/V)')
ylabel('d^2I/dV^2')

hold on

[Vplaspoints d2IdV2points]=ginput(2);

hold off

Vfloat=fnzeros(smoothplot);

Vfloat=Vfloat(1,1); % Floating Potential (V)

Vplasma=fnzeros(secondarydiff, [Vplaspoints(1,1),Vplaspoints(2,1)]);

Vplasma=Vplasma(1,1); % Plasma Potential (V)

Ilinrange=fnval(smoothplotelec,Vfloat:0.01:Vplasma);

Ielecsatb=polyval(IelecCoeff,Vplasma); % Electron Saturation Current at
Plasma Potential (A)

```

```

%%%%%%%%%%%%%%%%%%%%%%%%%%%%%%%%%%%%%%%%%%%%%%%%%%%%%%%%%%%%%%%%%%%%%%%%
%                               Plasma Parameters Calculation                               %
%%%%%%%%%%%%%%%%%%%%%%%%%%%%%%%%%%%%%%%%%%%%%%%%%%%%%%%%%%%%%%%%%%%%%%%%

TeM=trapz(Vfloat:0.01:Vplasma,Ilinrange)./(fnval(smoothplotelec,
Vplasma)); % Maxwellian Method Electron Temperature (eV)

neM=(fnval(smoothplotelec,Vplasma)./Aprobe).*(2.*pi.*me./(el.^2.*k.*
(TeM*11604.5))).^0.5; % Maxwellian Method Electron Density (m-3)

yDM=743.*(TeM./(neM.*1E-6)).^0.5; % Maxwellian Method Debye Length(m-3)

dEEDF=abs(min(DPACK(:,q)-Vplasma))/2500;

eV=permute(0:dEEDF:abs(min(DPACK(:,q)-Vplasma)),[2 1]);

d2IdV2=permute(fnval(secondarydiff,Vplasma:-dEEDF:min(DPACK(:,q))),[2
1]);

EEDF=(2.*me./(el.^2.*Aprobe)).*(2.*el.*eV./me).^0.5.*d2IdV2; % EEDF(m-3
eV-3/2)

ne=trapz(eV,EEDF);

Teff=2./3.*trapz(eV,eV.*EEDF); % EEDF Method Electron Temperature (eV)

yDef=743.*(Teff./(ne.*1E-6)).^0.5; % EEDF Method Electron Density(m-3)

figure(4);
plot(eV,EEDF,'b')
xlabel('Electron Energy (E/eV)')
ylabel('EEDF (m-3 eV-3/2)')

else

    disp('Input Error');

    return

end

Next=input('Next? (y/n)-->');

if Next==2

    Okay=2;

elseif Next==1

    ParamMat=cat(1,ParamMat,[p Iionsat Ielecsata Ielecsatb Vplasma Vfloat
neM ne TeM Teff yDM yDef]);

    EEDFMat=cat(2,EEDFMat,[eV EEDF]);

    continue

else

    disp('Input Error');

    return

end

end
end

```

```

%%%%%%%%%%%%%%%%%%%%%%%%%%%%%%%%%%%%%%%%%%%%%%%%%%%%%%%%%%%%%%%%%%%%%%%%
%                               Save File Algorithm                               %
%%%%%%%%%%%%%%%%%%%%%%%%%%%%%%%%%%%%%%%%%%%%%%%%%%%%%%%%%%%%%%%%%%%%%%%%

SaveParamID={'Set', 'Ionsat (A)', 'Ielecsata (A)', 'Ielecsatb (A)', 'Vplasma (V)',
            'Vfloat (V)', 'neM (m^-3)', 'ne (m^-3)', ...
            'TeM (eV)', 'Teff (eV)', 'yDM (m)', 'yDef (m)'};

SaveFile=input('Enter Save Filename -->', 's');

warning off MATLAB:xlswrite:AddSheet

xlswrite([SaveFile, '.xls'], SaveParamID, [SaveFile, ' cm'], 'A1')

xlswrite([SaveFile, '.xls'], ParamMat, [SaveFile, ' cm'], 'A2')

xlswrite([SaveFile, '.xls'], {'Average'}, [SaveFile, ' cm'], ['A', num2str(psize+2)]);

xlswrite([SaveFile, '.xls'], {'Standard Deviation'}, [SaveFile, '
cm'], ['A', num2str(psize+3)]);

xlswrite([SaveFile, '.xls'], mean(ParamMat(:, 2:size(ParamMat, 2)), 1), [SaveFile, '
cm'], ['B', num2str(psize+2)]);

xlswrite([SaveFile, '.xls'], std(ParamMat(:, 2:size(ParamMat, 2)), 0, 1), [SaveFile, '
cm'], ['B', num2str(psize+3)]);

VIString=[];

SetString=[];

EEDFString=[];

for p=1:psize
    SetString=cat(2, SetString, {'Set ', num2str(p), ' '});
    VIString=cat(2, VIString, {'Voltage, V(V)', 'Current, I(A)'});
    EEDFString=cat(2, EEDFString, {'Electron Energy(eV)', 'EEDF (m-3 eV-3/2)'});
end

xlswrite([SaveFile, '.xls'], SetString, [SaveFile, ' cm'], 'O1')
xlswrite([SaveFile, '.xls'], EEDFString, [SaveFile, ' cm'], 'O2')
xlswrite([SaveFile, '.xls'], EEDFMat, [SaveFile, ' cm'], 'O3')

xlswrite([SaveFile, '.xls'], SetString, ['Raw Data ', SaveFile, ' cm'], 'A1')
xlswrite([SaveFile, '.xls'], VIString, ['Raw Data ', SaveFile, ' cm'], 'A2')
xlswrite([SaveFile, '.xls'], DPACK, ['Raw Data ', SaveFile, ' cm'], 'A3')

deleteEmptyExcelSheets([cd, '/', SaveFile, '.xls']); % Empty Excel Sheet Delete Code
(Appendix E.3)

disp('Done!')

```

## APPENDIX B: AOES $T_n$ SOLVER

This solver is divided into two parts, i.e., B.1 and B.2. Code B.1 must be pre-loaded in MATLAB workspace before running code B.2. Code B.1 calculates the rotational line widths and positions for all tested rotational temperatures and convolves the discrete spectrum with instrumental broadening. Code B.2 extracts experimental data and uses the minimum  $\chi^2$  method to estimate the neutral gas temperature.

---

### B.1. AOES Line Width and Line Position Convolution Solver

```
%%%%%%%%%%%%%%%%%%%%%%%%%%%%%%%%%%%%%%%%%%%%%%%%%%%%%%%%%%%%%%%%%%%%%%%%
%                               Common Spectroscopy Constants                               %
%%%%%%%%%%%%%%%%%%%%%%%%%%%%%%%%%%%%%%%%%%%%%%%%%%%%%%%%%%%%%%%%%%%%%%%%

h=6.62606957E-34; % Planck's Constant (m2kgs-1)
c=299792458; % Speed of Light (ms-1)
k=1.3806488E-23; % Boltzmann Constant (JK-1)
nair=1.0003; % Refraction Index of Air

%%%%%%%%%%%%%%%%%%%%%%%%%%%%%%%%%%%%%%%%%%%%%%%%%%%%%%%%%%%%%%%%%%%%%%%%
%                               Nitrogen Vibro-rotational Constants and Terms                               %
%%%%%%%%%%%%%%%%%%%%%%%%%%%%%%%%%%%%%%%%%%%%%%%%%%%%%%%%%%%%%%%%%%%%%%%%

% 1 Denotes Upper State, 2 Denotes Lower State %
we1=2047.17;
we2=1733.39;
wexel=28.445;
wexe2=14.122;
weye1=2.0883;
weye2=-0.0569;
Be1=1.8247;
Be2=1.6374;
alphae1=0.01868;
alphae2=0.0179;
v1=0; % Upper State Vibrational Number
v2=2; % Upper State Vibrational Number
```

```

A=42.24;
De1=(4.*Be1.^3)/we1.^2;
De2=(4.*Be2.^3)/we2.^2;
betae1=De1.*(8.*wexel./we1-5.*alphae1./Be1-alphae1.^2.*we1./(24.*Be1.^3));
betae2=De2.*(8.*wexe2./we2-5.*alphae2./Be2-alphae2.^2.*we2./(24.*Be2.^3));
Te1=89136.88; % Upper State Electronic Term (cm-1)
Te2=59619.35; % Lower State Electronic Term (cm-1)
Bv1=Be1-alphae1.*(v1+0.5); % Upper State Rotational Term 1 (cm-1)
Bv2=Be2-alphae2.*(v2+0.5); % Upper State Rotational Term 1 (cm-1)
Dv1=De1+betae1.*(v1+0.5); % Upper State Rotational Term 2 (cm-1)
Dv2=De2+betae2.*(v2+0.5); % Upper State Rotational Term 2 (cm-1)
Gv1=we1.*(v1+0.5)-wexel.*(v1+0.5).^2+weye1.*(v1+0.5).^3; % Upper State Vibrational
    Term (cm-1)
Gv2=we2.*(v2+0.5)-wexe2.*(v2+0.5).^2+weye2.*(v2+0.5).^3; % Lower State Vibrational
    Term (cm-1)
Vv1v2=Te1-Te2+Gv1-Gv2;

%%%%%%%%%%%%%%%%%%%%%%%%%%%%%%%%%%%%%%%%%%%%%%%%%%%%%%%%%%%%%%%%%%%%%%%%%%
%           Rotational Line Position/Intensity Calculation Loop           %
%%%%%%%%%%%%%%%%%%%%%%%%%%%%%%%%%%%%%%%%%%%%%%%%%%%%%%%%%%%%%%%%%%%%%%%%%%

ConvSpecGroupStack=[];
TempStart=250; % Starting Rotational Temperature (K)
TempEnd=1500; % Ending Rotational Temperature (K)
dTemp=50; % Spacing Between Temperature Iterations (K)
CorrectedLambd=xlsread('CorrectedLambd.xls'); % Calibrated Spectrometer Wavelength
    (Obtained in Calibration Experiment) (nm)
DataSelect=CorrectedLambd(1380:1418); % Wavelength Range of Selected (0-2) Peak
for Trot=TempStart:dTemp:TempEnd;
    disp(['Fit Calculation for Temperature =',num2str(Trot), ' K'])
    SynSpecMat=[];
    for JR=0:50 % R Rotational Branch Calculations
        FvR1D0=Bv1.*(JR+1).*(JR+2)-Dv1.*(JR+1).^2.*(JR+2).^2;
        FvR2D0=Bv2.*JR.*(JR+1)-Dv2.*JR.^2.*(JR+1).^2;
        VRD0=Vv1v2+FvR1D0-FvR2D0;
        LRD0=1E-2./(VRD0.*nair);
        SJRD0=JR+1;
        IREmissD0=SJRD0.*exp(-100.*FvR1D0.*h.*c./(k.*Trot));
    end
end

```

```

if JR>=1

    FvR1D1=Bv1.*((JR+1).*(JR+2)-1)-Dv1.*(JR+1).^2.*(JR+2).^2+A;
    FvR2D1=Bv2.*(JR.*(JR+1)-1)-Dv2.*JR.^2.*(JR+1).^2+A;
    VRD1=Vv1v2+FvR1D1-FvR2D1;
    LRD1=1E-2./(VRD1.*nair);
    SJRD1=((JR+1).^2-1)./(JR+1);
    IREmissD1=SJRD1.*exp(-100.*FvR1D1.*h.*c./(k.*Trot));

else

    LRD1=[];
    SJRD1=[];
    IREmissD1=[];

end

if JR>=2

    FvR1D2=Bv1.*((JR+1).*(JR+2)-4)-Dv1.*(JR+1).^2.*(JR+2).^2+
        4.*A;
    FvR2D2=Bv2.*(JR.*(JR+1)-4)-Dv2.*JR.^2.*(JR+1).^2+4.*A;
    VRD2=Vv1v2+FvR1D2-FvR2D2;
    LRD2=1E-2./(VRD2.*nair);
    SJRD2=((JR+1).^2-4)./(JR+1);
    IREmissD2=SJRD2.*exp(-100.*FvR1D2.*h.*c./(k.*Trot));

else

    LRD2=[];
    SJRD2=[];
    IREmissD2=[];

end

end

SynSpecSeg=[LRD0 IREmissD0 SJRD0; LRD1 IREmissD1 SJRD1; LRD2
    IREmissD2 SJRD2];

SynSpecMat=cat(1, SynSpecMat, SynSpecSeg);

end

for JQ=1:50 % Q Rotational Branch Calculations

    FvQ1D0=Bv1.*JQ.*(JQ+1)-Dv1.*JQ.^2.*(JQ+1).^2;
    FvQ2D0=Bv2.*JQ.*(JQ+1)-Dv2.*JQ.^2.*(JQ+1).^2;
    VQD0=Vv1v2+FvQ1D0-FvQ2D0;
    LQD0=[];
    SJQD0=[];
    IQEmissD0=[];
    FvQ1D1=Bv1.*(JQ.*(JQ+1)-1)-Dv1.*JQ.^2.*(JQ+1).^2+A;

```

```

FvQ2D1=Bv2.*(JQ.*(JQ+1)-1)-Dv2.*JQ.^2.*(JQ+1).^2+A;
VQD1=Vv1v2+FvQ1D1-FvQ2D1;
LQD1=1E-2./(VQD1.*nair);
SJQD1=(2.*JQ+1)./(JQ.*(JQ+1));
IQEmissD1=SJQD1.*exp(-100.*FvQ1D1.*h.*c./(k.*Trot));
if JQ>=2
    FvQ1D2=Bv1.*(JQ.*(JQ+1)-4)-Dv1.*JQ.^2.*(JQ+1).^2+4.*A;
    FvQ2D2=Bv2.*(JQ.*(JQ+1)-4)-Dv2.*JQ.^2.*(JQ+1).^2+4.*A;
    VQD2=Vv1v2+FvQ1D2-FvQ2D2;
    LQD2=1E-2./(VQD2.*nair);
    SJQD2=4.*(2.*JQ+1)./(JQ.*(JQ+1));
    IQEmissD2=SJQD2.*exp(-100.*FvQ1D2.*h.*c./(k.*Trot));
else
    LQD2=[];
    SJQD2=[];
    IQEmissD2=[];
end
SynSpecSeg=[LQD0 IQEmissD0 SJQD0; LQD1 IQEmissD1 SJQD1; LQD2
    IQEmissD2 SJQD2];
SynSpecMat=cat(1, SynSpecMat, SynSpecSeg);
end
for JP=1:50 % P Rotational Branch Calculations
    FvP1D0=Bv1.*JP.*(JP-1)-Dv1.*JP.^2.*(JP-1).^2;
    FvP2D0=Bv2.*JP.*(JP+1)-Dv2.*JP.^2.*(JP+1).^2;
    VPD0=Vv1v2+FvP1D0-FvP2D0;
    LPD0=1E-2./(VPD0.*nair);
    SJPD0=JP;
    IPEmissD0=SJPD0.*exp(-100.*FvP1D0.*h.*c./(k.*Trot));
    if JP>=2
        FvP1D1=Bv1.*(JP.*(JP-1)-1)-Dv1.*JP.^2.*(JP-1).^2+A;
        FvP2D1=Bv2.*(JP.*(JP+1)-1)-Dv2.*JP.^2.*(JP+1).^2+A;
        VPD1=Vv1v2+FvP1D1-FvP2D1;
        LPD1=1E-2./(VPD1.*nair);
        SJPD1=(JP+1).*(JP-1)./JP;
        IPEmissD1=SJPD1.*exp(-100.*FvP1D1.*h.*c./(k.*Trot));
    end
end

```

```

else

    LPD1=[];

    SJPD1=[];

    IPEmissD1=[];

end

if JP>=3

    FvP1D2=Bv1.*(JP.*(JP-1)-4)-Dv1.*JP.^2.*(JP-1).^2+4.*A;
    FvP2D2=Bv2.*(JP.*(JP+1)-4)-Dv2.*JP.^2.*(JP+1).^2+4.*A;

    VPD2=Vv1v2+FvP1D2-FvP2D2;

    LPD2=1E-2./(VPD2.*nair);

    SJPD2=(JP+2).*(JP-2)./JP;

    IPEmissD2=SJPD2.*exp(-100.*FvP1D2.*h.*c./(k.*Trot));

else

    LPD2=[];

    SJPD2=[];

    IPEmissD2=[];

end

SynSpecSeg=[LPD0 IPEmissD0 SJPD0; LPD1 IPEmissD1 SJPD1; LPD2
IPEmissD2 SJPD2];

SynSpecMat=cat(1, SynSpecMat, SynSpecSeg);

end

SynSpecMat=sortrows(SynSpecMat,1);

%%%%%%%%%%%%%%%%%%%%%%%%%%%%%%%%%%%%%%%%%%%%%%%%%%%%%%%%%%%%%%%%%%%%%%%%%%
%                               Voigt Profile Matrix Loop                               %
%%%%%%%%%%%%%%%%%%%%%%%%%%%%%%%%%%%%%%%%%%%%%%%%%%%%%%%%%%%%%%%%%%%%%%%%%%

% Voigt Profile Broadening is Calculated for Wavelengths/Line Positions and Column-
stacked as a Matrix %

    dDataSelect=abs(DataSelect(1,1)-DataSelect(2,1)); % Spectrometer
Pixel Resolution (nm)

    dLambd=4*dDataSelect; % Bin Size (nm)

    LambdSynSpec=SynSpecMat(:,1)./1E-9;

    LambdAdd=permute(max(LambdSynSpec)+0.01:0.01:round(max(LambdSynSpec)
)+1,[2 1]);

    LambdFullSynSpec=cat(1,LambdSynSpec,LambdAdd);

    IntSynSpec=SynSpecMat(:,2);

    IntAdd=zeros(numel(LambdAdd),1);

    IntFullSynSpec=cat(1,IntSynSpec,IntAdd);

```

```

LambdGroup=min(DataSelect(:,1)):dLambd:max(DataSelect(:,1));
ConvSpecGroup=zeros(1,numel(LambdGroup));
VoiGroup=[];
FWHMLor=0.6; % Lorentz FWHM
FWHMGau=0.5; % Gaussian FWHM
for n=1:numel(LambdFullSynSpec)
    FWHMVoi=FWHMLor./2+sqrt(FWHMLor.^2./4+FWHMGau.^2); % Voigt FWHM
    VoiNorm=real((1-FWHMLor./FWHMVoi).*exp(-
        4.*log(2).*((LambdFullSynSpec-LambdFullSynSpec(n))
            ./FWHMVoi).^2)+(FWHMLor./FWHMVoi).*(1./(1+4.*
                ((LambdFullSynSpec-LambdFullSynSpec(n))
                    ./FWHMVoi).^2))+0.016.*(1-FWHMLor./FWHMVoi)
                    .* (FWHMLor./FWHMVoi).*(exp(- 0.4
                        .* ((LambdFullSynSpec-LambdFullSynSpec(n))
                            ./FWHMVoi).^2.25)-10./(10+((LambdFullSyn
                                Spec-LambdFullSynSpec(n))./FWHMVoi)
                                    ^2.25))));
    VoiGroup=cat(2,VoiGroup,permute(VoiNorm,[1 2]));
end

%%%%%%%%%%%%%%%%%%%%%%%%%%%%%%%%%%%%%%%%%%%%%%%%%%%%%%%%%%%%%%%%%%%%%%%%
%      Bin Probability Calculation for Minimum Chi-Squared Method (B.2)      %
%%%%%%%%%%%%%%%%%%%%%%%%%%%%%%%%%%%%%%%%%%%%%%%%%%%%%%%%%%%%%%%%%%%%%%%%

LineSum=zeros(numel(LambdGroup),1);
for n=1:numel(LambdFullSynSpec)
    for p=1:numel(LambdGroup);
        if LambdFullSynSpec(n)>=LambdGroup(p)-
            dLambd/2&&LambdFullSynSpec(n) <LambdGroup(p)+dLambd/2
            LineSum(p)=LineSum(p)+1;
        else
            end
    end
end

LineProb=LineSum./sum(LineSum); % Line Probability for Bins

%%%%%%%%%%%%%%%%%%%%%%%%%%%%%%%%%%%%%%%%%%%%%%%%%%%%%%%%%%%%%%%%%%%%%%%%
%                               Convolution Matrix Loop                               %
%%%%%%%%%%%%%%%%%%%%%%%%%%%%%%%%%%%%%%%%%%%%%%%%%%%%%%%%%%%%%%%%%%%%%%%%

for m=1:numel(LambdFullSynSpec)
    ConvSpecStack=[];

```

```

ConvIntSpec=zeros (numel (LambdFullSynSpec), 1);
ConvIntSpec (m)=IntFullSynSpec (m);
for n=1:numel (LambdFullSynSpec)
ConvSpec=trapz (LambdFullSynSpec, ConvIntSpec.*VoiGroup (:, n));
ConvSpecStack=cat (1, ConvSpecStack, ConvSpec);
for p=1:numel (LambdGroup);
if LambdFullSynSpec (n) >=LambdGroup (p) -dLambd/2&&
LambdFullSynSpec (n) <LambdGroup (p) +dLambd/2
ConvSpecGroup (p)=ConvSpecGroup (p)+ConvSpec;
else
end
end
end
end
ConvSpecGroupNorm=permute (ConvSpecGroup./max (ConvSpecGroup), [2 1]);
ConvSpecGroupStack=cat (2, ConvSpecGroupStack, permute (ConvSpecGroup
Norm, [1 2])); % Normalized Convolved Spectrum Stack for
Rotational Temperature Range
end
disp ('Done!')

```

## B.2. AOES Minimum $\chi^2$ Neutral Gas Temperature Solver

```
%%%%%%%%%%%%%%%%%%%%%%%%%%%%%%%%%%%%%%%%%%%%%%%%%%%%%%%%%%%%%%%%%%%%%%%%
%                               Definition of Set Plasma Parameters                               %
%%%%%%%%%%%%%%%%%%%%%%%%%%%%%%%%%%%%%%%%%%%%%%%%%%%%%%%%%%%%%%%%%%%%%%%%

TempMatrix=[];

ArgPres=input('Input Argon Pressure ----->'); % Set Argon Pressure for Save File
AxialH=input('Input Axial Height ----->'); % Set Axial Height for Save File

DataCollect=dir('*.txt'); % Collection of ASCII (*.txt) Output Files from
    SpectraSuite Software

DataCollSize=size(DataCollect,1);

%%%%%%%%%%%%%%%%%%%%%%%%%%%%%%%%%%%%%%%%%%%%%%%%%%%%%%%%%%%%%%%%%%%%%%%%
%                               Data Filename Sorter                                       %
%%%%%%%%%%%%%%%%%%%%%%%%%%%%%%%%%%%%%%%%%%%%%%%%%%%%%%%%%%%%%%%%%%%%%%%%

% This Code Extracts and Sorts Data Files According to Parameters Labeled in
% Filename. %

% Filename Should Have the Following Format:'[R.f. Power][Plasma Mode]*.txt' for
% Code to Work, e.g. 180WHmode*.txt %

% 20 Data Sets were Obtained for Each Measured Point. %

PlasPowMat=[];

for dc=1:DataCollSize

    DataCollName=DataCollect(dc).name;

    PPVal1=num2str(str2num(DataCollName(1)));
    PPVal2=num2str(str2num(DataCollName(2)));
    PPVal3=num2str(str2num(DataCollName(3)));

    PlasPowComp=str2num(strcat(PPVal1,PPVal2,PPVal3));

    PPMatSize=numel(PlasPowMat);

    if isempty(PlasPowMat)==1;

        PlasPowMat=cat(2,PlasPowMat,PlasPowComp);

    elseif PlasPowComp==PlasPowMat(PPMatSize);

    else

        PlasPowMat=cat(2,PlasPowMat,PlasPowComp);

    end

end

PlasPowMat=sort(PlasPowMat);

for PlasmPower=PlasPowMat % Sorting by R.f. Power and Plasma Mode
```

```

DataGroup=dir([num2str(PlasmPower), 'W*.txt']);
DataSize=size(DataGroup,1);
DataSelect=CorrectedLambd(1380:1418); % 0-2) Peak Calibrated Wavelength Range
(nm)
for dt=1:DataSize
    DataName=DataGroup(dt).name;
    for dn=1:numel(DataName);
        if DataName(dn)=='H'
            PlasmaType={'H'};
            disp('H-mode');
        elseif DataName(dn)=='E'
            PlasmaType={'E'};
            disp('E-mode');
        else
            end
        end
    end
    disp(DataName);
    DataAqui=dlmread(DataName, '\t', [17 1 3664 1]);
    DataSet=DataAqui(1380:1418); % (0-2) Peak Intensity Data From File
    DataSet=DataSet-min(DataSet); % Removal of Background Emission Noise
    DataSet=DataSet./max(DataSet); % Normalizing of (0-2) Peak Intensity Data
    DataSelect=cat(2,DataSelect,DataSet); % Stacking of Acquired and Processed
    Data
end

%%%%%%%%%%%%%%%%%%%%%%%%%%%%%%%%%%%%%%%%%%%%%%%%%%%%%%%%%%%%%%%%%%%%%%%%
%                               Minimum Chi-Squared Loop                               %
%%%%%%%%%%%%%%%%%%%%%%%%%%%%%%%%%%%%%%%%%%%%%%%%%%%%%%%%%%%%%%%%%%%%%%%%

Chi2Stack=[];
for Tmp=1:size(ConvSpecGroupStack,2);
    DataNum=numel(LambdGroup);
    Chi2StackH=[];
    for n=1:DataSize
        DataSelectChi=permute(interp1(DataSelect(:,1),
            DataSelect(:,n+1),LambdGroup), [2 1]));
        Chi2Val=sum(LineProb.*(DataSelectChi-
            ConvSpecGroupStack(:,Tmp)).^2)./(DataNum.*(DataNum-1));
    end
end

```

```

        Chi2StackH=cat(2,Chi2StackH,Chi2Val);

    end

    Chi2Stack=cat(1,Chi2Stack,Chi2StackH);

end

NeutralTemp=TempStart:dTemp:TempEnd;

TempDataSet=[];

for n=1:DataSize

    figure(1) % Chi-Squared Curve

    plot(NeutralTemp, Chi2Stack(:,n), 'o');
    xlabel('Neutral Gas Temperature, T_n (K)')
    ylabel('X^2 (arb. units)')

    [MinChi2 MinChi2I]=min(Chi2Stack(:,n));

    MinFitTemp=NeutralTemp(MinChi2I);

    TempDataSet=cat(1,TempDataSet,MinFitTemp);

    disp(['Estimated Neutral Temperature = ',num2str(MinFitTemp), ' K'])

    figure(2) % Measured and Convolved(0-2)Peaks at Best Fitted Temperature

    plot(LambdaGroup,ConvSpecGroupStack(:,MinChi2I),'k');
    xlabel('Wavelength (nm)')
    ylabel('Intensity (arb. units)')

    ylim([0 max(ConvSpecGroupStack(:,MinChi2I))]);

    hold on

    plot(DataSelect(:,1),DataSelect(:,n+1),'or');

    hold off

end

TempAve=mean(TempDataSet); % Mean Temperature for 20 Data Sets at Measured Point

TempStd=std(TempDataSet); % Standard Deviation for 20 Data Sets at Measured
Point

TempMatrix=cat(1,TempMatrix,[PlasmPower TempAve TempStd]); % Save File Matrix
Stack

end

%%%%%%%%%%%%%%%%%%%%%%%%%%%%%%%%%%%%%%%%%%%%%%%%%%%%%%%%%%%%%%%%%%%%%%%%
%                               Save File Algorithm                               %
%%%%%%%%%%%%%%%%%%%%%%%%%%%%%%%%%%%%%%%%%%%%%%%%%%%%%%%%%%%%%%%%%%%%%%%%

warning off MATLAB:xlswrite:AddSheet

TempID={'Plasma Power (W)', 'Average Neutral Temperature (K)', 'Standard Deviation
(K)'};

xlswrite([num2str(AxialH), ' cm Neutral Gas Temperature Data.xls'],
TempID,[num2str(ArgPres), ' mbar '], 'A1');

```

```
xlswrite([num2str(AxialH), ' cm Neutral Gas Temperature Data.xls'],  
        TempMatrix,[num2str(ArgPres), ' mbar '], 'A2');  
  
deleteEmptyExcelSheets([cd, '/', num2str(AxialH), ' cm Neutral Gas Temperature  
Data.xls']); % Empty Excel Sheet Delete Code (Appendix E.3)  
  
disp('Done!')
```

## APPENDIX C: ANALYTICAL H MODE FIELD MODEL

```
%%%%%%%%%%%%%%%%%%%%%%%%%%%%%%%%%%%%%%%%%%%%%%%%%%%%%%%%%%%%%%%%%%%%%%%%
%                               Chamber and Coil Dimensions                               %
%%%%%%%%%%%%%%%%%%%%%%%%%%%%%%%%%%%%%%%%%%%%%%%%%%%%%%%%%%%%%%%%%%%%%%%%

L=21.8E-2; % Effective Chamber Height (m)
D=2.4E-2; % Chamber-Coil Spacing (m)
b=14.5E-2; % Chamber Radius (m)
a=4.5E-2; % Planar Coil Radius (m)
N=6; % Number of Coil Turns

%%%%%%%%%%%%%%%%%%%%%%%%%%%%%%%%%%%%%%%%%%%%%%%%%%%%%%%%%%%%%%%%%%%%%%%%
%                               Iteration Parameters and Boundary Conditions                               %
%%%%%%%%%%%%%%%%%%%%%%%%%%%%%%%%%%%%%%%%%%%%%%%%%%%%%%%%%%%%%%%%%%%%%%%%

dr=0.5E-2; % Radial Iteration Spacing (m)
dri=0.1E-2; % Interpolated Radial Spacing (m)
dz=0.5E-2; % Axial Iteration Spacing (m)
dzi=0.1E-2; % Interpolated Axial Spacing (m)
[r,z]=meshgrid(-b:dr:b,0:dz:L+D); % Field Grid Allocation (m)
[ri zi]=meshgrid(-b:dri:b,0:dzi:L+D); % Interpolated Field Grid (m)
rlim=size(r,2); % Radial Limit
zlimL=size(0:dz:L,2); % Reactor Axial Limit
zlimLD=size(0:dz:L+D,2); % Reactor-Coil Axial Limit

%%%%%%%%%%%%%%%%%%%%%%%%%%%%%%%%%%%%%%%%%%%%%%%%%%%%%%%%%%%%%%%%%%%%%%%%
%                               R.f. Parameters and Constants                               %
%%%%%%%%%%%%%%%%%%%%%%%%%%%%%%%%%%%%%%%%%%%%%%%%%%%%%%%%%%%%%%%%%%%%%%%%

f=13.56E6; % RF Frequency (Hz)
w=2.*pi.*f; % RF Angular Frequency (rad s-1)
Irms=13.9; % RMS Coil Current (A)
Ip=Irms.*(2.^0.5); % Peak Coil Current (A)

%%%%%%%%%%%%%%%%%%%%%%%%%%%%%%%%%%%%%%%%%%%%%%%%%%%%%%%%%%%%%%%%%%%%%%%%
%                               Plasma and EM Field Physical Constants and Parameters                               %
%%%%%%%%%%%%%%%%%%%%%%%%%%%%%%%%%%%%%%%%%%%%%%%%%%%%%%%%%%%%%%%%%%%%%%%%

ne=5E17; % Electron Density (m-3)
```

```

Te=3; % Electron Temperature (eV)
TeK=Te.*11604.5; % Electron Temperature (K)
pr=0.03; % Argon Pressure (mbar)
Tn=800; % Neutral Gas Temperature (K)
me=9.1E-31; % Electron Mass (kg)
el=1.6E-19; % Electronic Charge (C)
MAr=39.948.*1.661E-27; % Argon Ion Mass (kg)
muo=4.*pi.*1E-7; % Permeability of Vacuum (N A-2)
epso=8.85E-12; % Permittivity of Vacuum (C2 N-1 m-2)
c=3E8; % Speed of Light (m s-1)
k=1.38E-23; % Boltzmann Constant (J K-1)
ng=pr*100./(k.*Tn); % Neutral Gas Density (m-3)

%%%%%%%%%%%%%%%%%%%%%%%%%%%%%%%%%%%%%%%%%%%%%%%%%%%%%%%%%%%%%%%%%%%%%%%%
%                               Collision Frequency Parameters                               %
%%%%%%%%%%%%%%%%%%%%%%%%%%%%%%%%%%%%%%%%%%%%%%%%%%%%%%%%%%%%%%%%%%%%%%%%

vel=((8.*k.*TeK)./(pi.*me)).^0.5; % Maxwellian Mean Electron Velocity (m s-2)
CollData=xlsread('ArgonCC.xls'); % Argon Collision Crosssection Data (Appendix E.1)
sigH=CollData(:,2); % Argon Collision Cross-Section (m-2)
EpsE=el.*CollData(:,1); % Electron Energies (J)
vc=ng.*sigH.*(2.*EpsE./me).^0.5+1i*w; % Direct Electron-Neutral Collision Frequency (Hz)
dFedistdEpsEMax=-2./pi.^(1./2)./(el.*Te).^(3./2)./(el.*Te).*exp(-EpsE./(el.*Te)); % Differential Maxwellian EEDF
ven=real(-1.5.*(trapz(EpsE,EpsE.^1.5.*dFedistdEpsEMax./vc)).^-1); % Electron-Neutral Collision Frequency (s-1)
CA=23-log(((ne.^0.5).*(Te.^(-1.5)))./(10.^2)); % Coulomb Algorithm
vei=(ne.*(el.^4).*CA)./(4.*pi.*(epso.^2).*(me.^0.5).*(el.*Te).^1.5); % Electron-Ion Collision Frequency (s-1)
wplasma=((el.^2.*ne)./(epso.*me)).^0.5; % Plasma Conductivity Parameter (s-1)
dela=(c./wplasma).*((vel.*wplasma)./(2.*c.*w)).^(1./3); % Anomalous Skin Depth (m)
vst=0.25.*vel./dela; % Stochastic Collision Frequency (s-1)
veff=ven+vei+vst; % Effective Electron Collision Frequency (s-1)
vperw=veff./w; % Effective Electron Collision Frequency per RF Angular Frequency Ratio

```

```

%%%%%%%%%%%%%%%%%%%%%%%%%%%%%%%%%%%%%%%%%%%%%%%%%%%%%%%%%%%%%%%%%%%%%%%%
%                               EM Field Initial Loop Parameters                               %
%%%%%%%%%%%%%%%%%%%%%%%%%%%%%%%%%%%%%%%%%%%%%%%%%%%%%%%%%%%%%%%%%%%%%%%%

Ktheta=N.*Ip./a; % Coil Current Density (A m-1)
alpha2=(muo.*el.^2.*ne)./(me.*(1-li.*vperw)); % Plasma Conductivity Parameter (m-2)
yn=permute((besselzero(1,100,1))./b,[2 1]); % Bessel Roots (m-2) (Appendix E.2)
kn=(alpha2+yn.^2).^0.5; % Eigenvalues for Bessel Functions (m-2)

%%%%%%%%%%%%%%%%%%%%%%%%%%%%%%%%%%%%%%%%%%%%%%%%%%%%%%%%%%%%%%%%%%%%%%%%
%                               vn Solver                                                  %
%%%%%%%%%%%%%%%%%%%%%%%%%%%%%%%%%%%%%%%%%%%%%%%%%%%%%%%%%%%%%%%%%%%%%%%%

IntMat=[];
da=a/1000;
for n=1:100
    rint=0:da:a;
    Jint=rint.*besselj(1,yn(n).*rint);
    Jtermint=trapz(rint,Jint);
    IntMat=cat(1,IntMat,Jtermint);
end

IntJTerm=-(Ktheta./(1+betan)).*permute(IntMat,[2 1]);
DiffJTerm=yn.*(b.^2)./2).*((besselj(0,yn.*b)-(1./(yn.*b)).*besselj(1,
    yn.*b)).^2);
vn=li.*w.*muo.*(IntJTerm./DiffJTerm);

%%%%%%%%%%%%%%%%%%%%%%%%%%%%%%%%%%%%%%%%%%%%%%%%%%%%%%%%%%%%%%%%%%%%%%%%
%                               EM Field Boundary Constants                               %
%%%%%%%%%%%%%%%%%%%%%%%%%%%%%%%%%%%%%%%%%%%%%%%%%%%%%%%%%%%%%%%%%%%%%%%%

An=vn.*yn./(yn.*sinh(yn.*D).*sinh(kn.*L)+kn.*cosh(kn.*L).*cosh(yn.*D));
Bn=(An./(2.*yn)).*exp(yn.*L).*(yn.*sinh(kn.*L)-kn.*cosh(kn.*L));
Cn=(An./(2.*yn)).*exp(-yn.*L).*(yn.*sinh(kn.*L)+kn.*cosh(kn.*L));

%%%%%%%%%%%%%%%%%%%%%%%%%%%%%%%%%%%%%%%%%%%%%%%%%%%%%%%%%%%%%%%%%%%%%%%%
%                               Azimuthal Electric Field Iteration Loop                               %
%%%%%%%%%%%%%%%%%%%%%%%%%%%%%%%%%%%%%%%%%%%%%%%%%%%%%%%%%%%%%%%%%%%%%%%%

Ethethaz=[];
for m=1:zlimL

```

```

Ethethar=[];

for n=1:rlim
    Ethethasumn=sum(An.*sinh(kn.*z(m,n)).*besselj(1,yn.*r(m,n)));
    Ethethar=cat(2,Ethethar,Ethethasumn);
end

Ethethaz=cat(1,Ethethaz,Ethethar);

end

for m=zlimL+1:zlimLD
    Ethethar=[];

    for n=1:rlim
        Ethethasumn=sum((Bn.*exp(-yn.*z(m,n))+Cn.*exp(yn.*z(m,n))).*besselj(1,yn.*r(m,n)));
        Ethethar=cat(2,Ethethar,Ethethasumn);
    end

    Ethethaz=cat(1,Ethethaz,Ethethar);

end

Ethetha=interp2(r,z,Ethethaz,ri,zi); % Azimuthal Electric Field (V m-1)
PhasorEth=angle(Ethetha); % Azimuthal Electric Field Phase Angle (rad)
EthethaReal=abs(Ethetha).*cos(PhasorEth); % Real Azimuthal Electric Field Component (V m-1)
EthethaImag=abs(Ethetha).*sin(PhasorEth); % Imaginary Azimuthal Electric Field Component (V m-1)
EthethaAbs=abs(Ethetha); % Absolute Azimuthal Electric Field (V m-1)

%%%%%%%%%%%%%%%%%%%%%%%%%%%%%%%%%%%%%%%%%%%%%%%%%%%%%%%%%%%%%%%%%%%%%%%%
%                               Radial Magnetic Field Iteration Loop                               %
%%%%%%%%%%%%%%%%%%%%%%%%%%%%%%%%%%%%%%%%%%%%%%%%%%%%%%%%%%%%%%%%%%%%%%%%

Bradiusz=[];

for m=1:zlimL
    Bradiusr=[];

    for n=1:rlim
        Bradiussumn=-(1i./w).*sum(An.*kn.*cosh(kn.*z(m,n)).*besselj(1,yn.*r(m,n)));
        Bradiusr=cat(2,Bradiusr,Bradiussumn);
    end

    Bradiusz=cat(1,Bradiusz,Bradiusr);

end
end

```

```

for m=zlimL+1:zlimLD
    Bradiusr=[];
    for n=1:rlim
        Bradiussumn=-(1i./w).*sum(yn.*(-Bn.*exp(-yn.*z(m,n))+Cn.*exp(yn.*z(m,n)))
            .*besselj(1,yn.*r(m,n)));
        Bradiusr=cat(2,Bradiusr,Bradiussumn);
    end
    Bradiusz=cat(1,Bradiusz,Bradiusr);
end
Bradius=interp2(r,z,Bradiusz,ri,zi); % Radial Magnetic Field (T)
PhasorBr=angle(Bradius); % Radial Magnetic Field Phase Angle (rad)
BradiusReal=abs(Bradius).*cos(PhasorBr); % Real Radial Magnetic Field Component (T)
BradiusImag=abs(Bradius).*sin(PhasorBr); % Imaginary Radial Magnetic Field
Component (T)
BradiusAbs=abs(Bradius); % Absolute Radial Magnetic Field (T)

%%%%%%%%%%%%%%%%%%%%%%%%%%%%%%%%%%%%%%%%%%%%%%%%%%%%%%%%%%%%%%%%%%%%%%%%
%                               Axial Magnetic Field Iteration Loop                               %
%%%%%%%%%%%%%%%%%%%%%%%%%%%%%%%%%%%%%%%%%%%%%%%%%%%%%%%%%%%%%%%%%%%%%%%%

Baxisz=[];
for m=1:zlimL
    Baxisr=[];
    for n=1:rlim
        Baxissumn=(1i./w).*sum(An.*yn.*sinh(kn.*z(m,n)).*besselj(0,yn.*r(m,n)));
        Baxisr=cat(2,Baxisr,Baxissumn);
    end
    Baxisz=cat(1,Baxisz,Baxisr);
end
for m=zlimL+1:zlimLD
    Baxisr=[];
    for n=1:rlim
        Baxissumn=(1i./w).*sum(yn.*(Bn.*exp(-yn.*z(m,n))+Cn.*exp(yn.*z(m,n)))
            .*besselj(0,yn.*r(m,n)));
        Baxisr=cat(2,Baxisr,Baxissumn);
    end
    Baxisz=cat(1,Baxisz,Baxisr);
end
end

```

```

Baxis=interp2(r,z,Baxisz,ri,zi); % Axial Magnetic Field (T)
PhasorBz=angle(Baxis); % Axial Magnetic Field Phase Angle (rad)
BaxisReal=abs(Baxis).*cos(PhasorBz); % Real Axial Magnetic Field Component (T)
BaxisImag=abs(Baxis).*sin(PhasorBz); % Imaginary Axial Magnetic Field Component (T)
BaxisAbs=abs(Baxis); % Absolute Axial Magnetic Field (T)

%%%%%%%%%%%%%%%%%%%%%%%%%%%%%%%%%%%%%%%%%%%%%%%%%%%%%%%%%%%%%%%%%%%%%%%%
%                               Total Magnetic Field                               %
%%%%%%%%%%%%%%%%%%%%%%%%%%%%%%%%%%%%%%%%%%%%%%%%%%%%%%%%%%%%%%%%%%%%%%%%

Bfield=(Bradius.^2+Baxis.^2).^0.5; % Total Magnetic Field (T)
PhasorBf=angle(Bfield); % Total Magnetic Field Phase Angle (rad)
BfieldReal=abs(Bfield).*cos(PhasorBf); % Real Total Magnetic Field Component (T)
BfieldImag=abs(Bfield).*sin(PhasorBf); % Imaginary Total Magnetic Field Component
(T)
BfieldAbs=abs(Bfield); % Absolute Total Magnetic Field (T)

%%%%%%%%%%%%%%%%%%%%%%%%%%%%%%%%%%%%%%%%%%%%%%%%%%%%%%%%%%%%%%%%%%%%%%%%
%   Magnetic Vector Potential for Contour Plot (Additional Feature)           %
%%%%%%%%%%%%%%%%%%%%%%%%%%%%%%%%%%%%%%%%%%%%%%%%%%%%%%%%%%%%%%%%%%%%%%%%

rAthetha=(1i./w).*(ri.*Ethetha); % Azimuthal Magnetic Vector Potential (A)
rAthethaAbs=abs(rAthetha); % Absolute Azimuthal Magnetic Vector Potential (A)
PhasorrAth=angle(rAthetha); % Azimuthal Magnetic Vector Phase Angle (rad)

%%%%%%%%%%%%%%%%%%%%%%%%%%%%%%%%%%%%%%%%%%%%%%%%%%%%%%%%%%%%%%%%%%%%%%%%
%                               Field Animation and Contour Plot                               %
%%%%%%%%%%%%%%%%%%%%%%%%%%%%%%%%%%%%%%%%%%%%%%%%%%%%%%%%%%%%%%%%%%%%%%%%

T=(2.*pi)./w; % R.f. Oscillation Period (s)
t=T/100; % Time Capture Interval (s)
timeplot=0:t:2*T;
timelim=size(timeplot,2);

FieldType=input('Select Field Animation Plot: \n [1] Electric Field Distribution \n
[2] Magnetic Field Distribution \n [3] Magnetic Field Contour Plot \n \n --> ');
if FieldType==1

    PlotLimitE=max((max(EthethaAbs)));

    for j=1:timelim

        surf(ri,zi,EthethaAbs.*cos(w.*timeplot(j)+PhasorEth),'EdgeColor','none')
        colormap(jet(256))
        colorbar('EastOutside')
    end
end

```

```

        caxis([-PlotLimitE PlotLimitE])
        xlim([-b b])
        ylim([0 L+D])
        zlim([-1.2.*PlotLimitE 1.2.*PlotLimitE])
        view(180,90)
        F(j)=getframe;

    end

    movie(F,1,12)

elseif FieldType==2

    PlotLimitB=max((max(BfieldAbs)));

    for j=1:timelim

        surf(ri,zi,BfieldAbs.*cos(w.*timeplot(j)+PhasorBf),'EdgeColor','none')
        colormap(jet(256))
        colorbar('EastOutside')
        caxis([0 PlotLimitB])
        xlim([-b b])
        ylim([0 L+D])
        zlim([-1.2.*PlotLimitB 1.2.*PlotLimitB])
        view(180,90)
        F(j)=getframe;

    end

    movie(F,1,12)

elseif FieldType==3

    PlotLimitA=max((max(rAthethaAbs)));

    v=cat(2,-logspace(-9,-6,10),logspace(-9,-6,10));

    for j=1:timelim

        contour(ri,zi,rAthethaAbs.*cos(w.*timeplot(j)+PhasorrAth),v,'k')
        xlim([-b b])
        ylim([0 L])
        zlim([-1.2.*PlotLimitA 1.2.*PlotLimitA])
        view(180,90)
        F(j)=getframe;

    end

    movie(F,1,12)

else

    disp('Input Error')

end

```

## APPENDIX D: POWER BALANCE MODEL

```
%%%%%%%%%%%%%%%%%%%%%%%%%%%%%%%%%%%%%%%%%%%%%%%%%%%%%%%%%%%%%%%%%%%%%%%%
%
%           Chamber and Coil Dimensions           %
%%%%%%%%%%%%%%%%%%%%%%%%%%%%%%%%%%%%%%%%%%%%%%%%%%%%%%%%%%%%%%%%%%%%%%%%

L=21.8E-2; % Effective Chamber Height (m)
D=2.4E-2; % Chamber-Coil Spacing (m)
B=8.6E-2-D; % Bottom of Coil Spacing (m)
M=9.9E-2; % Indented Cylinder Height (m)
O=10.8E-2; % Indented Cylinder Outer Radius (m)
b=14.5E-2; % Reactor Radius (m)
a=4.5E-2; % Planar Coil Radius (m)
rd=8E-2; % Effective Dielectric Plate Radius (m)
rs=0:dr:rd; % Radial Dielectric Iteration Coordinate (m)
N=6; % Number of Coil Turns

%%%%%%%%%%%%%%%%%%%%%%%%%%%%%%%%%%%%%%%%%%%%%%%%%%%%%%%%%%%%%%%%%%%%%%%%
%
%           Iteration Parameters and Boundary Conditions           %
%%%%%%%%%%%%%%%%%%%%%%%%%%%%%%%%%%%%%%%%%%%%%%%%%%%%%%%%%%%%%%%%%%%%%%%%

dr=0.1E-2; % Radial Iteration Spacing (m)
r=0:dr:a; % Radial Coil Iteration Coordinate (m)
rlim=size(r,2); % Radial Iteration Limit
z=L+D; % Axial Coordinate (m)

%%%%%%%%%%%%%%%%%%%%%%%%%%%%%%%%%%%%%%%%%%%%%%%%%%%%%%%%%%%%%%%%%%%%%%%%
%
%           RF Parameters and Constants           %
%%%%%%%%%%%%%%%%%%%%%%%%%%%%%%%%%%%%%%%%%%%%%%%%%%%%%%%%%%%%%%%%%%%%%%%%

f=13.56E6; % R.f. Frequency (Hz)
w=2.*pi.*f; % R.f. Angular Frequency (rad s-1)
pr=0.03; % Chamber Pressure (mbar)
CollData=xlsread('ArgonCC.xls'); % Argon Collision Cross Section Data
for Ip=15.0 % Peak Coil Current (A)
    Tn=583; % Neutral Gas Temperature (K)
    Te=4; % Electron Temperature (eV)
    CDM=8.8E4; % Exponential Factor for Druyvestyeyn-Maxwellian Transition Point
    me=9.1E-31; % Electron Mass (kg)
```

```

miamu=39.948; % Argon Ion Mass (amu)
mi=miamu.*1.66E-27; % Argon ion Mass (kg)
EpsIz=15.76; % Ionization Energy (eV)
EpsEx=12.14; % Excitation Energy (eV)
Kel=2.336E-14.*Te.^1.609.*exp(0.0618.*log(Te).^2-0.1171.*log(Te).^3); % Elastic
    Scattering Rate Constant (m3 s-1)
Kiz=2.34E-14.*Te.^0.59.*exp(-17.44./Te); % Ionization Scattering Rate
    Constant (m3 s-1)
Kex=2.48E-14.*Te.^0.33.*exp(-12.78./Te); % Excitation Scattering Rate
    Constant (m3 s-1)
EpsC=EpsIz+(Kex./Kiz).*EpsEx+(Kel./Kiz).*(3.*me./mi).*Te; % Collisional Energy
    Lost Per Ion-Electron Pair (eV)
EpsT=EpsC+5.2.*Te+2.*Te; % Total Energy Lost Per Ion-Electron Pair (eV)
Lo=1.2E-6; % Coil Inductance (H)

%%%%%%%%%%%%%%%%%%%%%%%%%%%%%%%%%%%%%%%%%%%%%%%%%%%%%%%%%%%%%%%%%%%%%%%%
%           Common EM Field Physical Constants and Parameters           %
%%%%%%%%%%%%%%%%%%%%%%%%%%%%%%%%%%%%%%%%%%%%%%%%%%%%%%%%%%%%%%%%%%%%%%%%

veffStack=[];
PabsStack=[];
PlossStack=[];
PHMStack=[];
PEMStack=[];
PstocStack=[];
for ne=logspace(15,17); % Electron Density (m-3)
    Vp=Ip.*w.*Lo; % Peak Coil Voltage (V)
    me=9.1E-31; % Electron Mass (kg)
    miamu=39.948; % Argon Ion Mass (amu)
    mi=miamu.*1.66E-27; % Argon ion Mass (kg)
    muo=4.*pi.*1E-7; % Permeability of Vacuum (N A-2)
    epso=8.85E-12; % Permittivity of Vacuum (C2 N-1 m-2)
    c=3E8; % Speed of Light (m s-2)
    el=1.6E-19; % Electronic Charge (C)
    k=1.38E-23; % Boltzmann Constant (J K-1)
    ng=pr*100./(k.*Tn); % Neutral Gas Density (m-3)
    yi=1./(ng.*1E-18); % Ion-Neutral Mean Free Path (m)
    hl=0.86.*(3+(L+B+D)./(2.*yi)).^-0.5; % Axial Sheath Diffusion
    hr=0.80.*((4+b./yi)).^-0.5; % Radial Sheath Diffusion

```

```

Aeff=2.*pi.*b.*(b.*hl+(L+B+D).*hr)+2.*pi.*O.*M.*hr+2.*pi.*rd.*(M-B+D).*hr;
% Effective Surface Area for Particle Loss (m 2)

%%%%%%%%%%%%%%%%%%%%%%%%%%%%%%%%%%%%%%%%%%%%%%%%%%%%%%%%%%%%%%%%%%%%%%%%
%                               Collision Frequency Parameters                               %
%%%%%%%%%%%%%%%%%%%%%%%%%%%%%%%%%%%%%%%%%%%%%%%%%%%%%%%%%%%%%%%%%%%%%%%%

TeK=Te.*11604.5; % Electron Temperature (K)
vel=((8.*k.*TeK)./(pi.*me)).^0.5; % Maxwellian Mean Electron Velocity
(m s-2)

sigH=CollData(:,2); % Collision Cross-Section (m-2)

EpsE=el.*CollData(:,1); % Electron Energies (J)

vc=ng.*sigH.*(2.*EpsE./me).^0.5+1i*w; % Direct Electron-Neutral Collision
Frequency (Hz)

dFedistdEpsEMax=-2./pi.^(1./2)./(el.*Te).^(3./2)./(el.*Te).*exp(-EpsE./
(el.*Te)); % Differential Maxwellian EEDF

ColldistF=dFedistdEpsEMax;

ven=real(-1.5.*(trapz(EpsE,EpsE.^1.5.*dFedistdEpsEMax./vc).^-1));

CA=23-log(((ne.^0.5).*(Te.^(-1.5)))/(10.^2)); % Coulomb Algorithm

vei=(ne.*(el.^4).*CA)/(4.*pi.*(epso.^2).*(me.^0.5).*(el.*Te).^1.5);
% Electron-Ion Collision Frequency (Hz)

wplasma=((el.^2.*ne)./(epso.*me)).^0.5; % Plasma Conductivity Parameter
(s-1)

dela=(c./wplasma).*((vel.*wplasma)/(2.*c.*w)).^(1./3); % Anomalous Skin
Depth (m)

vst=0.25.*vel./dela; % Stochastic Collision Frequency (Hz)

veff=ven+vei+vst; % Effective Electron Collision Frequency (Hz)

vperw=veff./w; % Effective Electron Collision Frequency per RF Angular
Frequency Ratio

%%%%%%%%%%%%%%%%%%%%%%%%%%%%%%%%%%%%%%%%%%%%%%%%%%%%%%%%%%%%%%%%%%%%%%%%
%                               H-Mode EM Field Physical Constants and Parameters                               %
%%%%%%%%%%%%%%%%%%%%%%%%%%%%%%%%%%%%%%%%%%%%%%%%%%%%%%%%%%%%%%%%%%%%%%%%

Ktheta=N.*Ip./a; % Coil Current Density (A m-1)

alpha2=(muo.*el.^2.*ne)./(me.*(1-li.*vperw)); % H-mode Plasma Conductivity
Parameter (m-2)

ynH=permute((besselzero(1,20,1))./b,[2 1]); % H-mode Bessel Solution
Roots (m-2)

kn=(alpha2+ynH.^2).^0.5; % Eigenvalues for H-Mode Bessel Functions (m-2)

```

```

%%%%%%%%%%%%%%%%%%%%%%%%%%%%%%%%%%%%%%%%%%%%%%%%%%%%%%%%%%%%%%%%%%%%%%%%
%           E-Mode EM Field Physical Constants and Parameters           %
%%%%%%%%%%%%%%%%%%%%%%%%%%%%%%%%%%%%%%%%%%%%%%%%%%%%%%%%%%%%%%%%%%%%%%%%

epsr=3.8; % Dielectric Constant (C2 N-1 m-2)
Eo=Vp./a; % Peak Coil Field (V m-1)
epspl=1-(((wplasma./w).^2)./(1-li.*(vperw))); % Permittivity of Plasma
(C2 N-1 m-2)
ynE=permute((besselzero(0,20,1))./b,[2 1]); % E-mode Bessel Solution Roots
(m-2)
qn=(ynE.^2-(w./c).^2.*epspl).^0.5; % Eigenvalues for E-Mode Bessel
Functions (m-2)
sn=(ynE.^2-(w./c).^2.*epsr).^0.5; % Eigenvalues for E-mode Bessel
Functions (m-2)

%%%%%%%%%%%%%%%%%%%%%%%%%%%%%%%%%%%%%%%%%%%%%%%%%%%%%%%%%%%%%%%%%%%%%%%%
%                               Sheath Thickness                               %
%%%%%%%%%%%%%%%%%%%%%%%%%%%%%%%%%%%%%%%%%%%%%%%%%%%%%%%%%%%%%%%%%%%%%%%%

Cd=eps0.*pi.*(rd.^2)./D; % Dielectric Capacitance (F)
ic=w.*Cd.*Vp; % Peak Capacitive Current (A)
Vc=(((9.*ic./(8.*pi.*rd.^2)).^2)./(1.73.*el.*eps0.*w.^2.*ne)).^2)./Te;
% Peak Capacitive Voltage (V)
Vs=Vc.*(rs./rd); % Sheath Voltage (V)
Js2=1.73.*el.*eps0.*w.^2.*ne.*(Te.*Vs).^0.5;
Sterm=(5.*Js2.^1.5)./(12.*el.^2.*w.^3.*eps0.*ne.^2.*Te);
S=(1./rd).*trapz(rs,Sterm); % Sheath Thickness (m)
DS=D+S; % Dielectric + Sheath Thickness (m)
EpsM=3.*Te./2; % Mean Electron Energy
DruvMaxRatio=1.27+14.60./EpsM; % Druvestyen Maxwellian Transition Change
Ratio
ubohm=(0.667.*el.*EpsM./mi).^0.5; % Bohm Velocity of Sheath Ions (ms-2)
LossTerm=ubohm.*Aeff.*EpsT.*el; % Loss Term for Loss Curve
Ploss=ne.*LossTerm.*(DruvMaxRatio.^(1./(1+(CDM.*ne./ng))));
% Electron Power Loss
PlossStack=cat(1,PlossStack,Ploss);

%%%%%%%%%%%%%%%%%%%%%%%%%%%%%%%%%%%%%%%%%%%%%%%%%%%%%%%%%%%%%%%%%%%%%%%%
%                               vn Solver (H-mode)                               %
%%%%%%%%%%%%%%%%%%%%%%%%%%%%%%%%%%%%%%%%%%%%%%%%%%%%%%%%%%%%%%%%%%%%%%%%

IntMatH=[];

```

```

for n=1:20

    Jint=r.*besselj(1,ynH(n).*r);

    Jtermint=trapz(r,Jint);

    IntMatH=cat(1,IntMatH,Jtermint);

end

betan=(1./(tanh(ynH.*L)).*(ynH.*tanh(kn.*L)+kn.*tanh(ynH.*DS))./
        ((ynH.*tanh(kn.*L).*tanh(ynH.*DS))+kn)); % Beta-n

IntJHTerm=- (Ktheta./(1+betan)).*permute(IntMatH,[2 1]);

DiffJHTerm=ynH.*(b.^2)./2.*(besselj(0,ynH.*b)-(1./(ynH.*b)).*besselj(1,
        ynH.*b)).^2);

vn=1i.*w.*muo.*(IntJHTerm./DiffJHTerm);

%%%%%%%%%%%%%%%%%%%%%%%%%%%%%%%%%%%%%%%%%%%%%%%%%%%%%%%%%%%%%%%%%%%%%%%%
%                               un Solver (E-mode)                               %
%%%%%%%%%%%%%%%%%%%%%%%%%%%%%%%%%%%%%%%%%%%%%%%%%%%%%%%%%%%%%%%%%%%%%%%%

IntMatE=[];

for n=1:20

    Jint=besselj(0,ynE(n).*r);

    Jtermint=trapz(r,Jint);

    IntMatE=cat(1,IntMatE,Jtermint);

end

IntJETerm=2.*1i.*w.*epsr.*Eo.*permute(IntMatE,[2 1]);

DiffJETerm=c.^2.*ynE.*sn.*b.^2.*(besselj(1,ynE.*b)).^2);

un=-IntJETerm./DiffJETerm;

%%%%%%%%%%%%%%%%%%%%%%%%%%%%%%%%%%%%%%%%%%%%%%%%%%%%%%%%%%%%%%%%%%%%%%%%
%                               H-Mode Field Boundary Constants                               %
%%%%%%%%%%%%%%%%%%%%%%%%%%%%%%%%%%%%%%%%%%%%%%%%%%%%%%%%%%%%%%%%%%%%%%%%

AnH=vn.*ynH./(ynH.*sinh(ynH.*DS).*sinh(kn.*L)+
        kn.*cosh(kn.*L).*cosh(ynH.*DS));

BnH=(AnH./(2.*ynH)).*exp(ynH.*L).*(ynH.*sinh(kn.*L)-kn.*cosh(kn.*L));

CnH=(AnH./(2.*ynH)).*exp(-ynH.*L).*(ynH.*sinh(kn.*L)+kn.*cosh(kn.*L));

%%%%%%%%%%%%%%%%%%%%%%%%%%%%%%%%%%%%%%%%%%%%%%%%%%%%%%%%%%%%%%%%%%%%%%%%
%                               E-Mode Field Boundary Constants                               %
%%%%%%%%%%%%%%%%%%%%%%%%%%%%%%%%%%%%%%%%%%%%%%%%%%%%%%%%%%%%%%%%%%%%%%%%

AnE=(epsr.*sn.*un)./(epsr.*sn.*cosh(qn.*L).*sinh(sn.*DS)+epsr.*qn.*
        sinh(qn.*L).*cosh(sn.*DS));

```

```

CnE=(AnE./(2.*epsr.*sn)).*exp(-sn.*L).*(epsr.*sn.*cosh(qn.*L)+
    epsr.*qn.*sinh(qn.*L));

DnE=(AnE./(2.*epsr.*sn)).*exp(sn.*L).*(epsr.*sn.*cosh(qn.*L)-epsr.*qn.*
    sinh(qn.*L));

%%%%%%%%%%%%%%%%%%%%%%%%%%%%%%%%%%%%%%%%%%%%%%%%%%%%%%%%%%%%%%%%%%%%%%%%
%                               H-Mode Power Iteration Loop                               %
%%%%%%%%%%%%%%%%%%%%%%%%%%%%%%%%%%%%%%%%%%%%%%%%%%%%%%%%%%%%%%%%%%%%%%%%

Ethethar=[];

for n=1:rlim

    Ethethasum=sum((BnH.*exp(-ynH.*(L+D+S))+CnH.*exp(ynH.*(L+D+S))).*
        besselj(1,ynH.*r(n)));

    Ethethar=cat(2,Ethethar,Ethethasum);

end

Ethetha=Ethethar;

PHMode=-pi.*Kthetha.*trapz(r,r.*Ethetha); % Absorbed H-mode Power (W)
PHModeAbs=abs(PHMode); % Absolute Absorbed H-mode Power (W)
PHModeReal=real(PHMode); % Real Component of Absorbed H-mode Power (W)
if isnan(PHModeReal)==1
    PHModeReal=0;
else
end

PHMStack=cat(1,PHMStack,PHModeReal);

%%%%%%%%%%%%%%%%%%%%%%%%%%%%%%%%%%%%%%%%%%%%%%%%%%%%%%%%%%%%%%%%%%%%%%%%
%                               E-Mode Power Iteration Loop                               %
%%%%%%%%%%%%%%%%%%%%%%%%%%%%%%%%%%%%%%%%%%%%%%%%%%%%%%%%%%%%%%%%%%%%%%%%

Bthethar=[];

for n=1:rlim

    Bthethasum=sum((CnE.*exp(sn.*(L+D+S))+DnE.*exp(-sn.*(L+D+S))).*
        besselj(1,ynE.*r(n)));

    Bthethar=cat(2,Bthethar,Bthethasum);

end

Bthetha=Bthethar;

Eradiusr=[];

for n=1:rlim

    Eradiussum=((1i.*c.^2)./(w.*epsr)).*sum(sn.*(CnE.*exp(sn.*(L+D+S))-
        DnE.*exp(-sn.*(L+D+S))).*besselj(1,ynE.*r(n)));

```

```

        Eradiusr=cat(2,Eradiusr,Eradiussum);

end

Eradius=Eradiusr;

PEMode=-(2.*pi./muo).*trapz(r,r.*Eradius.*conj(Btheta)); % Absorbed E-mode
Power (W)

PEModeAbs=abs(PEMode); % Absolute Absorbed E-mode Power (W)

PEModeReal=real(PEMode); % Real Component of Absorbed E-mode Power (W)

if isnan(PEModeReal)==1

    PEModeReal=0;

else

end

PEMStack=cat(1,PEMStack,PEModeReal);

%%%%%%%%%%%%%%%%%%%%%%%%%%%%%%%%%%%%%%%%%%%%%%%%%%%%%%%%%%%%%%%%%%%%%%%%%%
%                               Stochastic Sheath Power                               %
%%%%%%%%%%%%%%%%%%%%%%%%%%%%%%%%%%%%%%%%%%%%%%%%%%%%%%%%%%%%%%%%%%%%%%%%%%

Pstoc=0.61.*(me./el).^0.5.*epso.*w.^2.*Te.^0.5.*(trapz(rs,Vs.*2.*pi.*rs));
% Absorbed Sheath Power (W)

PstocStack=cat(1,PstocStack,Pstoc);

%%%%%%%%%%%%%%%%%%%%%%%%%%%%%%%%%%%%%%%%%%%%%%%%%%%%%%%%%%%%%%%%%%%%%%%%%%
%                               Total Absorbed and Reflected RF Power                               %
%%%%%%%%%%%%%%%%%%%%%%%%%%%%%%%%%%%%%%%%%%%%%%%%%%%%%%%%%%%%%%%%%%%%%%%%%%

Pabs=PHModeReal+PEModeReal+Pstoc; % Total Absorbed Power (W)

PabsStack=cat(1,PabsStack,Pabs);

veffStack=cat(1,veffStack,veff);

end

disp('Done');

end

ne=logspace(15,17);

loglog(ne,PabsStack)

hold on

loglog(ne, PlossStack)

hold off

PStack=[PabsStack PlossStack];

```

## APPENDIX E: AUXILLARY DATA AND RELATED PROGRAMS

### E.1. Argon Collision Cross Section Spreadsheet ('ArgonCC.xls')

**Table E.1:** Electron energies (eV) and the corresponding argon collision cross sections ( $\text{m}^{-2}$ )

Electron Energy (eV)	Argon Collision Cross Section ( $\text{m}^{-2}$ )
0	1E-19
0.01	6.5E-20
0.03	4.1E-20
0.1	1.63E-20
0.3	2.3E-21
1	1.55E-20
1.2	1.88E-20
1.5	2.42E-20
2	3.35E-20
2.5	4.25E-20
3	5.2E-20
4	7.15E-20
5	9.1E-20
6	1.1E-19
8	1.54E-19
10	1.85E-19
12	2.1E-19
15	2.25E-19
20	2.19E-19
25	1.9E-19
30	1.63E-19
40	1.29E-19
50	1.11E-19
60	1.02E-19
80	9E-20
100	8.2E-20
120	7.5E-20
150	6.9E-20
200	5.9E-20
250	5.2E-20
300	4.7E-20
400	4E-20
500	3.5E-20
600	3.1E-20
800	2.55E-20
1000	2.23E-20

**Table E.1**, continued...

1200	1.97E-20
1500	1.69E-20
2000	1.38E-20
2500	1.2E-20
3000	1.05E-20
4000	8.4E-21
5000	7.1E-21
6000	6.2E-21
8000	4.9E-21
10000	4.1E-21

## E.2. Bessel Zeros Function Code

The Bessel zeros function code ('besselzero.m') is downloadable from MATLAB Central:

<http://www.mathworks.com/matlabcentral/fileexchange/6794-bessel-function-zeros/content/besselzero.m>

```
-----  
  
function x=besselzero(n,k,kind)  
  
%%%%%%%%%%%%%%%%%%%%%%%%%%%%%%%%%%%%%%%%%%%%%%%%%%%%%%%%%%%%%%%%%%%%%%%%  
%  
% besselzero.m  
%  
% Find first k positive zeros of the Bessel function J(n,x) or Y(n,x)  
% using Halley's method.  
%  
% Written by: Greg von Winckel - 01/25/05  
% Contact: gregvw(at)chtm(dot)unm(dot)edu  
%  
%%%%%%%%%%%%%%%%%%%%%%%%%%%%%%%%%%%%%%%%%%%%%%%%%%%%%%%%%%%%%%%%%%%%%%%%  
  
k3=3*k;  
  
x=zeros(k3,1);  
  
for j=1:k3  
  
    % Initial guess of zeros  
    x0=1+sqrt(2)+(j-1)*pi+n+n^0.4;  
  
    % Do Halley's method  
    x(j)=findzero(n,x0,kind);  
  
    if x(j)==inf  
        error('Bad guess.');    end  
  
end  
  
x=sort(x);  
dx=[1;abs(diff(x))];  
x=x(dx>1e-8);  
  
x=x(1:k);  
  
function x=findzero(n,x0,kind)  
  
n1=n+1;    n2=n*n;  
  
% Tolerance  
tol=1e-12;  
  
% Maximum number of times to iterate  
MAXIT=100;  
  
% Initial error  
err=1;  
  
iter=0;  
  
while abs(err)>tol & iter<MAXIT  
  
    switch kind  
        case 1  
            a=besselj(n,x0);
```

```

        b=besselj(n1,x0);
    case 2
        a=bessely(n,x0);
        b=bessely(n1,x0);
    end

    x02=x0*x0;

    err=2*a*x0*(n*a-b*x0)/(2*b*b*x02-a*b*x0*(4*n+1)+(n*n1+x02)*a*a);

    x=x0-err;
    x0=x;
    iter=iter+1;

end

if iter>MAXIT-1
    warning('Failed to converge to within tolerance. ',...
        'Try a different initial guess');
    x=inf;
end

```

### E.3. Empty Excel Sheet Delete Code

The empty Excel sheet delete code ('deleteEmptyExcelSheets.m') is downloadable from MATLAB Central:

<http://www.mathworks.com/matlabcentral/fileexchange/25389-synthetic-microstructure-generator/content/deleteEmptyExcelSheets.m>

```
-----  
  
%created by: Quan Quach  
%date: 11/6/07  
%this function erases any empty sheets in an excel document  
  
function deleteEmptyExcelSheets(fileName)  
  
%the input fileName is the entire path of the file  
%for example, fileName = 'C:\Documents and Settings\matlab\myExcelFile.xls'  
  
excelObj = actxserver('Excel.Application');  
%opens up an excel object  
excelWorkbook = excelObj.workbooks.Open(fileName);  
worksheets = excelObj.sheets;  
%total number of sheets in workbook  
numSheets = worksheets.Count;  
  
count=1;  
for x=1:numSheets  
    %stores the current number of sheets in the workbook  
    %this number will change if sheets are deleted  
    temp = worksheets.count;  
  
    %if there's only one sheet left, we must leave it or else  
    %there will be an error.  
    if (temp == 1)  
        break;  
    end  
  
    %this command will only delete the sheet if it is empty  
    worksheets.Item(count).Delete;  
  
    %if a sheet was not deleted, we move on to the next one  
    %by incrementing the count variable  
    if (temp == worksheets.count)  
        count = count + 1;  
    end  
end  
excelWorkbook.Save;  
excelWorkbook.Close(false);  
excelObj.Quit;  
delete(excelObj);
```

## APPENDIX F: FITTING PARAMETERS FOR SIMULATION

Tables F.1, F.2 and F.3 list the fitting parameters for the absolute magnetic field simulations ( $|B_z|$  and  $|B_r|$ ) found in Chapter 6, Section 6.0.

**Table F.1:** Empirical fitting parameters for spatially resolved electron density,  $n_e(r, z)$  for different argon pressure.

Argon Pressure, $P/\text{mbar}$	Fitted Peak Electron Density, $n_{e, \text{peak}}/\text{m}^{-3}$	Radial Fitting Parameter, $\sigma_{r, n_e}$	Axial Fitting Parameter $\sigma_{z, n_e}$
0.03	$1.3 \times 10^{17}$	$0.2721(L - z) + 0.0387$	$0.06601 \exp \left( - \left( \frac{((L - z) - 0.1009)^2}{0.08554} \right) \right)$
0.07	$3.2 \times 10^{17}$	$0.259(L - z) + 0.0322$	0.065
0.2	$5.0 \times 10^{17}$	$0.0814(L - z) + 0.0441$	$0.1307 \exp \left( - \left( \frac{((L - z) - 0.07918)^2}{0.04616} \right) \right)$

**Table F.2:** Empirical fitting parameters for spatially resolved electron density,  $T_e(r, z)$  for different argon pressure.

Argon Pressure, $P/\text{mbar}$	Fitted Peak Electron Temperature, $T_{e, \text{peak}}/\text{eV}$	Radial Fitting Parameter, $\sigma_{r, T_e}$	Axial Fitting Parameter $\sigma_{z, T_e}$
0.03	3.75	$33.39(L-z)^2 - 4.143(L-z) + 0.2884$	0.150
0.07	3.10	$0.2344 \exp \left[ - \left( \left( \frac{(L-z) - 0.1015}{0.09049} \right)^2 \right) \right]$	$104.6(L-z)^3 + 38.09(L-z)^2 - 3.712(L-z) + 0.2132$
0.2	3.00	$14.76(L-z)^2 - 1.179(L-z) + 0.1226$	$0.1152 \exp \left[ - \left( \left( \frac{(L-z) - 0.08925}{0.1152} \right)^2 \right) \right]$

**Table F.3:** Heuristic fitting parameters for spatially resolved neutral gas temperature,  $T_n(r, z)$  for different argon pressures. Fitted  $T_n$  values were pegged at the minimum of 300 K (room temperature).

Argon Pressure, $P/\text{mbar}$	Fitted Peak Neutral Gas Temperature, $T_{n, \text{peak}}/\text{K}$	Radial Fitting Parameter, $\sigma_{r, T_n}$	Axial Fitting Parameter $\sigma_{z, T_n}$
0.03	1800	0.028	0.080
0.07	1900	0.032	0.080
0.2	2300	0.030	0.100

$L$  = Effective height of the chamber in m.

$z$  = Axial distance from the chamber lid in m.

•